Flow and Diffusion Measurements on Complex Fluids Using Dynamic NMR Microscopy

A thesis presented in partial fulfilment
of the requirements for the degree
of Doctor of Philosophy in Physics
at Massey University

Bertram Manz
1996

Abstract

This thesis deals with the measurement of fluid motion by NMR methods and the relationship of that motion both to the molecular organisation and to the fluid boundary conditions. The theory and technique of dynamic NMR microscopy are presented. A specially designed high gradient probe for Pulsed Gradient Spin Echo (PGSE) experiments is described.

First, the time evolution of electroosmotic flow in a capillary is measured. With increasing time after the application of an electrophoretic pulse a transition from plug flow to parabolic flow is found. The agreement of the measured flow profiles with theory is excellent.

Next, a two-dimensional velocity exchange experiment (VEXSY) is described. Experiments on unrestricted Brownian motion, laminar circular flow in a Couette cell and flow through microspheres are performed.

A major aspect of the thesis concerns molecular dynamics in semi-dilute polymer solutions close to a de-mixing transition. Therefore, a description of the Flory-Huggins model for the phase behaviour of polymer solutions is given along with a review of the literature on shear-induced effects in semi-dilute polymer solutions. PGSE experiments were performed in order to measure the temperature dependence of the self-diffusion coefficient of polystyrene in semi-dilute cyclohexane solutions near the de-mixing transition over a wide range of molar masses. The temperature dependence can be described by a Williams-Landel-Ferry (WLF) equation, characteristic of a glass transition. From the self-diffusion coefficients the values for the tube disengagement times were obtained.

NMR rheology experiments were performed on semi-dilute polystyrene/cyclohexane solutions near the de-mixing transition. The flow profiles exhibit power law behaviour, and from the power law index the entanglement formation times are extracted. A consistency of the values for the entanglement formation times and tube disengagement times was found.

As part of the study of polymer solutions at elevated temperatures, strong convectional effects were observed. In order to carry out diffusion measurements these effects were suppressed using better thermal equilibration. However, the

convection process itself was subject to NMR investigation. Convectional flow in a capillary was measured using PGSE NMR, VEXSY and dynamic NMR microscopy. The VEXSY experiment shows that the flow is stationary. The velocity propagator measured using dynamic NMR microscopy was used to calculate the echo attenuation function $E(q)$. It was found that the pronounced minima and maxima in the Stejskal–Tanner plots agree well with the measured $E(q)$ values.

Flow profiles of lyotropic liquid crystals are presented. Using deuterium NMR spectroscopy it is shown that the shear–induced alignment of molecules can be measured using NMR microscopy.

Acknowledgements

The following people have helped me with this work. It is a pleasure to thank them here.

Prof. Paul T. Callaghan, my first supervisor, for his constant support, enthusiasm and expertise.

Assoc. Prof. Rod K. Lambert, my second supervisor, for support and discussions.

The staff of the electronics workshop who built the shift register which enabled me to sleep at night while the experiments were running, and for helping me with many little problems.

The staff of the mechanical workshop for building a driving system for the Couette system and countless other items.

Grant Platt for building the dewars of the PGSE probe and for cutting and sealing my sample tubes.

Dr. Phil Back for designing and building the PGSE probe.

Dr. Bas Smeulders for supplying me with information about the Dobanol/Water system.

Dr. Joe Seymour who inspired me with his enthusiasm and gave me permission to use some of his data.

My fellow graduate students Andrew, Craig, Lucy and all other inhabitants of the NMR lab for being friends and colleagues.

The secretaries for their help with administration.

All members of the Physics department for maintaining a pleasant working environment.

The German Academic Exchange Service (DAAD) and the New Zealand Foundation for Research, Science and Technology for financial support.

Anna for putting up with me.

Contents

List of Figures

List of Tables

Chapter 1

Introduction

1.1 Introduction

Pulsed Gradient Spin Echo (PGSE) NMR is a well–established technique for measuring molecular displacements. In combination with NMR microscopy it provides a powerful and non–invasive tool to monitor flow and diffusion. A particular feature is the possibility of observing the dependence of flow or displacements on other physical parameters under investigation. An emphasis of this thesis is the measurement of the dependence of molecular displacements on time and on temperature in different systems.

Changes of molecular properties with time can be measured in different ways. If the parameter of interest is non–stationary, the easiest approach is simply to measure this parameter at different times. In the case of molecular displacements the time evolution of flow profiles provides a characteristic example. One particular case is the behaviour of electroosmotic flow after the application of an electric field. This flow can constitute a major disturbance in electrophoresis experiments. Knowledge of the flow profiles provides a test for theoretical models and thereby insight which may be used to compensate the disturbance. Using dynamic NMR microscopy we were able to measure the time evolution of electroosmotic flow.

Even in stationary flow, changes of molecular velocities can exist. A particular example is the laminar flow of a liquid between two rotating cylinders, where the fluid elements undergo circular motion. In such cases, the time dependence of molecular velocities can be monitored by a two–dimensional velocity exchange experiment. This method can also be used to extract the characteristic timescales of flow through a porous medium.

Polymer solutions are well–characterised model systems where many physical parameters can be chosen with ease, for example by varying the polymer chain

length, the concentration or the solvent quality. The latter property is strongly temperature dependent in the vicinity of the "theta" or de-mixing transition. A number of physical properties show significant changes in this vicinity and in this thesis we focus on changes in bulk hydrodynamic and microscopic Brownian dynamics. The PGSE method is widely used to measure the self-diffusion of polymers. The dependence of the polymer self-diffusion on parameters such as molar mass, concentration and time has been measured extensively. To the best of our knowledge, no measurements of the temperature dependence of the self-diffusion have been reported so far, and no theoretical model exists. We will describe such measurements at temperatures near the de-mixing transition. We will show that the temperature dependence of the self-diffusion coefficient can be described by a glass transition.

The entanglement concept has been highly successful in describing physical properties of polymers. A field which still lacks understanding is the shear rate dependence of the viscosity of polymers. It can often be described phenomenologically by one parameter, the so-called power law index. Theories for the non-linear viscoelastic behaviour state that this power law index is governed by entanglements. The characteristic relaxation time for entanglements shows a simple relationship to the self-diffusion coefficient. By measuring the power law index we have extracted this relaxation time and compared it to that obtained from measurements of the self-diffusion coefficient. Good agreement has been found.

The fact that shear rate changes influence the viscosity of polymer solutions raises the question of what happens on a molecular level. One hypothesis is that the molecules align in the flow field. With deuterium NMR spectroscopy one can directly measure the orientation of molecules. We show that in principle it is possible to measure the shear rate dependence of molecular orientations using NMR.

1.2 Organisation of the Thesis

All the experiments described in this thesis were performed using NMR. Therefore we introduce in chapter 2 the NMR phenomenon and review the basic theoretical and experimental concepts which will be required to understand the experiments described in later chapters. The principles of q-space, flow imaging and PGSE will be discussed.

In chapter 3 the flow imaging method will be applied to measure the time evolution of electroosmotic flow in a capillary. The experimental flow profiles are compared with a theoretical model.

A new two-dimensional exchange experiment is demonstrated in chapter 4. The VEXSY experiment correlates molecular displacements at one instant to the displacement of the same molecule at a later time. This method is demonstrated on unrestricted Brownian motion, laminar flow in a Couette cell, and flow through a bed of microspheres.

The next four chapters deal with polymer solutions. Chapter 5 introduces the basic polymer physics concepts and gives a review of the present literature on polymer solutions. In chapter 6 the PGSE method is used to measure the polymer self-diffusion coefficient of polystyrene/cyclohexane solutions. From this the tube disengagement times can be determined.

In chapter 7 a different approach is used. Here, the flow profiles of polymer solutions in the Couette cell are measured. Using a theoretical model for non-linear viscoelasticity the entanglement formation times for polymer coils can be obtained from the shape of these profiles. These times are compared with the values for the tube disengagement times obtained in chapter 6.

Chapter 8 deals with a problem which occurred during the early stages of the PGSE experiments described in chapter 6. At elevated temperatures, convectional motion can be a major problem when measuring self-diffusion. The timescale of convectional flow is investigated with three different techniques: PGSE, flow imaging and VEXSY.

Lyotropic liquid crystals also show interesting rheological behaviour. In chapter 9 flow profiles of such systems are measured. With deuterium NMR spectroscopy it is also shown that shear stress changes the orientation of molecules in the sample.

In chapter 10 we give some concluding remarks and discuss potential future work.

Chapter 2

Introduction to NMR and Imaging

The first nuclear magnetic resonance (NMR) experiments were performed just over 50 years ago independently by the groups of Purcell [1] and Bloch [2]. In the early days, NMR served mainly as a tool for measuring relaxation times. Hahn discovered the spin echo [3] in 1950, and when Ernst [4] pointed out that by the use of Fourier transformation (FT) the more efficient pulsed approach, which was pioneered by Hahn [5], could give the same multi–line spectra as the continuous wave (CW) method, a new tool for chemical analysis was born. Stejskal and Tanner [6] implemented the pulsed gradient spin echo (PGSE) method to measure molecular self–diffusion. In 1973, Mansfield [7] and Lauterbur [8] showed that proton density images can be obtained from a sample using magnetic field gradients. This discovery was the basis of a whole new field of research called magnetic resonance imaging (MRI) or NMR imaging. By combining the PGSE method with the NMR imaging method, one can obtain images of local velocity distributions in heterogeneous systems. This method is known as dynamic NMR imaging and was implemented by Callaghan *et al.* in 1988 [9]. The experiments of chapters 3, 7 and 9 were performed using the dynamic NMR imaging method, while chapter 6 deals with PGSE experiments. In chapter 4, we introduce a new exchange experiment, which bases on the dynamic imaging method. In chapter 8, we combine all three methods to measure convectional flow in a capillary.

In section 2.1, we will give a brief introduction to NMR. In section 2.2, we discuss some nuclear interactions which are important for the experiments later in this thesis. Section 2.3 describes basic spin manipulations which will be needed in section 2.4 to understand the imaging techniques. Finally, in section 2.5 we will give a brief description of the spectrometer and a specially designed probe for our

PGSE experiments described in chapter 6.

2.1 NMR Theory

There are many text books which deal with the topic of NMR theory. We refer to only a few of them [10]–[16] here.

Atomic nuclei are inherently quantum mechanical in their behaviour and are thus characterised by a set of quantum numbers. One quantum mechanical degree of freedom, which has no representation in the classical theory, is the spin. The spin quantum number I can only have integer or half–integer values. There are NMR experiments which can only be explained by a full quantum mechanical treatment [16] but, in many cases, a semi–classical treatment is sufficient. We will therefore give a brief quantum mechanical description of the nature of nuclear magnetisation, before proceeding with the semi–classical macroscopic description.

2.1.1 The Quantum Mechanical Description

2.1.1.1 Quantum Mechanical States and Operators

In quantum mechanics, the state of a particle can be described by a Hilbert vector $|\Psi(t)\rangle$. All observables are represented by hermitian operators A. A state $|\Phi\rangle$ is called an eigenstate of A if

$$A|\Phi\rangle = a|\Phi\rangle. \tag{2.1}$$

a is known as the eigenvalue of the state $|\Phi\rangle$. Two states $|\Phi_m\rangle$ and $|\Phi_n\rangle$ are called degenerate under A, if they are both eigenstates of A with the same eigenvalue. The eigenvalues of any hermitian operator are real numbers, and the eigenstates $|\Phi\rangle$ form a complete and orthogonal set. This means that any state $|\Psi\rangle$ can be expressed as a linear combination of the eigenstates $|\Phi\rangle$:

$$|\Psi\rangle = \sum_n a_n|\Phi_n\rangle \tag{2.2}$$

with

$$\langle\Phi_m|\Phi_n\rangle = \delta_{mn}. \tag{2.3}$$

If a particle is in a state $|\Psi\rangle$, which is not an eigenstate of the operator A, but given by the superposition in equation 2.2, the result of the measurement of the observable A represented by the operator A is given by

$$\langle\Psi|A|\Psi\rangle = \sum_{m,n} a_m^* a_n \langle\Phi_m|A|\Phi_n\rangle \tag{2.4}$$

$$= \sum_{m,n} a_m^* a_n c_n \langle\Phi_m|\Phi_n\rangle \tag{2.5}$$

$$= \sum_n |a_n|^2 c_n. \tag{2.6}$$

The meaning of this result is as follows. If we perform a single experiment on one particle, then the measurement will return the value c_n with a probability $|a_n|^2$. If we have a large number of identically prepared particles, then equation 2.6 represents an average of eigenvalues weighted by their respective probabilities. We will return to this so–called ensemble average at the end of this section.

2.1.1.2 Angular Momentum Operators

A quantum mechanical vector operator $\boldsymbol{I}$ is called an angular momentum operator, if its components I_x, I_y and I_z are observables satisfying the following relations [17]:

$$[I_x, I_y] = iI_z,\ [I_y, I_z] = iI_x,\ [I_z, I_x] = iI_y. \tag{2.7}$$

It follows that the three components of $\boldsymbol{I}$ cannot be observed at the same time. However, it is possible to show that

$$[\boldsymbol{I}^2, I_x] = [\boldsymbol{I}^2, I_y] = [\boldsymbol{I}^2, I_z] = 0. \tag{2.8}$$

In NMR, it is common to work in the basis where $\boldsymbol{I}^2$ and I_z commute. The eigenvalues of $\boldsymbol{I}^2$ are $I(I+1)$, where I is an integer or half–integer.

For example, a ^{1}H hydrogen nucleus (proton) has a value of $I = 1/2$, whereas a ^{2}H deuterium nucleus has $I = 1$. The eigenvalue m of I_z has $2I + 1$ possible values, being $m = -I, -I+1, \ldots, I-1, I$. For example, for protons m can have the two values of $m = -1/2$ and $m = 1/2$.

The quantum state of a nucleus, $|\Psi\rangle$, can be described as a combination of the basis states $|I, m\rangle$. Most of the time, we are dealing with nuclei for which I is the same and $|\Psi\rangle$ can be expressed as

$$|\Psi\rangle = \sum_{m=-I}^{I} a_m |m\rangle. \tag{2.9}$$

2.1.1.3 Nuclear Spins in a Magnetic Field

A particle spin is always linked with an angular momentum. The operator $\boldsymbol{L}$ of the angular momentum is just proportional to the spin operator $\boldsymbol{I}$:

$$\boldsymbol{L} = \hbar \boldsymbol{I}. \tag{2.10}$$

$\hbar$ is Planck's constant divided by 2π. Although the following model is wrong, it helps our intuition to imagine a nucleus as a spherical distribution of charged particles which rotates around its axis. Charged particles undergoing a circular motion

create a magnetic moment, which is proportional to the angular momentum:

$$\boldsymbol{\mu} = \gamma \boldsymbol{L}. \tag{2.11}$$

γ is known as the gyromagnetic ratio and is dependent on the nucleus in question. For protons, for example, γ has a value of $2.68 \cdot 10^8$ Hz T^{-1}, while for deuterons, γ is equal to $4.11 \cdot 10^7$ Hz T^{-1}. Our intuitive model fails for point-like particles, such as electrons, but equation 2.11 still remains correct.

The energy of a quantum mechanical state is characterised by the eigenvalues of the Hamilton (or energy) operator $\mathcal{H}$. For a particle with a magnetic moment $\boldsymbol{\mu}$ which is placed in a magnetic field $\boldsymbol{B}$, the associated Hamiltonian is

$$\mathcal{H} = -\boldsymbol{\mu} \cdot \boldsymbol{B}. \tag{2.12}$$

It is common to fix a coordinate system so that the z axis is along $\boldsymbol{B}$. Then equation 2.11 becomes

$$\mathcal{H} = -B_z \mu_z. \tag{2.13}$$

Note that μ_z is still a quantum mechanical operator. Substituting equations 2.10 and 2.11 into equation 2.13, we obtain

$$\mathcal{H} = -\gamma \hbar B_z I_z. \tag{2.14}$$

I_z has the eigenvalues m. This gives the discrete energy levels

$$E_m = -m\gamma\hbar B_z. \tag{2.15}$$

These discrete energy levels are called Zeeman levels.

The quantum mechanical selection rules state that there exist only first order transitions from the states $|m\rangle$ to states $|m \pm 1\rangle$. This corresponds to energy splittings of

$$\Delta E = \gamma \hbar B_z, \tag{2.16}$$

which is known as the Zeeman splitting. The frequency

$$\omega_L = \gamma B_z \tag{2.17}$$

is called the Larmor frequency.

2.1.1.4 The Ensemble Average

So far, our quantum mechanical treatment has referred to only one single particle. In an NMR experiment, we measure the signal of an ensemble of nuclei, which can be in different states $|\Psi\rangle$. We therefore have to average equation 2.6 over

the whole ensemble. This is done by splitting the ensemble into subensembles, in which all nuclei are in the same state $|\Psi\rangle$. p_Ψ is the probability that a nucleus is in the state $|\Psi\rangle$. The ensemble average of equation 2.6 is denoted by $\langle A\rangle$, and we obtain

$$\langle A\rangle = \overline{\langle\Psi|A|\Psi\rangle} = \sum_\Psi p_\Psi \langle\Psi|A|\Psi\rangle. \tag{2.18}$$

The bar denotes the ensemble average.

At this point, we define the density operator ρ, which is very useful for calculating the ensemble average. ρ is defined as [17, 18]

$$\rho = \sum_\Psi p_\Psi |\Psi\rangle\langle\Psi|. \tag{2.19}$$

The ensemble average of the expectation value of A, $\langle A\rangle$, can then be written as [17]

$$\langle A\rangle = \mathrm{tr}(A\rho). \tag{2.20}$$

2.1.1.5 Time Evolution

The dynamics of a quantum mechanical system is described by the Schrödinger equation [17, 18]:

$$i\hbar\frac{\partial}{\partial t}|\Psi(t)\rangle = \mathcal{H}|\Psi(t)\rangle. \tag{2.21}$$

$\mathcal{H}$ is again the Hamilton operator. If $\mathcal{H}$ is constant in time, the solution of equation 2.21 can be written as

$$|\Psi(t)\rangle = U(t)|\Psi(0)\rangle \tag{2.22}$$

with

$$U(t) = e^{-i\mathcal{H}t/\hbar}. \tag{2.23}$$

$U(t)$ is known as the evolution operator. Equations 2.22 and 2.23 can be used to calculate the time dependence of a state, if the initial state and the interaction are known.

The time evolution of the density operator ρ can be deduced from the Schrödinger equation and is given by the Liouville equation:

$$i\hbar\frac{\partial\rho}{\partial t} = [\mathcal{H},\rho]. \tag{2.24}$$

If $\mathcal{H}$ is constant in time, the solution of equation 2.24 is

$$\rho(t) = U(t)\rho(0)U^{-1}(t) \tag{2.25}$$

$$= e^{-i\mathcal{H}t/\hbar}\rho(0)e^{i\mathcal{H}t/\hbar}. \tag{2.26}$$

As an example, we calculate the time evolution of the expectation value of the operator I_x under a constant Hamiltonian. We assume $\rho(0) = I_x$. We obtain

$$\langle I_x(t) \rangle = \mathrm{tr}(I_x e^{-i\mathcal{H}t/\hbar} I_x e^{i\mathcal{H}t/\hbar}). \tag{2.27}$$

Finally, we can define a classical magnetisation vector $\boldsymbol{M}$ as

$$\boldsymbol{M} = N\gamma\hbar\boldsymbol{I}. \tag{2.28}$$

N is the number of spins per unit volume. With the density matrix, it can be shown [16] that in thermal equilibrium at temperatures such that $k_B T \gg \gamma\hbar B_z$, the average value $\langle M_z \rangle$ of the magnetisation along the magnetic field is

$$\langle M_z \rangle = \frac{N\gamma^2\hbar^2 I(I+1)}{3k_B T} B_z, \tag{2.29}$$

where k_B is the Boltzmann constant, and T is the absolute temperature. This macroscopic magnetisation vector $\boldsymbol{M}$ allows us for a classical picture of the quantum mechanical NMR phenomenon, which we will use from now on unless stated otherwise.

2.1.2 The Semi–Classical Picture

2.1.2.1 The Rotating Frame

The important parameter in the classical representation is the magnetisation vector $\boldsymbol{M}$. From classical electrodynamics it is known that a magnetic field $\boldsymbol{B}$ exerts a torque $\boldsymbol{M} \times \boldsymbol{B}$ on the magnetisation vector $\boldsymbol{M}$. From classical mechanics, we know that the torque is equal to the change in angular momentum:

$$\frac{d\boldsymbol{L}}{dt} = \boldsymbol{M} \times \boldsymbol{B}. \tag{2.30}$$

Since $\boldsymbol{L} = \gamma^{-1}\boldsymbol{M}$ (equation 2.11), we get

$$\frac{d\boldsymbol{M}}{dt} = \boldsymbol{M} \times (\gamma\boldsymbol{B}). \tag{2.31}$$

This equation holds, regardless of whether $\boldsymbol{B}$ is time dependent or not. We will now assume that $\boldsymbol{B}$ is constant in time. Then it is very useful to transform equation 2.31 into a coordinate frame, which rotates with as yet an arbitrary angular velocity Ω. Equation 2.31 then reads:

$$\frac{d\boldsymbol{M}}{dt} = \boldsymbol{M} \times (\gamma\boldsymbol{B} + \Omega). \tag{2.32}$$

Equation 2.32 tells us that the motion of $\boldsymbol{M}$ in the rotating frame obeys the same equation as in the stationary frame, provided the magnetic field $\boldsymbol{B}$ is replaced by an effective magnetic field $\boldsymbol{B}_{eff}$:

$$\boldsymbol{B}_{eff} = \boldsymbol{B} + \frac{\boldsymbol{\Omega}}{\gamma}. \tag{2.33}$$

It is most convenient now to choose as our rotating frame the frame, which rotates with the angular velocity $\boldsymbol{\Omega} = -\gamma \boldsymbol{B}$ around $\boldsymbol{B}$. In this frame, $\boldsymbol{M}$ remains stationary. This means that in the stationary frame, $\boldsymbol{M}$ rotates with the Larmor frequency around the static field $\boldsymbol{B}$.

2.1.2.2 Excitation

All modern pulse NMR spectrometers are equipped with a coil around the sample which is used to create an oscillating magnetic field perpendicular to the static field. Because the frequency of this oscillation is in the radio frequency range, this coil is called radio frequency (r.f.) coil. The same coil is also used as a detector for the change of magnetisation in the sample after the excitation of the nuclei, with which we will deal now.

In our stationary frame we define a coordinate frame with the unit vectors $\boldsymbol{i}$, $\boldsymbol{j}$, and $\boldsymbol{k}$ along the x, y, z axes, respectively, so that the z axis points along the static field $\boldsymbol{B}$ and the x axis along the alternating field. The static field can then be written as $\boldsymbol{B} = B_0 \boldsymbol{k}$. The alternating field $\boldsymbol{B}_1$ is assumed to oscillate with the Larmor frequency ω_L:

$$\boldsymbol{B}_1 = 2B_1 \cos \omega_L t \, \boldsymbol{i}. \tag{2.34}$$

We now break the oscillating field into two rotating components, $\boldsymbol{B}_r$ and $\boldsymbol{B}_l$, each of amplitude B_1, one rotating clockwise and the other anticlockwise, as shown in figure 2.1.

$$\boldsymbol{B}_r = B_1(\cos \omega_L t \, \boldsymbol{i} + \sin \omega_L t \, \boldsymbol{j}) \tag{2.35}$$

$$\boldsymbol{B}_l = B_1(\cos \omega_L t \, \boldsymbol{i} - \sin \omega_L t \, \boldsymbol{j}). \tag{2.36}$$

One of these components, $\boldsymbol{B}_l$, rotates in the same sense as the spin precession, due to the static field and will be responsible for the resonance phenomenon. The other component can be ignored if $B_1 \ll B_0$, which is the case in our experiments. We therefore can replace $\boldsymbol{B}_1$ by $\boldsymbol{B}_l$ to a very good approximation and write our total magnetic field as

$$\boldsymbol{B}(t) = B_1 \cos(\omega_L t) \, \boldsymbol{i} - B_1 \sin(\omega_L t) \, \boldsymbol{j} + B_0 \, \boldsymbol{k}. \tag{2.37}$$

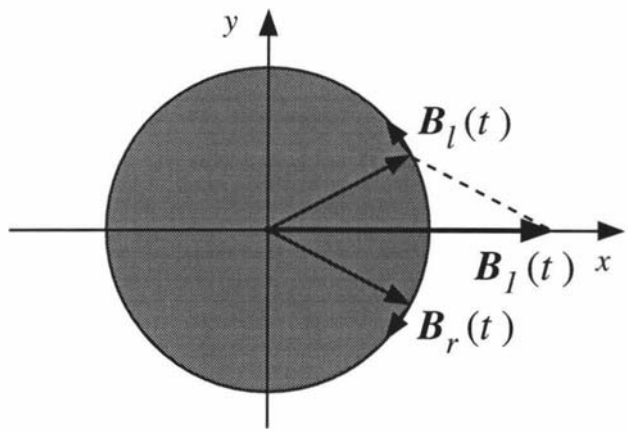

Figure 2.1: An oscillating magnetic field $\boldsymbol{B}_1(t)$ can be decomposed into the superposition of two counterrotating magnetic fields $\boldsymbol{B}_l(t)$ and $\boldsymbol{B}_r(t)$.

Equation 2.31 gives for each component:

$$\frac{dM_x}{dt} = \gamma(M_y B_0 + M_z B_1 \sin\omega_L t) \tag{2.38}$$

$$\frac{dM_y}{dt} = \gamma(M_z B_1 \cos\omega_L t - M_x B_0) \tag{2.39}$$

$$\frac{dM_z}{dt} = \gamma(-M_x B_1 \sin\omega_L t - M_y B_1 \cos\omega_L t) \tag{2.40}$$

Under the initial condition $\boldsymbol{M}(0) = M_0\boldsymbol{k}$, the solution for these equations is:

$$M_x = M_0 \sin\omega_1 t \sin\omega_L t \tag{2.41}$$

$$M_y = M_0 \sin\omega_1 t \cos\omega_L t \tag{2.42}$$

$$M_z = M_0 \cos\omega_1 t, \tag{2.43}$$

where $\omega_1 = \gamma B_1$.

The magnetisation vector $\boldsymbol{M}$ therefore precesses simultaneously around $\boldsymbol{B}_0$ with the Larmor frequency and around $\boldsymbol{B}_1$ with the frequency ω_1. In the rotating frame, where $\boldsymbol{B}_1$ is stationary, $\boldsymbol{M}$ just precesses around $\boldsymbol{B}_1$ with the frequency ω_1. By varying the duration of the oscillating magnetic field, one can tilt the magnetisation vector by an arbitrary angle. For example, if $\omega_1 t = \pi/2$, $\boldsymbol{M}$ is flipped by 90° from initially along the z axis into the xy plane. If $\omega_1 t = \pi$, $\boldsymbol{M}$ is flipped by 180°. By changing the phase of the oscillating field, the axis, around which $\boldsymbol{M}$ is rotated, can be changed. Usually, $\boldsymbol{M}$ is rotated around the x (or y) axis by 90° or 180°, and we denote these pulses as 90_x (90_y) or 180_x (180_x) pulses. Because the frequency of these pulsed signals is normally in the range of radio frequencies, these pulses are called radio frequency (r.f.) pulses.

The application of an r.f. pulse to a spin system can also be described using the quantum mechanical time evolution operator $U(t)$ defined in equation 2.23. The Hamiltonian describing an r.f. pulse which rotates the magnetisation around the x axis is given by [16]:

$$\mathcal{H}_{\text{Pulse}} = \hbar\omega I_x. \tag{2.44}$$

For a pulse which rotates the magnetisation around the y axis, I_x only has to be replaced by I_y in equation 2.44.

2.1.2.3 Relaxation

Equation 2.29 indicates that the thermal equilibrium magnetisation M_0 is along the direction of the magnetic field B_0. By r.f. pulse excitation, the spins are flipped from this thermal equilibrium position into positions which are energetically less favourable. According to equation 2.31 the spins would remain in a non-equilibrium position. Of course, there exists a characteristic timescale T_1, which depends on factors such as sample, temperature and strength of the static field B_0, in which the spins relax back to their thermal equilibrium position. This timescale T_1 is called longitudinal or spin-lattice relaxation time. As the name implies, the process involves an exchange with the reservoir, which is called lattice.

We therefore want to add a term to the equation for $\frac{dM_z}{dt}$, so that the solution for this term goes to M_0 for $t \gg T_1$, regardless of the value of $M_z(0)$. This can be achieved by the following term:

$$\frac{dM_z}{dt} = -\frac{M_z - M_0}{T_1}. \tag{2.45}$$

The solution is:

$$M_z(t) = M_z(0)e^{-t/T_1} + M_0(1 - e^{-t/T_1}). \tag{2.46}$$

The x and y components of $\boldsymbol{M}$ will decay to zero by the same relaxation process. The spins, however, interact with each other and tend to get to thermal equilibrium amongst themselves. This process is called spin-spin relaxation, and its timescale, T_2, is equal to or shorter than T_1. We therefore want to add to the transverse components of equation 2.31 a term which ensures that the solutions $M_{x,y}(t)$ decay to zero for $t \gg T_2$. Because the decay is dominated by the faster process, it is justified to omit the term with T_1. The phenomenological description for spin-spin relaxation can be written as:

$$\frac{dM_{x,y}}{dt} = -\frac{M_{x,y}}{T_2}. \tag{2.47}$$

Combining equations 2.45 and 2.47 with equation 2.31 gives the Bloch equations [10]:

$$\frac{dM_x}{dt} = \gamma(\boldsymbol{M} \times \boldsymbol{B})_x - \frac{M_x}{T_2} \tag{2.48}$$

$$\frac{dM_y}{dt} = \gamma(\boldsymbol{M} \times \boldsymbol{B})_y - \frac{M_y}{T_2} \tag{2.49}$$

$$\frac{dM_z}{dt} = \gamma(\boldsymbol{M} \times \boldsymbol{B})_z - \frac{M_0 - M_z}{T_1}. \tag{2.50}$$

From the values for T_1 and T_2 relaxation, one can extract useful information about the Hamiltonian and dynamics of a spin system. We will use the Bloch equations now to calculate the evolution of the magnetisation vector after applying a 90_x r.f. pulse.

2.1.2.4 Free Induction Decay

With the help of equations 2.41 – 2.43 we saw, that the magnetisation vector can be flipped from initially along the z axis into the xy plane by applying an r.f. pulse of the right duration. The solutions to the Bloch equations for the magnetisation directly after a 90_x pulse, when $\boldsymbol{M} = M_0\boldsymbol{j}$, are:

$$M_x = M_0 \sin(\omega_L t) e^{-t/T_2} \tag{2.51}$$

$$M_y = M_0 \cos(\omega_L t) e^{-t/T_2} \tag{2.52}$$

$$M_z = M_0(1 - e^{-t/T_1}). \tag{2.53}$$

The oscillating and decaying magnetisation in the xy plane is called free induction decay (FID) and is detected by the r.f. coil. A typical FID is shown in figure 2.2 for both x and y magnetisation. A complex Fourier transformation (FT) of this signal yields the absorption and dispersion spectrum of the sample [4]. The FT of the signal in figure 2.2 is a Lorentzian line with a width of $1/\pi T_2$. With the usual heterodyne detection, the peak will be centred at the frequency $\delta\omega = \omega_L - \omega_r$, where ω_r is the reference frequency of the mixing stage. The real part of the spectrum displayed in figure 2.3 (a) is the absorption spectrum, while the imaginary part displayed in (b) is the dispersion spectrum.

In practice, the signal is digitally sampled using N discrete sampling points in a time interval T. The spectrum obtained after a numerical FT then has a bandwidth of $1/T$, and the separation of the points in the frequency domain is $1/NT$.

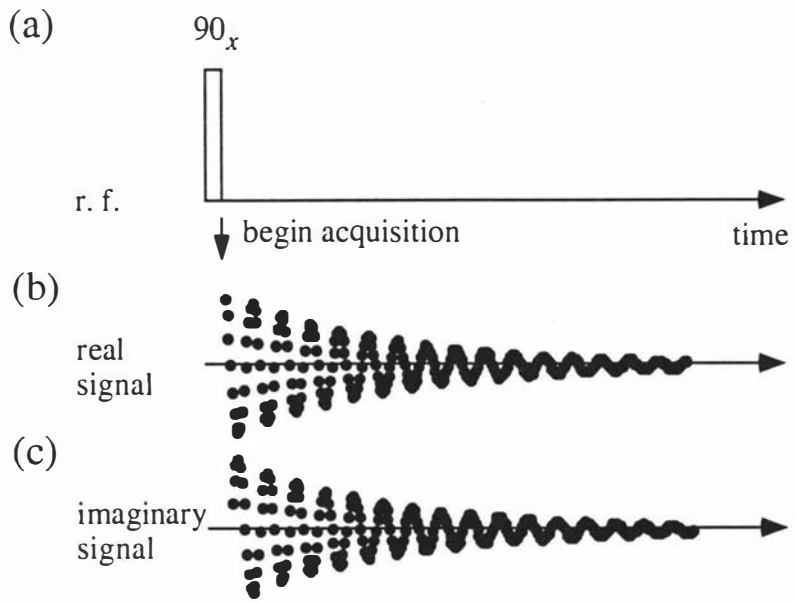

Figure 2.2: A typical free induction decay (FID) following a 90_x r.f. pulse which is displayed in (a). The real (b) and imaginary (c) parts of the signal are acquired by mixing the receiver signal with an in–phase and quadrature reference frequency.

2.2 Nuclear Interactions

2.2.1 Magnetic Field Inhomogeneity

Although modern NMR magnets are designed to provide homogeneous fields, the effect of local field inhomogeneities cannot be ignored. They result in a faster decay of the FID. The characteristic decay time, T_2^*, of the FID due to field inhomogeneities can be much shorter than the spin–spin relaxation time T_2. This results in an additional broadening of the spectral peaks, which is called inhomogeneous broadening in contrast to homogeneous broadening due to spin–spin relaxation. However, inhomogeneous broadening can be refocused by the spin echo technique, which we will discuss in section 2.3.

2.2.2 Chemical Shift

In a molecule, the nuclei are surrounded by the orbital electron clouds, which interact with the nuclear magnetic moment. The effect of the static magnetic field is that these orbits are perturbed in such a way that the magnetic field is shielded at the location of the nuclei. The magnitude of this effect depends on the shape of the electron orbits and therefore on the kind of chemical bonds between the atoms of a molecule. The result is that a nucleus "sees" a different magnetic

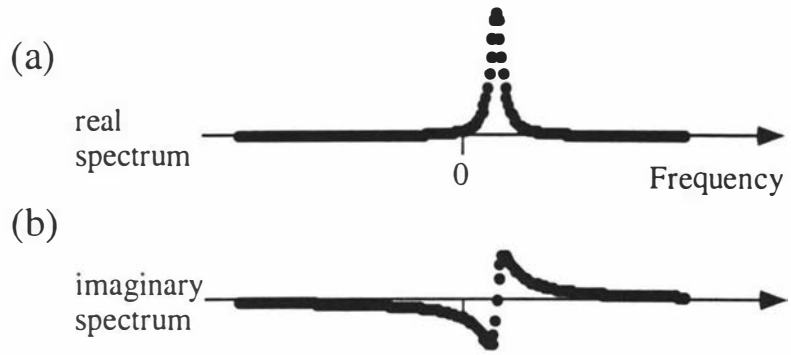

Figure 2.3: The Fourier transformation (FT) of the signal displayed in figure 2.2. The real part (a) gives the absorption spectrum, while the imaginary part (b) gives the dispersion spectrum.

field, depending on the electron orbit surrounding it. This results in a shift of the resonance peak in the absorption spectrum, called the chemical shift. In crystals, the magnitude of this effect also depends on the orientation of the chemical bond in the magnetic field, but in liquids, this orientation dependence gets averaged due to the rapid tumbling of the molecules. The Hamiltonian for the chemical shift is given by [10]:

$$\mathcal{H}_{CS} = -\sigma\hbar\omega_L I_z. \tag{2.54}$$

σ is called the isotropic chemical shift constant. From equation 2.54 it is obvious that the size $\Delta\omega$ of the chemical shift is proportional to the Larmor frequency ω_L and thus to the applied field B_0. A frequency independent parameter for this frequency shift is given by $\delta = \Delta\omega/\omega_L$. Because this shift is very small (of the order of 100 Hz for a Larmor frequency of 100 MHz), the chemical shift is usually given in parts per million (ppm). It is the chemical shift, which makes NMR such a valuable tool for chemical analysis, because nuclei with different chemical bonds will have different peak positions in the spectrum. Different atoms in a molecule can be distinguished with this method.

2.2.3 Dipolar Coupling

The intrinsic magnetic moment of a nucleus i produces a dipolar magnetic field, which interacts with the magnetic moment of a neighbouring nucleus j. The Hamiltonian for this dipolar interaction is given by [16]:

$$\mathcal{H}_D = \frac{\mu}{4\pi}\frac{\gamma^2\hbar^2}{r^3}\frac{1}{2}(1 - 3\cos^2\theta_{ij})(3I_{zi}I_{zj} - \boldsymbol{I}_i\boldsymbol{I}_j). \tag{2.55}$$

θ_{ij} is the angle between the connecting line of nuclei i and j and the static magnetic field.

Due to the rapid tumbling of the molecules, the dipolar coupling is usually very small in liquids. In solids, however, where the molecules are at fixed positions, the orientation dependence of the dipolar interaction leads to a significant broadening of the resonances.

2.2.4 Quadrupolar Coupling

Another interaction, which is important for nuclei with $I > 1/2$, is the quadrupolar coupling. It arises from the coupling of the nuclear quadrupole moment Q with the tensor of the electric field gradient caused by the electronic orbits. The Hamiltonian is given by [16]:

$$\mathcal{H}_Q = \frac{e^2Qq}{4I(2I-1)}\left(\frac{3\cos^2\theta - 1}{2}\right)(3I_z - I^2). \tag{2.56}$$

e is the electron charge, q is called the electric field gradient, and θ is the angle between the bond direction of the atom and the static magnetic field B_0. It is common to define the order parameter s and the quadrupolar splitting constant C_Q as:

$$s = \left\langle \frac{3\cos^2\theta - 1}{2} \right\rangle \tag{2.57}$$

$$C_Q = \frac{e^2qQ}{4\hbar}. \tag{2.58}$$

For a given I, the quadrupolar interaction shifts the energy levels with different m. For example, for a deuterium nucleus $I = 1$, and the energy levels are shifted as shown in figure 2.4 (a). The resulting absorption spectrum consists of a pair of lines, as shown in figure 2.4 (b). The amplitude of the line splitting is proportional to the order parameter s, which depends on the orientation of the molecule in the static magnetic field. The quadrupolar coupling therefore enables us to measure molecular orientations. We will use this method in chapter 9 to measure alignment of molecules in shear flow.

2.3 Spin Manipulations

2.3.1 The Spin Echo

The spin echo was first discovered by Hahn in 1950 [3]. Consider the pulse sequence shown in figure 2.5. The magnetisation vector for different times is shown in

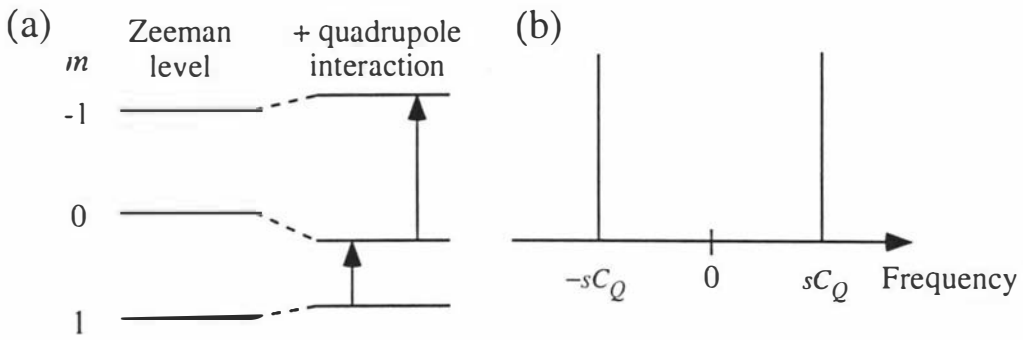

Figure 2.4: (a) The shift of the Zeeman levels due to the quadrupolar interaction is shown for a nucleus with $I = 1$. The two possible transitions are displayed by arrows. (b) The corresponding absorption spectrum consists of a pair of peaks separated by $2sC_Q$.

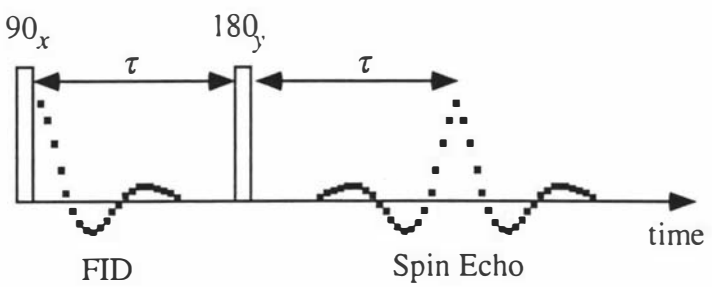

Figure 2.5: The spin echo pulse sequence. The FID decays exponentially with the time constant T_2^*. If after the time τ a 180° r.f. pulse is applied, the echo signal appears at a time τ after the 180° r.f. pulse.

figure 2.6. Just before the 90_x pulse, the magnetisation is assumed to be in thermal equilibrium along the z axis (figure 2.6 (a)). Immediately after the 90_x pulse, the magnetisation is then along the y axis (figure 2.6 (b)). Due to local field inhomogeneities, spins at different locations in the sample will precess with slightly different Larmor frequencies. As a result, the spins at one position in the sample will get out of phase with those in other positions, and the resultant signal decays (figure 2.6 (c)). Figure 2.6 (d) shows the effect of the 180_x pulse. During the second time delay τ, all the spins will again advance through the same angles as they did during the first time delay. At the time $t = 2\tau$, they are all in phase again (figure 2.6 (e)). This effect is called spin echo.

So far, we have neglected T_1 and T_2 effects. A detailed analysis [16] shows that the amplitude of the magnetisation at the time $t = 2\tau$ after the first pulse is

independent of T_1 and given by

$$M(2\tau) = M_0 e^{-2\tau/T_2}. \tag{2.59}$$

Equation 2.59 does not depend on local field inhomogeneities. Therefore it is possible to measure T_2 with the spin echo technique.

In liquids, the molecules move between different parts of the sample due to diffusional motion. The dephasing during the second delay time may differ from the dephasing during the first delay time, and the echo is not complete. If the local field variations are known, it is possible to measure self–diffusion in liquids. The first diffusion experiments were done by Hahn [3]. Carr and Purcell refined Hahn's method by applying many 180_x pulses [19]. Meiboom and Gill showed that slight errors in the flip angle of the 180° pulses are compensated if one uses 180_y pulses instead of 180_x pulses [20]. This pulse train is known as Carr–Purcell–Meiboom–Gill (CPMG) train. In 1965, Stejskal and Tanner came up with the idea of pulsed magnetic field gradients [6, 21]. The advantages of the Stejskal–Tanner experiment will be discussed in section 2.4.4.

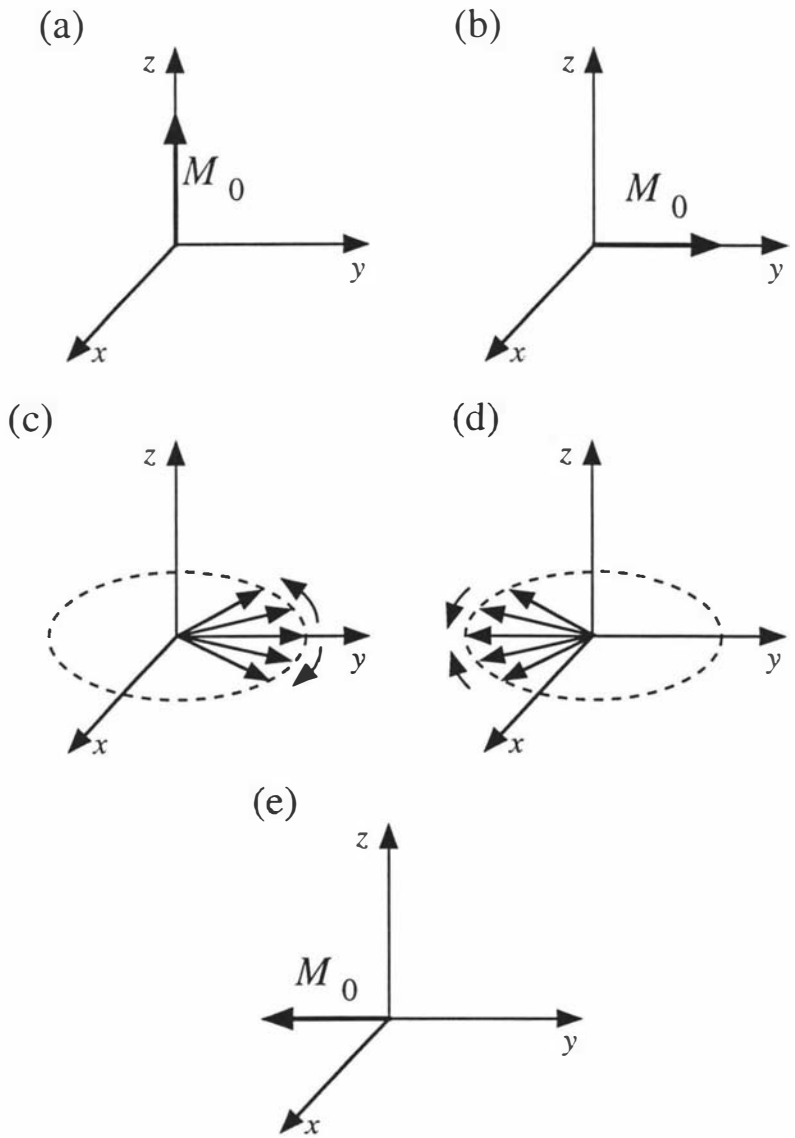

Figure 2.6: Formation of a spin echo by means of a $90_x - \tau - 180_x - \tau$ pulse sequence. (a) At the start, the magnetisation vector is parallel to the static magnetic field. (b) The 90_x r.f. pulse flips the magnetisation vector along the y axis. (c) The spins start to dephase due to local field inhomogeneities. (d) The 180_x r.f. pulse flips all spins by 180° around the x axis. (e) After the delay τ after the 180_x r.f. pulse all spins are in phase again.

2.3.2 The Stimulated Echo

In his original paper, Hahn also discussed the three pulse sequence shown in figure 2.7. There are three spin echoes at times $2\tau_1$, $2\tau_1 + 2\tau_2$, and $\tau_1 + 2\tau_2$ after the first r.f. pulse. They are the spin echoes of the first and second, first and third, and second and third r.f. pulse, respectively. Hahn found a fourth echo at time $t = 2\tau_1 + \tau_2$ after the first r.f. pulse. This is called the stimulated echo.

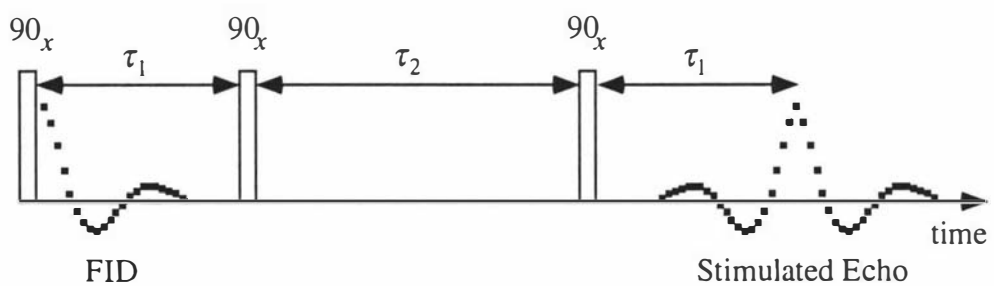

Figure 2.7: The stimulated echo pulse sequence. The stimulated echo appears at a time τ_1 after the third r.f. pulse.

In many samples, the spin–spin relaxation time T_2 is much shorter than the spin–lattice relaxation time T_1. In the stimulated echo pulse sequence, the transverse magnetisation is stored along the z direction by the second r.f. pulse before being tipped back into the transverse plane for detection. During the time τ_2, the magnetisation is aligned along the z axis and suffers only from T_1 relaxation. This can allow the echo formation over time intervals which would not be accessible by the spin echo. A clear disadvantage of the stimulated echo is the formation of multiple echoes due to the spin echoes of the three pulses, which can interfere with the stimulated echo. By applying a "crusher" gradient pulse between the second and third r.f. pulse, these unwanted spin echoes can be made to disappear.

Because of the problems with unwanted spin echo interferences, we use the stimulated echo method only in cases where we want particularly long delay times for the echo formation.

2.3.3 The Quadrupole Echo

In section 2.2.4 we saw that nuclei with spin quantum numbers $I > 1/2$ have a nonzero quadrupole moment Q. The dephasing of the magnetisation due to the quadrupolar coupling can be refocused by the quadrupole echo pulse sequence shown in figure 2.8. For the quadrupole echo pulse sequence it is important that the two r.f. pulses are phase shifted by 90 degrees which means that the 90_x

excitation pulse needs to be followed by a 90_y refocusing pulse. The magnetisation is refocused at the time 2τ after the first r.f. pulse.

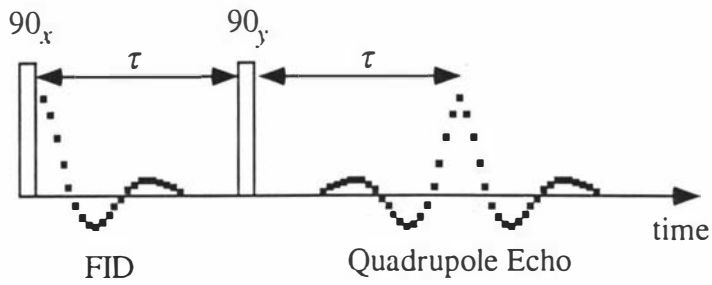

Figure 2.8: The quadrupole echo pulse sequence consists of two 90° r.f. pulses, which are out of phase by 90°. The echo signal appears at a time τ after the second 90° r.f. pulse.

The quadrupole echo pulse sequence will be used in chapter 9 to measure alignment of molecules in shear flow.

2.3.4 Two–Dimensional Spectroscopy

If two or more spins are coupled, the properties of such a system cannot be fully characterised by a conventional one–dimensional (1D) spectrum. Two–dimensional (2D) spectroscopy is a general concept which makes it possible to acquire more information about the system under investigation. It was first proposed by Jeener in 1973 [22] and the experimental realisation followed in 1974 by Ernst *et al.* [23].

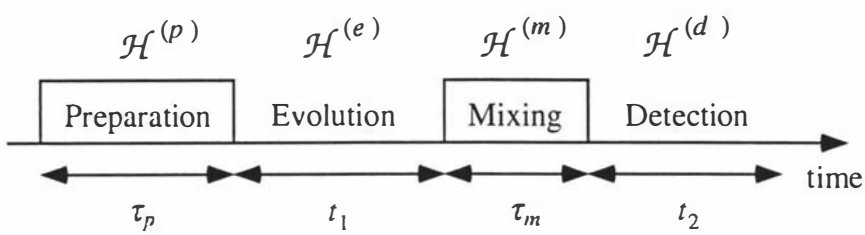

Figure 2.9: Basic scheme for a two–dimensional experiment.

In Ernst's terminology [12], a 2D spectrum represents a signal function $S(\omega_1, \omega_2)$ of two independent frequency variables. In the classic 2D time–domain experiment, the signal $s(t_1, t_2)$ is measured as a function of two independent time variables and is converted into a 2D frequency spectrum by a 2D FT. The pulse train consists of the sequence "preparation–evolution–mixing–detection", as shown in figure 2.9. In the preparation period τ_p, the spin system is prepared in a coherent

non–equilibrium state, which will evolve in the subsequent periods. In the simplest case, the preparation period is just one r.f. pulse. During the evolution period t_1, the spin system evolves freely under the influence of a specific Hamiltonian. The evolution during t_1 determines the frequencies in the ω_1–domain. The t_1–domain is sampled by carrying out a series of experiments with systematic incrementation of t_1. The mixing period τ_m may consist of one or more pulses separated by intervals. During the mixing period, the spins may change their magnetisation, orientation or other parameters which are characteristic of the system under investigation. The evolution of the spins during the detection period t_2 finally determines the frequencies in the ω_2–domain.

Ernst distinguishes between three types of 2D NMR spectroscopy: separation of interactions, correlation methods and exchange. If the Hamiltonian is composed of terms of different physical origin, it is often possible to decompose the complex 1D spectrum by the choice of two suitable effective Hamiltonians $\mathcal{H}^{(e)}$ and $\mathcal{H}^{(d)}$ for the evolution and detection period. In the 2D spectrum, the spectrum due to $\mathcal{H}^{(e)}$ is then along the ω_1 axis, while the spectrum due to $\mathcal{H}^{(d)}$ is along the ω_2 axis. With correlation methods, one can measure the interaction between spins. The simplest experiment is based on the sequence 90_x–t_1–(β)–t_2. This experiment is termed correlation spectroscopy (COSY). The transfer of coherence is induced by the pulse of flip angle β. From the appearance of cross–peaks in the 2D correlation spectra the coupling parameters can be identified. With exchange spectroscopy, dynamic processes, such as chemical exchange or spin diffusion, can be measured. The fundamental idea is the labelling of spins before exchange takes place, such that after the mixing time, the magnetisation can be traced back. One particular 2D exchange experiment, due to Spiess *et al.* [24, 25, 26], provides a relevant example. Here the ω_1 and ω_2 dimensions are dominated by dipolar or quadrupolar interactions in which the frequency offset relates directly to local bond angle. The mixing period consists of the storage of Zeeman order along the magnetic field direction so that the recall of magnetisation at a later time reveals angular correlations arising from the angular reorientation of polymer segments which occurred over the mixing time τ_m.

In chapter 4 this idea of exchange will be extended to a different frequency space. The equivalent ω_1 and ω_2 dimensions correspond to the movements Z_1 and Z_2 over two well defined time intervals, which are separated by the mixing time.

2.3.5 Signal Averaging and Phase Cycling

In many cases the signal acquired in one NMR experiment is not strong enough to extract meaningful data. One repeats therefore one experiment N times, adding

up the signal from the individual scans. This increases the signal amplitude by a factor of N, while the noise level increases by a factor of $N^{1/2}$. Thus, the signal–to–noise ratio increases by a factor of $N^{1/2}$. Between two scans, one has to wait for the magnetisation to come to thermal equilibrium. This is usually the case after times of 2–3 T_1. The T_1 value for protons in most liquids used in this thesis is less than 1 s. Therefore, repetition times of 1–1.5 s are considered long enough for the experiments in this thesis.

The NMR signal is usually overlapped by background interferences. These interferences can have various sources, such as d.c. offset in the amplifier of the receiver. By changing the phases of the r.f. pulses between different scans and adding or subtracting the signal in the correct way, one can suppress these interferences. Hoult and Richards [27] describe a four–step phase cycling which nullifies artifacts like d.c. offset in the receiver stage and imperfect phase settings of the r.f. pulses. For most experiments in this thesis, it was sufficient to employ a two–step phase cycle, which only nullifies the d.c. offset in the receiver. This two–step phase cycling is shown in figure 2.10.

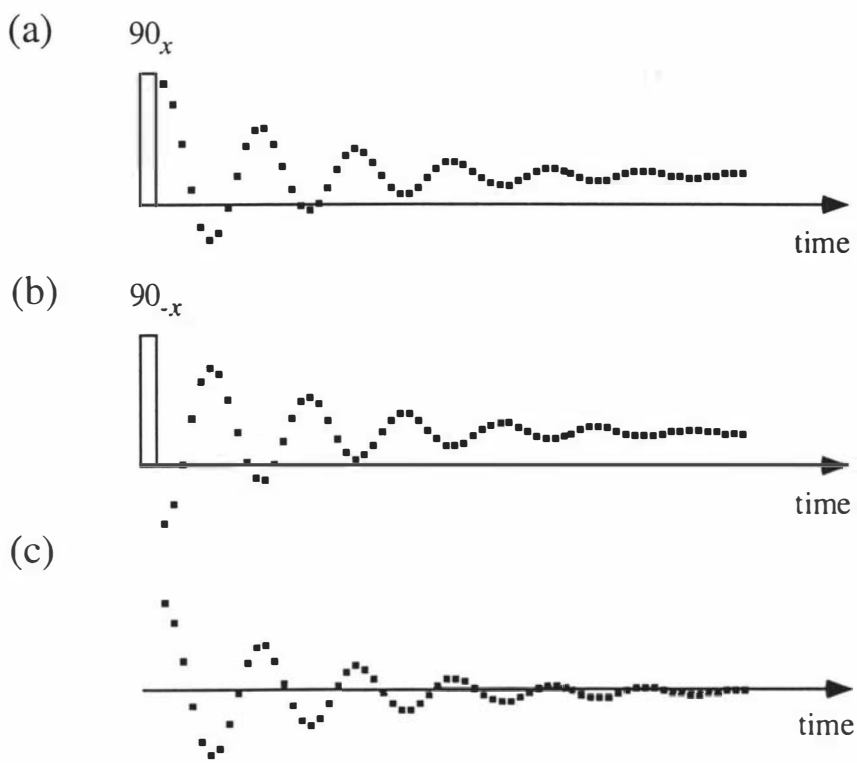

Figure 2.10: (a) The FID after a 90_x r.f. pulse is acquired with a d.c. offset on the receiver. (b) The FID after a 90_{-x} r.f. pulse. (c) Subtraction of the signals acquired in (a) and (b) cancels out the d.c. offset, but adds the FIDs.

2.3.6 The Effect of Magnetic Field Gradients

In NMR spectroscopy, one is usually concerned to get the magnetic field inside the sample as homogeneous as possible. Several layers of shim coils and specially designed pulse sequences ensure that the broadening due to field inhomogeneities is smaller that the natural linewidth. However, if one wants to extract the spatial dependence of molecules in the sample, one deliberately has to vary the magnetic field across the sample. These magnetic field variations are created by specially designed gradient coils through which large, switchable currents can be passed.

Because the field variations due to the switchable gradients are much smaller than the static field $\boldsymbol{B}_0$, only the component of the gradient parallel to $\boldsymbol{B}_0$ needs to be considered. The components of the field gradient can then be written as

$$G_x = \frac{\partial B_z}{\partial x} \tag{2.60}$$

$$G_y = \frac{\partial B_z}{\partial y} \tag{2.61}$$

$$G_z = \frac{\partial B_z}{\partial z}. \tag{2.62}$$

Because the magnetic field varies across the sample, the Larmor frequency will depend on the spatial coordinate $\boldsymbol{r}$. The local Larmor frequency $\omega(\boldsymbol{r})$ is given by

$$\omega(\boldsymbol{r}) = \gamma B_0 + \gamma \boldsymbol{G} \cdot \boldsymbol{r}. \tag{2.63}$$

Equation 2.63 is the basic equation for NMR imaging. In the next section we will use this equation to calculate the NMR signal of a sample in a linearly varying magnetic field.

2.4 Introduction to NMR Imaging

2.4.1 $\boldsymbol{k}$–Space Imaging

Consider a sample of local spin density $\rho(\boldsymbol{r})$. If we neglect relaxation effects, the complex NMR signal dS of a small volume element dV is given by

$$dS = \rho(\boldsymbol{r}) e^{i\omega(\boldsymbol{r})t} dV. \tag{2.64}$$

Using equation 2.63, we obtain

$$dS = \rho(\boldsymbol{r}) e^{i(\gamma B_0 + \gamma \boldsymbol{G}\cdot\boldsymbol{r})t} dV. \tag{2.65}$$

In the receiver, the radio–frequency signal is mixed with a reference frequency. This process is known as heterodyne mixing. If one chooses as a reference frequency γB_0, the signal oscillates only with a frequency $\gamma \boldsymbol{G} \cdot \boldsymbol{r}$, which is in the

audio-frequency range. Equation 2.65 can then be rewritten as

$$dS = \rho(\boldsymbol{r})e^{i\gamma \boldsymbol{G}\cdot\boldsymbol{r}t}dV. \tag{2.66}$$

Integration across the whole sample yields:

$$S(\boldsymbol{G}) = \int\int\int \rho(\boldsymbol{r})e^{i\gamma \boldsymbol{G}\cdot\boldsymbol{r}t}d^3r. \tag{2.67}$$

Equation 2.67 has the form of a Fourier transformation. To make this relationship more clear, we define a reciprocal space vector $\boldsymbol{k}$ as [28]

$$\boldsymbol{k} = (2\pi)^{-1}\gamma \boldsymbol{G}t. \tag{2.68}$$

The magnitude k of $\boldsymbol{k}$ therefore depends on both the duration and the magnitude of the gradient. The direction of $\boldsymbol{k}$ is given by the direction of $\boldsymbol{G}$.

With the reciprocal space vector $\boldsymbol{k}$. equation 2.67 can be written as

$$S(\boldsymbol{k}) = \int\int\int \rho(\boldsymbol{r})e^{i2\pi \boldsymbol{k}\cdot\boldsymbol{r}}d^3r. \tag{2.69}$$

The local spin density $\rho(\boldsymbol{r})$ can be obtained from equation 2.69 by inverse Fourier transformation:

$$\rho(\boldsymbol{r}) = \int\int\int S(\boldsymbol{k})e^{-i2\pi \boldsymbol{k}\cdot\boldsymbol{r}}d^3k. \tag{2.70}$$

Equations 2.69 and 2.70 state that S and ρ are mutually conjugate parameters. This is the fundamental relationship for NMR imaging. In practice, one scans the signal stepping the magnitude of all three components of G independently. A subsequent numerical FT yields $\rho(\boldsymbol{r})$. However, for a full three-dimensional image, this process is very time consuming. In many cases, one is only interested in the two-dimensional projection of one or a few thin planar slices through the sample, comparable to the slice of a micrograph. The key to this method is the excitation of a single, predetermined, layer of spins, a process known as selective excitation.

2.4.2 Selective Excitation

In order to select a thin layer (slice) of spins, we need to do two things. Firstly, we need to apply a gradient perpendicular to our selected slice. Then we need a method to excite the spins within a certain frequency range, which corresponds to the thickness of our slice, as shown in figure 2.11. We discuss the latter first.

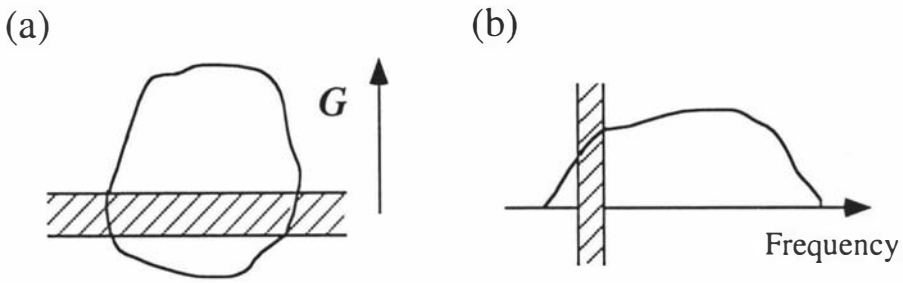

Figure 2.11: (a) Applying a gradient perpendicular to the selected slice (a) corresponds to a certain range of frequencies (b).

2.4.2.1 Hard Pulses and Soft Pulses

In order to find an r.f. pulse which excites only spins which have Larmor frequencies within a certain range, we consider an r.f. pulse with carrier frequency ω_p and duration T_p. The frequency spectrum of such a pulse is a $\mathrm{sinc}\, x = \frac{\sin x}{x}$ function, centred at ω_p with a width $2/T_p$. For example, a pulse with a duration of 2 ms has a bandwidth of 1 kHz.

Because the bandwidth of the r.f. pulse is inversely proportional to its duration, we will use short pulses if we want to excite all spins in the sample, and long pulses to excite thin slices. The correct tip angle θ is given in section 2.1.2.2 by $\theta = \gamma B_1 T_P$, where B_1 is the amplitude of the r.f. field. For a given bandwidth, B_1 can be varied in order to get the correct tip angle. By convention, the short, intense and therefore broadband r.f. pulses are called hard pulses, while the longer, weaker and narrowbanded r.f. pulses are called soft pulses.

For a perfect slice, the frequency spectrum of a rectangular shaped pulse is not very useful. The aim is a rectangular frequency spectrum, centred around the carrier frequency ω_s. An inverse FT shows that an r.f. pulse, in which the carrier frequency is modulated by a sinc function has the required frequency spectrum.

In practice, one cannot have a perfect sinc modulated pulse, because it extends to infinite times. It is a good approximation to truncate the soft pulse after two lobes to both sides of the central maximum. Such a truncated sinc shaped pulse of total duration T_s then has a bandwidth of $5/T_s$. In our experiments, we always used a soft pulse duration of $T_s = 2$ ms, making a bandwidth of 2.5 kHz.

Having found a method to excite spins within a certain frequency range, we can now return to the problem of slice selection.

2.4.2.2 Slice Selection

To select a slice of a given thickness Δz, we apply a gradient perpendicular to the slice. The strength G_s of this gradient is given by the thickness of the slice and the bandwidth $\Delta\omega$ of the soft pulse:

$$G_s = \gamma^{-1}\frac{\Delta\omega}{\Delta z}. \tag{2.71}$$

It can be shown [11] that the spins dephase during a 90° slice selective soft pulse due to the gradient. They can subsequently be rephased if a gradient pulse with amplitude $-G_s$ and duration $T_s/2$ is applied. A 180° soft pulse in a spin echo sequence does not need any refocusing.

We now return to equation 2.70 and take into account that we excite only thin slices in one direction. This leads us to the two–dimensional imaging method.

2.4.3 Fourier Imaging in Two Dimensions

Having established a method to limit our experiment to two dimensions, we must encode the signal for these remaining directions. If the slice gradient is applied in the direction of the static field (z direction), equation 2.69 simplifies to

$$S(k_x, k_y) = \int\int \rho(x, y)e^{i2\pi(k_x x + k_y y)}dxdy. \tag{2.72}$$

Now we can imagine $\boldsymbol{k}$–space as a plane with k_x and k_y axes, and we will sample a finite number N^2 of points (grid) in that plane. If this grid is based on Cartesian coordinates, the sampling method is called Fourier imaging (FI) [29].

Because of the time dependence of equation 2.68, we can obtain points along one line in $\boldsymbol{k}$–space if we sample the signal in the presence of a gradient. This gradient is called the read gradient. Unless otherwise stated, this direction always corresponds to the x direction in our experiments. This line in $\boldsymbol{k}$–space being sampled in the presence of a read gradient now has to be moved up and down the k_y axis. This can be achieved by applying the gradient G_y for a period before sampling. This so–called phase gradient causes a phase shift which varies linearly with position along the y axis, while the read gradient causes a frequency shift along the x axis.

In order to sample along the full grid in $\boldsymbol{k}$–space, it is necessary to sample for positive as well as negative k–values. k_y can easily be reversed by reversing the gradient. As for the read gradient, however, it is not obvious how to obtain negative times.

By using the spin echo method, we can shift the time origin. The echo appears with a delay τ after the 180° pulse and from that time on the signal resembles

the FID. Therefore we assign negative times to times before the echo appears. We usually set the sampling interval so that the echo appears in the centre of the acquisition time.

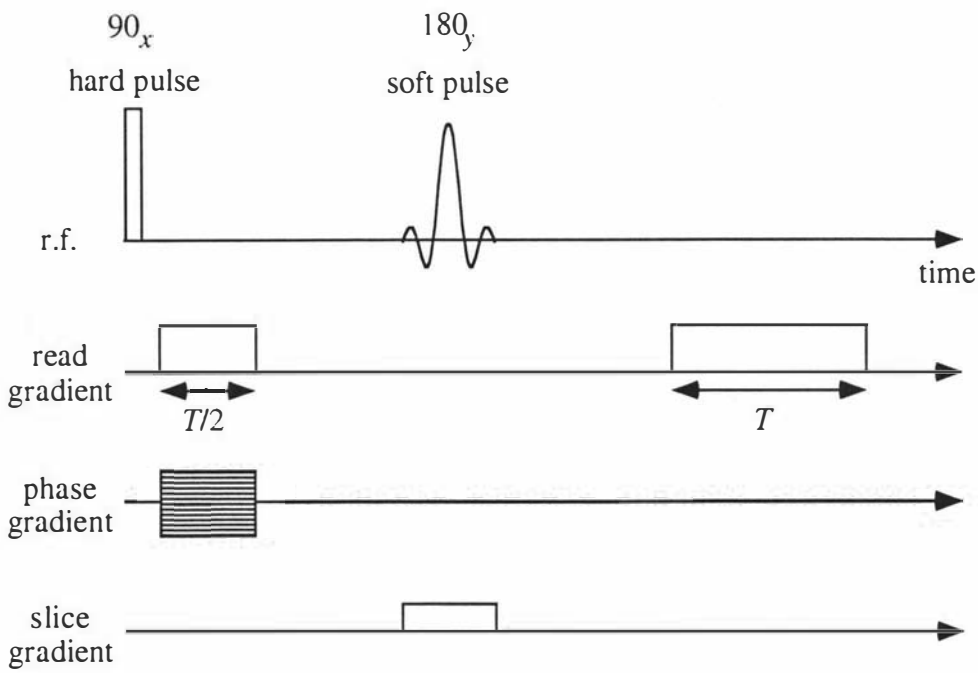

Figure 2.12: The spin warp pulse sequence for Fourier imaging. The read gradient is on during signal acquisition. The phase gradient is incremented between each scan.

The pulse sequence for FI, called spin warp [30], is shown in figure 2.12. The spin echo sequence consists of a hard 90° excitation pulse and a slice selective soft 180° soft pulse. In principle, we could also use a soft 90° and a hard 180° pulse. However, we favour the first method, because inhomogeneities in the r.f. field can lead to leakages of the hard 180° pulse. A soft 180° pulse refocuses only spins from a small region, in which the r.f. field is expected to be more homogeneous than across the whole sample. Spins in regions outside the slice can create an FID when using the (soft 90)–(hard 180) sequence if the 180° pulse is not perfect but, say, only a 160° pulse.

The read gradient between the 90° and the 180° pulses is called precursor read gradient. It dephases the spins in order to shift the echo maximum to the centre of the acquisition time. The phase gradient is increased in N steps from $-G_p$ to G_p between different scans. N is the number of encoding steps in each direction. The acquisition time T was defined in section 2.1.2.4.

A typical experiment has $N = 128$ steps for encoding in each direction of $\boldsymbol{k}$–space. With a repetition time T_r and N_{av} signal averages, the total experiment

time is $T_{exp} = N_{av} N T_r$. Normally, we choose $T_r = 1$ s and $N_{av} = 2$, giving a typical experiment time of $T_{exp} = 256$ s, which is just over 4 minutes for a two–dimensional image.

We saw that with the spin warp method we can obtain images of the spin density distribution $\rho(x, y)$ in a sample. It does not matter, whether the molecules are stationary or not. In the next section, we will discuss the PGSE method which is sensitive to displacements of molecules, but has not the spatial resolution of the spin warp. In section 2.4.5 we combine the spin warp and the PGSE techniques to form a three–dimensional experiment, with which we can obtain flow and diffusion maps.

2.4.4 Measuring Self–Diffusion: The Pulsed Gradient Spin Echo

The first NMR measurements of molecular displacements were reported by Hahn in 1950 [3]. He observed a decrease of the echo signal due to self–diffusion in an inhomogeneous static magnetic field. The idea is that the dephasing of the spins due to local field inhomogeneities does not get refocused by the 180° pulse if the spins change position during the echo delay. This method is still in use. With superconducting magnets, where one coil is reversed, self–diffusion coefficients of polymers can be measured down to $2 \cdot 10^{-15}$ m^2 s^{-1} [31].

A big disadvantage of the steady gradient method is that the gradient is on the whole time, especially during the r.f. pulses and acquisition. This broadens the spectrum, and the bandwidth of transmitter and receiver therefore limit the strength of the gradient which can be applied. McCall *et al.* suggested in 1963 to switch the gradient off during the r.f. pulses and acquisition, but have high gradients in the delays between [32]. In 1965, Stejskal and Tanner performed the first practical implementation of this idea, the so–called pulsed gradient spin echo (PGSE) method [6]. The pulse sequence is shown in figure 2.13. A review of different techniques to measure self–diffusion based on the PGSE method is given in [33].

We expect that the echo signal depends on both relaxation and gradient. The effects of T_2 relaxation can be removed by normalising the echo signal $S(g, \delta, \Delta)$ to its value $S(0)$ with no gradient applied. The ratio $S(g, \delta, \Delta)/S(0)$ is called echo attenuation $E(g, \delta, \Delta)$. It can be shown [6, 21] that $E(g, \delta, \Delta)$ is given by

$$E(g, \delta, \Delta) = e^{-\gamma^2 g^2 \delta^2 D(\Delta - \delta/3)}, \tag{2.73}$$

which is the Stejskal–Tanner equation. D is the self–diffusion coefficient of the sample. A plot of $\log E(g, \delta, \Delta)$ vs. $\gamma^2 g^2 \delta^2 \quad (\Delta - \delta/3)$ is called a Stejskal–Tanner plot and is expected to give a straight line with slope $-D$. An example for a

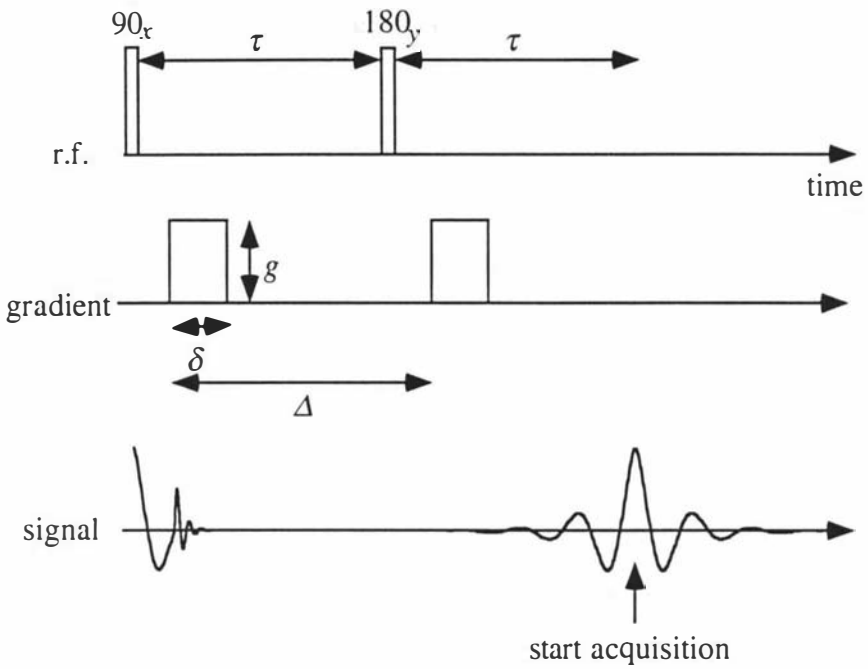

Figure 2.13: The Pulsed Gradient Spin Echo

Stejskal–Tanner plot is shown in figure 2.16 (37). Because there is no gradient applied during the data acquisition, the PGSE method yields the whole spectrum of the sample. For a multi–component system, it is therefore possible to measure the self–diffusion coefficient for each component in the same experiment, a method which was first demonstrated by James and McDonald in 1973 [34].

Our PGSE experiments were performed on polymer solutions with a polymer/solvent ratio of around 5/95. The self–diffusion coefficient of the solvent $D_s \approx 10^{-9}$ m^2 s^{-1}, while the self–diffusion coefficient of the polymer $D_p < 10^{-11}$ m^2 s^{-1}. Because $D_s \gg D_p$, it is possible to eliminate the strong solvent peak in the spectrum by a pair of gradient pulses. By successively increasing the duration of the gradient pulses and leaving all other parameters the same, it is possible to measure D_p. In our experiments, we used values of Δ between 10 ms and 40 ms and gradient strengths of up to 4.5 T m^{-1}. The duration δ of the gradient pulses was incremented from $\delta = 1$ ms in 16 steps of 0.5 ms or 1 ms, depending on the sample. With these parameters, it is possible to measure self–diffusion coefficients down to 10^{-15} m^2 s^{-1}.

The PGSE method is very useful for measuring *uncorrelated* motion. In the next section, we will combine the PGSE method with the spin warp technique.

This gives us a technique to measure correlated motion as well. Because this is an imaging method, we have the same spatial resolution as with the spin warp method.

2.4.5 Dynamic NMR Imaging

2.4.5.1 Introduction to q–Space

In order to discuss the phase shift of moving molecules due to gradient pulses, we need to introduce some new parameters. A molecule i can be characterised by the function $\boldsymbol{r}_i(t)$ which describes its position at any time t. In the PGSE experiment shown in figure 2.13, the phase shift $\Delta\Phi$ is given by

$$\Delta\Phi = \gamma\delta\boldsymbol{g}\cdot(\boldsymbol{r}-\boldsymbol{r}'). \tag{2.74}$$

The total signal is an ensemble average aver the whole sample in which each phase term is weighted by the average propagator $\overline{P}_s(\boldsymbol{R},t)$ [35] which gives the probability that a molecule moves the distance $\boldsymbol{R}=\boldsymbol{r}'-\boldsymbol{r}$ during the time t. The echo signal $E_\Delta(\boldsymbol{g})$ is then

$$E_\Delta(\boldsymbol{g}) = \int \overline{P}_s(\boldsymbol{R},\Delta)e^{i\gamma\delta\boldsymbol{g}\cdot\boldsymbol{R}}d\boldsymbol{R}. \tag{2.75}$$

Signal attenuations due to T_2 relaxation can be removed by normalising $E_\Delta(\boldsymbol{g})$ to $E_\Delta(\boldsymbol{g}=0)=1$.

Equation 2.75 is again a Fourier relationship. We therefore define a reciprocal space vector $\boldsymbol{q}$ such that [11]

$$\boldsymbol{q} = (2\pi)^{-1}\gamma\delta\boldsymbol{g}. \tag{2.76}$$

Equation 2.75 can then be written as

$$E_\Delta(\boldsymbol{q}) = \int \overline{P}_s(\boldsymbol{R},\Delta)e^{i2\pi\boldsymbol{q}\cdot\boldsymbol{R}}d\boldsymbol{R}. \tag{2.77}$$

Equation 2.77 gives the normalised echo signal in a PGSE experiment. In the next section we combine the PGSE and spin warp techniques. This will enable us to obtain velocity and diffusion maps.

2.4.5.2 The Dynamic Spin Echo

The dynamic spin echo pulse sequence is shown in figure 2.14. It is the same as the spin warp pulse sequence in figure 2.12 with a pair of gradient pulses added, which is stepped in amplitude. The dynamic spin echo is therefore a three–dimensional experiment. The echo signal $S(\boldsymbol{k},\boldsymbol{q})$ is now given by

$$S(\boldsymbol{k},\boldsymbol{q}) = \int \rho(\boldsymbol{r})e^{i2\pi\boldsymbol{k}\cdot\boldsymbol{r}}\int \overline{P}_s(\boldsymbol{R},\Delta)e^{i2\pi\boldsymbol{q}\cdot\boldsymbol{R}}d\boldsymbol{R}d\boldsymbol{r}. \tag{2.78}$$

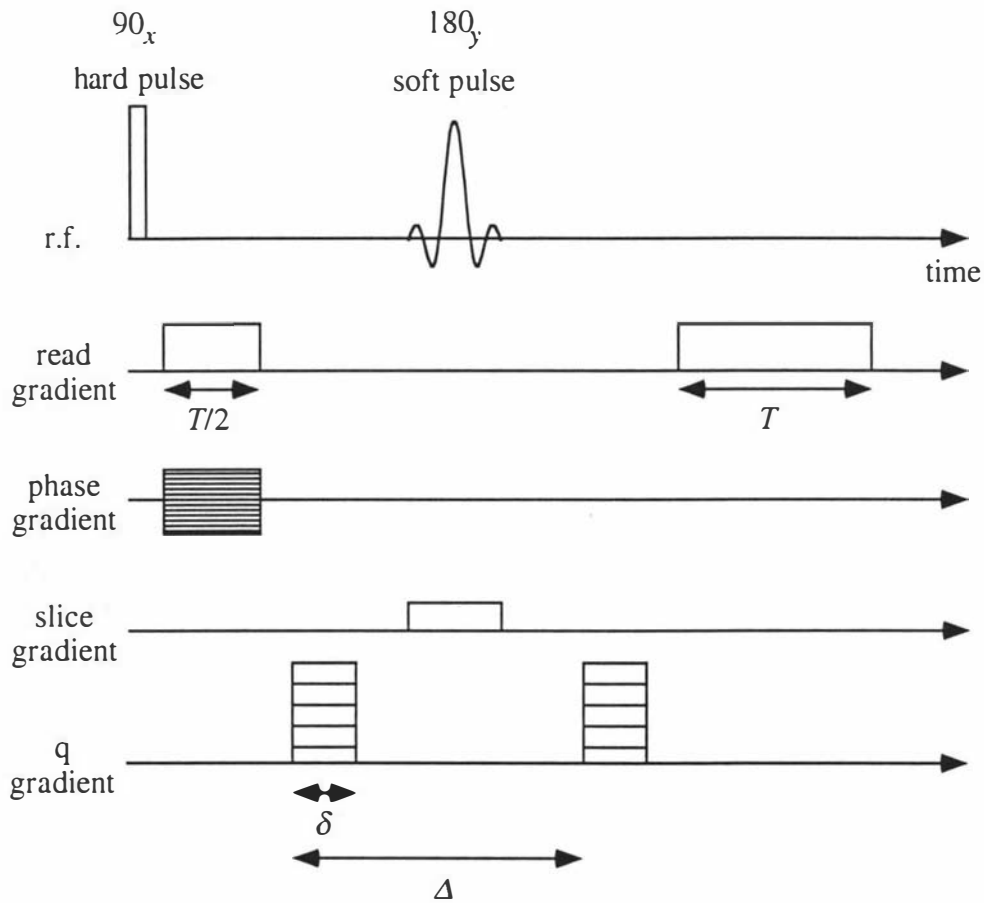

Figure 2.14: The dynamic spin echo pulse sequence for flow imaging incorporating both $\boldsymbol{k}$ space and $\boldsymbol{q}$ space encoding.

$\overline{P}_s(\boldsymbol{R}, \Delta)$ is now the average propagator in a small volume element. In equation 2.78 we can carry out the $\boldsymbol{R}$ integration:

$$E_\Delta(\boldsymbol{q}, \boldsymbol{r}) = \int \overline{P}_s(\boldsymbol{R}, \Delta) e^{i2\pi \boldsymbol{q}\cdot\boldsymbol{R}} d\boldsymbol{R}. \tag{2.79}$$

Equation 2.78 becomes then

$$S(\boldsymbol{k}, \boldsymbol{q}) = \int \rho(\boldsymbol{r}) E_\Delta(\boldsymbol{q}, \boldsymbol{r}) e^{i2\pi \boldsymbol{k}\cdot\boldsymbol{r}} d\boldsymbol{r}. \tag{2.80}$$

By normalising $E_\Delta(\boldsymbol{q}, \boldsymbol{r})$ to $E_\Delta(0, \boldsymbol{r}) = 1$ and using the inverse FT of equations 2.79 and 2.80, we can obtain $\rho(\boldsymbol{r})$ and $\overline{P}_s(\boldsymbol{R}, \Delta)$:

$$\rho(\boldsymbol{r}) = \int S(\boldsymbol{k}, \boldsymbol{q} = 0) e^{-i2\pi \boldsymbol{k}\cdot\boldsymbol{r}} d\boldsymbol{k} \tag{2.81}$$

$$E_\Delta(\boldsymbol{q}, \boldsymbol{r}) = \int S(\boldsymbol{k}, \boldsymbol{q}) e^{-i2\pi \boldsymbol{k}\cdot\boldsymbol{r}} d\boldsymbol{k} / \rho(\boldsymbol{r}) \tag{2.82}$$

$$\overline{P}_s(\boldsymbol{R}, \Delta) = \int E_\Delta(\boldsymbol{q}, \boldsymbol{r}) e^{-i2\pi \boldsymbol{q}\cdot\boldsymbol{r}} d\boldsymbol{q} \tag{2.83}$$

For purely Brownian motion with diffusion coefficient D, the propagator $\overline{P}_s(\boldsymbol{R}, \Delta)$ is a Gaussian with width $2D\Delta$. If the molecules are also undergoing coherent motion with velocity v, the peak of the propagator is shifted by $v\Delta$ [11].

The dynamic spin echo enables us to measure correlated and uncorrelated displacements of molecules, with a velocity resolution of a few microns per second and a spatial resolution on the order of 10 microns.

The dynamic spin echo and the pulsed gradient spin echo are methods to measure changes in position of molecules. In chapter 4 we will demonstrate the VEXSY pulse sequence which enables us to monitor changes in molecular velocities.

2.5 Hardware and Software

So far, we have looked at the different techniques to obtain information about the spatial distribution of molecules or their displacements. In this section we will briefly describe the hardware and software used for the experiments in this thesis.

2.5.1 The Bruker AMX300 Spectrometer

All the experiments in this thesis were performed using a commercial Bruker AMX300 spectrometer. Unless stated otherwise, the experiments were performed in a superconducting magnet with a magnetic field strength of 7 T, corresponding to a Larmor frequency of 300 MHz for protons.

A variety of r.f. coils is available with the Bruker microimaging probe. In our experiments we used either a 15 mm diameter cavity resonator coil or a 5 mm diameter saddle coil. The power of the r.f. transmitter is 50 W, giving 90° pulse durations of 15 μs and 5 μs, respectively. The Bruker microimaging gradient coil provides magnetic field gradients in all three directions. The currents are provided by Bruker AFPA30 power supplies and can go up to 30 A. At maximum current, gradient strengths of 0.35 T m^{-1} in the x and y directions, and 1.2 T m^{-1} in the z direction are available. All gradient coils are actively shielded and have eddy current ringdown times of less than 1 ms.

The temperature can be controlled in the range between $-50°$ C and $+200°$ C by a Bruker VT2000 temperature control unit. Compressed air is blown past a heating coil and then along the sample. The temperature is measured by a copper–constantan thermocouple sitting in the air stream just below the sample. Cooling below room temperature can be achieved by using cold nitrogen gas from the evaporation of liquid nitrogen. With this setup, the temperature can be controlled with an accuracy of $\pm 0.1°$ C.

The data were acquired by running the program UXNMR on an ASPECT X32 computer. The time domain data are stored as 4 byte integers in a serial file where the in-phase and quadrature phase components alternate. Processed data are stored as matrices in separate files for real and imaginary parts of the images. The dimensions of these matrices depend on the size of the corresponding images.

The UXNMR software has the nice feature of AU programs. These macro-type programs are written in the C language and can be called from UXNMR. They can also call many UXNMR commands. They are very convenient if one wants to do a set of experiments on the same sample. An example of an AU program for several experiments with different temperatures is shown in appendix C.

For the experiments in chapters 3 and 7 it was necessary to have available external TTL pulses at fixed times in the pulse sequence. The UXNMR software provides these with the commands `setf2^n` and `setf2|n`. `n` is a number between 0 and 7 and corresponds to the output channel at back panel 1 (BP1) of the spectrometer console. An example for the implementation of TTL pulses in a pulse sequence is shown in appendix B. In section 7.1.1 we will have a closer look at such a pulse sequence.

2.5.2 The FX60 Spectrometer

The experiments in section 4.3.2 required stronger gradient pulses than those which are available with the Bruker microimaging probe. They were therefore performed by using the microimaging probe and 1.4 T electromagnet of a modified Jeol FX60 spectrometer. A detailed description of this spectrometer is given in [36] and [37]. The experiments were driven by the AMX300 spectrometer operating at 60 MHZ. The r.f. transmitter output of the AMX300 was connected to the input of the duplexor of the FX60, while the receiver was connected to the output of the preamplifier. Although the cables to connect transmitter and receiver of the AMX300 to the FX60 probe were much longer than in a typical NMR spectrometer, the loss of signal-to-noise was less than a factor of 2.

2.5.3 The High-Gradient Probe

The experiments in chapter 6 required very high field gradients as well as accurate temperature control. The available Bruker microimaging probe has a very good temperature control, but the gradients are not sufficiently strong. On the other hand, the existing probes for the FX60 spectrometer can produce large gradients, but the temperature control is poor. Therefore we decided to build a new probe for the AMX300 spectrometer, which can produce high gradients.

The body of this new probe is made from aluminium. The plans for all components can be found in appendix A.

2.5.3.1 The Gradient Coils

The rapidly changing magnetic fields arising from fast switching of the gradient pulses cause eddy currents in surrounding metal layers, especially in the magnet bore. These fields have the undesirable effect of persisting after the gradient pulse has been turned off, but can be significantly reduced by shielding the field outside the coil. This can be achieved by a second gradient coil (secondary coil) which is outside the first (primary) coil. The field of the secondary coil is designed to cancel the field of the primary coil outside as much as possible. This procedure is known as active shielding and was first suggested by Mansfield and Chapman in 1986 [38]. Our primary coil is a pair of Maxwell coils with 92 turns of copper wire. The specifications of both primary and secondary coil are given in table 2.1. The coils are connected to the power supply as shown in figure 2.15. The current through the screen coil can be adjusted by the variable resistor R_z in order to reduce eddy currents to a minimum.

	Inductance [μH]	Resistance [Ω]
Primary Coil	335	1.09
Secondary Coil	30.6	0.51

Table 2.1: Specifications of the gradient coils.

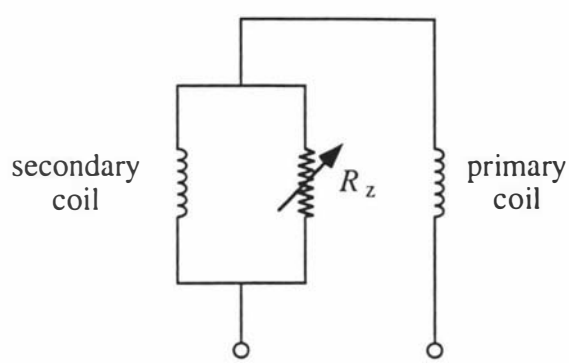

Figure 2.15: Circuit diagram showing the connection of primary and secondary coils.

2.5.3.2 Gradient Calibration

The gradient was calibrated by measuring the self-diffusion coefficient of water at an ambient temperature of 20° C with the PGSE method. A plot of $\log E$ vs. $\gamma^2\delta^2 I^2 \delta^2 \Delta_r$ is shown in figure 2.16 (a). Using the literature value for the self-diffusion coefficient of water of $2.04 \cdot 10^{-9}$ m^2 s^{-1} [39], we can work out the gradient strength to be 0.50 ± 0.05 T m^{-1} A^{-1}. This calibration method is considered to be very accurate, but does not yield any information about the homogeneity of the gradient. Therefore, the magnetic field inside the gradient coil was also mapped using a Hall probe. A graph of field strength vs. distance is shown in figure 2.16 (b). It shows that the gradient is constant within a range of ±5 mm from the centre. A linear regression in this region yields again a gradient of 0.5 T m^{-1} A^{-1} which is the same as we obtained by the self-diffusion method.

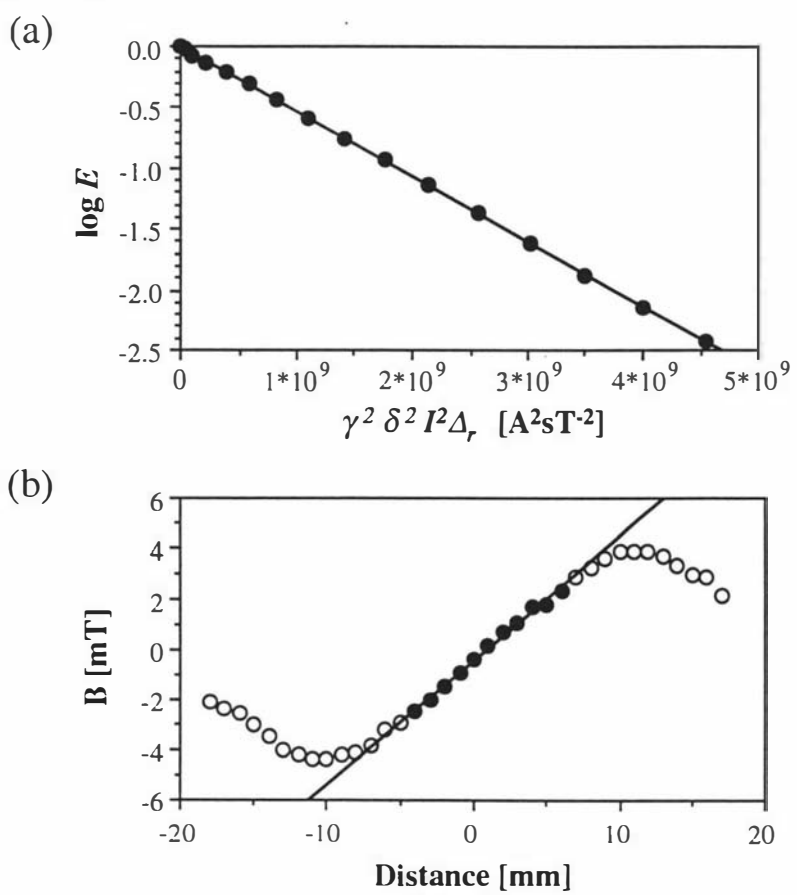

Figure 2.16: (a) A Stejskal–Tanner plot of doped water in the high gradient probe. By using the literature value of $2.04 \cdot 10^{-9}$ m^2 s^{-1}, we calibrate the gradient to be 0.5 T m^{-1} A^{-1}. (b) The magnetic field along the coil axis for a current of 1 A, measured with a Hall probe. The full circles indicate the range of constant gradient. The line is a regression of these points and yields a gradient of 0.5 T m^{-1} A^{-1}.

2.5.3.3 Gradient Eddy Currents

In order to be able to optimise the parameters for our PGSE experiments, it is important to know how long the eddy currents will persist after the gradient is turned off. This can be achieved by recording the FID after a variable delay τ after turning off the gradient, as shown in figure 2.17 (a). This procedure is known as pre-emphasis test. We recorded 8 FIDs after delay times τ of τ = 0.15, 0.3, 0.5, 1.0, 2.0, 5.0, 10.0 and 20.0 ms after switching off the gradient pulse. These are shown in figure 2.17 (b) and (c) for two different gradient strengths. For short delay times τ, the fields due to eddy currents distort the FID significantly, but we can see that the eddy currents have decayed after 2 ms even for gradients as large as 7.5 T m^{-1}. This means that we need to have a delay of at least 2 ms each time the gradient is turned off. A delay of 2 ms is considered short and does not cause any problems in our experiments.

It was also found that none of the FIDs changed when repeating the same experiment. From this we conclude that the eddy currents are coherent. Signal averaging would therefore add the distorted FIDs *in phase*.

In the PGSE experiments, the echo signal becomes unstable for gradients larger than 4.5 T m^{-1}. It was found that this effect is *incoherent* between different scans. As we could see from the "switch-off" test, instabilities due to eddy currents are *coherent*. Therefore we believe that sample movement, which is expected to be more randomised than eddy currents, causes these instabilities. A possible improvement would be a stronger sample support than the one used at the moment which will be described in the next section. Alternatively, the PGSE-MASSEY method [40] could be used. However, for our experiments in chapter 6 a maximum gradient of 4.5 T m^{-1}, which could be achieved without any changes, was sufficient.

2.5.3.4 Temperature Control

The sample temperature is controlled by the Bruker VT2000 temperature control unit. Heater and air tube fit on an adaptor which directs the air flow to the sample. The temperature is monitored by a copper-constantan thermocouple which sits permanently in the air stream 8 cm below the sample. With a plug connector it can be connected to the VT2000 unit. Because the temperature is monitored below the sample, we calibrated the sample temperature for different readings of the thermocouple. This was done by using a thermocouple of a Fluke 80TK thermocouple module inside an NMR tube at the centre of the r.f. coil. The calibration curve is shown in figure 2.18.

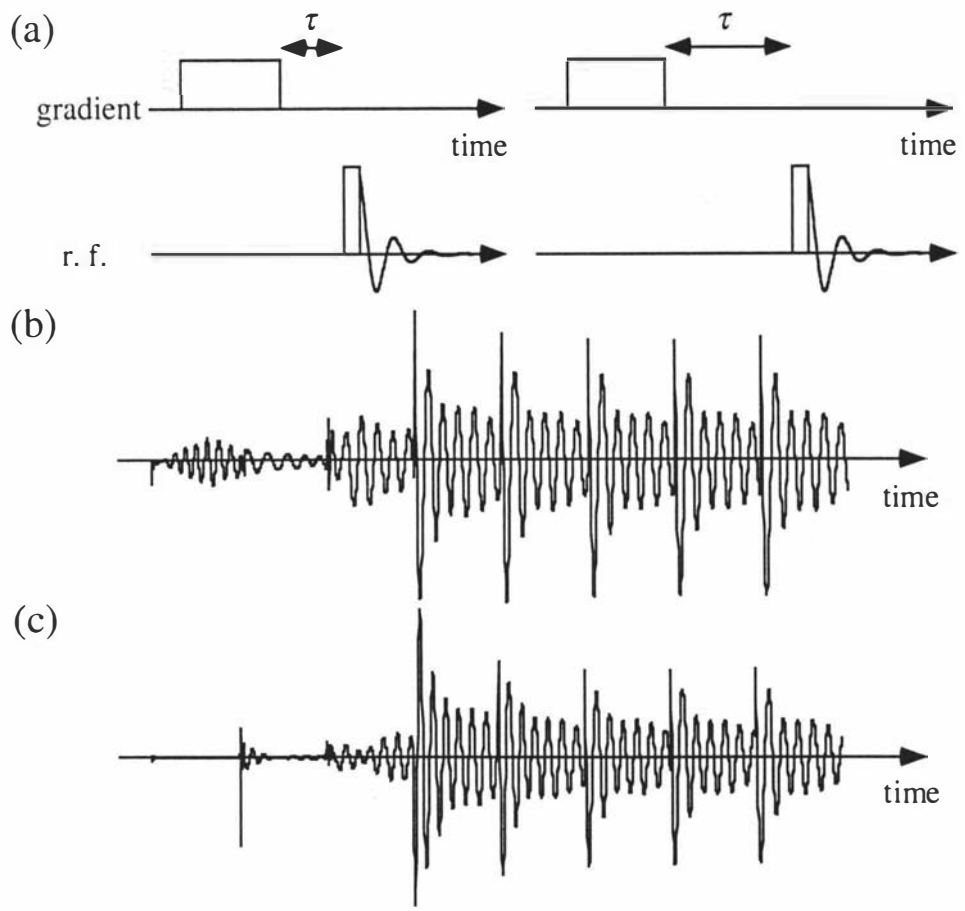

Figure 2.17: (a) The decay time of eddy currents is measured by reading the FID after a delay time τ after the application of a 10 ms gradient pulse. The FID is undistorted if the eddy currents have decayed. (b) – (c) "Switch–off" test for gradient values of 3.0 and 7.5 T m^{-1}. Eight FIDs are shown recorded after delay times τ of τ = 0.15, 0.3, 0.5, 1.0, 2.0, 5.0, 10.0 and 20.0 ms after switching off the gradient pulse. The FID is undistorted after delays of 1 ms (b) and 2 ms (c), respectively.

2.5.3.5 r.f. Stage

The sample is kept inside a glass dewar for thermal insulation. The 4 mm o.d. sample tube is held from the top end by a teflon screw pressing on an o–ring. The whole setup is shown in appendix A. In order to maximise signal–to–noise, the r.f. coil was required to be as small in diameter as possible. It is mounted on a 6 mm o.d. glass tube inside the dewar. The coil is a single winding saddle coil with an inductance of 80 nH. The tuning circuit is shown in figure 2.19. The variable capacitors can be adjusted once the probe is inside the magnet by fibre glass rods. The sensitivity of the r.f. resonator is characterised by the Q–factor

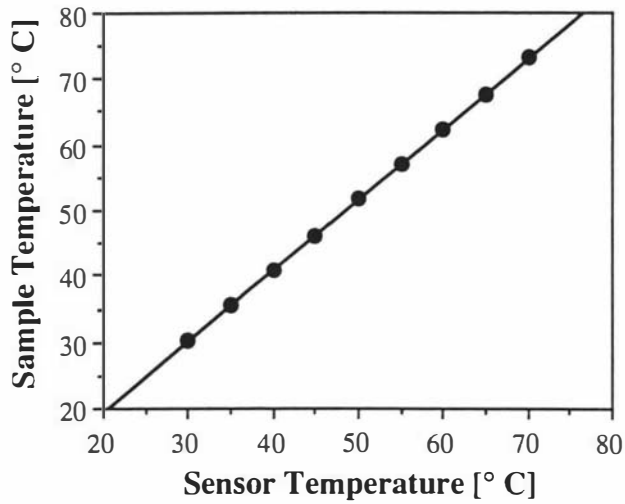

Figure 2.18: Temperature calibration curve of the high gradient probe.

which is defined by

$$Q = \frac{\nu}{\Delta\nu}, \tag{2.84}$$

where ν is the resonance frequency and $\Delta\nu$ is the width of the resonance curve. At $\nu = 300$ MHz we get $\Delta\nu = 4$ MHz and therefore $Q = 75$.

Figure 2.20 shows photographs of the probe.

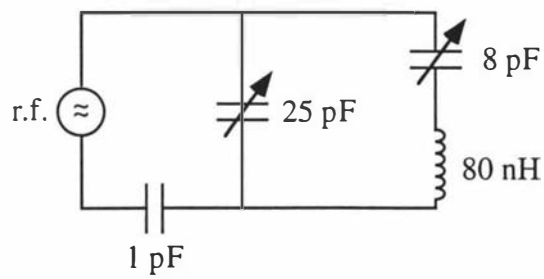

Figure 2.19: A circuit diagram of the r.f. stage.

2.5.4 Data Processing

Once the data were acquired by UXNMR, they were transferred to Macintosh computers for further processing and hard copy output.

The PGSE experiments were analysed using the application *PGSE-AMX300*. This program is based on the applications *BrukerTranslate* and *PGSE-FX60* written by A. Coy [41]. It extracts the echo signal for each q–value from the serial file, does a Fourier transformation and works out the echo attenuation $E(q)$. These

values are stored in a new file which can be read by *pgseplot* [41]. From there on, the data can be read by applications such as *CricketGraph* or *DeltaGraph*.

The flow experiments were analysed using the application *ImageShow* developed by Y. Xia [37] and A. Coy [41]. After the q-space FT. the flow and diffusion maps are stored as *ImageShow* files and can be analysed further.

For the analysis of the flow profiles in chapter 7 various other computer programs had to be written. We will describe their functions at a later stage in section 7.1.

(a)

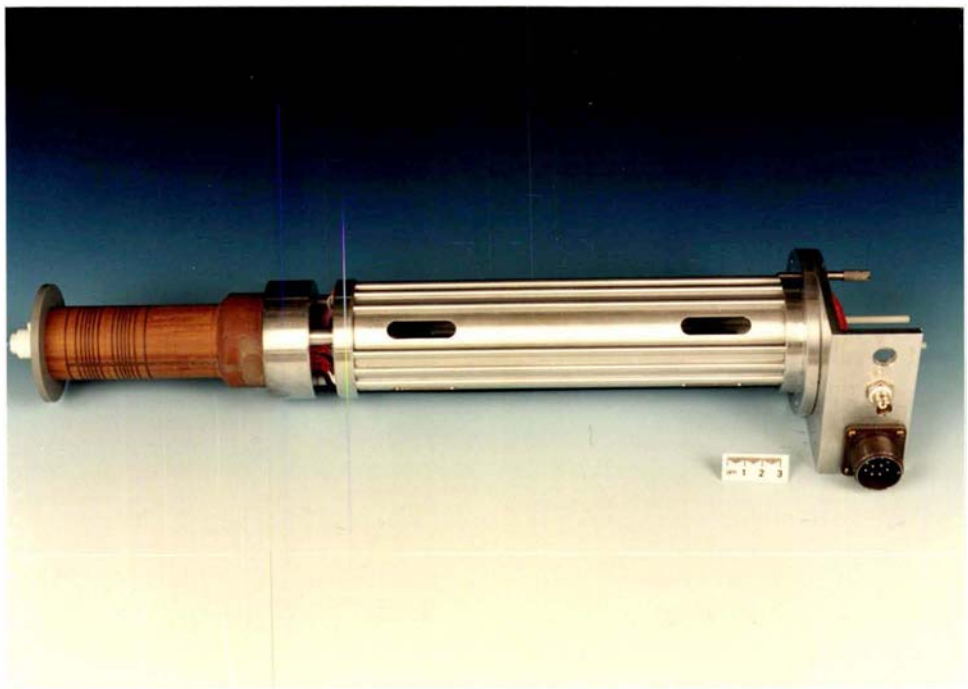

(b)

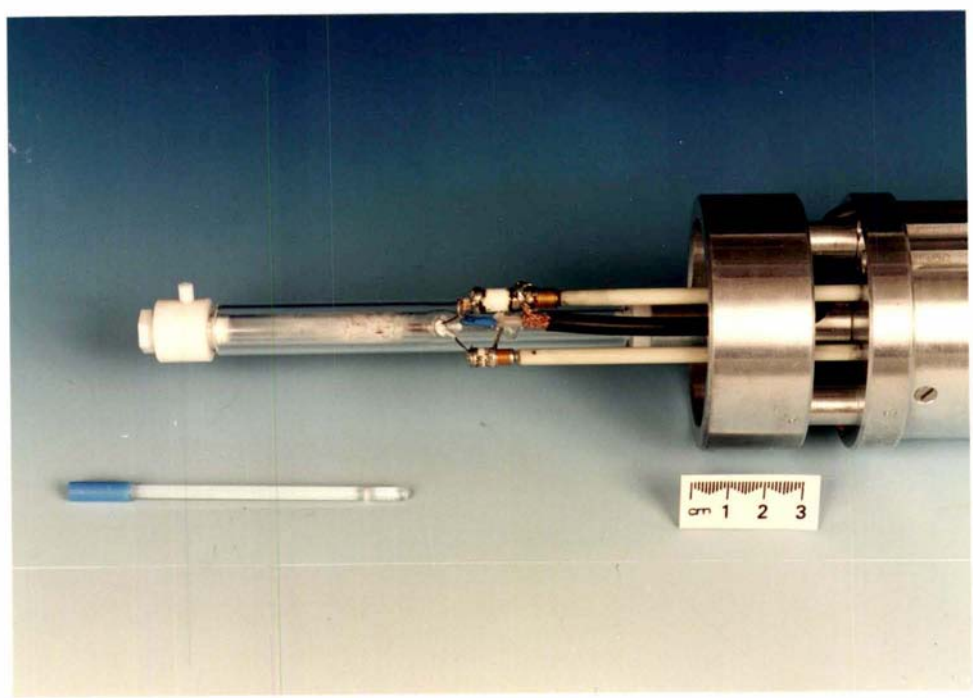

Figure 2.20: (a) The high gradient probe. (b) The top of the high gradient probe. The gradient coils and sample holder are taken off in order to show the dewar and the r.f. stage.

Chapter 3

Imaging of Electroosmotic Flow

3.1 Introduction

In this chapter we will describe microimaging measurements on flow which is varying in space as well as in time. We investigate the time evolution of electroosmotic flow in a capillary following the application of pulsed electric fields in a weak ionic solution.

3.1.1 Electrophoresis and NMR

When an electric field of magnitude E_{dc} is present in an electrolyte solution, ions drift along the electric field lines. This ion transport is known as electrophoresis. In molecular biology, electrophoresis is one of the most important methods of analysis of transport properties. Because of ionic collisions and solvent friction, ions of a particular species reach a terminal velocity v of

$$v = \mu E_{dc}, \tag{3.1}$$

where μ is the electrophoretic mobility of the molecule under investigation in a particular environment. μ depends on the shape and size of the molecule as well as its charge and temperature. For molecular ions, mobilities usually lie in the range of 1 to $5 \cdot 10^{-8}$ $m^2\ s^{-1}\ V^{-1}$ [42]. Thus, for electric fields with magnitudes up to 100 V cm^{-1}, the upper limit for drift velocities is about 0.5 mm s^{-1}.

For microscopically visible particles, the electrophoretic mobilities can be measured directly by observing the moving particles with a microscope. If they cannot be observed directly, they must either be adsorbed on microscopically visible carrier particles to permit direct mobility measurement, or studied indirectly by techniques in which the movement of macroscopic amounts of material in the electric field is detected. Zone methods have been widely adapted for this purpose. A strip

of filter paper is saturated with buffer solution, and a small amount of a solution of the material under investigation is applied as a narrow band. On application of a potential difference between the ends of the strip, each component migrates at a rate which is mainly determined by its mobility. After an appropriate time, the strip is removed, dried and developed to show the positions and concentrations of the different components. These techniques are described in textbooks on electrophoresis, for example in [43].

In section 2.4.5 we saw that with the dynamic spin echo method it is possible to measure flow profiles with a resolution down to a few microns per second. By taking advantage of chemical shift sensitivity one can also resolve different components in a mixture. The combination of NMR with electrophoresis is called electrophoretic NMR (ENMR). In principle it is possible to determine electrophoretic mobilities and diffusion coefficients for each line in the NMR spectrum.

The first observations of electrophoretic drift via NMR were reported by Packer *et al.* [44] in 1972. They found that the echo envelope in a modified Carr–Purcell sequence depended on the current density with and without gradient pulses, but the effects were enhanced by the gradient pulses. It was suggested that the effects were associated with magnetic field gradients resulting from electrical current through the sample and the spiral motion of ions under the influence of the main magnetic field. Later experiments are referred to in a review by Johnson [42].

One might fear that the movement of charged particles would interfere with the static magnetic field. Two problems might occur. Firstly, moving charged particles create a magnetic field. If the movement is along the static magnetic field (z direction), as it is in the natural arrangement in a superconducting magnet, the magnetic field created by this current has components only in the xy plane. Therefore there is no magnetic field created in the z direction. When an electromagnet is used, the ionic current creates a magnetic field which cannot be ignored. However, it can be compensated for by external shim coils.

The other effect which has to be discussed is the perturbed orbit of charged particles in a magnetic field. Since the force on a charged particle moving in a magnetic field is perpendicular to both velocity and field, no effect is expected when the current and the main magnetic field are parallel. In fact, molecular collisions randomise the direction and magnitude of the velocities apart from a small polarisation resulting from the applied electric field, and there is little effect for any orientation of current and main magnetic field.

However, there is another effect which can be a severe problem in electrophoresis experiments. We will deal with this so–called electroosmosis in the next section.

3.1.2 Electroosmosis

The electrophoretic migration of ions results in ionic collisions with the neutral solvent molecules which transfer momentum in the direction of ion flow. However, for an ionic solution in which the charge distribution is homogeneous, the oppositely directed flow of anions and cations causes local cancellation of such effects so that ion migration occurs against a stationary solvent. Because this cancellation is dependent on local charge neutrality, any inhomogeneity in charge distribution can drastically alter the local balance in electrophoretic drag forces. The resulting fluid transport is known as electroosmosis [42, 45, 46]. The velocities associated with electroosmosis are comparable to or even larger than the electrophoretic drift velocities.

Untreated glass or plastic surfaces in contact with electrolyte solutions are always charged, and the positive and negative ions in solution are distributed under the influence of the electric field. Close to the surface, a layer with a high concentration of counterions, known as the Debye layer, is the result. As a consequence, the application of an electric field causes inhomogeneous electrophoretic currents. Because the Debye layer is generally very thin, the electroosmotic drag will result in an apparent slip of the fluid along the boundary. Outside this layer the flow profile will be determined by the hydrodynamics of a neutral fluid experiencing the electroosmotic flow as a boundary condition.

Electroosmotic flow can be reduced by increasing the viscosity of the fluid or by reducing the charge on the surface by coating it with a polymer. In cases where it is not possible to reduce the electroosmotic flow significantly, it is important to know the shape and time dependence of the flow profile. Electroosmotic flow can be measured by observing a boundary layer in the electrophoretic cell with a microscope. However, this method requires the solution to be doped with microscopically visible particles. With dynamic NMR microscopy it is possible to observe the movement of the solvent directly and non-invasively. In this chapter we measure the time evolution of electroosmosic flow with the dynamic spin echo method and compare our results with theoretical predictions.

3.2 Theory

Consider the case of a capillary of radius R_0 in which electroosmotic flow develops at the wall. If the fluid is incompressible and confined then the surface flow must be balanced by a counterflow. Under equilibrium, constant electric field conditions, and given a Newtonian fluid, we expect that the rate of strain, $\partial v/\partial r$, will vary linearly with radius, resulting in a quadratic velocity profile, $v(r)$. The

difference with the usual parabolic profile associated with Poiseuille flow is simply that the net flow rate is now zero and the non-slip boundary condition, $v(R_0) = 0$, is replaced by, $v(R_0) = v_{DS}$, the slip velocity associated with the electroosmotic surface drag. In consequence we may write

$$v(r) = -v_{DS}\left(1 - 2(\frac{r}{R_0})^2\right). \tag{3.2}$$

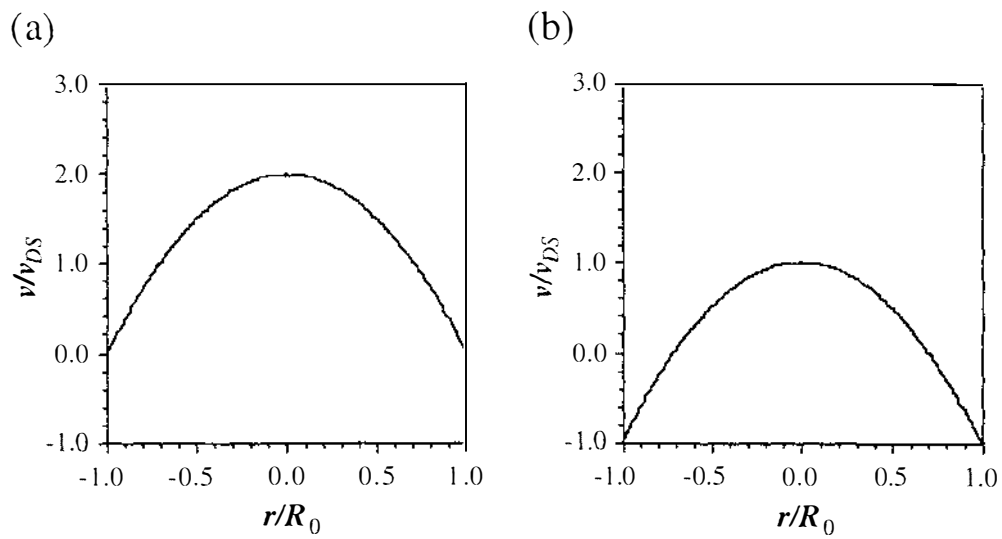

Figure 3.1: (a) The usual parabolic flow profile for Poiseuille flow in a capillary with radius R_0. (b) A parabolic flow profile, where the net flow is zero.

Because we shall be concerned with the development of the flow profile subsequent to the application of the electric field, we shall require a more general expression, $v(r,t)$, where t refers to the time delay after the field pulse and the constant electric field velocity profile is simply the limit as $t \to \infty$. The phenomenon of the time evolution of the electroosmotic flow profiles has been studied theoretically in a number of possible geometries, such as outside a single plane, between two planes, and in a cylinder by Söderman *et al.* [47]. For the purpose of introducing those aspects of the theory relevant to the present experimental study, the important findings and expressions relating to capillary geometry will be sketched now.

Because of the uneven charge distribution in the layer of solution adjacent to the surface, the electric field exerts a force on this layer such that the layer is accelerated to an equilibrium velocity in a very short time, typically less than a microsecond. At the point where the electric potential from the surface can be neglected (certainly less than 10 Debye screening lengths, which corresponds in

most cases to less than 100 nm) this equilibrium velocity is given by [46]

$$v_{DS} = v(r \approx R - 100\text{nm}, t > 1\mu\text{s}) = \frac{\epsilon_0 \epsilon_r}{\eta} E\zeta \tag{3.3}$$

where ϵ_r is the dielectric constant of the solution, ϵ_0 the permittivity of free space, η the viscosity of the solution, E the magnitude of the electric field, and ζ the so-called zeta potential which is the electric potential at the surface of shear. Equation 3.3 is only valid if the thickness of the Debye layer is much smaller than the capillary radius.

The layer of solution moving with this velocity then exerts frictional stress on the adjacent layer and, as time evolves and the electric field is maintained, layer after layer of the solution will be eventually set into motion. Provided no counter flow results, the infinite-time velocity profile will correspond to the constant value given by equation 3.3 at all distances from the wall. We shall be concerned with the condition of zero net transport in which counterflow is required and the steady state profile of equation 3.2 results.

In the theoretical treatment of Söderman *et al.* one neglects times shorter than that required to establish surface layer flow and distances smaller than the "surface layer". It is also important to assume the steady state conditions relevant to the experiments to be described, i.e. that subsequent to the electrophoretic (EFP) pulse associated with velocity measurement, that an equal but oppositely directed pulse is applied in order to avoid electrolysis effects, and that, furthermore, many such pulse pairs are applied in succession as part of the imaging process. The process of counterflow is taken into account in the calculations by using a time-dependent but coordinate-independent pressure gradient along the cylinder axis. The time dependent value of the pressure gradient is obtained from the requirement of zero mean flow through any given cross-section of the cylinder. Given these assumptions, $v(r,t)$ can be expressed in terms of the Kelvin functions $\mathrm{ber}(x)$ and $\mathrm{bei}(x)$, which are defined by the following equation [48]:

$$\mathrm{ber}(x) + i\,\mathrm{bei}(x) = J_0(xe^{i3\pi/4}). \tag{3.4}$$

$J_0(x)$ is the zeroth order Bessel function of the first kind. $\mathrm{ber}(x)$ and $\mathrm{bei}(x)$ can be written as power series:

$$\mathrm{ber}(x) = \sum_{k=0}^{\infty} \frac{(-1)^k}{(2k)!^{2k}} \left(\frac{1}{4}x^2\right)^{2k} \tag{3.5}$$

$$\mathrm{bei}(x) = \sum_{k=0}^{\infty} \frac{(-1)^k}{(2k+1)!^{2k+1}} \left(\frac{1}{4}x^2\right)^{2k+1} \tag{3.6}$$

According to Söderman *et al.* [47] it may be shown that the velocity at time t and at distance r from the tube centre is given by

$$\begin{aligned} v(r,t) = \sum_{n=1}^{\infty} & \left[K_n \left(\mathrm{ber}(S_n r) - \frac{2\,\mathrm{bei}'(S_n R)}{S_n R} \right) \right. \\ & \left. + L_n \left(\mathrm{bei}(S_n r) - \frac{2\,\mathrm{ber}'(S_n R)}{S_n R} \right) \right] \cos(n\omega_0 t) \\ & + \left[L_n \left(\mathrm{ber}(S_n r) - \frac{2\,\mathrm{bei}'(S_n R)}{S_n R} \right) \right. \\ & \left. K_n \left(\mathrm{bei}(S_n r) - \frac{2\,\mathrm{ber}'(S_n R)}{S_n R} \right) \right] \sin(n\omega_0 t) \end{aligned} \tag{3.7}$$

where

$$\mathrm{ber}'(x) = \frac{d\,\mathrm{ber}(x)}{dx} \tag{3.8}$$

$$\mathrm{bei}'(x) = \frac{d\,\mathrm{bei}(x)}{dx} \tag{3.9}$$

and

$$K_n = v_{DS} \frac{4}{n\pi} \sin(n\pi\alpha/2) \sin(n\pi/2) S_n R \times \frac{S_n R\,\mathrm{bei}(S_n R) - 2\,\mathrm{ber}'(S_n R)}{(S_n R\,\mathrm{ber}(S_n R) - 2\,\mathrm{bei}'(S_n R))^2 + (S_n R\,\mathrm{bei}(S_n R) - 2\,\mathrm{ber}'(S_n R))^2} \tag{3.10}$$

$$L_n = v_{DS} \frac{4}{n\pi} \sin(n\pi\alpha/2) \sin(n\pi/2) S_n R \times \frac{S_n R\,\mathrm{ber}(S_n R) - 2\,\mathrm{bei}'(S_n R)}{(S_n R\,\mathrm{ber}(S_n R) - 2\,\mathrm{bei}'(S_n R))^2 + (S_n R\,\mathrm{bei}(S_n R) - 2\,\mathrm{ber}'(S_n R))^2} \tag{3.11}$$

with

$$S_n = (\rho\omega_0 n/\eta)^{1/2}. \tag{3.12}$$

v_{DS} is the velocity defined in equation 3.3, and α is the fraction of time the EFP pulses are on. (For the cycle shown in figure 3.2 (a), α is given by $2\tau_p/\tau$.) In the definition of S_n, ρ and η are the solution density and viscosity, respectively, while $\omega_0 = 2\pi\nu$ is the angular frequency of application of the pulse sequence.

In the experiments to be described here, the cycle of EFP pulses differs from that shown in figure 3.2 (a) in that the time delay between the EFP pulse pair is not equal to the pair separation. However this delay was sufficient for relaxation of the solution velocity to zero before the application of the next pulse pair. Figure 3.2 (b) shows the velocity profile at successively increasing time after the completion of the second EFP pulse in a pair of pulses each of 1.5 s duration and separated by 1.5 s. Because the delay time used in the experiments was 1.5 s, it is clear that the experimental situation corresponds to complete relaxation.

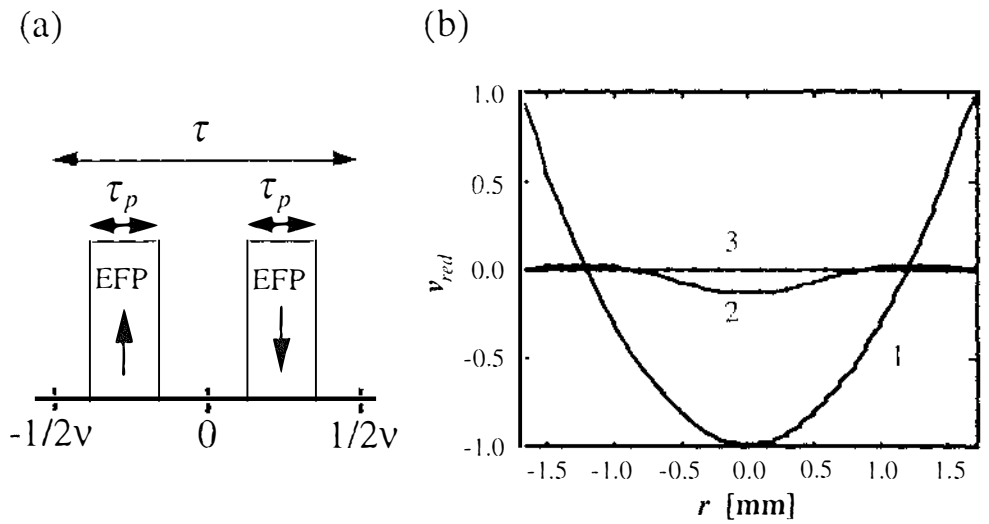

Figure 3.2: (a) Schematic electric field gradient pulse cycle which defines the frequency ν and duty cycle $\alpha = 2\tau_p/\tau$, used in equations 3.7, 3.10 and 3.11. (b) Normalised theoretical velocity profiles, obtained from equation 3.7. Curve 1 shows the profile shortly before the completion of a 1.5 s EFP pulse (the second of the pair in (a)). Curves 2 and 3 show the profiles at 0.25 s and 0.75 s , respectively, after the completion of the second EFP pulse, in a pair of pulses each of 1.5 s duration and separated by 1.5 s. The cylindrical tube is assumed to have a diameter of 3.4 mm.

3.3 Experimental Section

A solution of 1 mM KCl in water was contained within a glass tube of 5 mm o.d. and 3.4 mm i.d. Two platinum electrodes were sealed in the ends of the tube, the separation distance between the ends of the electrodes being 70 mm. The arrangement of the electrophoresis cell is shown in figure 3.3. EFP pulses were generated by applying pulses of 100 V amplitude to the electrodes using a specially constructed programmable high voltage unit which can provide output currents of up to 100 mA at a voltage of up to 550 V [49]. This high voltage unit was controlled using TTL pulses generated by the spectrometer. In each of these experiments the pulse sequence repetition time was 1.5 s and, after each data acquisition, a reversed EFP pulse of identical amplitude and duration was applied so as to inhibit gas formation in the cell. The pulse program for the AMX300 spectrometer is given in appendix B.

The EFP pulse was switched on a time τ_1 prior to the start of the dynamic spin echo pulse sequence and turned off subsequent to velocity encoding but prior to signal acquisition, as shown in figure 3.4. The two-dimensional image of the capillary cross section with a slice thickness of 4 mm was obtained with a 10 mm

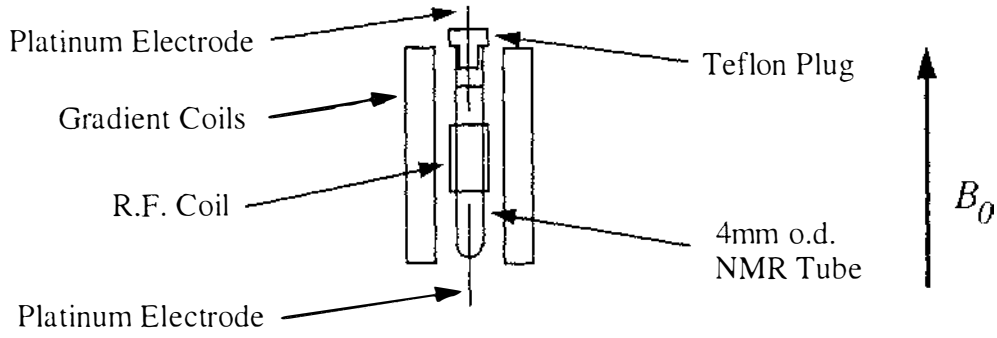

Figure 3.3: Schematic arrangement of the electroosmotic cell in the NMR probe.

field of view and 128^2 pixels giving a spatial resolution of 78 μm per pixel.

Because the velocities to be measured were on the order of tens of microns per second, it was necessary to maximise velocity sensitivity in the face of molecular Brownian motion. This was achieved by maximising the separation time, Δ, between the PGSE pulse pair since Brownian displacements increase as $\sqrt{\Delta}$ whereas displacements due to flow increase as Δ. The upper limit to Δ is determined by signal loss due to spin relaxation. By using the stimulated echo sequence shown in figure 3.4 the spins were subjected to T_1 rather than T_2 relaxation over most of the separation time.

In order to obtain the dependence of the velocity profile on delay time, t, the time τ_1 between the start of the EFP pulse and the start of the soft r.f. pulse was varied between 25 ms and 1000 ms in a set of separate experiments. The short time delay between the r.f. pulse and the first PGSE pulse was added to τ_1 in order to provide an estimate of the time delay relevant to the velocity measurement. Because of the finite time needed to encode for velocity, it was desirable to keep this duration Δ smaller than τ_1 in order to optimise time resolution. As Δ was varied it was necessary to adjust the duration and maximum amplitude of the PGSE pulses so as to retain optimal velocity sensitivity.

Because the electroosmotic velocities are so small, it is important to establish that measurements are free from artifacts caused, for example, by eddy current induced phase shifts. This was done by obtaining a velocity image without the EFP pulse for each of the pulse parameter sets used in this work. The residual apparent velocity images, which represented only a weak perturbation close to the noise background, were nonetheless subtracted from the images obtained with EFP pulses in order to correct for any background artifacts.

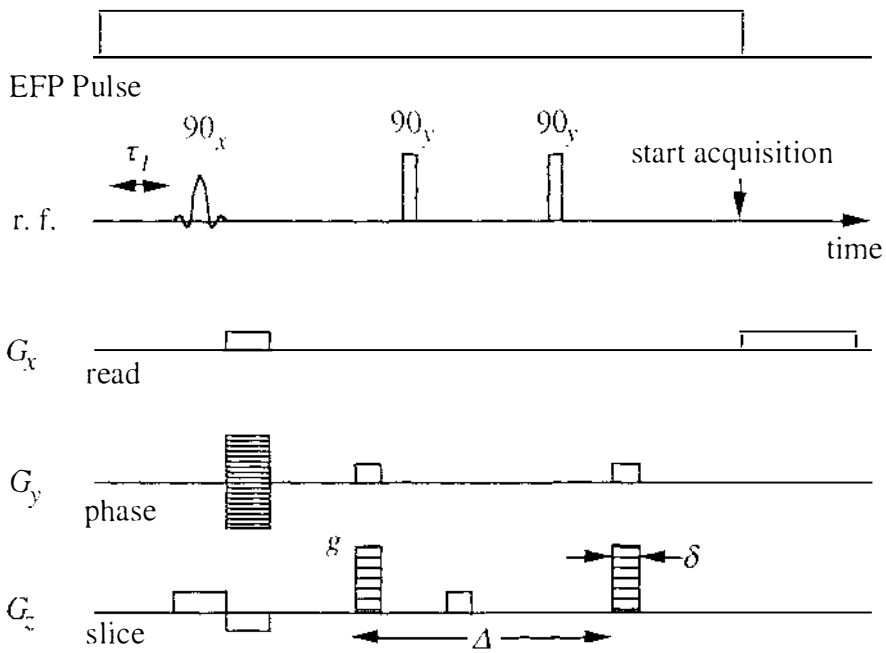

Figure 3.4: The stimulated echo pulse sequence used to phase–encode the image for velocity. The EFP pulse is switched off subsequent to velocity encoding but prior to signal acquisition. Note that τ_1 defines the time delay between the start of the EFP pulse and the start of the soft r.f. pulse. A further delay of 5.3 ms occurs before the start of velocity encoding.

3.4 Results

Figure 3.5 shows a set of velocity images obtained for a transverse section of the capillary at successively increasing values of delay time, τ_1. These images demonstrate a symmetric, well–behaved velocity distribution for values of $\tau_1 < 500$ ms, but for $\tau_1 > 500$ ms there is clear evidence of asymmetric flow in which cellular separation of counterflowing fluid is apparent, possibly due to convective effects. This will be discussed in the next section, and in chapter 8 we will have a closer look at the phenomenon of convection. We shall therefore confine our quantitative analysis of velocity profiles here to the short time regime. In order to compare our results with theoretical predictions, we have plotted a sequence of diametral profiles of velocity in figure 3.6. In each case two theoretical profiles are shown in which the delay time t is set to the start and finish times of the velocity encoding PGSE gradient pair respectively. We would hope that the experimental data might be represented by an appropriate mean of these curves. Note that there is a clear transition from plug flow to parabolic flow profiles with increasing delay time τ_1.

It should also be noted that there are no adjustable parameters used in gen-

erating the theoretical profiles, save for the scaling constant, v_{DS}. The value of this constant was determined by adjusting its value so that the theoretical profiles best agreed with the data in figure 3.6 (a). The value so obtained, $v_{DS} = 0.095$ mm s^{-1}, was then used in generating all other profiles. From the value of v_{DS} we may calculate ζ to be 80 mV (using the value 78.5 for ϵ_r), a value which is quite reasonable for glass [45, 50].

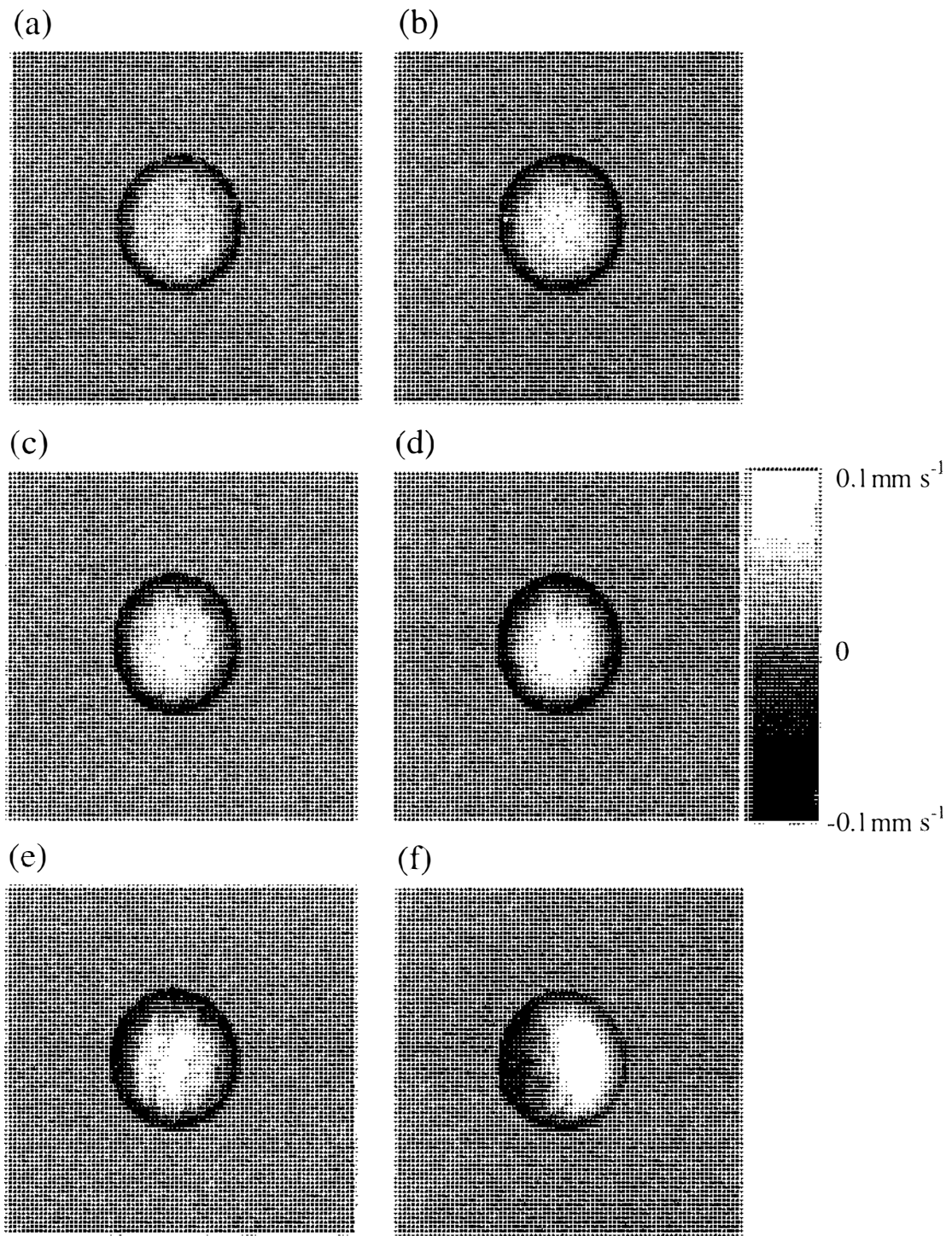

Figure 3.5: Velocity images obtained for a transverse section of the capillary at successively increasing values of delay time τ_1. These delays are respectively (a) 50, (b) 100, (c) 200, (d) 300, (e) 500, and (f) 1000 ms. Note the asymmetric flow distribution in the image obtained at the longest time delay. The spatial field of view is 10 mm.

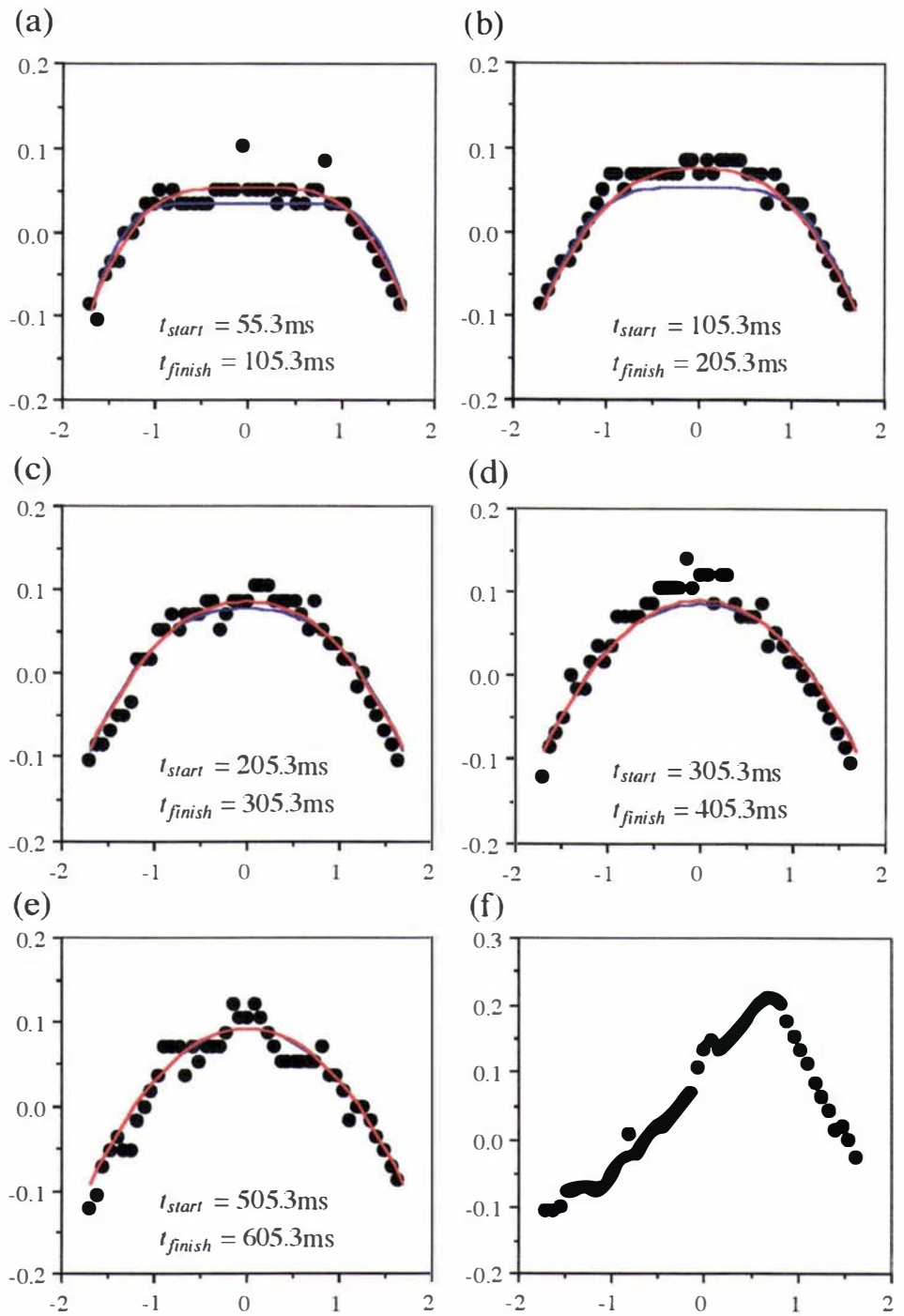

Figure 3.6: Diametral profiles of velocity obtained from the images shown in figure 3.5, along with the theoretical predictions of equation 3.7. In each case (except (f)) two theoretical profiles are calculated using delay times corresponding to the start (blue) and end (red) of velocity phase–encoding. The horizontal axis denotes the distance r in mm, while the vertical axis gives the velocity in mm s^{-1}. Note that the only adjustable parameter is v_{DS}, which is obtained by fitting the data from (a) for $\tau_1 = 50$ ms. This value is then used subsequently in calculating the absolute profiles shown in (b) – (e). There is a clear transition from plug flow to parabolic flow profiles with increasing τ_1. The asymmetric flow in (f) is possibly due to convective effects.

3.5 Discussion

Although the experimental flow profiles agree very well with the predictions, it should be noted that resistive heating of the sample is a serious problem in ENMR experiments. In order to work out the temperature increase, we consider a sample having electric conductivity κ_{el}, length d and cross-sectional area A. When a potential difference U is applied across the sample for a period t_1, the energy W_{el} deposited in the sample is

$$W_{el} = \frac{U^2}{R} t_1, \tag{3.13}$$

where $R = l/\kappa_{el}A$ is the electrical resistance. The thermal energy W_{th} required to heat the sample by δT is given by

$$W_{th} = \rho d A c_p \delta T. \tag{3.14}$$

where ρ and c_p are the density and specific heat of the sample. If no heat is exchanged with the environment, both energies must be equal:

$$W_{el} = W_{th}. \tag{3.15}$$

The temperature increase δT is then given by

$$\delta T = \frac{E^2 \kappa_{el}}{\rho c_p} t_1, \tag{3.16}$$

where $E = U/d$ is the strength of the electric field pulse. In our experiments we used values of $U = 100$ V and $d = 7$ cm. For a solution of 1 mM KCl in water $\kappa_{el} = 0.0147\ \Omega^{-1}\ \mathrm{m}^{-1}$ [51] at a temperature of 25° C. With these values, along with the literature values for $\rho = 996.9\ \mathrm{kg\ m^{-3}}$ and $c_p = 4180\ \mathrm{J\ K^{-1}\ m^{-3}}$ of water at 25° C [51], we obtain a temperature increase of $\delta T = 7$ mK for an EFP pulse of 1 s duration. Because this temperature increase is expected to be homogenous across the whole sample and, for short EFP pulses, smaller than temperature fluctuations due to other effects (e.g. heating of the gradient coil, absorption of r.f. power), we conclude that convective effects are not important for our analysis, except for the longest τ_1 value used in our experiments.

In order to estimate the minimum vertical temperature gradient ΔT across the sample, for which convection will occur, we assume now that the asymmetric flow distribution in figure 3.5 (f) is caused by convection. In chapter 8 the phenomenon of convection will be discussed in detail. Convection can only occur if the Rayleigh number R defined in equation 8.1 exceeds the critical value R_c which strongly increases with decreasing aspect ratio defined as the ratio of the width L of the fluid layer to its depth d. For the estimations here, we assume as in chapter 8

the value of R_c to be $R_c \approx 10^7$ for our setup. We set $R = R_c$ for $t_1 = 1$ s. With the literature values of volume expansion $\alpha = 1.6 \cdot 10^{-4}$ K^{-1}, thermal diffusivity $\kappa_{th} = 1.4 \cdot 10^{-7}$ m^2 s^{-1}, and kinematic viscosity $\nu = 8.0 \cdot 10^{-7}$ m^2 s^{-1} [51] we obtain a minimum temperature difference of $\Delta T = 2$ K. As stated above, these calculations neglect any heat exchange with the environment, but it is clear that convection due to resistive heating governs the upper limit of the τ_1 values for which electroosmotic flow can be observed in our experiments.

Because the critical Rayleigh number R_c strongly increases with decreasing aspect ratio of the cell under investigation, the most efficient way to avoid convection is to reduce the aspect ratio. This can be achieved by either reducing the width L of the fluid layer or by increasing its depth d. Equation 8.1 states that $R \propto d^3$, and therefore R_c can be increased without changing R by reducing L. This means that the onset of convection is reduced most efficiently by using a smaller tube diameter.

With the current setup, the lower limit of τ_1 is determined by the available gradient strength in order to get a reasonable velocity resolution. Wu *et al.* [52] demonstrated that it is possible to reconstruct the velocity profile in a system with cylindrical symmetry by using only one gradient which is oriented along the flow direction. By using the high gradient probe described in section 2.5.3 it would therefore be possible to measure flow profiles for values of $\tau_1 < 50$ ms. The lowest limit of τ_1 is reached when the displacements of the molecules due to electric field pulses are smaller than the displacements due to Brownian motion.

In this chapter we have demonstrated that NMR microscopy is a powerful tool to monitor the time evolution of electroosmosis. We could measure flow profiles with a velocity resolution of around 15 μm s^{-1}. We have shown that electroosmotic flow velocities are of the same magnitude as the ionic electrophoretic motion, but that electroosmotic velocities typically reach a steady state distribution in a capillary geometry on a timescale of 100 milliseconds, rather than at the sub–nanosecond relaxation times pertinent to the ionic electrophoretic response. A pleasing aspect is the good agreement between theory and experiment.

Chapter 4

Velocity Exchange Spectroscopy

In the previous chapters we introduced some methods which may be used to image flow profiles. In chapter 3 we saw that there is an easy method to measure the time variation of velocity profiles with a time resolution τ of the order of $\tau \approx 50$-100 ms and a spatial resolution of the order of 100 μm. In chapter 7 we will reduce the pixel size in one dimension down to 30 μm by using two slice selective r.f. pulses in the imaging plane. In this chapter we demonstrate a 2D velocity exchange experiment, which has a time resolution of less than 5 ms and which correlates molecular velocities in the whole sample and is therefore not restricted by the pixel size.

4.1 Introduction

In section 2.3.4 we gave a brief introduction to 2D spectroscopy. In this chapter we will demonstrate a somewhat analogous experiment performed in a very different frequency space. Here, the equivalent f_1 and f_2 domains correspond to the movements Z_1 and Z_2 over two well defined time intervals, which are themselves separated by a further time delay, τ_m, the equivalent of the "mixing" time in our experiment. The conjugate "preparation" and "detection" domains are the q space of the PGSE method. The PGSE gradient pulse pairs are stepped so as to phase-encode the spins for molecular translational motion. Both pairs of q-pulses are applied in the same direction so that a spin isochromat (a set of molecules travelling at constant velocity) will have identical Z_1 and Z_2 displacements, thus contributing to points on the diagonal in (Z_1, Z_2) space. On the other hand a migration of spins from one region of the displacement spectrum to another over

the time τ_m will lead to cross-peaks. In this manner the molecular velocities may be correlated. In Ernst's terminology [12] this experiment can be classified as an exchange experiment and has been termed Velocity EXchange SpectroscopY (VEXSY) [53]. The idea has some features in common with two pulse sequences proposed by Cory, Garroway and Miller [54], for the measurement of diffusion based on compartment size selection. In the first, these authors suggested applying two PGSE pulse pairs separated by a delay time so that the echo attenuation due to the second pair would be weighted by attenuation which was caused by the first pair of gradient pulses. When applied to the diffusion of spins in porous media, this could lead to a final echo amplitude which would indicate leakage from pores. In the second they suggested that applying two orthogonally-directed gradient pulse pairs in quick succession could be used to measure pore eccentricity if the spins were compartmentalised into regions of differing pore shape. By contrast VEXSY is a two-dimensional experiment in which correlations are observed between differing isochromats of the motional spectrum corresponding to a single direction of displacement.

An obvious question which arises concerns what possible advantage this velocity correlation approach might have over direct velocity imaging. The imaging of velocity profiles uses some applied contrast in the imaging pulse sequence which is sensitive to fluid velocity. However, such a method is always limited in sensitivity by the available signal-to-noise ratio in the chosen volume element. The advantage of correlation spectroscopy over simply imaging the velocity field, is the benefit derived from long range homogeneity in the fluid behaviour. This is precisely the same advantage implicit in the COSY experiment. It is not necessary to carry out the COSY on a single molecule if the behaviour in question is common to the entire ensemble of such molecules. Similarly, if there is a local heterogeneity of the translational motion spectrum, which is homogeneous over the wider fluid sample, then it is possible to perform the two-dimensional spectroscopy without the usual signal-to-noise limitation of the voxel. This permits a much higher spatial resolution than is commonly available. Furthermore it is possible to perform this spectroscopy with chemical shift selectivity.

4.2 Theoretical Considerations

Consider the double PGSE pulse sequence shown in figure 4.1. Following the first 90_x pulse, the transverse magnetisation is phase encoded according to the displacement R_1 which occurs over the duration Δ between the first PGSE pulse pair. With the notation from section 2.4.5, the average propagator for motion

is given by $\overline{P_s}(\boldsymbol{R}_1, \Delta)$. Then the normalised magnetisation remaining after the second gradient pulse is given by equation 2.77:

$$E_\Delta(\boldsymbol{q}_1) = \int \overline{P_s}(\boldsymbol{R}_1, \Delta) e^{i2\pi \boldsymbol{q}_1 \cdot \boldsymbol{R}_1} d\boldsymbol{R}_1 .$$

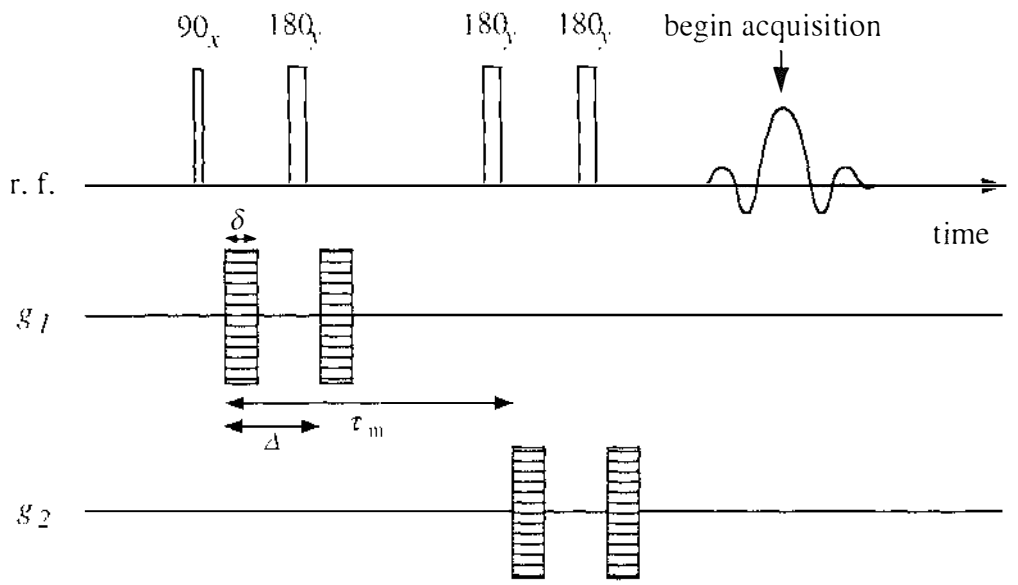

Figure 4.1: RF and gradient pulse sequence for velocity exchange spectroscopy (VEXSY) in which successive PGSE pulse pairs (g_1 and g_2) are applied separated by a delay time τ_m.

Following a time delay τ_m, spins associated with molecules which displaced by $\boldsymbol{R}_1$ during the first phase-encoding period, may have moved to a different part of the displacement spectrum. To account for this we introduce a conditional probability distribution $P(\boldsymbol{R}_1, \tau_m | \boldsymbol{R}_2, \Delta)$ which is assumed to be common to the entire molecular ensemble. This propagator gives the conditional probability that a molecule which moved by $\boldsymbol{R}_1$ over the time delay Δ, will displace by $\boldsymbol{R}_2$ over Δ when this latter measurement is made after the delay τ_m. Following the application of the second gradient pulse pair ($\boldsymbol{q}_2$) the remaining transverse magnetisation is

$$E_\Delta(\boldsymbol{q}_1, \boldsymbol{q}_2, \tau_m) = \int \int \overline{P_s}(\boldsymbol{R}_1, \Delta) P(\boldsymbol{R}_1, \tau_m | \boldsymbol{R}_2, \Delta) e^{i2\pi(\boldsymbol{q}_1 \cdot \boldsymbol{R}_1 + \boldsymbol{q}_2 \cdot \boldsymbol{R}_2)} d\boldsymbol{R}_1 d\boldsymbol{R}_2 \quad (4.1)$$

Let us suppose that $\boldsymbol{q}_1$ is applied along direction Z and $\boldsymbol{q}_2$ along Y. Then inverse Fourier transformation with respect to $(\boldsymbol{q}_1, \boldsymbol{q}_2)$ returns the two-dimensional Fourier spectrum $\overline{P_s}(Z_1, \Delta) P(Z_1, \tau_m | Y_2, \Delta)$. Clearly we are faced with an ambiguity where Y is not collinear with Z since we could not distinguish molecules whose motion had the same components Z_1 and Y_2 along the $\boldsymbol{q}_1$ and $\boldsymbol{q}_2$ directions during each pulse pair, from those which changed during delay τ_m from a Z_1 motion along

q_1 to a Y_2 displacement along q_2. For example we could not distinguish between constant oblique velocity and a velocity which changed in direction. This is shown more clearly in figure 4.2. Consequently, we shall consider an exchange experiment in which q_1 and q_2 are parallel and define a unique displacement direction Z. Thus the two-dimensional spectrum becomes

$$S(Z_1, Z_2) = \overline{P_s}(Z_1, \Delta) P(Z_1, \tau_m | Z_2, \Delta) \tag{4.2}$$

Here we note, in relation to the second experiment of Cory *et al.*, that when molecules are compartmentalised in pores of differing shape, $P(Z_1, \tau_m | Z_2, \Delta)$ is not common to the molecular ensemble. For example, for spherical pores with variable diameters d, $P(Z_1, \tau_m | Z_2, \Delta)$ is zero for pores with $d < Z_1$ or $d < Z_2$, but finite for pores with $Z_1 < d$ and $Z_2 < d$. We shall not consider this possibility here and instead deal with a unique conditional probability function.

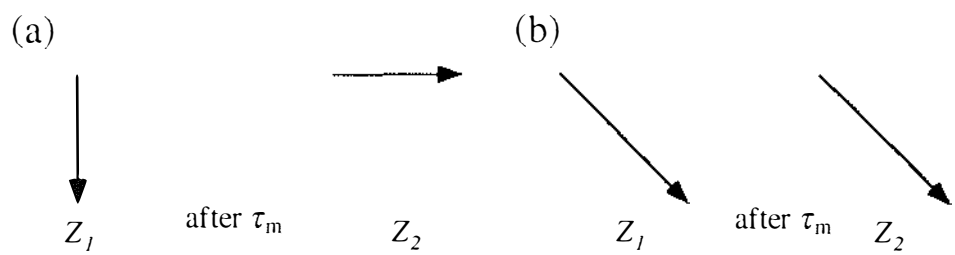

Figure 4.2: The two types of displacement in (a) and in (b) can not be distinguished if the first q–gradient encodes in vertical direction and the second in horizontal direction.

4.3 Experimental

4.3.1 Unrestricted Brownian Motion

In the special case of unrestricted Brownian motion, Z_1 and Z_2 are entirely uncorrelated and both $\overline{P_s}(Z_1, \Delta)$ and $P(Z_1, \tau_m | Z_2, \Delta)$ are independent Gaussians. Therefore we get with equation 4.2

$$S(Z_1, Z_2) = \frac{1}{4\pi D \Delta} e^{-(Z_1^2 + Z_2^2)/4D\Delta}. \tag{4.3}$$

The experiment was carried out using the NMR signal of water doped with 0.1% $CuSO_4$ to reduce T_1. The q-space phase encoding was carried out in 64^2 steps using q–pulses of duration $\delta = 12$ ms, separation $\Delta = 12$ ms and amplitude $g = 0.9$ T m^{-1}. The delay time τ_m was 42 ms. The two-dimensional VEXSY

spectrum $S(Z_1, Z_2)$ is shown in figure 4.3, both as an intensity map and as two profiles taken across orthogonal directions. The standard deviation of the the circular-symmetric Gaussian is

$$\sigma^2 = 2D\Delta \tag{4.4}$$

With a measured width of 7 μm we get $D = 2.0 \cdot 10^{-9}$ m^2 s^{-1}, which is in excellent agreement with the expected value of $D = 2.04 \cdot 10^{-9}$ m^2 s^{-1} [39].

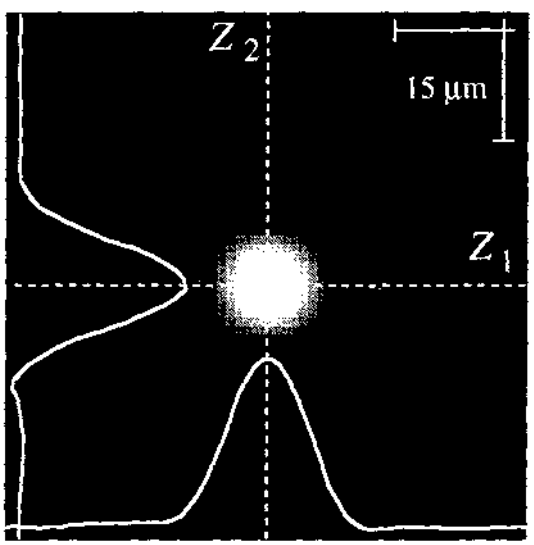

Figure 4.3: A two-dimensional VEXSY spectrum $S(Z_1, Z_2)$ for unrestricted Brownian motion of water molecules and orthogonal slice profiles through this image showing the Gaussian displacement spectrum associated with self-diffusion.

4.3.2 Laminar Newtonian Flow in a Couette Cell

4.3.2.1 Calculation of the VEXSY Spectra

For a stationary velocity distribution, $P(Z_1, \tau_m | Z_2, \Delta)$ is the Dirac delta function $\delta(Z_1 - Z_2)$, and equation 4.2 becomes

$$S(Z_1, Z_2) = \overline{P_s}(Z_1, \Delta)\delta(Z_1, Z_2). \tag{4.5}$$

This corresponds to a purely diagonal spectrum with distribution $\overline{P_s}(Z_1, \Delta)$ along each orthogonal axis.

We now calculate the two-dimensional spectrum of a Newtonian fluid undergoing circular motion in a Couette cell which will be considered in chapter 7, starting with the distribution of velocity components on a circular annulus with a

given radius r and a fixed angular velocity ω. At this stage it is easier to do the calculations in the complex representation. v, v_1 and v_2 are the complex velocities, and v_x, v_y, v_{1x}, v_{1y} and v_{2x}, v_{2y} are the real and imaginary parts of v, v_1 and v_2, such that

$$v = v_x + iv_y \tag{4.6}$$

$$v_1 = v_{1x} + iv_{1y} \tag{4.7}$$

$$v_2 = v_{2x} + iv_{2y} \tag{4.8}$$

In the experiment, we only measure the velocity component along the gradient direction, which we can represent by the real part of the complex velocity. The velocity component in this direction for an element of fluid subtending an angle θ is given by

$$v_x = |v| \cos\theta = \omega r \cos\theta. \tag{4.9}$$

Since the angular distribution $P(\theta)$ is uniform and $P(\theta)d\theta = P(v_x)dv_x$, the velocity distribution is given by

$$P(v_x) = \frac{1}{2\pi\omega r}\left(1 - \frac{v_x^2}{\omega^2 r^2}\right)^{-1/2}. \tag{4.10}$$

When the substitution $Z_1 = v_x\Delta$ is made, the average propagator $\overline{P_s}(Z_1, \Delta)$ follows directly.

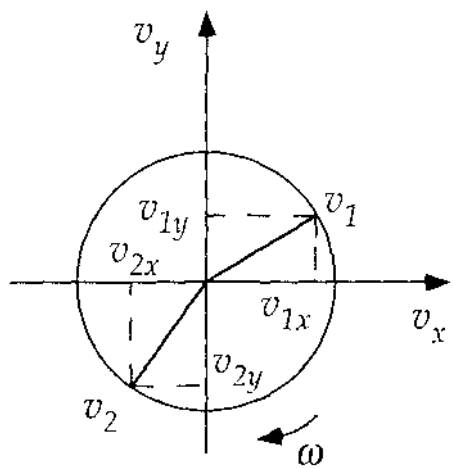

Figure 4.4: With the representation of the circular motion in the complex plane it is easy to work out the probability distributions $P(v_x)$ and $P(v_{1x}, \tau_m | v_{2x}, \Delta)$

We now have to work out the conditional probability $P(v_{1x}, \tau_m | v_{2x}, \Delta)$ that a fluid element which has the velocity component v_{1x} will have the velocity component v_{2x} along the same direction if the measurement is made at a time τ_m later.

From figure 4.4 we see that for a fluid element which starts with the complex velocity v_1, the velocity v_2 after a time τ_m will be given by

$$v_2 = v_1 e^{i\omega\tau_m}. \tag{4.11}$$

Working out the real part v_{2x} yields

$$v_{2x} = v_{1x}\cos\omega\tau_m - v_{1y}\sin\omega\tau_m. \tag{4.12}$$

The result in equation 4.12 is ambiguous. We notice that v_{2x} depends on v_{1x} as well as v_{1y}, but from the experiment we have no information about the size of v_{1y}. Because we know that the fluid element undergoes a circular motion, we know that

$$v_{1x}^2 + v_{1y}^2 = \omega^2 r^2, \tag{4.13}$$

but the sign of v_{1y} is unknown. Thus, we rewrite equation 4.12 using equation 4.13 as

$$v_{2x} = v_{1x}\cos\omega\tau_m \pm \sqrt{\omega^2 r^2 - v_{1x}^2}\sin\omega\tau_m. \tag{4.14}$$

This means that for a given v_{1x}, v_{2x} can only have two different values, and $P(v_{1x}, \tau_m | v_{2x})$ must then be the sum of two Dirac Delta functions:

$$\begin{aligned} P(v_{1x}, \tau_m | v_{2x}) &= \frac{1}{2}\delta\left(v_{2x} - \left[v_{1x}\cos\omega\tau_m + \sqrt{\omega^2 r^2 - v_{1x}^2}\sin\omega\tau_m\right]\right) \\ &\quad + \frac{1}{2}\delta\left(v_{2x} - \left[v_{1x}\cos\omega\tau_m - \sqrt{\omega^2 r^2 - v_{1x}^2}\sin\omega\tau_m\right]\right). \end{aligned} \tag{4.15}$$

Equation 4.15 has the character of a Lissajous figure. Making the substitutions $Z_1 = v_{1x}\Delta$ and $Z_2 = v_{2x}\Delta$ and combining the average propagator of equation 4.10 with the conditional probability distribution of equation 4.15 we obtain the two-dimensional VEXSY spectrum,

$$\begin{aligned} S_\omega(Z_1, Z_2) &= \frac{1}{2\pi\omega r}\left[1 - \frac{Z_1^2}{(\Delta r\omega)^2}\right]^{-1/2} \times \\ &\quad \left[\frac{1}{2}\delta\left(\frac{Z_2}{\Delta} - \left[\frac{Z_1}{\Delta}\cos\omega\tau_m + \sqrt{\omega^2 r^2 - \frac{Z_1^2}{\Delta^2}}\sin\omega\tau_m\right]\right)\right. \\ &\quad \left. + \frac{1}{2}\delta\left(\frac{Z_2}{\Delta} - \left[\frac{Z_1}{\Delta}\cos\omega\tau_m - \sqrt{\omega^2 r^2 - \frac{Z_1^2}{\Delta^2}}\sin\omega\tau_m\right]\right)\right]. \end{aligned} \tag{4.16}$$

This is the displacement spectrum for flow in a circular annulus with radius r. In the case of the Couette flow between concentric cylinders, in which the outer cylinder of radius r_o is stationary and the central cylinder of radius r_i rotates with the angular velocity ω_0, the fluid angular velocity varies across the gap. Applying no-slip boundary conditions on each side, the VEXSY spectrum $S(Z_1, Z_2)$ can be obtained from equation 4.16 by integrating with respect to the appropriate angular velocity distribution. Alternatively, we may rewrite equation 4.16 in terms of the local tangential speed v, so that

$$\begin{aligned} S_v(Z_1, Z_2) = & \frac{1}{2\pi v^2}\left[1 - \frac{Z_1^2}{(\Delta v)^2}\right]^{-1/2} \times \\ & \left[\frac{1}{2}\delta\left(\frac{Z_2}{\Delta} - \left[\frac{Z_1}{\Delta}\cos(v\tau_m/r) + \sqrt{v^2 - \frac{Z_1^2}{\Delta^2}}\sin(v\tau_m/r)\right]\right)\right. \\ & \left. + \frac{1}{2}\delta\left(\frac{Z_2}{\Delta} - \left[\frac{Z_1}{\Delta}\cos(v\tau_m/r) - \sqrt{v^2 - \frac{Z_1^2}{\Delta^2}}\sin(v\tau_m/r)\right]\right)\right]. \end{aligned} \tag{4.17}$$

The velocity field for a Newtonian fluid is given by [55]

$$v(r) = \omega_0 \frac{r_i^2}{r}\frac{r_o^2 - r^2}{r_o^2 - r_i^2}. \tag{4.18}$$

Since the normalised radial weighing function is given by $f(r) = 2r/(r_o^2 - r_i^2)$, the VEXSY spectrum is

$$S(Z_1, Z_2) = \frac{2}{r_o^2 - r_i^2}\int_{r_i}^{r_o} r S_v(Z_1, Z_2) dr. \tag{4.19}$$

Such a spectrum contains a complex ridge structure reminiscent of the patterns formed by the sharp edged Pake patterns [56] in 2D separated field spectra of powders published by Ernst [12] and 2D exchange spectra by Spiess et al. [26]. In these examples, the patterns arise from the distribution of molecular orientations in powder samples, while in the examples shown below, the patterns arises from the distribution of these edges as the rotation angle varies from zero to a finite value across the Couette flow.

4.3.2.2 Measurement of the VEXSY Spectra

The pulse sequence shown in figure 4.1 is a little naive. In particular it makes no allowance for the difficulty which arises from inhomogeneous local fields. Any such variation can lead to incomplete echo refocusing when the fluid motion causes

spins to move to different field regions during the delay time τ_m. The best way to protect the spins from the varying background field is to use a closely–spaced CPMG pulse train to continually refocus the transverse magnetisation. However the usual resilience of this train to errors in the r.f. field applies only to on–resonant molecules. This creates a difficulty because of the the need to preserve both the in–phase (M_y) and quadrature (M_x) component of the magnetisation following the phase–encoding by the first q–gradient pulse pair. One solution is to separately record the M_y and M_x signals using appropriate phase–cycling. Another solution would be to use the compensated CPMG sequence of Gullion *et al.* [57], where an appropriate phase–cycling of the 180° pulses refocuses both components of the magnetisation. We have used the former method, as shown in the pulse sequence of figure 4.5, by the device of a "(z–storage)–(homospoil)–(recall)" segment of the pulse sequence in which each component is separately placed along the in–phase magnetisation direction in independent acquisitions. Providing that the delay between the CPMG pulses is smaller than the time associated with the background frequency spread, the method works extremely well.

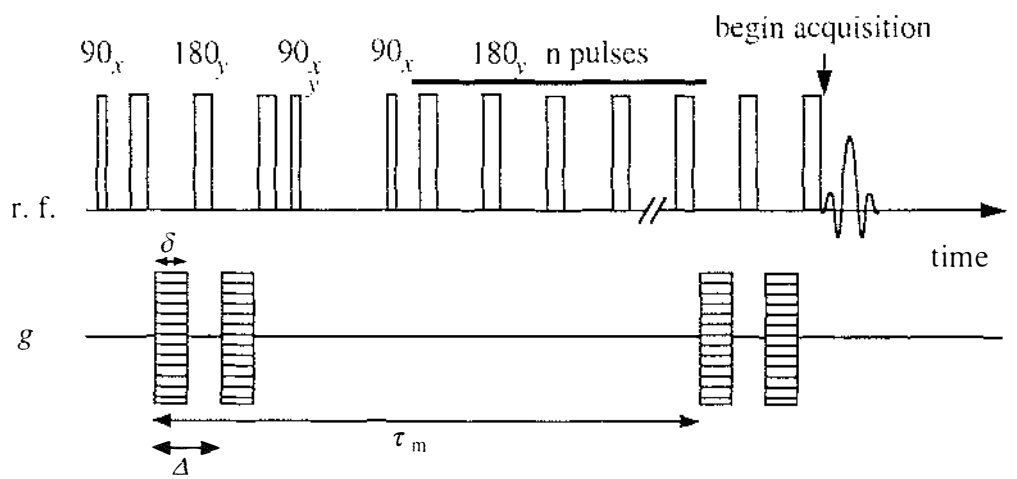

Figure 4.5: The modified VEXSY sequence using a CPMG train to preserve both quadrature components of the phase–encoded transverse magnetisation.

The experiment was carried out using the same rotating Couette system as described in detail in chapter 7. The space between the cylinders was filled with water containing a small amount (0.5%) of high molar mass polyethylene oxide (WSR301. Union Carbide Ltd). The polymer solute had the effect of increasing the viscosity and thus ensuring laminar flow at the rotational speeds used. The inner 5 mm NMR tube was filled with D_2O so as to reduce the magnetic susceptibility mismatch and so minimise the spread of local fields across the sample. This Couette system was placed in the imaging probe of a 1.4 T electromagnet and

the experiment was performed using the AMX300 spectrometer operating at 60 MHz, as described in section 2.5.2. Because of the need to work with τ_m values much larger than the reciprocal linewidth (around 200^{-1} Hz^{-1}), it was necessary to employ the CPMG sequence of figure 4.5.

A single rotation speed of 10 cycles per second was used and τ_m was varied by changing the number of CPMG loops in the period between the two q–pulse pairs. The corresponding values of $\omega\tau_m$ (expressed in cycles) were 0.15, 0.50, 1.00 and 2.00. The measurements were carried out using values of $\delta = 1$ ms, $\Delta = 2.58$ ms and with a repetition time of 1 s. In each case 64^2 q-steps were used and four steps of phase cycling were performed, each experiment lasting 4.5 hours. These results are shown as VEXSY spectra in figure 4.6 along with the corresponding theoretical VEXSY maps calculated by assuming a constant velocity gradient. The agreement is excellent.

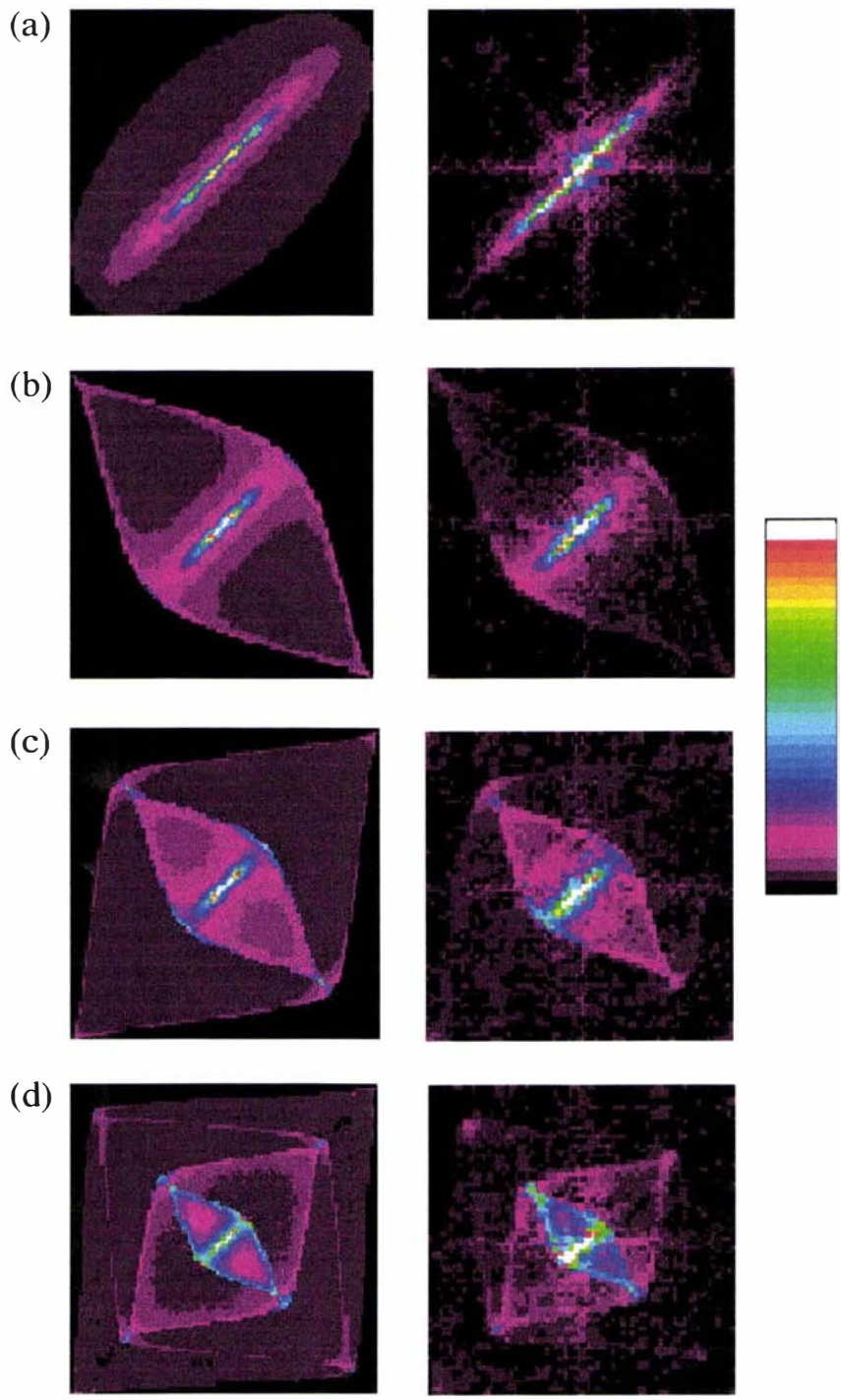

Figure 4.6: Succession of two–dimensional VEXSY spectra $S(Z_1, Z_2)$ for cylindrical Couette flow where $\omega_0 \tau_m$ corresponds to (a) 0.15, (b) 0.50, (c) 1.00, and (d) 2.00. Theoretical images are shown on the left with the corresponding experimental data on the right. The image full width corresponds to a displacement of 0.85 mm. The colour scale represents the amplitude of $S(Z_1, Z_2)$.

4.3.3 Flow Through Micropores

Having demonstrated the VEXSY method on purely random motion in section 4.3.1 and purely correlated motion in section 4.3.2, we now investigate the velocity exchange in a more complex flow. We observed the motion of water moving vertically through a bed of closely–packed polystyrene spheres with diameter of 90 μm inside a tube with a diameter of 1.9 mm. The average water flow rate in the tube was chosen to be $v_0 = 3$ mm s^{-1}, but was much higher between the spheres to satisfy the continuity equation. Estimating a filling factor of the spheres in the tube of around 0.5–0.7, we estimate that the average velocity of the water between the spheres is on the order of 6–10 mm s^{-1}. This flow rate was chosen so that the time taken for a molecule moving with the average velocity to move around one sphere corresponds to a convenient delay time τ_m on the order of 10 ms.

Figure 4.7 (a) shows a two–dimensional image of a 0.5 mm thick slice through the sample. Although the slice thickness is more than 5 times larger than the diameter of the spheres, the distribution of the spheres is still clearly visible. In figure 4.7 (b) we show a flow image of the same sample. Values of $\Delta = 20$ ms, $\delta = 2$ ms, and $g = 0.06$ T m^{-1} were used. Because Δ is longer than the time τ_m which we estimated before to be on the order of 10 ms, figure 4.7 (b) only displays *time averaged* velocities. Throughout the whole sample, we obtain a mean velocity of $v_{mean} = 5.6$ mm s^{-1}. The velocity propagators are broadened significantly due to the velocity spread in each pixel [58].

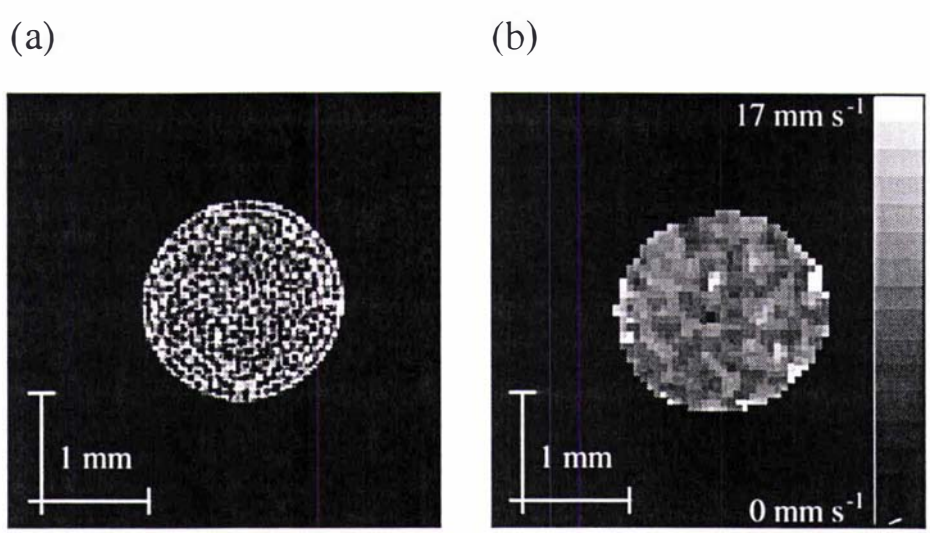

Figure 4.7: (a) A two–dimensional image of water in a bed of packed polystyrene spheres. (b) A flow image of the same sample. Both images are taken from [58].

Having used the dynamic spin echo method to obtain information about the average velocity of a fluid in a porous medium, we now use the VEXSY method to obtain information about the change of velocities with time. Because we expect the correlation time to be short (10 ms or less), it is necessary to have the delays δ and Δ as short as possible. This requires large gradients. Therefore, we used the high gradient probe which is described in section 2.5.3 for the experiments in this section. In the experiment 64^2 q–steps were used with a maximum gradient amplitude of 3 T m^{-1}, a gradient pulse duration δ of 1 ms and a delay Δ of 4 ms. The choice of these parameters ensures that the distance the molecules move due to Brownian motion during the time Δ ($\sqrt{\langle x^2 \rangle} = \sqrt{2D\Delta} = 4.2\mu$m) is much smaller than the distance a molecule moves with the average velocity during the same time Δ ($z = v_{av}\Delta \approx 32\mu$m). In other words, the broadening of the VEXSY spectrum is *not* due to Brownian motion, but to dispersion in the velocities.

In figure 4.8 we show some experimental VEXSY spectra. Figure 4.8 (a) displays the VEXSY spectrum of the stationary fluid. As expected, we get a spectrum with Gaussian profiles, similar to the one in figure 4.3. The spectra in figure 4.8 (b)–(d) were recorded with a flow rate of 3 mm s^{-1} in the tube and different mixing times. There is a clear transition from moderately stationary flow for short mixing times to correlated randomised flow as the mixing time is increased. The spectra are confined to the first quadrant because of the dominant motion of the water molecules along the tube.

Note also that the position of the peak maximum shifts from the centre (zero velocity) in figure 4.8 (a) by 3 pixels (corresponding to a velocity value of $v = 3$ mm s^{-1}) in (b)–(d). Although most of the molecules are moving with $v = 3$ mm s^{-1}, there are some molecules, which are moving with velocities of up to $v_{max} = 24$ mm s^{-1}. This information was not obtainable with the spin warp pulse sequence discussed before, because the large spread of velocities in one pixel broadens the velocity propagators and thus makes it impossible to use large gradients. In order to get a good velocity resolution, one has to use a long delay Δ. However, this means that one measures only the time averaged velocity.

One might wonder why the VEXSY spectra don't show a stronger correlation for a mixing time which corresponds to the time taken for a molecule moving with the average velocity to move around one sphere. This timescale is 20 ms in our experiment. In the VEXSY experiment, we do an instantaneous velocity encoding, wait a delay time τ_m, and do another instantaneous velocity encoding. The spectra in figure 4.8 (b)–(d) show that the molecules change their velocities very quickly on a timescale of 10 ms and lose memory about their previous velocities after that time. In a simple PGSE experiment with the same setup, strong displacement

correlations have been observed [58]. The PGSE experiment encodes for location of the molecules, waits a delay time Δ, and encodes again for location. The PGSE experiment therefore measures the *average* velocity of a molecule during the time Δ, while the VEXSY experiment correlates two velocities of the same molecule obtained at different, short, time intervals. In this case, the VEXSY method is less susceptible to time averaging.

4.4 Conclusions

In this chapter, we demonstrated a new 2D exchange experiment where the frequency dimensions f_1 and f_2 are not the usual chemical shift or dipolar coupling, but the displacements Z_1 and Z_2 of molecules over well defined time intervals. By applying the VEXSY pulse sequence to systems with known behaviour we could show the reliability of this method. The VEXSY spectrum of a sample of water undergoing unrestricted diffusion is a 2D Gaussian. From the width of this Gaussian we could work out the self–diffusion coefficient which is in excellent agreement with the literature value. The VEXSY spectra of laminar Newtonian flow in a Couette cell are also in good agreement with the simulations.

Of course, in these cases there are methods which can provide information about the velocity field more directly. With the dynamic spin echo method it is possible to obtain velocity and diffusion maps. However, many modern NMR spectrometers only have one gradient available for diffusion studies. We have shown here that with the VEXSY method it is possible to obtain information about the velocity field with only one gradient.

From the experiments in section 4.3.3 we could see that the dynamic spin echo measures the distribution of velocities averaged over the time Δ. As a contrast, the VEXSY method correlates velocities of the same molecule over the mixing time τ_m. Both yield the same result for stationary flow, but can be very different for fluctuating flows, as we have shown above. The VEXSY method is therefore a powerful tool for the investigation of fluctuating velocity fields. However, the limits are also obvious. Because the VEXSY method uses two phase–encoding gradients, the acquisition time for one experiment is usually on the order of 1 or 2 hours. If only one gradient direction is available, the stimulated echo cannot be used due to multiple spin echo interferences, and the exchange times which can be used in the experiments are limited by T_2 relaxation rather than T_1 relaxation.

In chapter 8 we will use the VEXSY method to investigate the flow field caused by convection in a capillary.

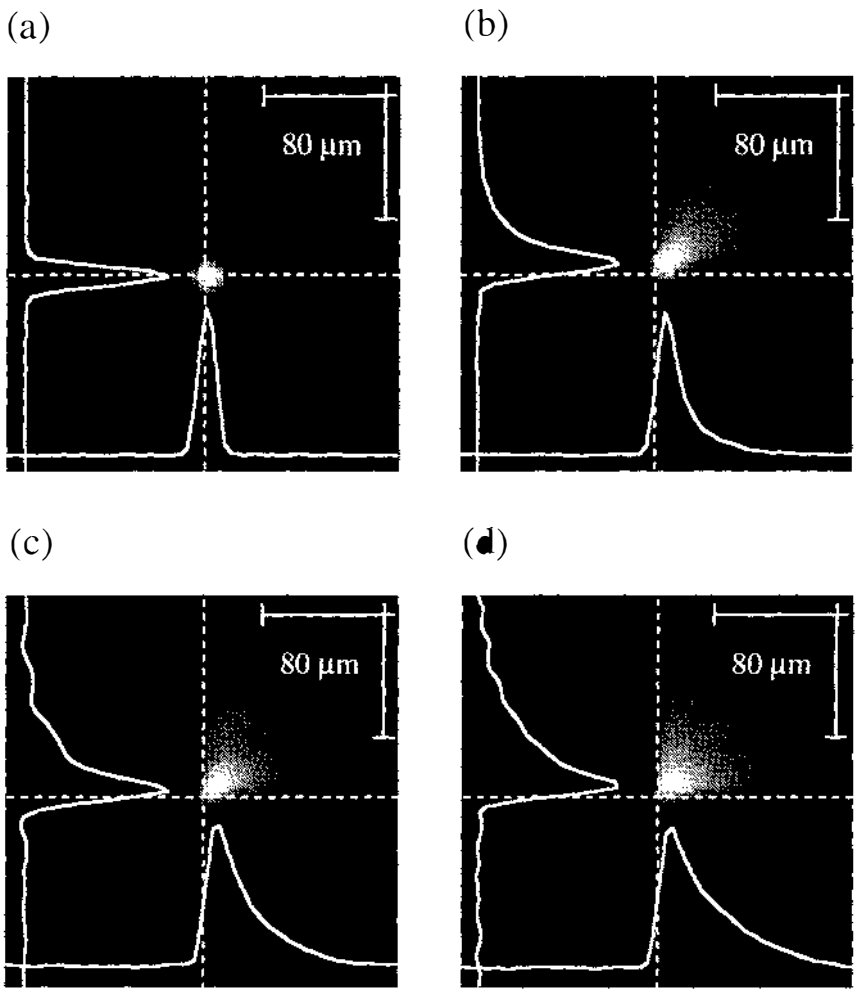

Figure 4.8: The two-dimensional VEXSY spectra $S(Z_1, Z_2)$ of water in a bed of packed polystyrene spheres for (a) stationary water and (b)–(d) at a constant flow rate. the mixing times are (b) 6 ms, (c) 10 ms, and (d) 20 ms. The image full width corresponds to a velocity of 0.26 mm.

Chapter 5

Polymer Physics

In this chapter the basic ideas of polymer physics are introduced as far as they are needed to understand the experiments in chapters 6 and 7.

5.1 Introduction

5.1.1 Definition of a Polymer

Polymers are large molecules made up of many atoms linked together by covalent bonds. They usually contain carbon and other atoms such as hydrogen, oxygen, and nitrogen. As the name suggests, groups of simpler blocks (monomers) are linked together in some systematic way. Although the final molecule does not need to be entirely linear, it is usually the case that the final linking process results in a chain-like structure of the polymer molecule. Many textbooks are available which deal with polymer physics, for example [59]-[66].

5.1.2 Molecular Weights and Polydispersity

In a real polymer sample, the degree of polymerisation varies from one polymer molecule to another. N_i denotes the number of polymer molecules in the sample with the molecular mass M_i. The average molecular mass for the sample can be defined as number average

$$M_n = \frac{\sum_{i=1}^{\infty} N_i M_i}{\sum_{i=1}^{\infty} N_i} \tag{5.1}$$

or weight average

$$M_w = \frac{\sum_{i=1}^{\infty} N_i M_i^2}{\sum_{i=1}^{\infty} N_i M_i}. \tag{5.2}$$

The ratio M_w/M_n measures the spread of the distribution of chain lengths and is known as the polydispersity of the sample. A polymer sample is called monodisperse if $M_w/M_n = 1$.

5.1.3 Polystyrene

Polystyrene (PS) is a polymer material which is very widely used, for example as a packing or heat insulating material. In Kingzett's Chemical Encyclopedia it is described as "one of the cheapest and most widely used thermoplastic materials. (...) In bulk, it is a clear glass–like material of low density, with a high moisture–resistance. Polystyrene is a very efficient electrical insulator, especially at high frequencies" [67]. The chemical structure of the monomer was established around 1930 by the pharmacist E. Simon. The structure of the polymer is shown in figure 5.1. The monomer unit consists of an ethylene group with a benzinic ring as a side–group. Its molecular mass is 104 g mol^{-1} and has a density of $1.04 - 1.065 \cdot 10^3$ kg m^{-3} [68].

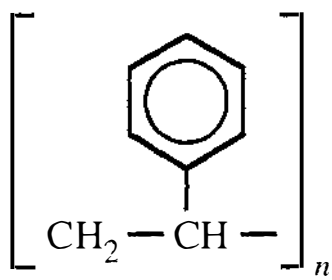

Figure 5.1: The Polystyrene Molecule.

PS has some properties which make it suitable for precise experiments. It is possible to obtain samples with up to 10^5 monomer units and an acceptably small polydispersity. PS dissolves well in organic solvents, such as benzene or carbon tetrachloride, but not as well in cyclohexane. Light is strongly scattered by these solutions, a property which makes it a perfect sample for light scattering experiments.

The PS samples used in this thesis were obtained from Polymer Laboratories Ltd., Church Stretton, Shropshire, UK. Their specifications are given in table 5.1.

5.2 Dynamics of Polymer Chains in Solution

Polymer chains in solution exhibit different types of dynamics, depending on the concentration of the solution. The theory goes back to the hydrodynamic model

M_w [g mol^{-1}]	M_w/M_n
200 000	1.02
330 000	1.04
500 000	1.06
770 000	1.04
1 030 000	1.05
1 450 000	1.06
1 750 000	1.06
3 040 000	1.04
4 000 000	1.06
6 850 000	1.06
9 350 000	1.20
15 000 000	1.25
20 000 000	1.30

Table 5.1: Specifications of the PS Samples.

of Flory [69] and Huggins [70]. De Gennes proposed the process of reptation [71] which was extended by Doi and Edwards [72]. In this section we describe these theories as far as necessary to understand the experimental results in chapters 6 and 7.

5.2.1 Random Coils in Dilute Solutions

One of the most important aspects in polymer physics is the fact that the exact chemical composition of the monomer units plays little part in governing the dynamics of polymer molecules.

A polymer molecule can be modelled as a succession of N links of length b, as shown in figure 5.2 (a). If one assumes that all the link orientations are random, the mean end-to-end length of the polymer is

$$\overline{R} = \langle R^2 \rangle^{1/2} = \sqrt{\langle (\boldsymbol{R}_N - \boldsymbol{R}_1)^2 \rangle} = \sqrt{N} b. \tag{5.3}$$

However, this assumption neglects the fact that in a polymer chain the links occupy a certain volume in space. This is shown in figure 5.2 (b). The links cannot interpenetrate, and this exclusion leads to modifications of the chain statistics. In order to account for this excluded volume, one introduces the exponent ν which lies in the interval $1/2 < \nu < 1$ [59, 73] and writes

$$\overline{R} \propto N^{\nu}. \tag{5.4}$$

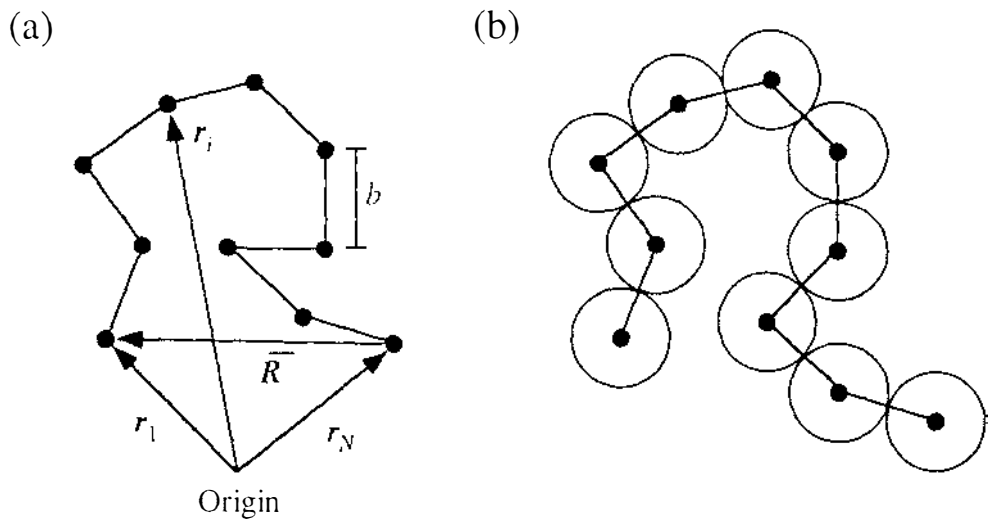

Figure 5.2: (a) A polymer molecule can be modelled as a succession of N links. (b) The links cannot interpenetrate each other. This is modelled by excluding some volume around the links from the configuration space.

The value $\nu = 1/2$ corresponds to a chain with independent links and $\nu = 1$ to a rigid chain. The effect of the excluded volume is therefore a swelling of the chain and its behaviour is between that of a random chain and a completely stretched chain or rod. The value of ν depends on the theoretical model and usually has a value of $\nu \approx 0.5 - 0.6$. Instead of choosing $\overline{R}$ to characterise the mean size of the polymer in solution, it is common to use the radius of gyration R_g, because this can be measured directly. It is defined as

$$R_g^2 = \frac{1}{N^2} \left\langle \sum_{i<j} (\boldsymbol{R}_i - \boldsymbol{R}_j)^2 \right\rangle . \tag{5.5}$$

R_g scales in the same way with the chain length N as $\overline{R}$. Therefore we can write

$$R_g \propto N^{\nu}. \tag{5.6}$$

The viscosity of a polymer solution will depend on the mean size of the polymer under investigation. The important parameter here is not R_g, but the hydrodynamic radius R_h. It is defined as

$$\frac{1}{R_h} = \frac{1}{N^2} \left\langle \sum_{i<j} \frac{1}{|\boldsymbol{R}_i - \boldsymbol{R}_j|} \right\rangle . \tag{5.7}$$

5.2.2 Thermodynamics of Polymer Solutions

In order to calculate the thermodynamic behaviour of polymer solutions, the mean-field lattice approximation of Flory [69] and Huggins [70] has been very suc-

cessful. In this model, one considers the polymer solution on a three-dimensional lattice, where each solvent molecule and each monomer unit occupy one lattice site. This is shown in figure 5.3. Because the monomer units are connected, there are less configurations available than in an ideal solution. This reduces the entropy of mixing S^m.

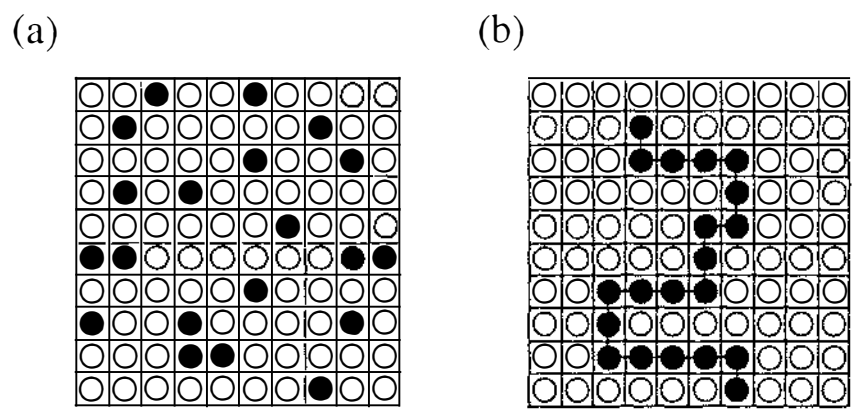

Figure 5.3: (a) In an ideal solution the solvent (○) and solute (●) molecules are randomly distributed. (b) In a polymer solution the segments must be linked together.

If there are N_s solvent molecules and N_p polymer molecules each with x monomer units, the entropy of mixing can be approximated by [69]

$$\Delta S^m = -k_B \left[N_s \log \frac{N_s}{N_s + xN_p} + N_p \log \frac{N_p}{N_s + xN_p} \right]. \tag{5.8}$$

It is more convenient to use volume fractions instead of the number of molecules. The volume fractions for solvent (ϕ_s) and polymer (φ_p) are defined as:

$$\Phi_s = \frac{N_s}{N_s + xN_p} \tag{5.9}$$

$$\Phi_p = \frac{xN_p}{N_s + xN_p} \tag{5.10}$$

Equation 5.8 becomes then

$$\Delta S^m = -k_B (N_s + xN_p) \left[\Phi_s \log \Phi_s + \frac{\Phi_p}{x} \log \Phi_p \right]. \tag{5.11}$$

By introducing the Flory interaction parameter χ [69, 73] which characterises the interaction between polymer and solvent molecules and decreases with increasing temperature, one can write the free energy of mixing as

$$\Delta G^m = k_B T (N_s + xN_p) \left[\Phi_s \log \Phi_s + \frac{\Phi_p}{x} \log \Phi_p + \chi \Phi_s \Phi_p \right]. \tag{5.12}$$

5.2.3 Osmotic Pressure and the Flory Temperature

From equation 5.12 it is possible to obtain the osmotic pressure Π of the polymer solution [73]

$$\Pi = \frac{k_b T}{\bar{v}_s}\left[\frac{\Phi_p}{x} + (\frac{1}{2} - \chi)\Phi_p^2 + \cdots\right]. \tag{5.13}$$

This is a virial expansion of van't Hoff's law [74]. The term $(\frac{1}{2} - \chi)$ is known as the second virial coefficient. If this term is zero, the polymer solution behaves like an ideal solution. Because of the temperature dependence of χ, this occurs at a particular temperature which is called the Flory, or theta, temperature Θ. A solvent is called a theta solvent if $\chi = \frac{1}{2}$. At the theta temperature, the polymer coil takes on its "natural size", and excluded volume effects are cancelled out. Above the theta temperature, $\chi < \frac{1}{2}$ and polymer–solvent contacts are favoured. The coil expands in this region. Below the theta temperature, $\chi > \frac{1}{2}$ and the coil collapses into a globule. This coil–to–globule transition has been a topic of extensive research in recent years [75]–[82].

Theta temperatures can vary widely, depending on the particular polymer and solvent. For example, for polystyrene in cyclohexane, it is 35° C [83], while for polystyrene in benzene it is −50° C [68] and 22° C for polystyrene in dioctyl phthalate (DOP) [84].

The interaction parameter χ does not depend on the temperature alone, but also on other parameters such as Φ_p and x. Strictly speaking, the theta temperature is defined for an infinitely long chain in a solution with infinitesimal concentration.

5.2.4 Phase Equilibria

For the formation of a single phase solution ΔG^m of equation 5.12 must always be negative. However, this is not the only condition, as is illustrated in figure 5.4. The curve in figure 5.4 (a) is always concave upwards, and this means that any point Q on the curve has a lower free energy than a two phase system of the same overall composition. However, if the free energy curve has a shape such as that shown in figure 5.4 (b), the free energy is smaller if a two–phase system is formed, if the polymer concentration is between Φ_{p1} and Φ_{p2}. The points P_1 and P_2 can be connected by a line which is a tangent at both points. This line represents the free energy of a phase separated mixture, and each position on the line represents different proportions of the two phase separated mixtures. Any hypothetical single phase mixture between these compositions has a larger free energy than the phase separated mixture, so that the system is immiscible over this composition range. The composition range where phase separation occurs is defined by the points of

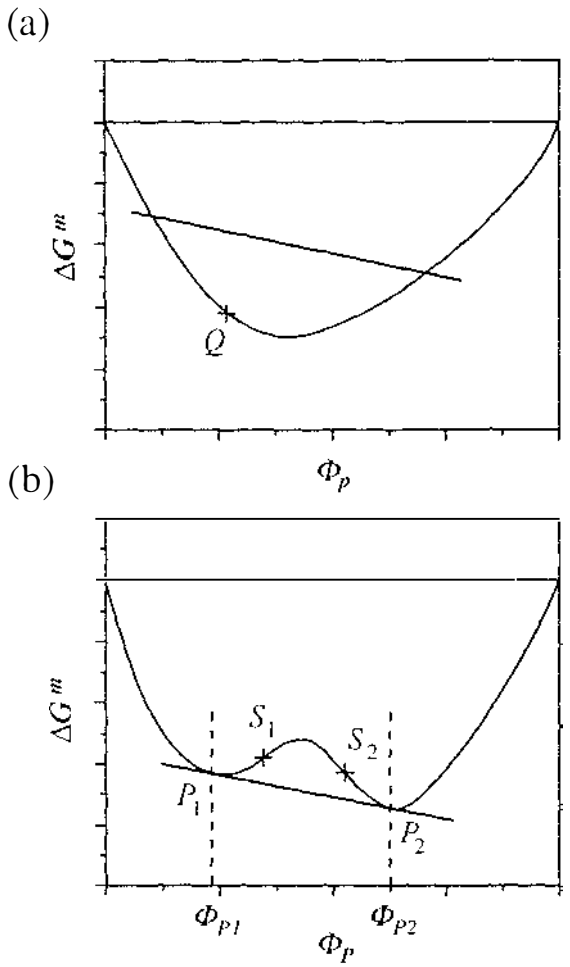

Figure 5.4: Schematic diagrams of the free energies of mixing as a function of polymer concentration. Polymer and solvent always form a single phase in (a), while in (b) phase separation can occur. The straight line represents the free energy for a phase–separated mixture.

contact of the double tangent. This gives the relationship

$$\left[\frac{\partial \Delta G^m}{\partial N_p}\right]_{\Phi_1} = \left[\frac{\partial \Delta G^m}{\partial N_p}\right]_{\Phi_2}. \tag{5.14}$$

The derivative $\frac{\partial \Delta G^m}{\partial N_p}$ is the chemical potential μ_p of the polymer. The meaning of equation 5.14 is that the chemical potentials μ_{p1} at point P_1 and μ_{p2} at point P_2 must be equal:

$$\mu_{p1} = \mu_{p2}. \tag{5.15}$$

The phase separation points P_1 and P_2 can be calculated from equation 5.14.

The points P_1 and P_2 represent the compositions of the two phases that would be present in equilibrium. However, the shape of the free energy curve around

P_1 and P_2 is *locally* still concave upwards until the inflection points S_1 and S_2 are reached. This means that mixtures that have compositions between points P_1 and S_1 or P_2 and S_2 are stable against separation into phases consisting of *local* compositions. The points S_1 and S_2 can be obtained by setting the second derivative of ΔG^m to zero:

$$\frac{\partial^2 \Delta G^m}{\partial \Phi_2^2} = 0. \tag{5.16}$$

The compositions of the phase separated domains obtained from equations 5.15 and 5.16 depend on the temperature. These equations can be solved at different temperatures to obtain a phase diagram shown in figure 5.5 (a). The line obtained from solving equation 5.15 is called binodal, while the line obtained from solving equation 5.16 is called spinodal. The metastable region lies between both curves which meet at a point C. The critical temperature T_c and critical composition Φ_c are defined in figure 5.5 (b). Because the polymer solution undergoes a transition from a single phase solution to a two phase mixture when crossing the binodal, this transition is often called de–mixing transition. The onset of the phase separation is marked by the appearance of turbidity at the so–called cloud–point temperature and can easily be detected with optical methods.

Figure 5.6 (a) shows the dependence of the de–mixing transition on the chain length. Shultz and Flory [85] found that the critical temperature T_c and critical concentration Φ_c depend on the chain length x as

$$\frac{1}{T_c} = \frac{1}{\Theta} + \frac{1}{\Theta\Psi}\left(\frac{1}{\sqrt{x}} + \frac{1}{2x}\right) \tag{5.17}$$

$$\Phi_c = \frac{1}{1+\sqrt{x}} \tag{5.18}$$

The dependence of T_c on the chain length is shown in figure 5.6 (b). The limit of T_c for infinite chain lengths is the theta temperature, and Ψ is the so–called entropy parameter [73]. Perzynski *et al.* report phenomenological relationships between T_c, Φ_c and M_w for polystyrene in cyclohexane [86]. They found

$$\frac{1}{T_c} = \frac{1}{307\mathrm{K}} \cdot \left(1 + \frac{14.6}{\sqrt{M_w}}\right) \tag{5.19}$$

$$\Phi_c = 6.8 \cdot M_w^{-0.38} \qquad (\mathrm{g\ cm^{-3}}). \tag{5.20}$$

Equation 5.19 is in good agreement with the Flory–Huggins model (equation 5.17), while equation 5.20 is in clear opposition equation 5.18.

The de–mixing curves obtained by solving equation 5.14 do not describe the experimental data satisfactorily. The dependence of χ on molar mass, polymer concentration and temperature has been measured by Scholte [87] for polystyrene with molar masses up to $M_w = 5.2 \cdot 10^5$ g mol^{-1} in cyclohexane. From these

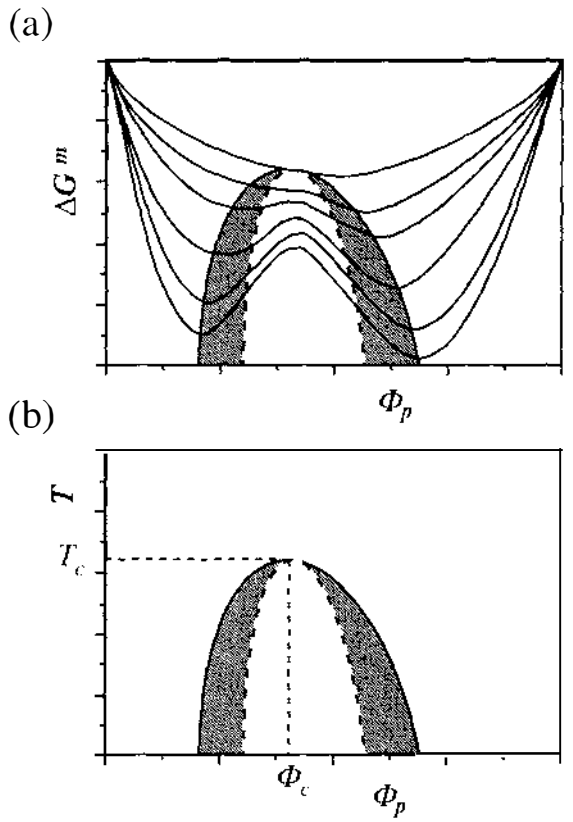

Figure 5.5: (a) Free energy curves for different temperatures. (b) Schematic representation of a phase diagram.

values of χ the spinodals and binodals can be calculated. Einaga *et al.* suggested an empirical correction for χ [88]. In this approach χ does not depend only on T, but also on Φ and x. Other corrections use a virial expansion of the chemical potential [89]. The so-called apparent second virial coefficient Γ is assumed to depend on T, Φ and x as well. These models describe the experimental data [85] much better, but are still not satisfactory. A review on this topic is given in [63].

5.2.5 Concentration Regimes

Sufficiently dilute polymer solutions may be viewed as systems in which "islands" of polymer coils are scattered around in a "sea" of solvent. The spatial distribution of chain molecules is therefore quite inhomogeneous and undergoes considerable fluctuations. As the polymer concentration increases, the distribution of polymer coils becomes more homogenous and local fluctuations get more and more suppressed. Collisions may cause the chains to overlap and entangle in a complex fashion. The concentration where this transition occurs depends on the size of the

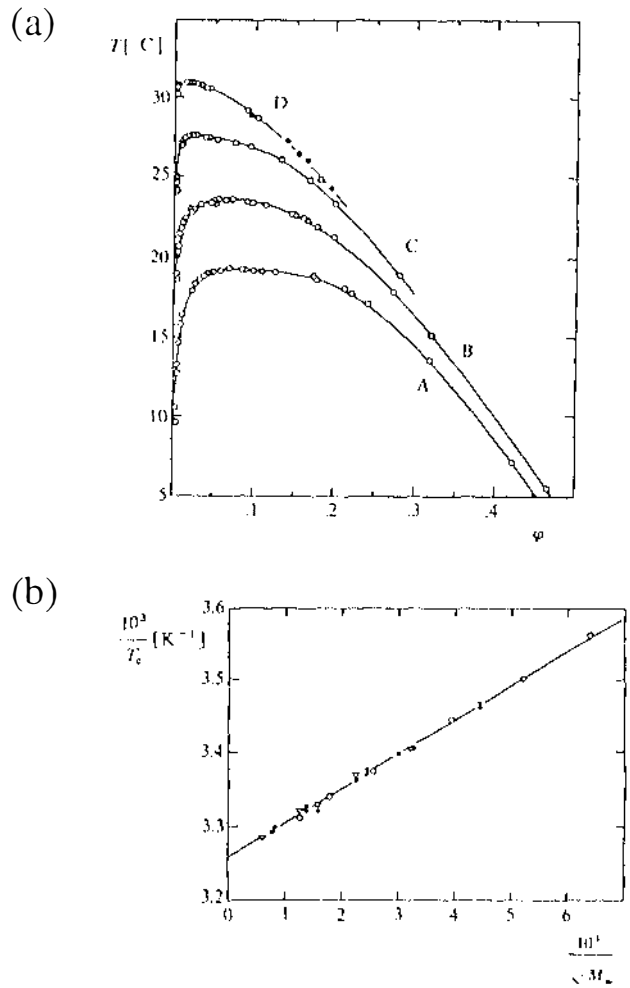

Figure 5.6: (a) Measured cloud–point curves for various solutions of polystyrene in cyclohexane. φ is the volume fraction of the solute. The molar masses are given by: $10^{-4}M_w = 4.36$ (A), 8.9 (B), 25 (C), and 127 (D). (b) Dependence of the critical temperature on the molar mass. Both diagrams taken from [85].

polymer chain. It is common to define the overlap concentration c^* as

$$c^* = \frac{3M_w}{4\pi N_A R_g^3}, \tag{5.21}$$

where N_A is Avogadro's constant.

It is important to note that c^* is not a critical concentration. No sharp changes in the concentration dependence of physical properties of the solution take place at this concentration. However, the macroscopic distribution of chain segments across the solution becomes homogenous when the polymer concentration is increased beyond c^*. When viewed microscopically, even solutions with concentrations above c^* are not uniform. The segment density in each volume element fluctuates about

a mean value c. Because of the chain connectivity, these fluctuations cannot take place independently. They have been observed by light scattering [90, 91] and can be enhanced by external shear and lead to shear-induced phase transitions. We will come back to this effect later in section 5.4.

From equation 5.21 it follows that if M_w is sufficiently high, there is a rather wide range where the concentration is higher than c^*, but its absolute value is still low. Such solutions are dilute in the sense that the concentration of polymer is small, but concentrated enough for coils to overlap. They are called semi-dilute.

As the concentration increases, the polymer solution enters a regime where the chains overlap extensively. Density fluctuations are mainly screened. The concentration where the transition from semi-dilute to concentrated solutions occurs is termed c^{**} and is independent of M_w.

Equation 5.21 allows us to estimate the dependence of c^* on M_w. Because of relationship 5.6 R_g scales as M_w^ν. Therefore

$$c^* \propto M_w^{1-3\nu}. \tag{5.22}$$

Adam and Delsanti [92] measured R_g of PS in a theta solvent at different molar masses and obtained the phenomenological relationship

$$c^* = 51 \cdot M_w^{-1/2} \tag{5.23}$$

which is in agreement with relationship 5.22 for $\nu = 1/2$. A graph of equation 5.23 is shown in figure 5.7.

5.2.6 The Reptation Model

If the polymer concentration is high enough for entanglements to take place, the motion of each polymer chain is restricted by neighbouring chains. This effect due to chain uncrossability is called topological constraint and shown in figure 5.8 (a). Brochard and de Gennes [93] suggested replacing the chain by a wire trapped in a curvilinear tube fixed in space (figure 5.8 (b)). It can only move along its own path. Figure 5.8 (c) shows the primitive path which is given by the shortest path between the ends of the polymer and has the same topology relative to the obstacles as the chain. A primitive chain can then be used to describe the simplified motion of the polymer moving along the primitive path by neglecting small scale fluctuations across the path. Doi and Edwards [72] extended this idea by approximating the chain of discrete molecules by a continuous chain. They calculated different time scale regimes of polymer reptation [61, 72]. If the time over which diffusion is measured is longer than the longest relaxation time τ_d of the Doi-Edwards model, the diffusion is a long range centre-of-mass diffusion

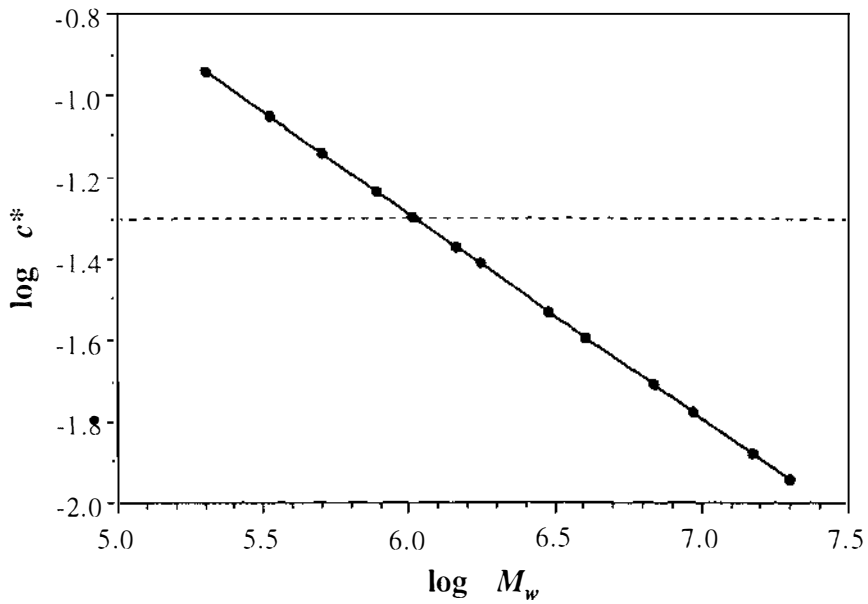

Figure 5.7: A graph of c^* vs. M_w for PS in a theta solvent using equation 5.23. The data points indicate the M_w values of the samples from table 5.1, and the dashed line is at $c^* = 5\%$.

and can be described by a time independent Brownian self-diffusion coefficient D_s. The so-called tube disengagement or reptation time τ_d is a relaxation time characterising the time it takes for a primitive chain to disengage from the tube it was confined to initially and is given by

$$\tau_d = \frac{2R_g^2}{\pi^2 D_s}, \tag{5.24}$$

where R_g is the radius of gyration of the polymer coil which was defined in equation 5.5. According to Doi and Edwards, D_s scales as N^{-2} and R_g^2 roughly as N, and thus the reptation time scales as $\tau_d \propto N^3$.

D_s also depends on the polymer concentration Φ. The Doi-Edwards theory predicts that D_s scales for semi-dilute polymer solutions as

$$D_s \propto N^{-2}\Phi^{\frac{2-\nu}{1-3\nu}}. \tag{5.25}$$

For a good solvent $\nu = 0.6$, and $\nu = 0.5$ for a theta solvent. Therefore we obtain two different scaling regimes:

$$D_s \propto N^{-2}\Phi^{-1.75} \quad \text{for a good solvent} \tag{5.26}$$

$$D_s \propto N^{-2}\Phi^{-3.0} \quad \text{for a theta solvent} \tag{5.27}$$

The scaling of D_s with N^{-2} has been investigated experimentally by different techniques. A review is given in [63]. However, the $D_s \propto N^{-2}$ dependence is not

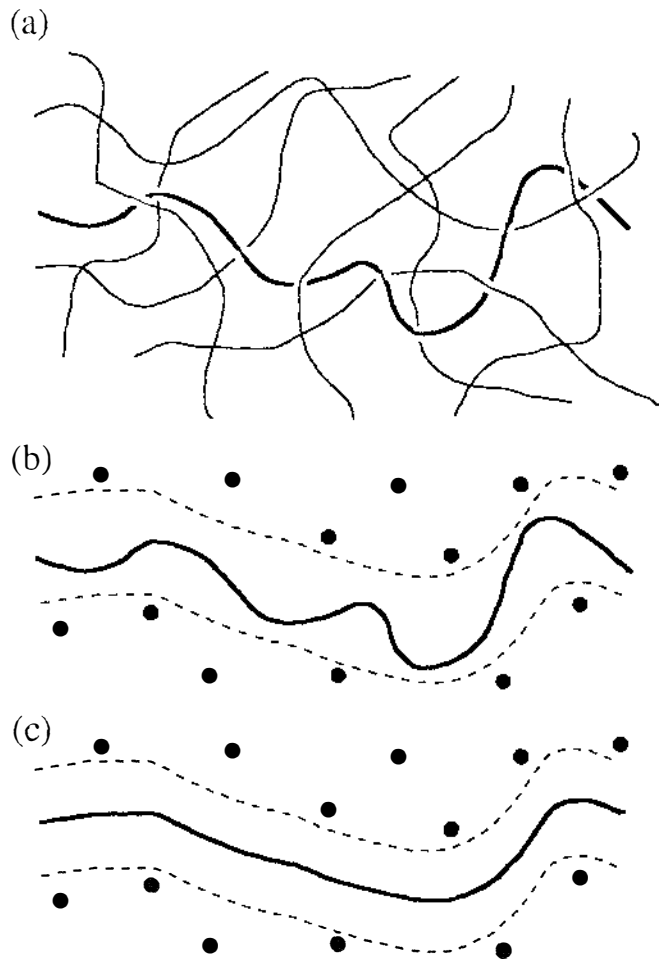

Figure 5.8: (a) Entangled polymer chains with one polymer highlighted. (b) Schematic picture of the highlighted polymer in (a) placed on a plane with dots showing the other polymer chains crossing this plane. The Doi–Edwards tube is shown as well. (c) The primitive chain in the Doi–Edwards tube.

only characteristic for reptation [94, 95, 96]. Furthermore, other scaling exponents for reptation may be possible, for example $D_s \propto N^{-2.4}$, given the known scaling of zero shear viscosity as $\eta_0 \propto N^{3.4}$ [97].

The concentration dependence of D_s in good and theta solvents has been examined by several groups with different methods [98]–[106]. The $D_s \propto N^{-2}$ dependence could be confirmed for concentrations above the overlap concentration. The first experimental results in semi-dilute solutions were reported by Hervet *et al.* in 1979 [98, 107]. These authors performed forced Rayleigh scattering studies on PS chains in benzene solutions. They report a scaling of $D_S \propto M^{-2}\Phi^{-1.75}$. Callaghan and Pinder [100] and Meerwall *et al.* [102] performed PGSE NMR experiments on PS in a good solvent. Both groups found a transition from $D_s \propto \Phi^{-1.75}$

to $D_s \propto \Phi^{-3.0}$ with increasing concentration. However, this transition is very smooth over a wide concentration range. Wesson *et al.* [101] and Kim *et al.* [104] measured the polymer and tracer diffusion in good solvents via forced Rayleigh scattering. They also found a smooth transition from $D_s \propto \Phi^{-1.75}$ to $D_s \propto \Phi^{-3.0}$ behaviour. Amis *et al.* [99] and Wheeler *et al.* [105] measured the self-diffusion coefficients of PS in theta solutions via light scattering. These authors also report a smooth transition between the two scaling regimes. Nemoto *et al.* [103] re-analysed the D_s data reported in [101] using a concentration and temperature dependent local viscosity correction. With this correction term the data reported in [101] fit better into the scaling predictions of the Doi-Edwards model. Fleischer *et al.* [106] performed PGSE NMR experiments on PS in deuterated benzene and in deuterated chloroform in semi-dilute concentration. The scaling law $D_s \propto M_w^{-2}$ could be confirmed, but no linear region with a concentration exponent of -1.75 could be found. The concentration exponent of the master curve decreased from about -1.8 to -3.0 at the end of the semi-dilute region, and then exhibited a further dramatic decrease.

Because there seems to be no sharp transitions between scaling in good and theta solvents, the question arises whether there is a universal scaling law for $D_s(\Phi)$. Phillies suggests in a series of papers [108]-[111] that reptation is not an important process in polymer solutions. Instead he suggests a universal scaling law for the concentration dependence of D_s:

$$D_s(\Phi) = D_0 e^{-\alpha \Phi^{\lambda}}. \tag{5.28}$$

where D_0, α and λ are adjustable parameters. With this empirical equation, he can obtain a good fit to the experimental data mentioned above. A major criticism of this description is that the apparent success of equation 5.28 reflects more the flexibility of the stretched exponential form than the universality of diffusion mechanisms in semi-dilute polymer solutions [105].

To our knowledge, there have so far been no studies of the temperature dependence of D_s near the de-mixing transitions of polymer solutions. In chapter 6 we report on PGSE NMR measurements of the temperature dependence of D_s for polymer solutions at different chain lengths and different concentrations. We will show then that there exists a single temperature scaling dependence.

5.3 Rheology of Polymer Solutions

5.3.1 Introduction and Definitions

Rheology is the interdisciplinary science of deformation and flow of condensed matter. The term was suggested by E. C. Bingham who also founded the Society and the *Journal of Rheology* in 1929. Rheologists study the behaviour of materials which, because of their nature or because they are subject to large deformations, do not obey either Hooke's law of elasticity or Newton's law of viscosity.

Macroscopic flow is described by constitutive equations and parameters which relate observed stresses and rates of straining to material properties. In principle, knowing all relevant molecular properties, the parameters of the continuum's mechanical equations of motion should be obtainable.

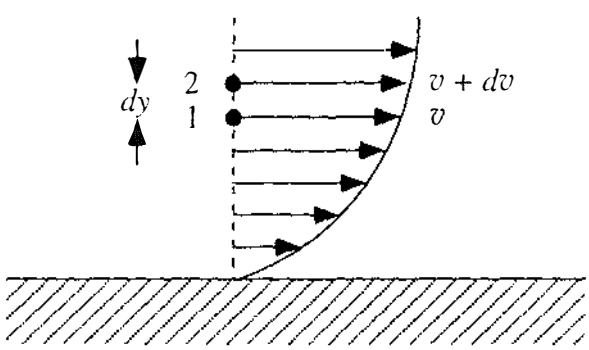

Figure 5.9: A velocity profile of fluid flowing along a boundary.

The laminar flow of a real fluid along a solid boundary is shown in figure 5.9. The velocity increases with the distance from the boundary. Two volume elements 1 and 2 starting in adjacent layers on the same vertical line as shown in figure 5.9 move different distances $d_1 = vdt$ and $d_2 = (v + dv)dt$ in an infinitesimal time dt. One defines the shear strain γ and shear rate $\dot{\gamma}$ as

$$\gamma = \frac{d_2 - d_1}{dy}, \tag{5.29}$$

$$\dot{\gamma} = \frac{dv}{dy}. \tag{5.30}$$

The shear stress τ is defined as the shearing force between the fluid layers per unit of contact area. For laminar motion, τ is dependent on $\dot{\gamma}$. The shear viscosity η is defined as:

$$\eta = \frac{\tau}{\dot{\gamma}}. \tag{5.31}$$

Fluids for which η is constant are known as Newtonian fluids. Other fluids are classed as non–Newtonian fluids.

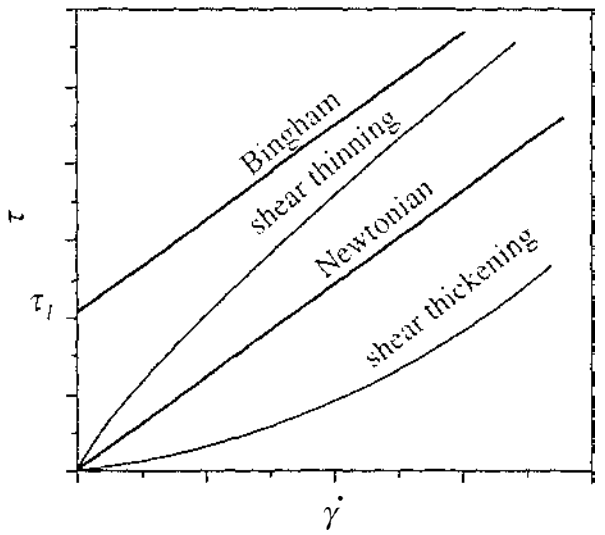

Figure 5.10: A shear stress vs. shear rate diagram for Newtonian and non–Newtonian fluids.

Some examples for non–Newtonian fluids are shown in figure 5.10. A Bingham fluid is characterised by the yield stress τ_1 which is the minimum stress required for the fluid to flow. The fluid exhibits solid–like properties up to the stress τ_1 sufficient to cause a transition to flow. The shear stress vs. shear rate relationship is given by

$$\tau - \tau_1 = \eta\dot{\gamma}, \qquad \tau > \tau_1. \tag{5.32}$$

Toothpaste is a classical example of a Bingham fluid.

For many polymer melts and solutions it is found that the viscosity defined in equation 5.31 is dependent on the shear rate. A typical graph of viscosity vs. shear rate looks like the one shown in figure 5.11. In region A, the viscosity can be approximated by a power law

$$\eta \propto \dot{\gamma}^{n-1}. \tag{5.33}$$

n is known as the power law index. For $n = 1$ the viscosity is independent on the shear rate and the fluid is Newtonian. If $n < 1$, the viscosity decreases with increasing shear rate. Such a fluid is called shear thinning, while a fluid with $n > 1$ is shear thickening.

5.3.2 Dependence of Non–Newtonian Viscosity on Shear Rate

For polymer solutions with different concentrations it has been found that with decreasing concentration, the onset of non–Newtonian behaviour shifts to higher

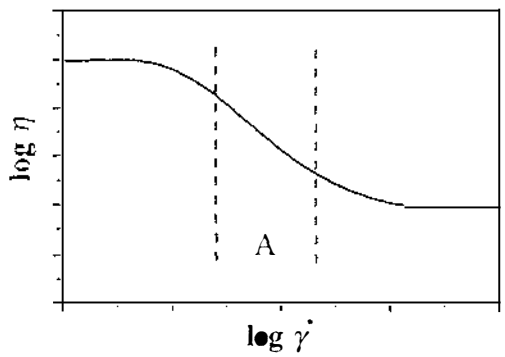

Figure 5.11: A viscosity vs. shear rate diagram for a non–Newtonian fluid. In the region A the viscosity can be approximated by the power law of equation 5.33.

shear rates [112]. At high shear rates, the plot of $\log \eta$ vs. $\log \dot{\gamma}$ becomes linear, but the slope becomes less negative with decreasing concentration. Graessley showed that all these curves can be plotted on one master curve by plotting $\log \frac{\eta}{\eta_0}$ vs. $\log \dot{\gamma}\tau_\eta$, where η_0 is the viscosity at zero shear rate and τ_η the entanglement formation time which is characteristic for each solution [113]. He gives an implicit equation for this master curve [112]:

$$\frac{\eta}{\eta_0} = \left(\frac{2}{\pi}\right)^{5/2} \left[\cot^{-1}\theta + \frac{\theta}{1+\theta^2}\right]^{3/2} \left[\cot^{-1}\theta + \frac{\theta(1-\theta^2)}{(1+\theta^2)^2}\right], \tag{5.34}$$

where

$$\theta = \frac{\eta}{\eta_0}\frac{\dot{\gamma}\tau_\eta}{2}. \tag{5.35}$$

The η vs. $\dot{\gamma}$ relationship obtained from equation 5.34 is shown in figure 5.12. The numerically obtained power law index is shown in the same figure.

The concept underlying Graessley's theory is that the viscosity is governed by entanglements of the polymer coils. If the inverse of the shear rate is smaller than the time to form entanglements, the viscosity will decrease with increasing shear rate. It is therefore not surprising that the time τ_η is found to be of the same order as τ_d, where τ_d is the tube disengagement time from the Doi–Edward model and is defined in equation 5.24.

Equation 5.34 is difficult to handle for analytical calculations. Williams calculated $\eta(\dot{\gamma})$ by modelling the polymer molecules as elastic dumbbells [114]. He obtained a monotonically decreasing function of $\dot{\gamma}$ which is algebraically complicated, but roughly obeys the form

$$\frac{\eta}{\eta_0} = \left(\frac{1}{1+(\dot{\gamma}\tau_\eta)^2}\right)^{1/2}. \tag{5.36}$$

Here τ_η is the relaxation time of the elastic dumbbell. The graphs of equations 5.34 and 5.36 are displayed in figure 5.12. Because Graessley's theory is based on entanglements of the polymer coils, it is a more realistic model than Williams' for semi–dilute polymer solutions. Therefore, we will use Graessley's theory for working out the entanglement formation time from the measured power law index.

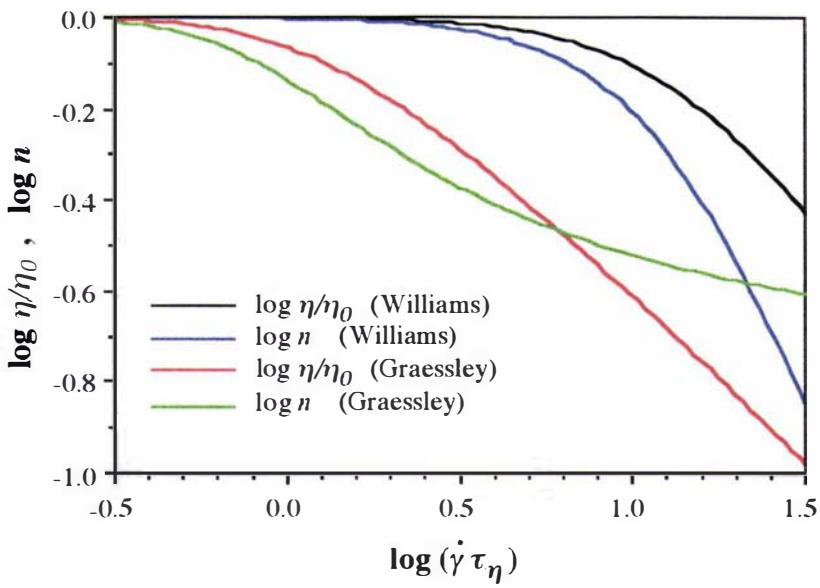

Figure 5.12: The viscosity is plotted vs. shear rate using equations 5.34 and 5.36. The shear rate dependence of the power law exponent using equation 5.37 is also shown for both theories.

A generalised, shear–rate dependent power law index can be defined as

$$n(\dot{\gamma}) = 1 + \frac{d \log \eta}{d \log \dot{\gamma}}. \tag{5.37}$$

Using equation 5.36, an analytical expression for $n(\dot{\gamma})$ can be obtained:

$$n(\dot{\gamma}) = \frac{1}{1 + (\dot{\gamma}\tau_\eta)^2}. \tag{5.38}$$

This curve is also shown in figure 5.12.

In chapter 7 we will use equation 5.37 along with Graessley's finding for $\eta(\dot{\gamma}\tau_\eta)$ in equation 5.34 to obtain the temperature dependence of τ_η from the measured power law indices.

Adam and Delsanti measured the longest viscoelastic relaxation time for PS in cyclohexane in the Newtonian regime [115]. They found that this parameter scales as $M_w^x \Phi^y$, where x and y are numerical constants with the values of $x \approx 3.8$ and $y \approx 2.8$. The reptation model predicts $x = y = 3.0$ for theta solutions [61]. In chapter 7 we will compare these findings with our results for τ_η.

5.3.3 The Glass Transition

When a polymeric material is cooled from the liquid or rubbery state, it becomes much stiffer as it goes through a certain temperature range. This stiffening is the result of one of two possible events: crystallisation or glass transition. For crystallisation to occur, the polymer molecules must be sufficiently regular along their length to allow formation of crystallisation lattices, and the cooling rate must be slow enough. When a polymer fails to crystallise, the amorphous, liquidlike structure of the polymer is retained, but the molecular motion frozen, and the material turns into a glass. Such a glass transition occurs over a finite temperature interval, but is still realised abruptly enough to merit the term transition. It can be recognised by the change in many properties of the material, such as an increase in viscosity or a change of the specific heat and thermal expansion.

The values of the glass transition temperature T_g reported for a certain polymer often differ by as much as $10 - 20°$ C, because the glass transition occurs over a temperature range rather than at a single, sharply defined temperature, and because the observed T_g varies somewhat depending on the method of measurement used and the thermal history of the sample. For polystyrene, T_g has a literature value of 373 K [68]. If the polymer is in solution, T_g can be much lower. This decrease can be attributed to the introduction of additional free volume with the solvent [116]. For example, for polystyrene in cyclohexane a T_g of around 280 K has been reported [117].

Near the glass transition, the self-diffusion coefficient $D_s(T)$ can be described by a law named after Williams, Landel and Ferry (WLF) [118, 119, 120]:

$$D_s(T) = D_0 e^{-\frac{B}{T - T_g}}. \tag{5.39}$$

The ratio $a_T(T)$ of mechanical and electrical relaxation times at temperature T to their values at a reference temperature T_s can be expressed by the equation [118, 120]

$$\log a_T(T) = -c_1 \frac{T - T_s}{c_2 + T - T_s}, \tag{5.40}$$

where c_1 and c_2 are constants which depend on the choice of T_s.

In chapter 6 we will measure the temperature dependence of D_s of PS/CYH solutions near the de-mixing transition. We will show that it can be described by equation 5.39. In chapter 7 we will measure the power law exponent $n(T)$ in order to obtain $\tau_\eta(T)$ for the same samples. We will show that the behaviour of $\tau_\eta(T)$ near the de-mixing transition can be described by equation 5.40.

5.4 Flow–Induced Structures in Polymer Solutions

When a polymer solution is subjected to shear, the free energy of mixing given by equation 5.12 must be adjusted by an additional term which accounts for the entropy change due to flow. A large number of different phenomena has been observed, ranging from macroscopic phase separations through mesoscopic concentration fluctuations to microscopic alignment of molecules. Reviews on this topic have been published by Rangel–Nafaile *et al.* [121] and Larson [122]. A recently published book by Nakatani [123] contains several detailed articles with a large number of references. In this section we will give a short review on this topic.

5.4.1 Shear–Induced Phase Transitions

The first systematic investigations on shear–induced phase transitions were performed by Kuhn and Silberberg in 1952 [124]. They observed that a solution of polystyrene and ethyl cellulose in benzene, which was phase separated at room temperature, resulted in a homogenous one–phase solution when a velocity gradient was applied. After the velocity gradient was turned off, the solution phase separated again. The shift in the phase transition temperature was found to be dependent on the shear rate.

Ver Strate and Philippoff reported in 1974 [125] on experiments where a clear polymer solution, PS in dioctyl phthalate (DOP), was pumped from a reservoir through a capillary into a second reservoir. Above a certain shear rate which was found to depend on polymer, solvent, temperature and concentration, the solution turned cloudy upon passing into the capillary and clear when leaving it. This effect was interpreted as a phase separation induced by a shear rate dependent change in free energy. This phase separation was found to be reversible.

An irreversible shear–induced change in the refractive index has been observed in PS/CYH solutions by Debeauvais *et al.* and has been interpreted as degradation of the polymer coils [126]. Because this was found to happen at shear rates higher than we used in the experiments of chapter 7, this degradation was not important for our experiments.

Rangel–Nafaile *et al.* observed a shear–dependent increase in the cloud–point temperature of PS/DOP solutions. They found a shift of up to 28° C in the phase transition temperature at a shear rate of 220 s^{-1} [121]. In a review they also summarised a whole variety of shear–induced changes in the degree of mixing of polymer solutions. These effects include shear–induced cloudiness, precipitation of gel–like particles and flow–induced crystallisation.

Barham and Keller reported on the existence of different distinct types of rheological behaviour in high molecular weight PMMA solutions, depending on the shear rate. These types were attributed to the formation of layers formed by the mutual entanglement of molecules in the flowing solution and those adsorbed along the rheometer surfaces. They can be much thicker than the radius of gyration and are called adsorption–entanglement layers. With increasing shear rate, these layers grow, and wild fluctuations in shear stress are observed. At higher shear rates, spontaneous local phase separations occur, and finally these phase separations grow until a stable two–phase system has been established [127]. Link and Springer also reported the onset of shear–induced phase separations in very dilute PS/DOP solutions [128].

A theoretical model for these shear–induced shifts in the phase transition temperature has been suggested independently by Rangel–Nafaile *et al.* [121] and Wolf [129]. These authors add a shear–dependent term to the free energy of mixing ΔG_m in equation 5.12 which corresponds to the elastic free energy stored in the system due to chain deformation and is proportional to the shear stress tensor $\boldsymbol{\tau}$.

5.4.2 Enhanced Concentration Fluctuations

The thermodynamic approach by Rangel–Nafaile *et al.* has been criticised by Helfand and Fredrickson [130], and by Onuki [131], who have considered this problem from the point of view of the growth of concentration fluctuations upon the application of shear. In their treatment, the Flory interaction parameter χ is assumed to be shear–dependent. Milner extended the Helfand–Fredrickson model to the case of entangled polymers [132]. The shear–dependence of χ has been measured by Hammouda *et al.* [133] for PS/DOP solutions. A steep increase of χ was found when the shear rate $\dot{\gamma}$ exceeded a critical value $\dot{\gamma}_c$ which was below the spinodal value $\dot{\gamma}_s$ where phase separation occurred.

Hashimoto *et al.* performed light scattering experiments on a binary polymer solution under shear [134]. With increasing shear rate, they report on five different regimes of concentration fluctuations, including the formation of polymer–rich droplets which elongate with increasing shear rate.

Wu *et al.* have studied the orientation dependence of the enhanced concentration fluctuations in the Couette geometry [135]. They showed that the structures were aligned in the plane defined by the direction of flow and the direction of shear. As the shear rate was increased, the structures rotated by 90° in this plane. Their length was found to be of order 1000 Å. For high shear rates, Yanase *et al.* found the dichroism $\Delta n''$ to be time–dependent [136]. This effect is believed to be caused

by a shear–induced phase transition.

The direct visualisation of enhanced concentration fluctuations in semi–dilute polymer solutions has been reported by Moses *et al.* [137]. With a microscope, periodic structures with a length scale of approximately 10 μm could be seen. These structures are in qualitative agreement with the ones found from the characteristic butterfly patterns in light scattering [134] and neutron scattering [138] experiments. Ji and Helfand calculated the polymer structure factor using a phenomenological approach to write down a coupled set of Langevin equations for polymer concentration, velocity and strain [139]. The calculated butterfly patterns were found to be in qualitative agreement with the experiments by Wu *et al.* [135].

5.4.3 Shear–Induced Ordering

So far, we have only considered shear effects on scales much larger than the size of the molecules. However, for randomly oriented chain molecules, one expects that an inhomogeneous flow field somehow alters the configuration of the molecules.

Nakatani *et al.* [140] performed NMR experiments on sheared polymer melts. In the next section we will describe these experiments in more detail.

Link and Springer and Muller *et al.* measured the shear dependence of all three radii of gyration of PS coils in DOP via light scattering [128] and of polymer melts via neutron scattering [141]. Both groups found that the coils elongate in the plane defined by the flow and shear directions, in qualitative agreement with the theory.

5.5 Rheo–NMR

In chapter 2 we showed that NMR spectroscopy is a technique to measure interactions on a molecular level. For example, the dipolar and quadrupolar interactions are both dependent on the orientation of the molecule in the magnetic field, while the relaxation times T_1 and T_2 reveal information about the dynamics of the molecule under investigation. NMR is therefore an ideal technique to monitor changes on a molecular level due to macroscopic shear. Such a combination of rheological experiments with NMR was first demonstrated by Nakatani *et al.* and termed rheo–NMR [140]. These authors designed a cone and plate rheometer to operate inside a standard NMR probe. This apparatus was used to monitor the proton linewidth of polymer melts under shear. An increase in the linewidth was found with increasing shear which has been attributed to a redistribution of the initially isotropic dipolar coupling.

Grabowski and Schmidt describe a cone and plate viscometer which attaches to a standard NMR probe. With this setup it is possible to monitor the dependence of viscosity and order parameter defined in equation 2.57 on the shear rate simultaneously [142].

All these methods make some assumptions about the velocity profile in the rheometer. With dynamic NMR imaging it is possible to measure the flow profile directly. This approach has been used by Callaghan *et al.* in different experiments. Velocity profiles of non-Newtonian fluids have been monitored both in capillary flow [143] and in the Couette geometry [55]. In principle, it is possible to measure the flow field and NMR specific parameters at different flow rates. From the experimental flow profiles the local shear rate can be obtained and therefore the shear dependence of NMR parameters. No assumptions about the flow field need to be made.

Hopkins *et al.* reported on the NMR measurement of flow profiles in a Couette cell using oscillating magnetic field gradients [144]. This method, however, assumes cylindrical symmetry of the sample which is not the case if it is not centred accurately.

5.6 Rheometers

The shear stress vs. shear rate relationship is measured in a rheometer. One somehow has to measure the torque required to shear the fluid at a certain speed. Figure 5.13 shows two common rheometers. The plate in figure 5.13 (a) or the outer cylinder in figure 5.13 (b) is spun, and the torque exerted by the liquid on the cone (a) or inner cylinder (b) is monitored. If this is performed for different rotation frequencies, a graph like in figure 5.10 can be obtained.

In the Couette geometry it is possible to obtain an analytical expression for the velocity profile of a power law fluid across the gap [55]. If the inner cylinder has radius r_i and spins with the angular velocity ω_0, the angular fluid velocity at radius r is given by

$$v(r) = \omega_0 r \frac{1 - (\frac{r}{r_o})^{-2/n}}{1 - (\frac{r_i}{r_o})^{-2/n}}. \tag{5.41}$$

r_o is the radius of the outer cylinder.

In chapter 7 we will use a reduced spatial coordinate r_s which we define as:

$$r_s = r \frac{1 - (\frac{r}{r_o})^{-2/n}}{1 - (\frac{r_i}{r_o})^{-2/n}}. \tag{5.42}$$

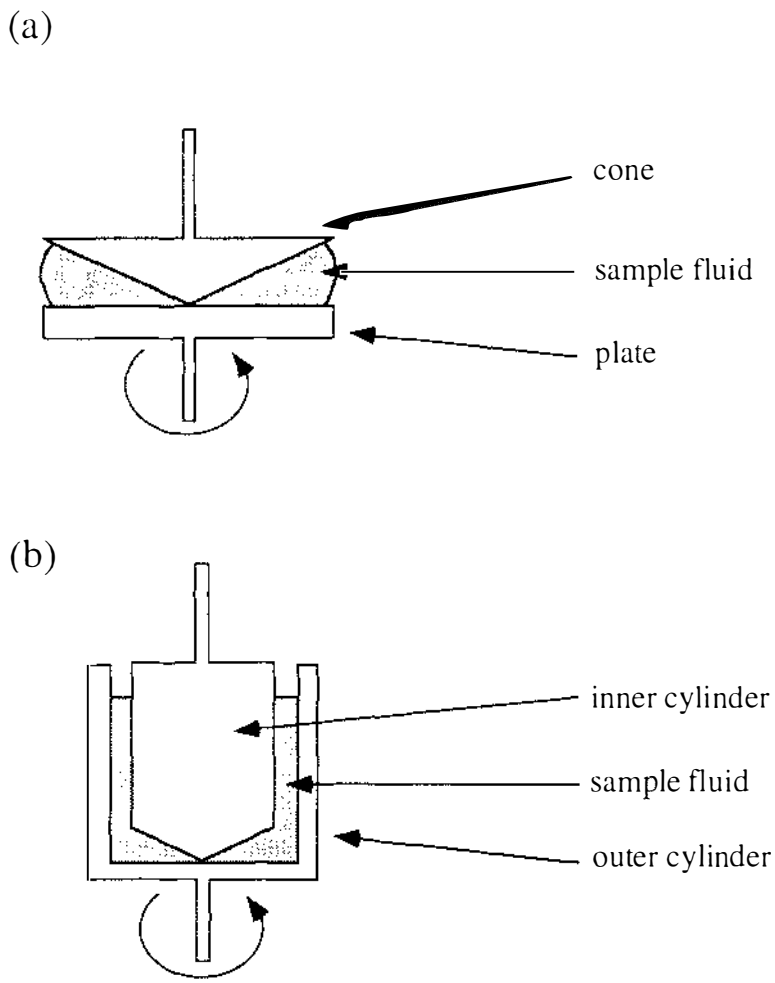

Figure 5.13: Two of the most widely used rheometers are (a) the cone and plate rheometer and (b) the Couette rheometer.

The shear rate in a system with cylindrical symmetry is given by [145]

$$\dot{\gamma} = r\frac{\partial}{\partial r}\left(\frac{v(r)}{r}\right). \tag{5.43}$$

With the velocity profile of equation 5.41 this gives

$$\dot{\gamma} = \frac{2\omega_0}{n}\frac{(\frac{r}{r_o})^{-2/n}}{1-(\frac{r_i}{r_o})^{-2/n}}. \tag{5.44}$$

These equations will be used in chapter 7. The velocity profile $v(r)$ will be measured there, and n will be obtained by a least squares fit of equation 5.41.

From equation 5.44 follows that a graph of $\log\dot{\gamma}$ vs. $\log r$ is a straight line with slope $-2/n$ for a power law fluid. This alternative method of measuring n will be used in chapter 9.

Chapter 6

Diffusion Measurements on Polymer Solutions

In this chapter we report on PGSE measurements of the self–diffusion coefficient of PS in CYH. The temperature dependence of D_s has been measured close to the de–mixing transition for a wide range of different molecular weights. It has been found that D_s decreases by at least one order of magnitude at the de–mixing temperature. We will show that this effect can be modelled by a glass transition.

6.1 Polystyrene in Cyclohexane

Cyclohexane (CYH) is, at room temperature, a clear, low viscosity fluid with a high refractive index $\tilde{n}$. Its chemical composition is C_6H_{12}, and the structure of the molecule is given in figure 6.1. Some physico–chemical constants of CYH are given in table 6.1.

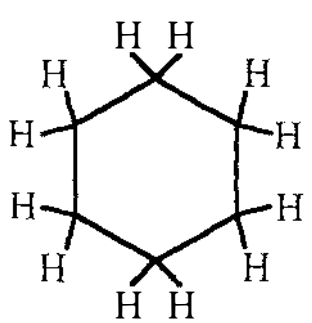

Figure 6.1: The Cyclohexane Molecule.

CYH is a poor solvent for PS at room temperature. The theta temperature for PS/CYH solutions is 34.5° C [83]. Above the theta temperature, the solutions

Parameter	Value
ρ at 20° C	0.7791 g cm^{-3}
$\tilde{n}$ at 34.5° C	1.424
η at 34.5° C	$7.68 \cdot 10^{-4}$ N s m^{-2}
melting point	6.5° C
boiling point	81° C

Table 6.1: Some physico–chemical parameters of cyclohexane.

of PS and CYH are clear liquids. At the de–mixing temperature, which depends on polymer concentration and molecular weight according to equations 5.19 and 5.20, the solution turns cloudy. If the temperature is lowered further, the solution phase separates into a polymer–rich phase at the bottom and a solvent–rich phase at the top. For high molecular weight polymers ($M_w > 10^6$ g mol^{-1}) it was found that these two phases could not be mixed satisfactorily after phase separation occurred. All experiments on the PS/CYH system were therefore performed on fresh samples which had not yet undergone the phase transition.

6.2 Experimental Section

6.2.1 Sample Preparation

The difficulty of obtaining a homogeneous solution of PS in CYH is well known in the literature [92, 146, 147]. All samples used in this chapter were prepared in the following way. A small amount of PS (typically 1 mg) was weighed into a 2 mm o.d. NMR tube. The right amount of CYH was then filled into the tube to make a solution with the required mass concentration. The tube was subsequently sealed and stored at 60° C for at least 6 weeks with occasionally centrifuging the sample back and forth. Special care was taken that the sample temperature never went below 40° C.

In order to avoid convectional flow inside the tube during the experiments at elevated temperatures, it was necessary to centre each sample tube inside a 4 mm o.d. NMR tube filled with tap water. With such a setup it was found that diffraction–like patterns in the Stejskal–Tanner plots of the PGSE experiments, which are discussed in detail in chapter 8, disappeared completely.

6.2.2 Measurement of the Self–Diffusion Coefficient

The temperature dependence of D_s was measured for the PS samples from table 5.1 with a mass concentration of 5 % in CYH. In a second set of experiments, the temperature dependence of D_s was measured for the PS sample with $M_w = 1.75 \cdot 10^6$ g mol^{-1} at different concentrations.

The experiments were performed using the high gradient probe described in section 2.5.3. Due to artifacts in the echo signal for high gradient currents (which could be due to sample vibration or eddy currents), the PGSE pulse sequence from section 2.4.4 had to be modified slightly. Instead of using rectangular shaped gradient pulses, ramped gradient pulses were applied. Each ramp step had a duration of 50 μs and a current amplitude of up to 1 A. The pulse program *pgseramp* is given in appendix B. Although it is possible to obtain an equation for the echo attenuation using ramped gradient pulses [148], it was found that such corrections were not necessary in our case where the ramp time is short compared to the duration of the gradient pulse.

In a multi–component system it is, in principle, possible to measure the self–diffusion coefficient of each component in one single PGSE experiment by simply measuring the echo attenuation of each peak in the NMR spectrum. In our case, however, the solvent signal is much larger in amplitude than the signal coming from the polymer and will dominate the spectrum. Because the solvent and surrounding water diffuse much faster than the polymer, it is possible to attenuate the solvent and water signal completely by a pair of PGSE pulses. The only signal remaining is from the polymer. By now successively increasing the duration of the PGSE pulses one can measure the self–diffusion of the polymer without any solvent interferences.

Due to the large range of molecular weights investigated ($2 \cdot 10^5$ g mol^{-1} – $2 \cdot 10^7$ g mol^{-1}), D_s is expected to vary by 4 orders of magnitude according to equation 5.25. The short T_2 value of PS limits the diffusion time Δ to a maximum value of 40 ms. Therefore the experimental parameters had to be adjusted individually for each sample. This was done as follows. The gradient pulse duration δ_{min} for the first q slice was chosen to be between 0.5 and 3 ms, depending on the sample. The gradient amplitude g was then adjusted such that the NMR signal of the water and the solvent were attenuated completely. The only signal left was the polymer signal. The increment of the gradient pulse duration δ_{inc} between each q slice was then chosen such that the attenuation of the polymer signal in the final q slice was around 0.4 at a temperature of 42° C. The echo time Δ was between 20 ms and 40 ms. With this procedure, the gradient duration was incremented in 16 steps with a step size δ_{inc} between 0.25 ms and 1 ms. The gradient amplitude was left

the same for all experiments with one sample and ranged between 0.75 T m^{-1} and 5.0 T m^{-1}. The experimental parameters for each sample are given in tables 6.2 and 6.3.

The question arises whether a delay time of $\Delta = 40$ ms is sufficiently long to measure Brownian diffusion for the high molar masses. We will see later that this is not the case. The tube disengagement time τ_d increases as M_w^3 and becomes significantly longer than 40 ms for $M_w > 4 \cdot 10^6$ g mol^{-1}. By using a stimulated echo pulse sequence the maximum delay time Δ which can be used is limited by T_1 instead of T_2. In practice this means that Δ can be made up to around 500 ms long. However, because of the $\tau_d \propto M_w^3$ relationship, the point where $\Delta \approx \tau_d$ could only be extended to $M_w \approx 9 \cdot 10^6$ g mol^{-1}. Therefore, even with a stimulated echo pulse sequence we cannot measure Brownian self-diffusion for the highest molar masses.

M_w [g mol^{-1}]	δ_{min} [ms]	δ_{inc} [ms]	Δ [ms]	g [T m^{-1}]
200 000	3.0	0.5	20	0.75
330 000	3.0	0.25	20	1.2
500 000	2.0	0.5	20	2.4
770 000	2.0	0.75	20	2.4
1 030 000	2.0	1.0	20	2.4
1 450 000	2.0	1.0	20	3.0
1 750 000	2.0	1.0	20	3.0
3 040 000	2.0	1.0	25	4.5
4 000 000	2.0	1.0	25	4.5
6 850 000	0.5	1.0	30	5.0
9 350 000	0.5	1.0	40	5.0
15 000 000	1.0	1.0	40	5.0
20 000 000	1.0	1.0	40	5.0

Table 6.2: The experimental parameters for the PGSE experiments on 5% PS/CYH solutions with different molar masses.

For each sample D_s was measured starting at a temperature of 47° C (320 K) and lowering the temperature in steps of one degree until reaching the de-mixing temperature. Before each PGSE experiment the sample was left at a constant temperature for 5 minutes in order to equilibrate. All this was done automatically using the AU program *pgsesleep* which is given in appendix C.

After acquisition the serial data file was transferred to a Macintosh computer as described in section 2.5.4 for further analysis.

Φ [%]	δ_{min} [ms]	δ_{inc} [ms]	Δ [ms]	g [T m^{-1}]
1	2.0	0.5	20	1.5
2	1.0	1.0	20	1.5
3	1.0	1.0	20	2.25
5	2.0	1.0	20	3.0
7	1.0	1.0	20	3.0
10	1.0	1.0	20	4.5

Table 6.3: The experimental parameters for the PGSE experiments on PS/CYH solutions with different concentrations.

6.3 Results

6.3.1 The Temperature Dependence of D_s at Different Molar Masses

Figure 6.2 shows a typical set of Stejskal–Tanner plots for one sample. As mentioned before, the same experimental parameters were used for all PGSE experiments on one sample. The temperature was decreased from 47° C to the de–mixing temperature in steps of 1 degree. $D_s(T)$ was obtained by the slope of the regression line through the points of each individual Stejskal–Tanner plot. In figure 6.3 we show $D_s(T)$ for PS/CYH solutions with a mass concentration of 5% using PS with different molar masses. For all molar masses, $D_s(T)$ decreases monotonically with decreasing temperature. At a particular temperature which depends on the molar mass M_w, $D_s(T)$ drops sharply. We assign this temperature as the de–mixing temperature T_p. Figure 6.4 shows a graph of T_p vs. $M_w^{-1/2}$ along with Perzynski's curves for T_c vs. $M_w^{-1/2}$ and Φ_c vs. $M_w^{-1/2}$ from equations 5.19 and 5.20. We expect T_p to be equal to T_c only at the critical concentration Φ_c. From figure 5.5 it is obvious that $T_p < T_c$ at all other concentrations. This is in agreement with our measured values for T_p displayed in figure 6.4.

Equation 5.25 states that $D_s \propto M_w^{-2}$. Figure 6.5 shows a graph of $\log D_s$ vs. $\log M_w$ at different temperatures. For comparison, a line of slope -2 is also shown. In the range $5.5 \leq \log M_w \leq 6.5$ the $D_s \propto M_w^{-2}$ law can be confirmed. The deviation for $\log M_w < 5.5$ is probably caused by the lack of entanglements. Figure 5.7 shows that for these molar masses the concentration of 5% is below the entanglement concentration c^*.

We will show later that for $\log M_w > 6.4$ the tube disengagement time τ_d is of the same order as or larger than the echo time $\Delta = 40$ ms over which D_s has been measured for these molar masses. This means that we did not measure

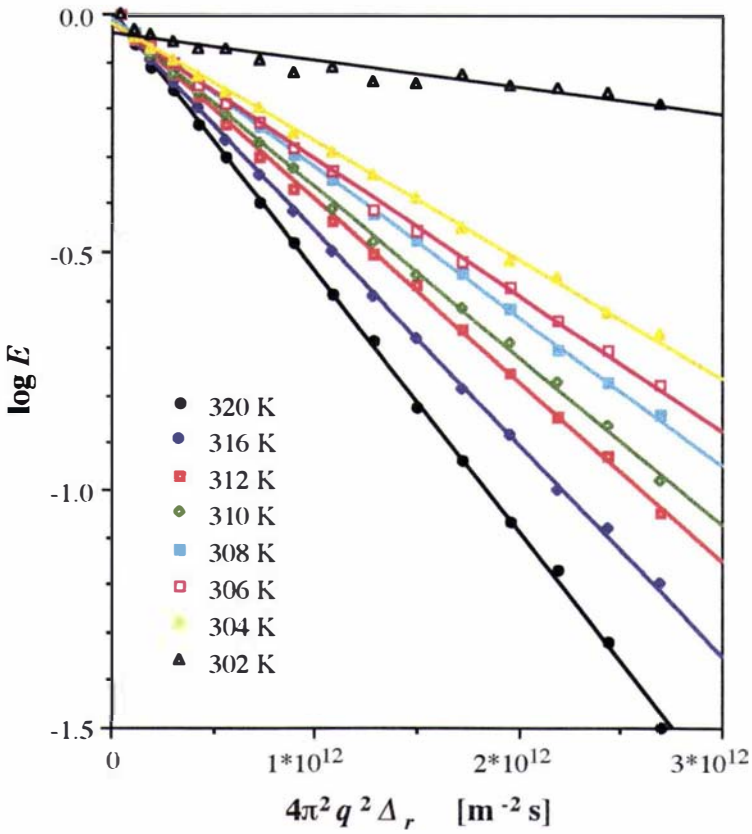

Figure 6.2: A series of Stejskal–Tanner plots of PGSE experiments at different temperatures of a 5% PS/CYH solution with $M_w = 1.75 \cdot 10^6$ g mol^{-1}. For each data set the regression line is shown. The self–diffusion coefficient $D_s(T)$ is obtained by the slope of the regression line.

self–diffusion for $\log M_w > 6.5$, but rather internal modes of the polymer reptation. Therefore it is not surprising that D_s deviates from the $D_s \propto M_w^{-2}$ law for $\log M_w > 6.5$.

The temperature dependence of D_s will be discussed in section 6.4. In the next section we investigate the concentration dependence of D_s.

6.3.2 The Temperature Dependence of D_s at Different Concentrations

The values for $D_s(T)$ were obtained in the same way as in the previous section. Figure 6.6 shows a graph of D_s vs. T for PS/CYH solutions with different mass concentrations Φ and a molar mass of $1.75 \cdot 10^6$ g mol^{-1}. As seen in the graph shown in figure 6.3, $D_s(T)$ decreases monotonically with decreasing temperature. Again, $D_s(T)$ drops sharply at the de–mixing temperature T_p. It can also be seen from figure 6.6 that T_p shows only little variation with the concentration.

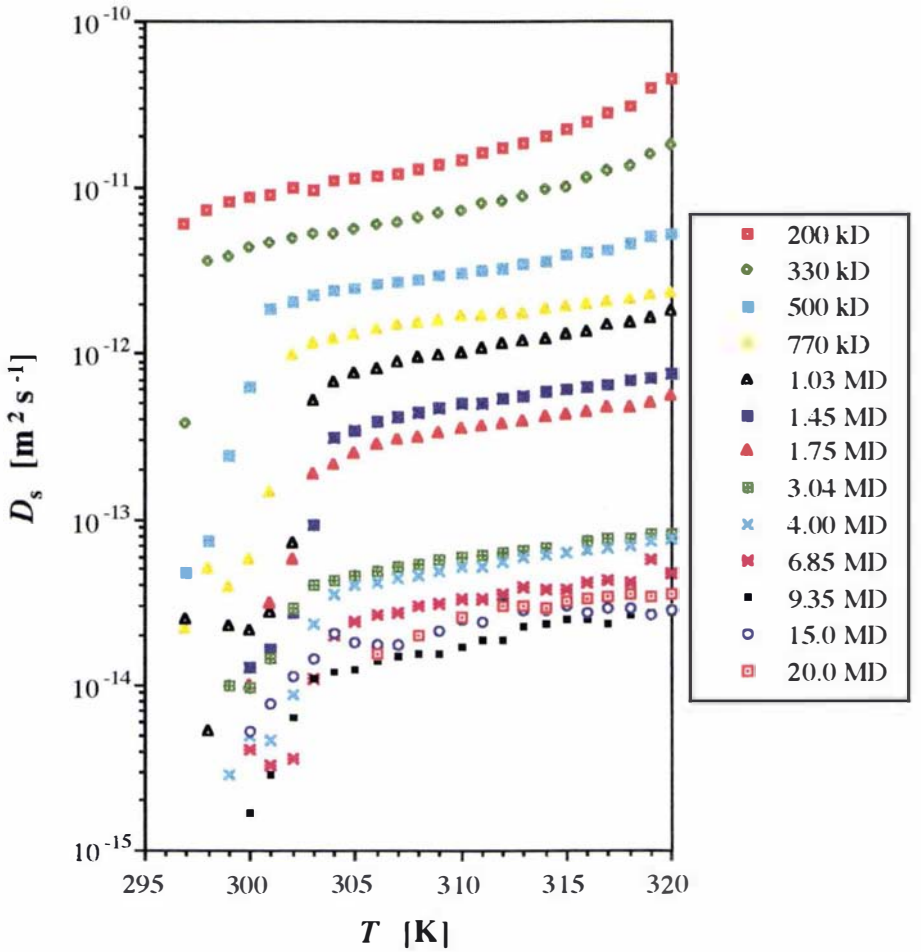

Figure 6.3: D_s is shown as a function of temperature for different molar masses which are given in units of g mol^{-1}. The concentration is fixed at 5%.

This is in agreement with previous measurements of cloud–point curves by Shultz and Flory [85], which show only small variations over a wide concentration range around the critical concentration (figure 5.6 (a)).

It should be noted that the experiments in this section were *not* reproducible, even with fresh samples. For samples mixed at a later stage, it was found that the values of D_s were generally higher than the ones reported here. The Stejskal–Tanner plots of such samples showed the same single exponential behaviour as in figure 6.2. This indicates that polymer degradation or insufficient mixing of the solution is not the cause for such behaviour. However, the *temperature dependence* of D_s was still similar to previous experiments. Therefore we can only discuss the concentration dependence of D_s qualitatively. In section 6.4 we will try to give an explanation for this non–reproducibility.

Figure 6.7 shows a graph of $\log D_s$ vs. $\log \Phi$ at different temperatures. For

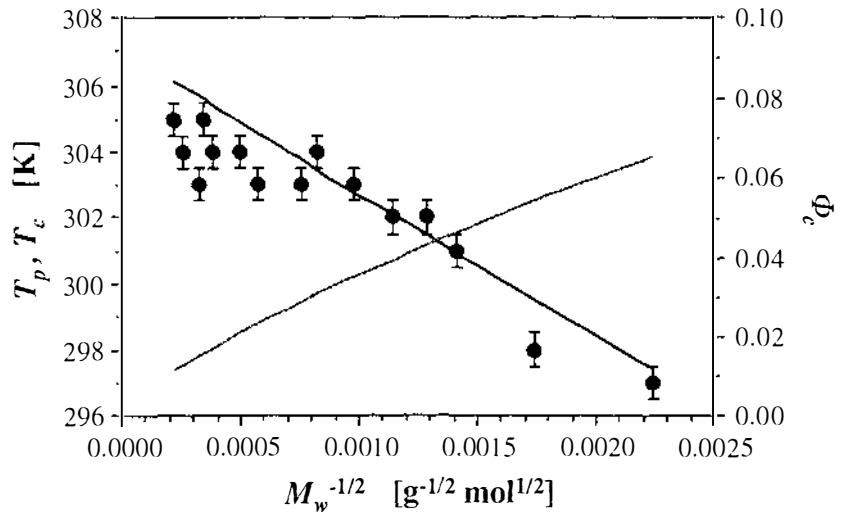

Figure 6.4: The de–mixing temperature T_p (dots), the critical temperature T_c (black line) and the critical concentration Φ_c (grey line) are plotted vs. $M_w^{-1/2}$. Note that $T_p = T_c$ when $\Phi_c = 5\%$ and $T_p < T_c$ in all other cases.

comparison with equations 5.26 and 5.27 we also show two lines with slopes -1.75 and -3.0 in the same graph. In the range $1\% < \Phi < 3\%$, D_s scales approximately as $D_s \propto \Phi^{-1.75}$. For $\Phi > 3\%$ the scaling law changes and is close to $D_s \propto \Phi^{-3.0}$. Figure 6.7 shows that the concentration where this changeover occurs does not depend on the temperature. As stated in section 5.2.6, such a crossover in scaling of $D_s(\Phi)$ has been observed earlier. However, the amount of data is too small to make a quantitative decision of whether the transition obeys the scaling of the Doi–Edwards theory of equations 5.26 and 5.27 or Phillies' stretched exponential law of equation 5.28.

The entanglement concentration can be worked out using equation 5.23. For the sample we used, $M_w = 1.75 \cdot 10^6$ g mol^{-1} and therefore $c^* = 3.9\%$. This concentration is close to the concentration where the crossover in the scaling of $D_s(\Phi)$ occurs. This crossover may therefore be due to a lack of entanglements.

The temperature dependence of D_s will be discussed in the next section.

6.4 Discussion

6.4.1 Reptation Times

With equation 5.24 we can work out the values for the reptation times τ_d. The temperature dependence of R_g for PS/CYH solutions with different molar masses

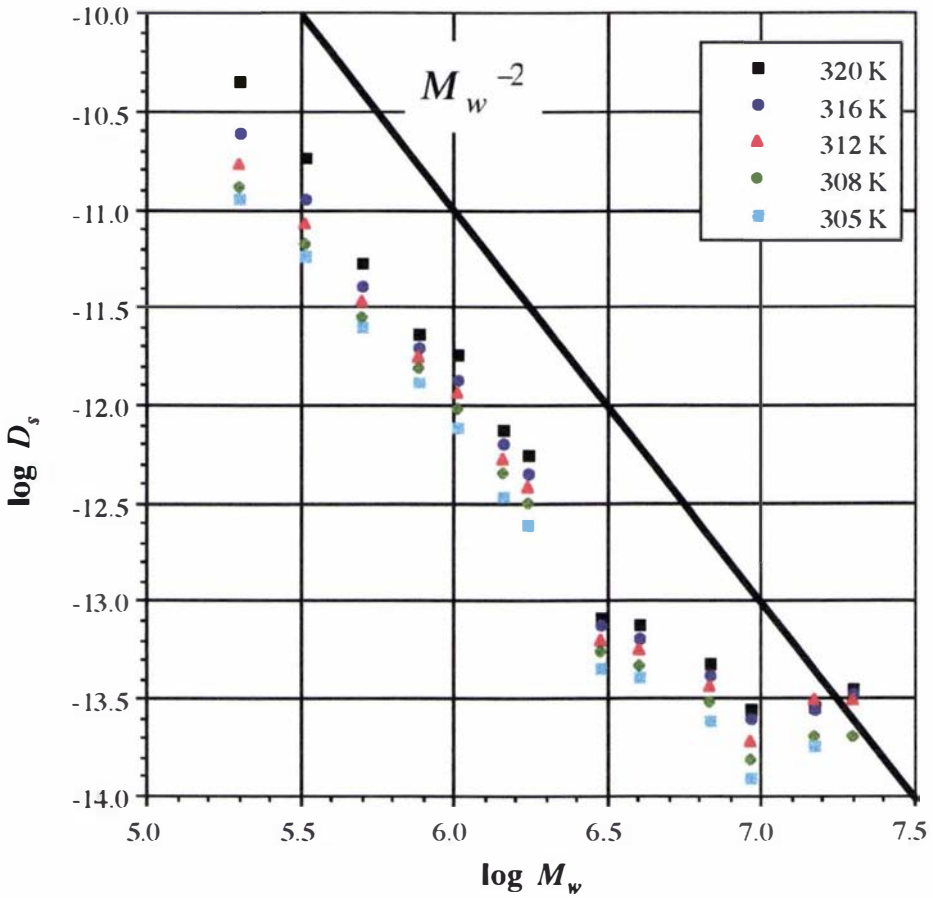

Figure 6.5: $\log D_s$ is shown as a function $\log M_w$ at different temperatures. For comparison with equation 5.25 a line with slope -2 is also shown.

has been analysed by Arai *et al.* [81]. They found that R_g varies by approximately 10% in the range $30°C \leq T \leq 45°C$. This small change will be neglected in the following calculations. Using Arai's values for R_g at $T = \Theta$, $R_g(M_w)$ can be calculated using relationship 5.4. Because we measured $D_s(T)$ close to the theta temperature, we set $\nu = 0.5$. With this method, we obtained values of $\tau_J(T)$ for different molar masses. Figure 6.8 shows a graph of τ_J vs. M_w at different temperatures. From the graph it is obvious that $\tau_J \propto M_w^3$. As mentioned before, our experimental data break away from this scaling rule for large values of M_w. This is due to the fact that τ_J is of the same order or larger than the echo time Δ used in the PGSE experiment. In chapter 7 we will introduce a different method to estimate τ_J for large values of M_w and compare both methods.

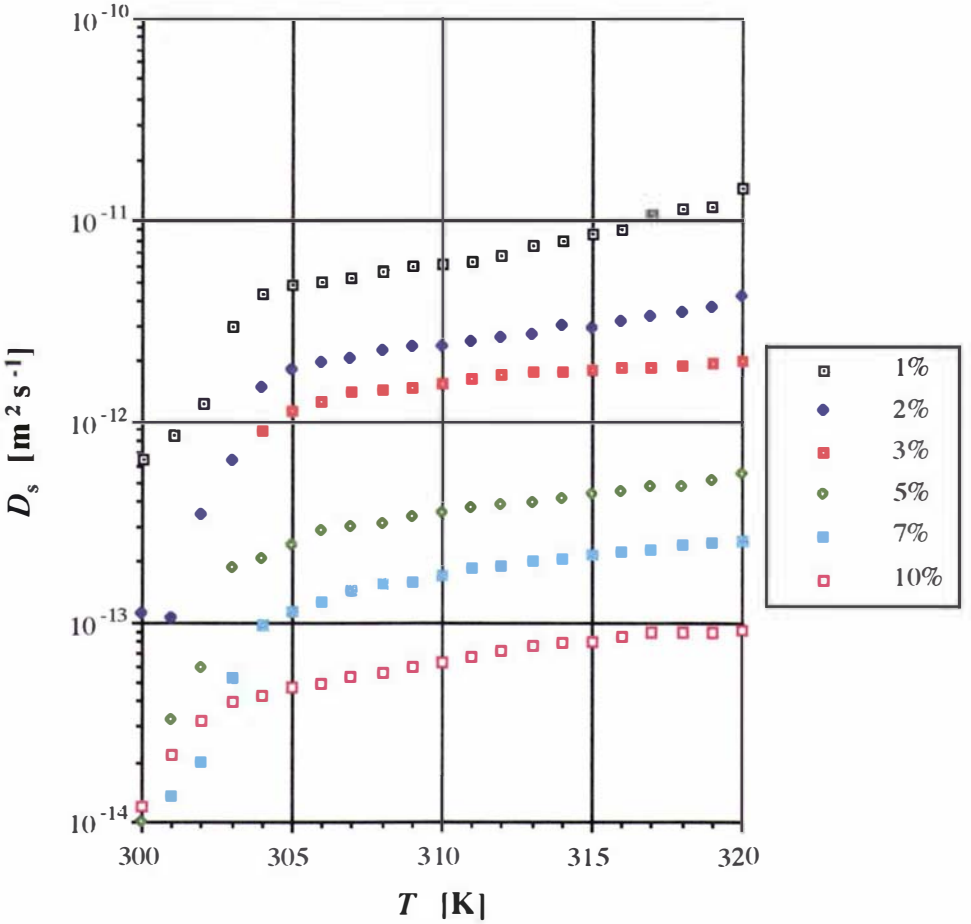

Figure 6.6: D_s for PS in CYH with $M_w = 1.75 \cdot 10^6$ g mol^{-1} is shown as a function of temperature at different concentrations which are given in units of mass percentages.

6.4.2 Concentration Fluctuations

Now we will discuss the temperature dependence of D_s which is shown in figures 6.3 and 6.6. For very dilute solutions, the temperature dependence of D_s is given by the Einstein equation [59]

$$D_s(T) = \frac{k_B T}{6\pi\eta_s(T)R_h}, \tag{6.1}$$

where k_B, $\eta_s(T)$ and R_h are Boltzmann's constant, the viscosity of the solvent and the hydrodynamic radius (equation 5.7), respectively. This equation does not account for entanglements and cannot explain the temperature dependence of D_s shown in figures 6.3 and 6.6. Because both graphs show the same temperature behaviour, we will confine ourselves in the following to analysing the behaviour in figure 6.3.

We will suggest two different models. The first one goes back to the hydrody-

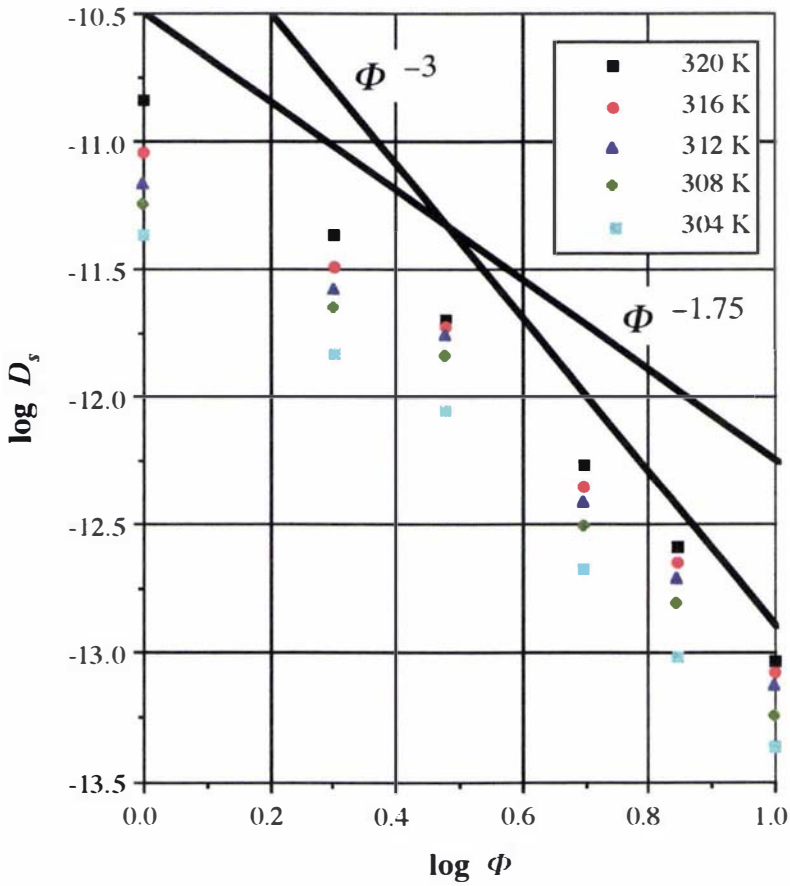

Figure 6.7: $\log D_s$ is shown as a function of $\log \Phi$ at different temperatures. For comparison with equations 5.26 and 5.27 two lines with slope -1.75 and -3.0 are also shown.

namic model and is based on the concentration fluctuations in polymer solutions mentioned in section 5.2.5. The second model suggests that $D_s(T)$ can be described by a glass transition which has been introduced in section 5.3.3. We will see that the latter model gives a much better description.

Spatial fluctuations in the polymer concentration result, according to equation 5.25, in spatial fluctuations of the self–diffusion coefficient. It is known that near the critical point these fluctuations increase both in amplitude Φ_a and correlation length ξ [149]. If concentration fluctuations govern the behaviour of $D_s(T)$ near the de–mixing transition, it should be possible to find values of $\Phi_a(T)$ and $\xi(T)$. We will show here that the effect of concentration fluctuations alone is too small to explain the behaviour of $D_s(T)$ shown in figures 6.3 and 6.6.

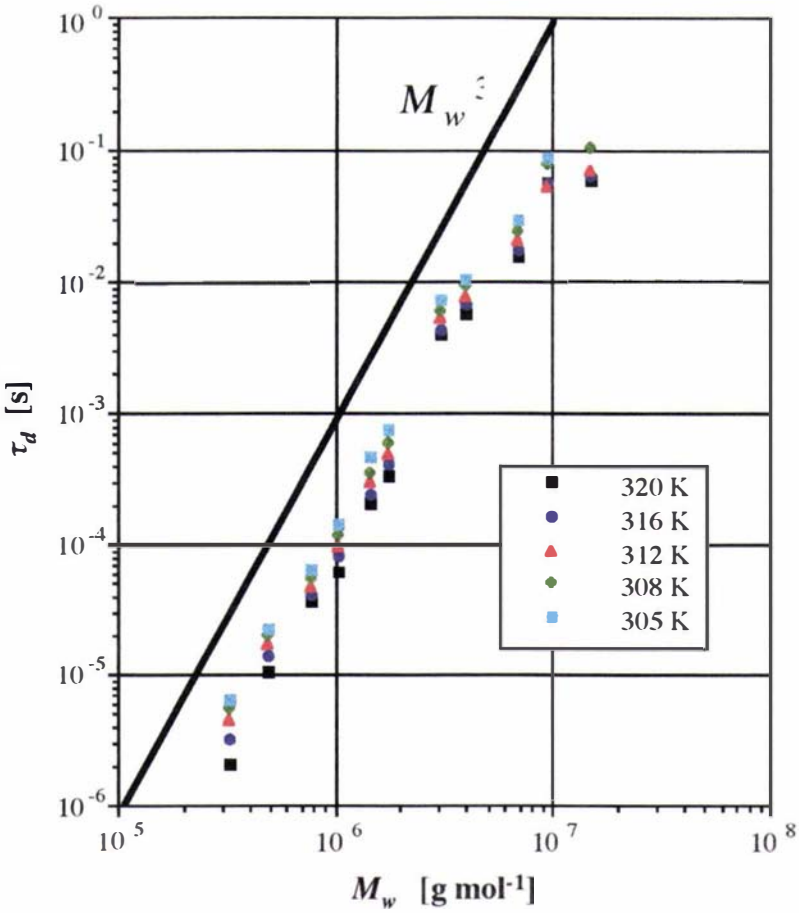

Figure 6.8: τ_d is shown as a function M_w at different temperatures. For comparison with equation 5.24 a line showing the $\tau_d \propto M_w^3$ relationship is also drawn.

6.4.2.1 Some Calculations

For simplicity, we assume that the concentration fluctuations are one–dimensional along the z direction and sinusoidal around a mean value Φ_0 with a wavelength λ, as shown in figure 6.9 (a) and (b). The amplitude of the fluctuations is Φ_a:

$$\Phi(z) = \Phi_0 + \Phi_a \cos\left(\frac{2\pi z}{\lambda}\right). \tag{6.2}$$

The Stejskal–Tanner plots in figure 6.2 show no curvature. This means that, although the self–diffusion coefficient $D_s(z)$ is not constant across the sample, it can be described by an effective constant D_{eff} which is some sort of average diffusion constant. This implies that the mean square displacement $\langle z^2 \rangle = D_{eff}\Delta$ of the polymer molecules over the time Δ must be much larger than the square of the wavelength of the fluctuations:

$$\lambda^2 \ll D_{eff}\Delta. \tag{6.3}$$

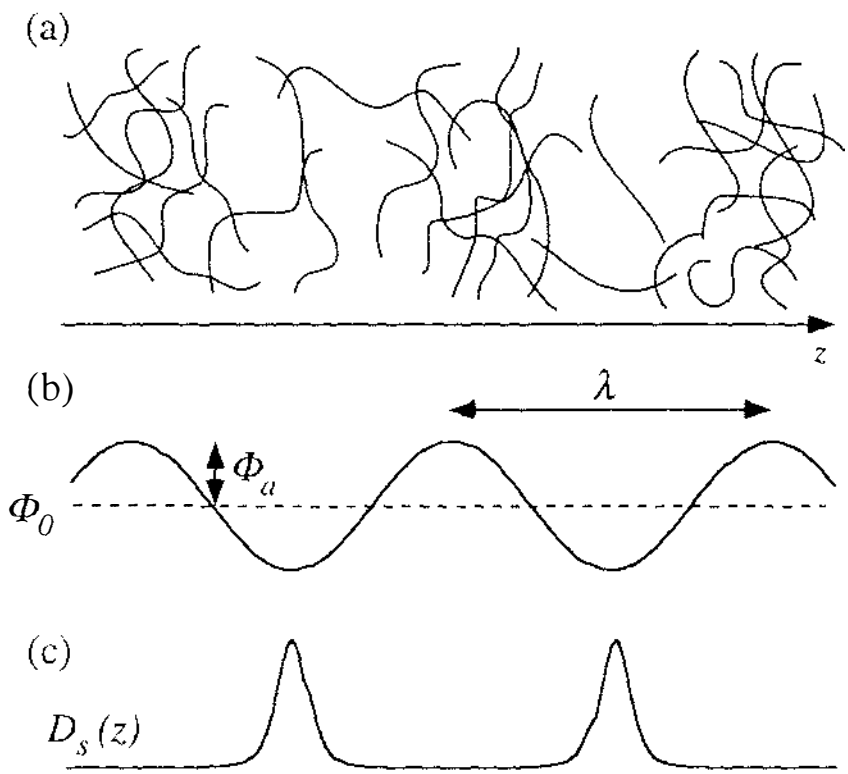

Figure 6.9: (a) The spatial distribution of polymer coils assuming one–dimensional sinusoidal concentration fluctuations. (b) The function $\Phi(z)$. (c) The spatial distribution of $D_s(z)$ assuming sinusoidal concentration fluctuations.

We now assume that D_s scales as in a theta solvent like $D_s \propto \Phi^{-3}$. The function $D_s(z)$ is shown schematically in figure 6.9 (c). The time t taken for a molecule to move over distances much smaller than λ is then proportional to Φ^3. For distances much larger than λ we therefore find

$$t \propto \overline{\Phi^3}, \tag{6.4}$$

where $\overline{\Phi^3}$ is the average of Φ^3:

$$\overline{\Phi^3} = \frac{1}{\lambda}\int_0^{\lambda} \Phi^3(z)\, dz. \tag{6.5}$$

Using equation 6.2, this average can be calculated. Expanding $\Phi^3(z)$ and taking into account that

$$\int_0^{\lambda} \cos\frac{2\pi z}{\lambda}\, dz = \int_0^{\lambda} \cos^3\frac{2\pi z}{\lambda}\, dz = 0 \tag{6.6}$$

and

$$\int_0^{\lambda} \cos^2\frac{2\pi z}{\lambda}\, dz = \frac{\lambda}{2}, \tag{6.7}$$

we obtain

$$\overline{\Phi^3} = \Phi_0(\Phi_0^2 + \frac{3}{2}\Phi_a^2). \tag{6.8}$$

Using relationship 6.4 and $D_{eff} = \langle z^2 \rangle / t$, we get

$$D_{eff} = D_0 \frac{1}{1 + \frac{3}{2}\frac{\Phi_a^2}{\Phi_0^2}}, \tag{6.9}$$

where D_0 is the value of D_{eff} for $\Phi_a = 0$.

It is important to note that D_{eff} does not depend on the wavelength λ of the concentration fluctuations. However, for our calculations it was essential that $\lambda^2 \ll D_{eff}\Delta$. This means that a molecule has to move over many wavelengths in order to be able to describe it by an effective diffusion constant. The actual value of λ is not important under these conditions.

6.4.2.2 Comparison With the Experimental Values

We now compare the results of equation 6.9 with our values of $D_s(T)$ from figure 6.3. We still assume that the wavelength λ of the concentration fluctuations is small compared to the mean square displacement of the polymer molecules over the time Δ. Then the amplitude Φ_a is the only adjustable parameter in equation 6.9.

Because $D_s(T)$ in figure 6.3 decreases with decreasing temperature, we expect, from equation 6.9, Φ_a to increase with decreasing temperature. Because Φ_a must be in the range $0 \leq \Phi_a \leq \Phi_0$, D_{eff} is restricted to values between $\frac{2}{5}D_0 \leq D_{eff} \leq D_0$. However, close to the de–mixing temperature we observe a sharp decrease of $D_s(T)$ by at least a factor of 5. This implies that the effect of concentration fluctuations alone is too weak to explain our experimental results.

One might wonder whether our results would be more realistic if we chose $D_s(\Phi)$ to vary in our calculations as $D_s(\Phi) \propto \Phi^{-1.75}$ instead of $D_s(\Phi) \propto \Phi^{-3.0}$. The result is that the variation of $D_s(\Phi)$ would be smaller, and D_{eff} would be even closer to D_0 for large fluctuations than in equation 6.9.

We therefore conclude that our simple model of concentration fluctuations alone cannot explain the measured $D_s(T)$ values shown in figure 6.3. The fact that experiments are not reproducible indicates that changes occur in the sample when de–mixing takes place, which take a long time to relax. This suggests that the polymer enters some kind of glassy state at the de–mixing transition. This will be discussed in the next section.

6.4.3 Glass Transition

Equation 5.39 yields an analytical expression for $D_s(T)$ with three adjustable parameters. With our experimental values for $D_s(T)$ it is in principle possible to obtain the three parameters $D_\mathfrak{I}$, B and T_g by a least squares fit. However, for numerical stability of the fitting algorithm, it is much better to use the values of $\log D_s(T)$:

$$\log D_s(T) = \log D_\mathfrak{I} - \frac{B}{T - T_g}. \tag{6.10}$$

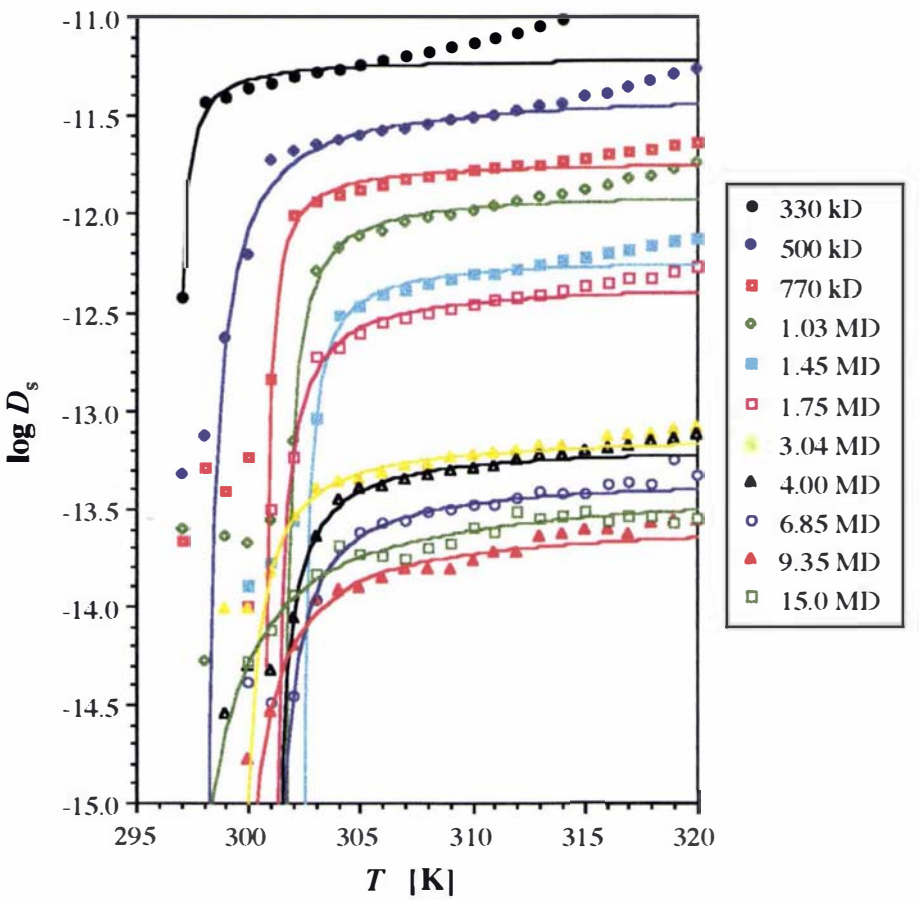

Figure 6.10: The same values of D_s are shown as in figure 6.3. The lines were obtained using a least squares fit of equation 6.10.

Equation 6.10 was fitted to the data points shown in figure 6.3. Because we are interested in the behaviour close to the de-mixing transition, the data were only fitted in the temperature range $T_p \leq T \leq 313$ K. The fitting parameters $\log D_\mathfrak{I}$, B and T_g are given for each value of M_w in table 6.4. The fitting curves along with the experimental values of $\log D_s(T)$ are displayed in figure 6.10. The agreement is satisfactory. Figure 6.11 compares the values of T_g with the values

of T_p which were obtained in section 6.3.1. T_g is significantly below T_p. This discrepancy can be understood, because T_p was chosen as the temperature where $D_s(T)$ suddenly dropped. T_g on the other hand is the temperature where D_s would be zero. Also, the value of T_g is strongly dependent on the slope of $D_s(T)$ in the de–mixing regime. Therefore it is not surprising that the values of T_g scatter more strongly than T_p. In order to obtain more accurate values of T_g, one would need to measure $D_s(T)$ in smaller temperature steps, especially near the de–mixing transition. With the present experimental setup this is not possible, because of the existing temperature gradient in the sample, which will be discussed in detail in chapter 8.

M_w [g mol^{-1}]	$\log D_0$	B [K]	T_g [K]
330 000	-11.2	0.38	296.7
500 000	-11.4	1.55	297.8
770 000	-11.7	0.48	300.6
1 030 000	-11.9	0.72	301.4
1 450 000	-12.2	0.64	302.2
1 750 000	-12.3	0.95	300.9
3 040 000	-13.1	1.15	299.4
4 000 000	-13.2	0.99	300.9
6 850 000	-13.3	1.28	300.9
9 350 000	-13.6	1.94	299.0
15 000 000	-13.4	3.33	296.4

Table 6.4: The parameters obtained from the least squares fit of the data shown in figure 6.3 using equation 6.10.

A question which arises is the following. The glass transition temperature for bulk PS is around 100° C, so why should T_g for PS in solution be very close to the de–mixing temperature? For a dilute solution of PS in CYH, T_g is far below the value of T_g for bulk PS [117]. With increasing concentration, we expect the value of T_g for the solution to approach the value for bulk PS. T_g for a solution with a mass concentration of 5% may still be well below T_c. As stated in the previous section, large concentration fluctuations are present when the temperature T approaches T_c. Some parts of the sample will be very dilute, and others very concentrated. In these parts the local value of T_g is higher than T so that these parts enter the glassy state. Such a glassy state can be visualised as a state where the polymer concentration is very high, and the coils are strongly entangled. The amount and topology of such entanglements strongly depend on the thermal history of the

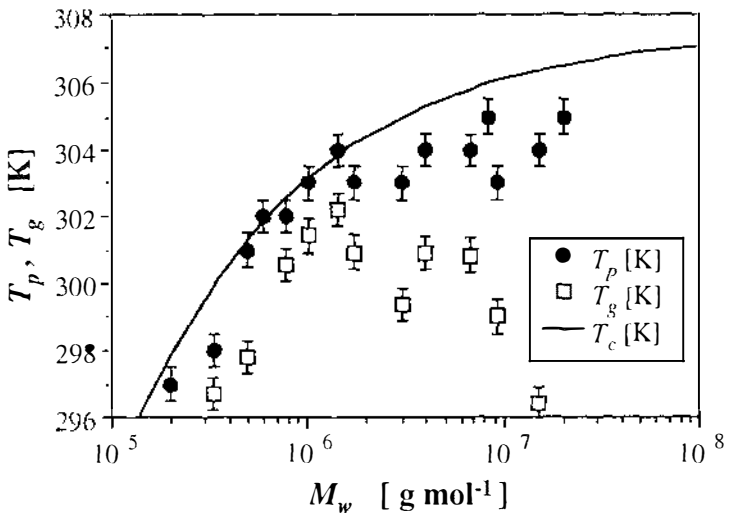

Figure 6.11: The glass transition temperature T_g is plotted vs. M_w. The de–mixing temperature T_p is also shown along with T_c from figure 6.4.

sample. The polymer coils may form knots which are hard to disentangle. A sample which has been prepared at a different time than a previous sample will have a totally different thermal history, and experiments cannot be expected to be reproducible. Furthermore, these entanglements can take a long time to relax which explains the fact that experiments are not reproducible once the sample has undergone the de–mixing transition.

6.5 Conclusions

In this chapter we reported on PGSE experiments to measure the temperature dependence of the self–diffusion coefficient of semi–dilute polymer solutions near the de–mixing transition. Different samples with a wide range of molar masses were used. For all molar masses, we could show that the temperature dependence of D_s can be described by a WLF equation which is characteristic for a glass transition. This glass transition occurs close to the critical temperature and is triggered by large concentration fluctuations which are present in critical polymer solutions.

The $D_s \propto M_w^{-2}$ relationship which is predicted by the reptation model could be confirmed. For very high molar masses ($M_w > 4 \cdot 10^6$ g mol^{-1}), a deviation was found. This could be attributed to the fact that the reptation time is of the same order as or longer than the diffusion time. The concentration dependence

of D_s appears to show a cross-over from $D_s \propto \Phi^{-1.75}$ behaviour to $D_s \propto \Phi^{-3.0}$ behaviour with increasing concentration. However, it could not be decided whether the apparent exponent varies smoothly as in Phillies' model or shows a well-defined cross-over between asymptotic behaviour as in the reptation model.

From the experimental values for D_s the reptation times could be extracted. In chapter 7 we introduce an independent method to obtain these parameters. We will then compare these values with the ones reported in this chapter.

Chapter 7

Flow Measurements on Polymer Solutions

In this chapter we perform rheo–NMR experiments on semi–dilute PS/CYH solutions in order to determine the values of the entanglement formation times τ_η close to the de–mixing transition. We will compare these values with τ_d determined in the previous chapter and those quoted in the literature.

7.1 Instrumentation

7.1.1 The Couette Cell

The Couette cell makes it possible to work with small sample volumes and high shear rates [55]. Accurate temperature control is possible which is essential for the investigation of phase transitions. A diagram of the Couette cell used for the experiments in this chapter is shown in figure 7.1. It consists of two concentric precision glass NMR tubes. The outer tube has an inner diameter of 9.0 mm while the inner tube has an outside diameter of 5.0 mm. This inner tube is centred inside the outer tube by two teflon spacers placed above the annular space occupied by the sample liquid. It is driven by an aluminium shaft connected to an electric motor sitting on top of the superconducting magnet. The rotation speed can be adjusted by using different gear stages and by altering the voltage.

The voltage is controlled by an 8 bit shift register driven by the TTL output on BP1 of the spectrometer console, as described in section 2.5.1. The shift register is described in detail in [150]. Two TTL pulses are needed. The `setf2^3` and `setf2|3` commands provide a TTL pulse on channel H which resets the shift register. A number of `setf2^4` and `setf2|4` commands provides a number of TTL pulses on channel M which step the shift register in order to increment the

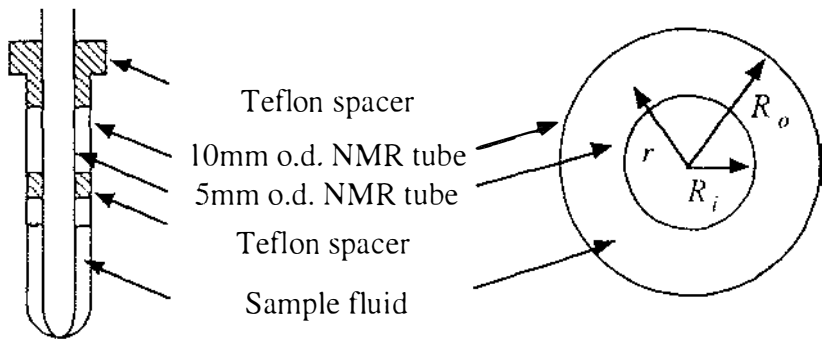

Figure 7.1: The Couette cell used for the experiments in this thesis.

output voltage. The loop counter $L8$ defines the number of pulses and can have values between 0 and 255.

The pulse sequence *motorstep* is given in appendix B and shown graphically in figure 7.2. It starts with a resetting pulse on channel H and then provides $L8$ TTL pulses on channel M. It is called from the AU program *motorstep* given in appendix C. For turning the motor off, the AU program and pulse sequence *motoroff* just provides a resetting pulse. Because the AU programs *motorstep* and *motoroff* execute pulse sequences, it is not possible to change the motor speed during signal acquisition.

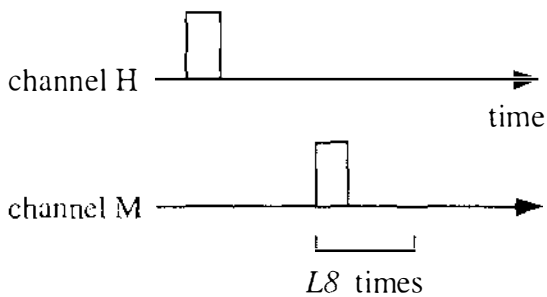

Figure 7.2: The pulse sequence *motorstep*.

In the early stages of our Couette experiments the shift register sometimes was not shielded by a surrounding metal box and was reset by pick-up of sparks from switching electric equipment in the lab. In order to avoid losing a whole set of experiments by such interferences, the pulses for driving the shift register were also implemented in the dynamic spin echo pulse sequence. The motor speed is then set to its correct value before each new scan in q-space. Therefore a maximum of one q-slice is lost. This procedure is not necessary any more, because the shift register could be shielded against electromagnetic interferences by a surrounding metal box.

7.1.2 Data Analysis

Although our Couette cell does not measure the torque (and therefore the viscosity), we can still extract important rheological information from our data. The power law index n can be extracted from the experimental velocity profiles using equation 5.41, where n is the only adjustable parameter and can be fitted using a least squares fit. The computer program *PowerLawFit* was written for this purpose. It reads the experimental v vs. r data and fits n from equation 5.41 by a least squares fit, where r_i, r_o and ω_0 are given parameters. The data are then displayed as v vs. $r(1-(r/r_0)^{-2/n}$. n is independent of r if a straight line results. Otherwise n depends on r and therefore on $\dot{\gamma}$, and the data have to be analysed with a different method.

The local shear rate $\dot{\gamma}(r)$ can be calculated using equation 5.43. The computer program *Derivative* numerically calculates the derivative of a xy data set using a regression line through up to nine neighbouring points. It follows from equation 5.44 that a graph displaying $\log\dot{\gamma}$ vs. $\log r$ has the slope $-2/n$. A change in slope of such a graph therefore indicates a shear rate dependence of n. None of the experiments reported in this chapter showed this effect. Because a numerical derivative of noisy data is not very accurate, n was obtained by a least squares fit which is numerically much more robust.

7.2 Experimental

7.2.1 Sample Preparation

Each sample used for the experiments in this chapter was prepared in a 10 mm o.d. NMR tube which was subsequently used as the outer cylinder of the Couette cell shown in figure 7.1. Approximately 50 mg of PS was weighed into the NMR tube, and the right amount of CYH was added to make a solution with a mass concentration of 5%. PS samples with $10^{-6}M_w = 1.75$, 6.85, 9.35 and 15.0 g mol^{-1} were used. The molecular weight distributions are given in table 5.1. The tube was subsequently closed with a plastic cap and stored in a glass bottle inside a water bath at 60° C for at least 6 weeks. In order to speed up the mixing process, the samples were occasionally stirred. The glass bottles were filled with small amounts of CYH to reduce solvent evaporation from the sample tubes.

After the mixing period, a 5 mm o.d. NMR tube with the teflon spacers was inserted into the sample tube and connected to the Bruker NMR probe. All items in contact with the sample were pre–heated at 60° C to prevent the sample from de mixing.

As in the previous chapter, only fresh samples were used.

Once the sample was removed from the glass bottle, solvent evaporation started, and the experiments had to be performed immediately. At the start of each set of experiments, the level of the fluid layer was marked on the glass tube and compared to the level at the end of the experiments. The data were only analysed if the solvent evaporation during the experiments was negligible.

7.2.2 Flow Measurements

The flow experiments were performed in the superconducting magnet using the standard Bruker probe. Figure 7.3 (a) shows a horizontal slice through the Couette cell. As expected, the sample is distributed homogenously in the gap, and the inner tube is centred correctly. In figure 7.3 (b) we show two profiles of the radial fluid velocity, one for a Newtonian fluid and one for a shear thinning fluid. The characteristic curvature for shear thinning behaviour is obvious.

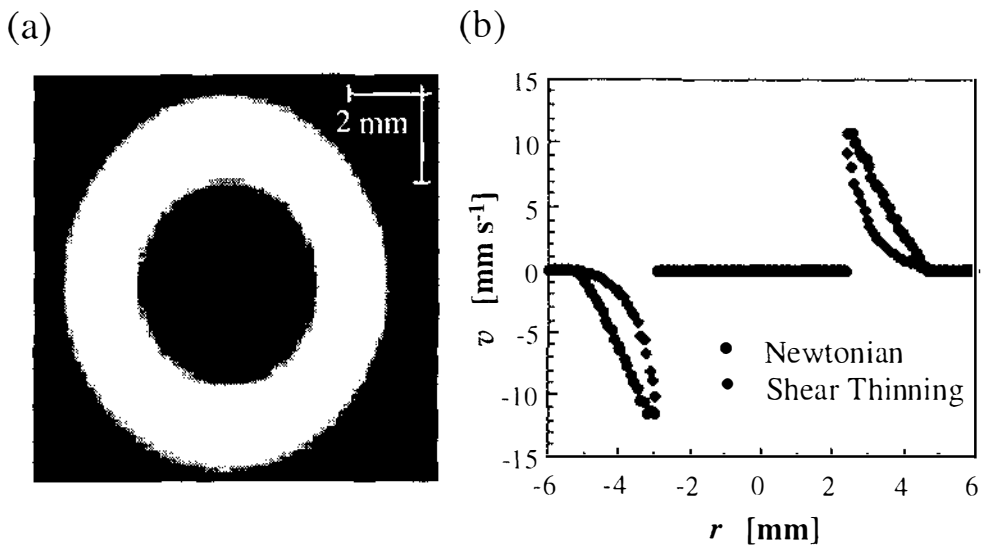

Figure 7.3: (a) A proton spin density image through a horizontal slice of the Couette cell. (b) Flow profiles of a Newtonian and shear thinning liquid inside the Couette cell.

For a quantitative analysis of the flow profiles, it is desirable to have a better spatial resolution. This can be achieved by modifying the dynamic spin echo pulse sequence shown in figure 2.14 slightly. Due to the translational symmetry of the sample along the cylindrical axis, no slice selection is needed when imaging in the horizontal plane and neglecting end effects. This is justified if the height of the sample is large compared to the radius, which is the case with our setup. Both r.f. pulses can now be made slice selective to excite the sample in two orthogonal

planes, as shown in figure 7.4 (a). One slice is shifted off centre to excite a small sector of the sample. A proton density image of such a sector is shown in figure 7.4 (b). The flow imaging pulse sequence is graphically shown in figure 7.5, and the code is given in appendix B.

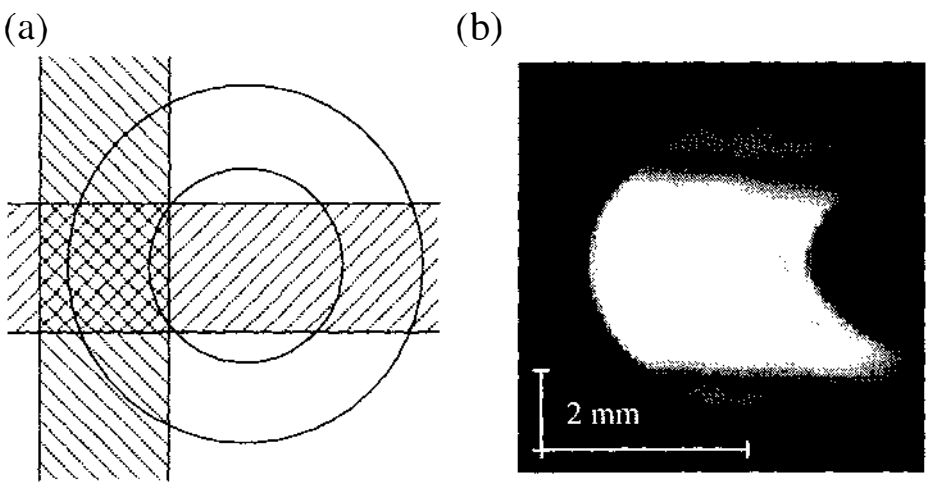

Figure 7.4: (a) By selecting two orthogonal vertical slices one can image a small sector of the Couette cell. (b) A proton density image of such a sector using the pulse sequence shown in figure 7.5. Note the enhanced spatial resolution compared to the image shown in figure 7.3 (a), and that the resolution is set to be greater across the gap and thus leading to the apparent distortion.

A problem which arises when exciting only parts of a moving sample is the following. If the delay time between two scans is shorter than T_1, a combination of fresh spins and partly excited spins in the region of interest (ROI) can create interferences in the NMR signal. Molecules near the stationary cylinder will barely move at all, and molecules near the centre of the gap may move out of the ROI during the delay between two scans. These molecules will be replaced by fresh spins coming from outside the ROI. For molecules close to the rotating tube, the rotation speed is fast enough, so that these molecules can return into the ROI between two scans. These interferences can be avoided by making the delay time between two scans longer than T_1. In our case, this is not very practical, because CYH has a T_1 value of several seconds. Another way to avoid such interferences is to destroy the magnetisation in the whole sample after each scan. This can be achieved by the application of a hard 90 degree excitation pulse followed by a gradient pulse (crusher gradient). This method works well, and all experiments in this chapter were performed using this so–called crusher method.

For each of the four samples, flow profiles were measured at different rotation speeds and different temperatures. The rotation frequency of the inner tube was

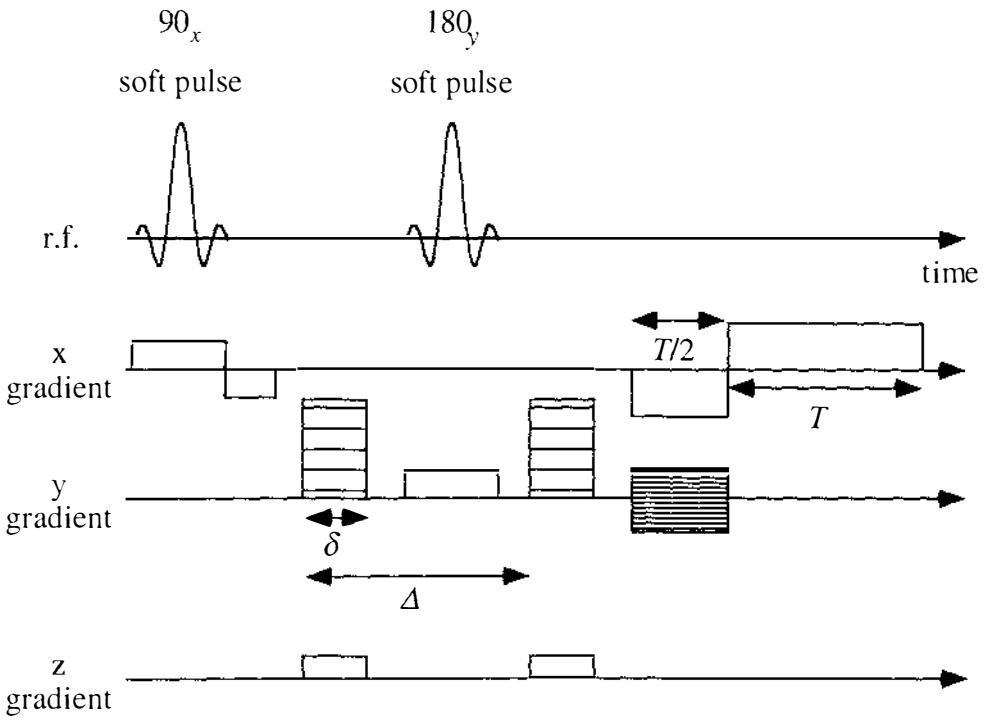

Figure 7.5: The pulse sequence for measuring the velocity profile in a small sector of the Couette cell. It uses two vertical slice selective soft r.f. pulses. There is no slice selection in the horizontal plane. Velocity encoding and phase encoding are in the same direction. The gradient pulses in the z direction generate spoiler gradients to attenuate the FID signal of the 180° pulse.

$0.5\,s^{-1}$, $0.75\,s^{-1}$ and $1.0\,s^{-1}$. Starting at a temperature of 47° C (320 K), the three flow profiles were recorded at each temperature. The temperature was decreased in steps of 2 degrees until reaching 39° C, then in steps of 1 degree until reaching T_p. The onset of the phase separation can be noted from a change in the shape of the velocity propagators.

In each experiment, the echo time Δ and the gradient pulse duration δ were kept constant. The gradient pulse amplitude was incremented in 16 q–steps from zero to g_{max}. The experimental parameters for each rotation speed are given in table 7.1.

The adjustment of motor speed and temperature was done automatically using the AU program *bertsleep* which is given in appendix C. After a change of temperature the sample was allowed to equilibrate for 10 minutes before the start of the flow imaging pulse sequence.

After data acquisition a 2D FT in the two spatial directions was performed on the spectrometer. The resulting files containing the real and imaginary data were

rotation speed [s^{-1}]	Δ [ms]	δ [ms]	g_{max} [T m^{-1}]
0.5	40	2.0	0.25
0.75	40	1.3	0.25
1.0	40	1.0	0.25

Table 7.1: The experimental parameters for the flow imaging experiments at different rotation speeds.

transferred to a Macintosh computer, where the FT in the third dimension and further analysis were performed.

7.3 Results

Figure 7.6 (a) shows a typical set of velocity profiles for one sample at different temperatures. From these profiles it is clear that the sample becomes more shear thinning with decreasing temperature. As described in section 7.1.2, a least squares fit was used to fit the power law exponent n from equation 5.41 to the experimental velocity profiles. The resulting fit curves are also shown in figure 7.6 (a). In order to examine whether n exhibits a spatial dependence, we plot if figure 7.6 (b) $v(r)$ vs. the reduced spatial coordinate r_s defined in equation 5.42 along with the fit curves. The resulting straight lines are a proof that n is constant over the whole sample. Such a uniformity provides independent evidence that shear–induced phase transitions are not apparent.

The values of $n(T)$ obtained with this method are displayed in figure 7.7 for all samples. The sample with $M_w = 1.75 \cdot 10^6$ g mol^{-1} exhibits Newtonian behaviour at all temperatures and rotation speeds. For all other samples, $n(T)$ decreases with decreasing temperature. Also, $n(T)$ decreases with increasing rotation speed of the inner cylinder. This is in qualitative agreement with Graessley's $n(\dot{\gamma}\tau_\eta)$ curve shown in figure 5.12. A quantitative analysis will be given in the next section.

With the method described in section 7.1.2, the local shear rates $\dot{\gamma}(r)$ can be worked out from the experimental velocity profiles. Those are plotted on a double logarithmic scale in figure 7.8 for the velocity profiles shown in figure 7.6. The shear rates are not constant across the sample, but exhibit a power law relationship, as expected from equation 5.44. Because the numerical derivative is very susceptible to noise in the velocity profiles, the $\dot{\gamma}(r)$ curves have large errors in the regions of slow velocities.

Figure 7.6 shows that n does not depend on the spatial variation of the shear rate. However, it depends on changes in the shear rate due to changes in the

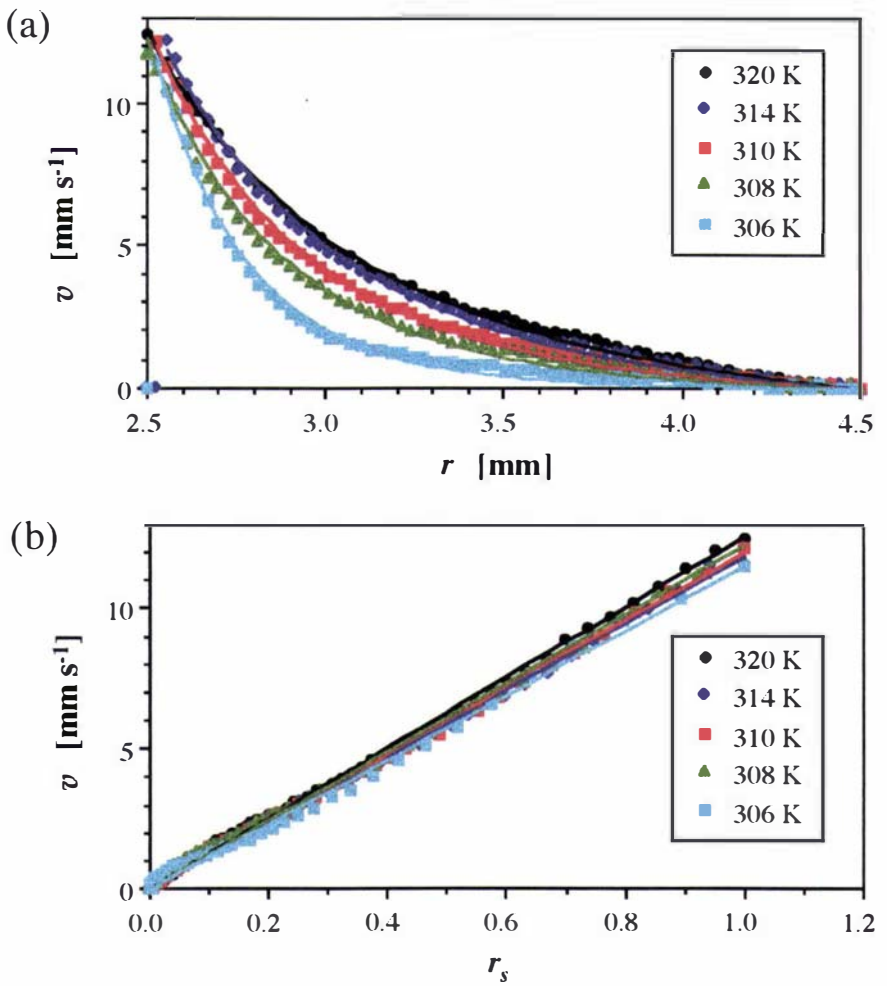

Figure 7.6: (a) Velocity profiles of the sample with $M_w = 15.0 \cdot 10^6$ g mol^{-1} at different temperatures. The fitted curves are shown as lines. (b) The same data sets as shown in (a), but plotted vs. r_s defined in equation 5.42. The slope for each curve is simply ω_0. Note that r_s depends strongly on the value of n. The linear behaviour indicates that n is constant across the sample.

rotation speed. This apparent contradiction suggests that it is the *maximum* shear rate which governs the apparent value of n. This fact will be used in the next section to work out the entanglement formation times of each polymer solution.

7.4 Discussion

7.4.1 Shear–Induced Phase Transitions

For temperatures below $T = 306$ K the velocity propagators fluctuate wildly. We attribute this behaviour to the de–mixing transition and assign T_ρ a value of 305 K $\pm$ 0.5 K. No evidence has been found that T_ρ changes with M_w. This is in

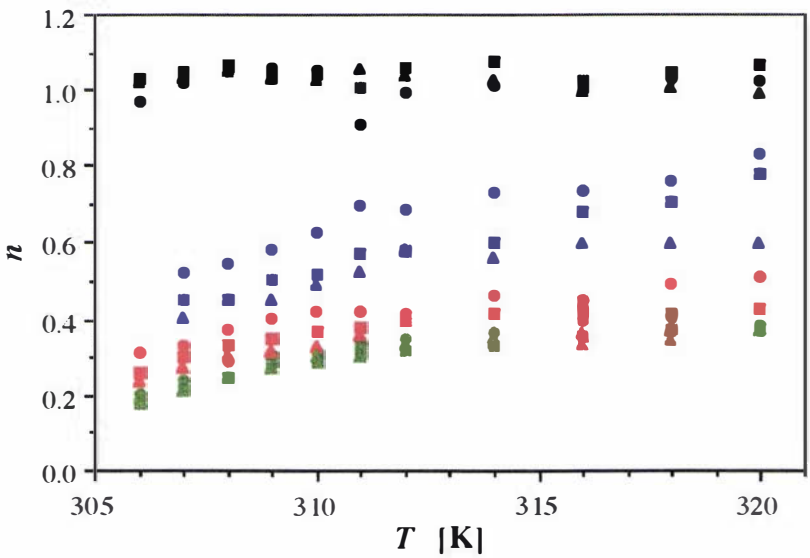

Figure 7.7: The power law exponent n is plotted vs. T for the four samples at different rotation speeds. The black, blue, red and green symbols represent the data for $10^{-6}M_w$ = 1.75, 6.85, 9.35 and 15.0 g mol^{-1}, respectively. The different rotation speeds are represented by circles (0.5 Hz), squares (0.75 Hz) and triangles (1.0 Hz).

qualitative agreement with the values of T_p obtained with the PGSE method and shown in figures 6.4 and 6.11. There, T_p is at a constant value of 304 K $\pm$ 1 K for $M_w > 10^6$ g mol^{-1}. The difference in the values of T_p measured here and in chapter 6 is probably due to the different thermocouples used to control and monitor the temperature.

Figure 7.7 also shows that there is no dependence of T_p on the rotation speed of the inner cylinder. This means that in the range of shear rates achievable with our rheometer (up to 100 s^{-1}), there is no evidence of a shear–induced shift in the phase transition temperature. This is in agreement with other experimental results for PS/CYH solutions reported in section 5.4.

7.4.2 Entanglement Formation Times

In chapter 6 we were able to show that the entanglement concept could describe the behaviour of the polymer self–diffusion coefficient for semi–dilute PS/CYH solutions. Graessley's theory which is described in section 5.3.2 provides a result for the shear rate dependence of the power law exponent for entangled polymer solutions, where the entanglement formation time τ_η is the only parameter. We will use this concept to work out τ_η from the experimental values of n.

Using Graessley's curve of $\log n$ vs. $\log(\dot{\gamma}\tau_\eta)$ shown in figure 5.12, we work out the value of $\dot{\gamma}\tau_\eta$ corresponding to each value of n shown in figure 7.7. The shear

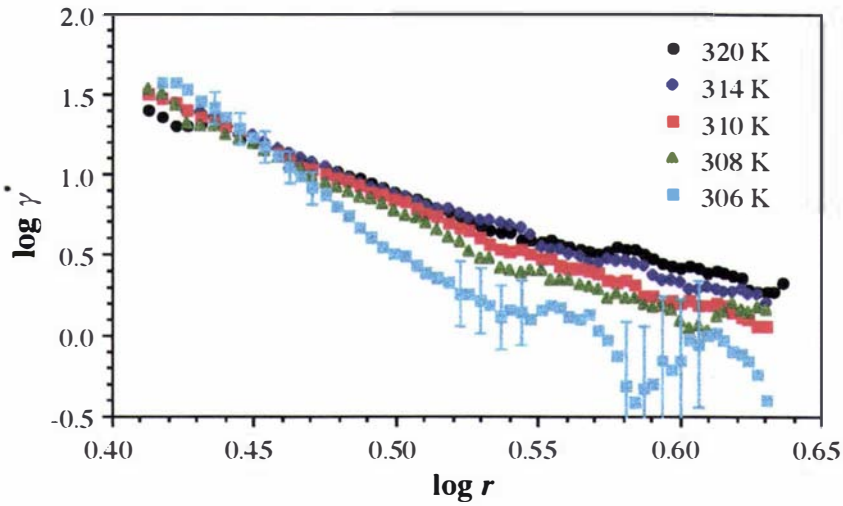

Figure 7.8: The shear rate $\dot{\gamma}$ is plotted vs. r for the data sets shown in figure 7.6. The molar mass is $M_w = 15.0 \cdot 10^6$ g mol^{-1}.

rates $\dot{\gamma}$ can be calculated from the velocity profiles using equation 5.43 and are shown in figure 7.8 for the sample with $M_w = 15.0 \cdot 10^6$ g mol^{-1}. It is obvious that $\dot{\gamma}$ is not constant across the sample, and the question arises which value of $\dot{\gamma}$ to choose. At the end of section 7.3 we suggested that it is the maximum shear rate $\dot{\gamma}_{max}$ which dominates the rheological behaviour of the sample. Therefore $\dot{\gamma}_{max}$ is the natural choice to determine the values of τ_η. We recall that τ_η is expected to be two to three times larger than the tube disengagement time τ_d for the same sample. In order to compare both parameters, they are plotted in the same graph in figure 7.9 at the temperature $T = 308$ K, which is also the theta temperature. Both τ_η and τ_d display roughly the same scaling with increasing M_w. We recall that the values for τ_d for $M_w > 4.0 \cdot 10^6$ g mol^{-1} are below the expected values from the $\tau_d \propto M_w^3$ behaviour, because τ_d is larger or of the same order as the echo time Δ in the PGSE experiments. We also show the results from Adam and Delsanti [115] for the longest viscoelastic relaxation times in the Newtonian regime. There is qualitatively the same scaling, although the absolute values differ.

The sample with $M_w = 1.75 \cdot 10^6$ g mol^{-1} is expected to be Newtonian. With a value of $\tau_d \approx 10^{-4}$ s and a maximum shear rate of $\dot{\gamma}_{max} = 10$ s^{-1}, we estimate $\dot{\gamma}\tau_\eta < 10^{-2}$. From the $\log n$ vs. $\log(\dot{\gamma}\tau_\eta)$ relationship shown in figure 5.12 we then obtain $n = 1$, in agreement with our experimental values of n.

There seems to be a small shear rate dependence of the values of τ_η in figure 7.9. This may be attributed to the uncertainty in the values for $\dot{\gamma}_{max}$ obtained by a numerical derivation of the velocity profiles. As stated above, uncertainties in the velocity profiles are enhanced by the numerical derivation.

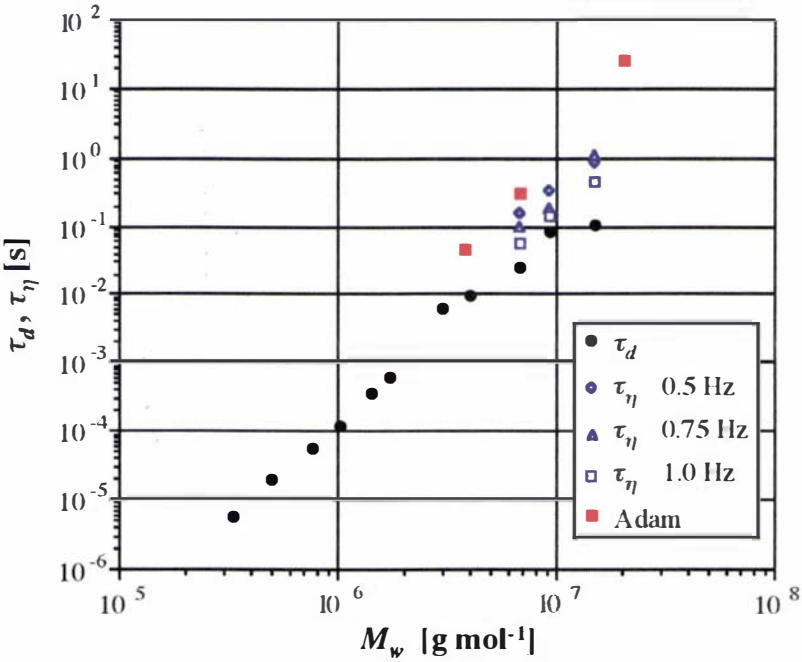

Figure 7.9: The entanglement formation times τ_η are plotted along with the tube disengagement times τ_d from figure 6.8 at the temperature $T = 308$ K. For comparison, the longest viscoelastic relaxation times from [115] are displayed as well.

7.4.3 Glass Transition

In chapter 6 we showed that the temperature dependence of the self–diffusion coefficient near the de–mixing transition can be described by a WLF equation which is typical for a glass transition. Equation 5.40 gives us the temperature dependence of the characteristic mechanical relaxation time. In the case of our rheological experiments, this relaxation time is the entanglement formation time τ_η. Therefore it should be possible to find parameters c_1 and c_2 which model the behaviour of τ_η near the de–mixing transition.

The values of $\tau_\eta(T)$ were obtained for each value of M_w and rotation speed as described above. Figure 7.10 shows these values normalised to the respective value of τ_η at the reference temperature of $T_s = 316$ K. The curve of the best fit of equation 5.40 is also shown. The agreement is acceptable. As stated before, an uncertainty in the values of $\dot{\gamma}_{max}$ may be the cause for the scattering of the data points. However, there is clearly a trend for longer relaxation times when approaching the phase transition.

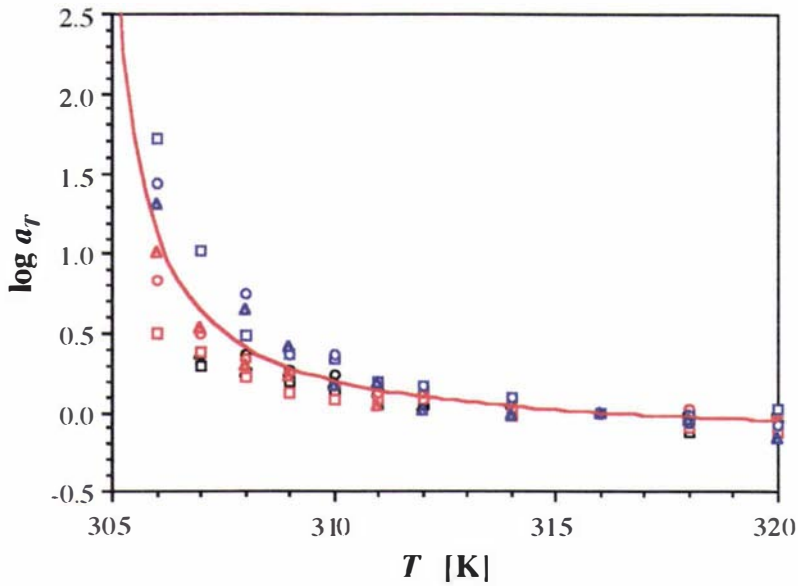

Figure 7.10: The temperature dependence of the normalised relaxation time a_T is shown for different values of M_w and different rotation speeds. The black, blue and red symbols represent the data for $10^{-6}M_w = 6.85, 9.35$ and 15.0 g mol^{-1}, respectively. The different rotation speeds are represented by squares (0.5 Hz), circles (0.75 Hz) and triangles (1.0 Hz). The best fit to all points using equation 5.40 is shown as a line. The parameters are $c_1 = 0.19$ and $c_2 = 11.7$ K.

7.5 Conclusions

In this chapter we performed rheo–NMR experiments on semi–dilute PS/CYH solutions. Although we did not measure the viscosity, we were able to extract the power law index from the shape of the velocity profile. It was found that the shear rate shows a large variation across the sample space. Also, the maximum shear rate which governs the flow profile of the sample depends on the power law index. This shows how important the knowledge of the flow profile inside the rheometer is.

Using Graessley's theory which is based on the reptation model, we worked out temperature dependence of the entanglement formation times. Comparison with the values for the tube disengagement times measured in chapter 6 showed very good agreement. We showed that this temperature dependence could also be modelled by a glass transition. This is also in agreement with our previous findings in chapter 6.

Generally, the tube disengagement times are measured by measuring the self–diffusion coefficient. However, for large values of M_w, D_s gets very small and the experiments become more difficult to perform, as we have shown in chapter 6.

The method described in this chapter provides an alternative. We have shown that this method works particularly well for long τ_η. For short τ_η very high shear rates are required to find non–Newtonian behaviour. Thus we have two complementary methods which can be used to measure the disentanglement times of polymer solutions: For short τ_η and small values of M_w, the measurement of the self–diffusion coefficient using the PGSE method provides better results. With increasing M_w, the PGSE experiments become harder to perform, and the flow imaging method provides better results. It is also important to note that the latter method measures the NMR signal of the solvent and is therefore not limited by the generally short T_2 relaxation time of the polymer molecules.

Chapter 8

Convection in a Capillary

8.1 Introduction

Consider a horizontal layer of an incompressible fluid, which is heated from below, as shown in figure 8.1. The fluid at the bottom will be less dense than the fluid at the top. This potentially unstable arrangement will have the tendency to redistribute itself in such a way that the denser layer tends to move to the bottom. However, this tendency of the fluid to move will be inhibited by its own viscosity. We expect therefore that the temperature gradient must exceed a critical value before the instability can manifest itself. The flow caused by this instability is known as convection. Convection in general means fluid motions caused by temperature differences with the temperature gradient pointing in any direction, but in this work we will only consider the case, where the fluid is heated from below.

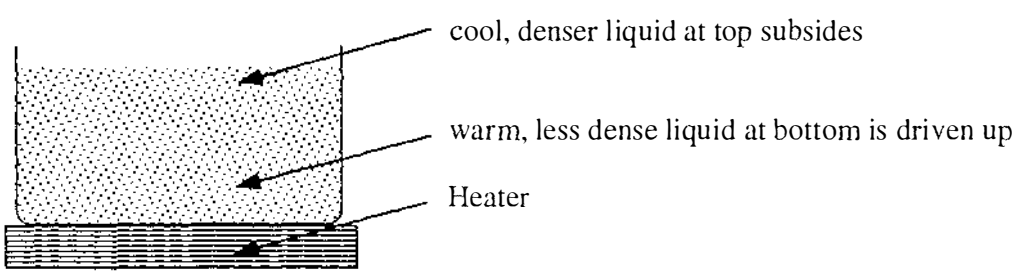

Figure 8.1: If an incompressible fluid is heated from below, the warmer and less dense layer at the bottom tends to rise, while the cooler and denser layer at the top tends to sink. The resulting flow is known as convection.

The earliest systematic experiments on convectional flow are those of Bénard in 1900 [152, 153]. He showed that a certain temperature gradient must be exceeded before instability can set in, and that the motions have a stationary cellular

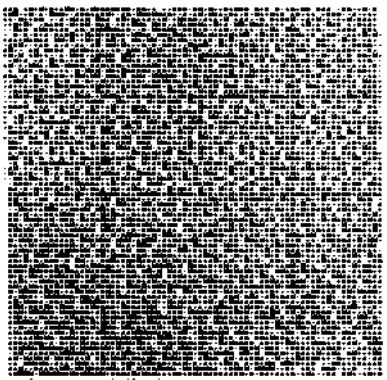

Figure 8.2: Original photograph showing Bénard cells at natural size in a layer of whale oil. Taken from [151].

character with a remarkable symmetry. If the experiment is performed with sufficient care, the cells align themselves in a hexagonal structure. A photograph from Bénard's work is shown in figure 8.2. Lord Rayleigh [154] showed a few years later that the onset of instability is characterised by the numerical value of the non–dimensional parameter R, which is known as the Rayleigh number and defined as follows:

$$R = \frac{g\alpha\Delta T}{\kappa_{th}\nu} d^3. \tag{8.1}$$

g denotes the acceleration due to gravity, d the depth of the layer, ΔT is the temperature difference across the sample, and α, κ_{th}, and ν are the coefficients of volume expansion, thermal diffusivity, and kinematic viscosity, respectively, and defined in the following way:

$$\alpha = V^{-1}\left(\frac{\partial V}{\partial T}\right)_p \tag{8.2}$$

$$\kappa_{th} = \frac{\lambda}{\rho c_p} \tag{8.3}$$

$$\nu = \frac{\eta}{\rho}. \tag{8.4}$$

c_p, η, λ and ρ are the specific heat at constant pressure, the viscosity, thermodynamic conductivity and density, respectively.

Rayleigh's treatment of the Bénard problem neglects surface effects. He introduced what we now call the Rayleigh–Bénard problem, which refers to convection caused by heating from below which is *not* affected by surface tension effects. Rayleigh also showed that when R just exceeds a critical value R_c, a stationary pattern must exist. Chandrasekhar calculated the theoretical value of R_c to be 1708 [155], which compares well with Silverston's experimental value of 1700 ± 51 [156]. These calculations assumed that the width of the fluid layer is much larger than its depth, so that end effects can be neglected. The width can be charac-

terised by the nondimensional aspect ratio $\Gamma = L/d$ which is the ratio of the width L of the fluid layer divided by its depth d. Most studies of convectional flow deal with large aspect ratios. For small values of Γ the non-slip boundary conditions tend to damp the onset of critical flow. The theoretical treatments of convection in circular containers by Charlson and Sani [157] and by Catton and Edwards [158] both show a sharp increase of R_c for small aspect ratios. For example, for $\Gamma = 0.06$, a value of $R_c > 10^7$ has been reported [158], whereas R_c decreases rapidly to $R_c = 1708$ for $\Gamma > 5$ [157].

Good review articles about recent experiments on thermal convection have been published by Normand *et al.* [159] and by Cross and Hohenberg [160]. Many references can be found in Koschmieder's book [151].

Usually, the convectional cells are made visible by small particles of metal powder in the fluid. Because NMR is a non-invasive technique, it is possible to image the velocity profiles directly. To our knowledge, there is only one MRI study [161] on convection. The authors of this study found steady convective states of Rayleigh-Bénard convection in porous media. These states, which have not yet been fully understood, depend in a complex manner on the pore packing. We will show that such convective states also exist in a simple NMR tube and give a more quantitative analysis of the velocity profiles.

In this chapter, we try to answer the question of what happens if we perform a PGSE experiment to measure self-diffusion in a sample where convection is present. In chapter 6 we mentioned that convection causes problems, and we had to find a special setup to overcome this. In the following sections, we will have a close look at these problems. We will use three different techniques to measure molecular displacements: The PGSE pulse sequence introduced in section 2.4.4, the spin warp flow imaging pulse sequence from section 2.4.5, and the VEXSY pulse sequence from chapter 4.

8.2 Experimental

For all the experiments in this section we used a solution of 5% polystyrene (M_w = 127 000) in cyclohexane. The sample was filled inside a 4 mm o.d. NMR tube. The height of the sample inside the tube was 25 mm and therefore larger than the height of the r.f. coil (15 mm). No slice selection was used in either experiment. The sample was heated inside the r.f. coil by a stream of 50° C hot air from below. The temperature difference was 4 K across a sample length of 2.5 cm. We now try to estimate the Rayleigh number for our setup. The viscosity η of polystyrene/cyclohexane solutions at 50° C has been measured by Papazian [162].

For a molecular weight of $M_w = 127\,000$ and a concentration of 5 % he obtains $\eta = 1.43 \cdot 10^{-3}$ Pa s. For a rough estimate of the Rayleigh number it is justified to take the literature values [51] of c_p, λ and ρ for cyclohexane alone. We finally get values of α, κ_{th} and ν of

$$\alpha = 2 \cdot 10^{-3}\ \mathrm{K}^{-1}, \tag{8.5}$$

$$\kappa_{th} = 1.3 \cdot 10^{-7}\ \mathrm{m}^2\ \mathrm{s}^{-1}, \tag{8.6}$$

$$\nu = 8.4 \cdot 10^{-7}\ \mathrm{m}^2\ \mathrm{s}^{-1}. \tag{8.7}$$

With these values we estimate the Rayleigh number for our setup:

$$R \approx 10^7. \tag{8.8}$$

Given a radius of the fluid layer of 1.7 mm and a height of 25 mm, we obtain an aspect ratio of $\Gamma = 0.07$. The critical Rayleigh number for this aspect ratio is of the same order [158], and we hope that our value of R in equation 8.8 is large enough to see instabilities. Note that for such a small aspect ratio surface effects can be ignored.

8.2.1 The PGSE Experiment

The PGSE experiment was performed in the same fashion as the experiments in chapter 6. The gradient amplitude $g = 0.36$ T m^{-1} was kept the same for each q–step, while the gradient pulse duration δ was stepped from 3 ms to 10.5 ms in steps of 0.5 ms. The delay Δ between the q–pulses was 40 ms. Figure 8.3 (a) shows the Stejskal–Tanner plot for this experiment. The data points are not on a straight line, as they were for the experiments in chapter 6, but exhibit pronounced minima and maxima akin to a diffraction pattern. Such diffraction behaviour has been observed in PGSE experiments before, but unlike the present case, that effect arose from restricted diffusion [163]. When analysing such data it is helpful to consider the function $E(q)$ from section 2.4.5 and plot it as $\log E(q)$ vs. q. The q–value of the first diffraction minimum q_{min} is the inverse of a characteristic length scale ξ in the sample [163]. Figure 8.3 (b) shows the same data as (a), but plotted vs. q instead of $4\pi^2 q^2 \Delta$. In our case, the situation is completely different from the case of restricted diffusion, because there are no restrictions like pores in our sample. The apparent diffraction effects must therefore be caused by something else. In the next section, we will report on measuring the flow profile in the sample using the spin warp technique.

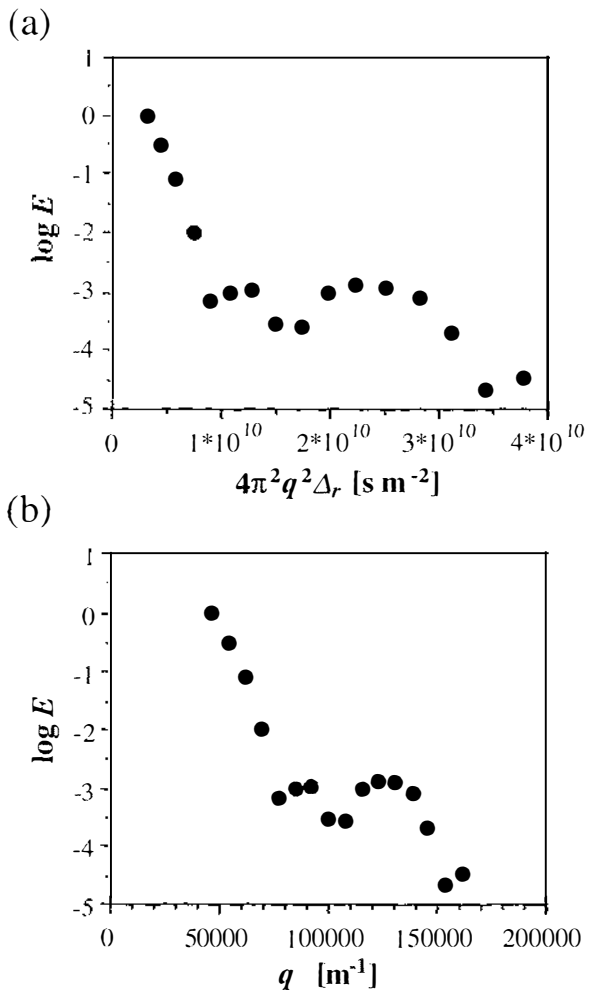

Figure 8.3: (a) A Stejskal–Tanner plot of the echo attenuation of a PGSE experiment of a polymer solution undergoing convectional flow. Note the pronounced minima and maxima, which have a close resemblance to a diffraction pattern. (b) The same data as in (a), but plotted vs. q.

8.2.2 The Flow Imaging Experiment

The flow image was recorded using the dynamic spin echo pulse sequence. As mentioned before, no slice selection was used in order to compare the data with those obtained in the previous section. The duration of the q-pulses was 2 ms, the amplitude was stepped from 0 to 0.72 T m^{-1} in 16 q-steps, and the separation between the q-pulses was 40 ms. The velocity image is shown in figure 8.4 (a). It shows a remarkable similarity to the velocity image shown in figure 3.5 (f), from which we conclude that the latter has indeed been caused by convection instead of electroosmotic flow. Figure 8.4 (a) shows also that there is only one Bénard cell in the whole tube. The flow profile inside the tube looks therefore like the one

displayed in figure 8.5 (a).

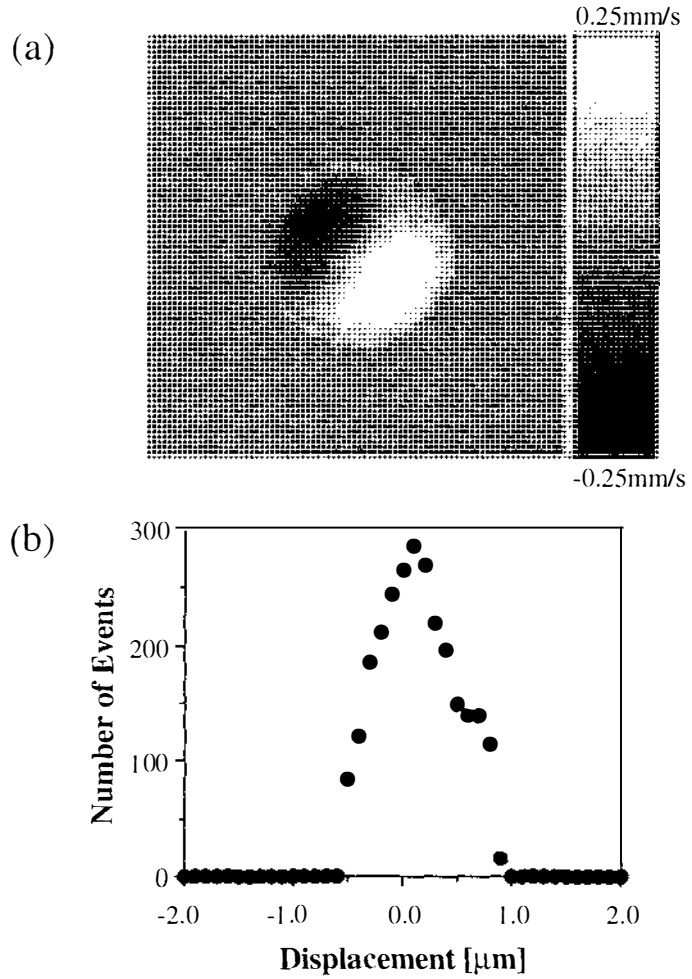

Figure 8.4: (a) A velocity image of a polymer solution in a 4 mm o.d. NMR tube, which is heated from below. (b) From the velocity image in (a) it is possible to extract the average velocity propagator $\overline{P_s}(R, \Delta)$.

From the velocity image in figure 8.4 (a) we can work out the average displacement propagator $\overline{P_s}(R, \Delta)$ by counting all the velocity values. A plot of $\overline{P_s}(R, \Delta)$ vs. R is shown in figure 8.4 (b). Knowing $\overline{P_s}(R, \Delta)$, we can calculate the expected echo attenuation using equation 2.77 from section 2.4.5:

$$E_\Delta(q) = \int \overline{P_s}(R, \Delta) e^{i2\pi \mathbf{q} \cdot R} dR.$$

A numerical cosine Fourier transformation of the data shown in figure 8.4 (b) yields $E(q)$, which is plotted in figure 8.6, both as a Stejskal–Tanner plot in (a) and vs. q in (b). The position of the minima and maxima agree very well with the data obtained using the PGSE experiment, which are shown in figure 8.3.

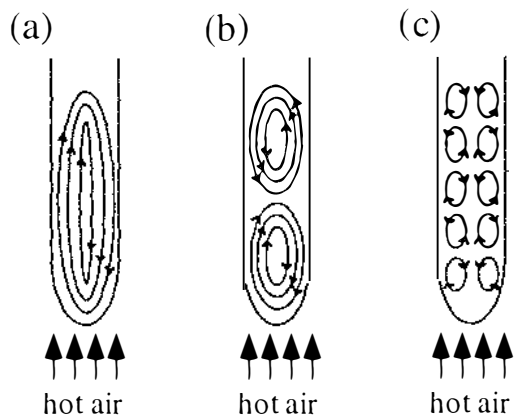

Figure 8.5: (a) – (c) Three different types of convection flow which could be present inside the glass tube. From the velocity profile in figure 8.4 (a) we see that we are dealing with the type displayed in (a).

This shows that one has to be very careful when interpreting data from PGSE experiments at elevated temperatures. Convection can cause effects which look like restricted diffusion in a Stejskal–Tanner plot. Because a temperature gradient in the sample can also be caused by heating of the gradient coil due to large currents, such convection effects can also be a particular problem in experiments involving large gradients.

8.2.3 The VEXSY Experiment

In chapter 4 we introduced the VEXSY pulse sequence as a tool to investigate complex flow. Knowing the velocity profile in our convection cell, it is easy to work out what the VEXSY spectra must look like. Figure 8.4 (a) shows that the maximum velocity of the molecules in the sample is $v_{max} = 0.25$ mm s^{-1}. With a sample height of 25 mm, the fastest molecules complete one cycle of figure 8.5 (a) in about 200 s. We expect to see cross–peaks in the VEXSY spectrum for mixing times of the order of the time the molecules take to complete half a cycle. With our setup, the minimum mixing time for which we expect to see cross–peaks in the VEXSY spectrum would therefore be on the order of 100 s. It is clear that this time is at least two orders of magnitude outside our time resolution, which in the present case is limited by T_1. On the other hand, if we could manage to reduce the size of the convection cells by two or three orders of magnitude, the VEXSY experiment would be a very valuable tool to probe the size of the cells by varying the mixing time. The cell structure would then resemble the one shown in figure 8.5 (c).

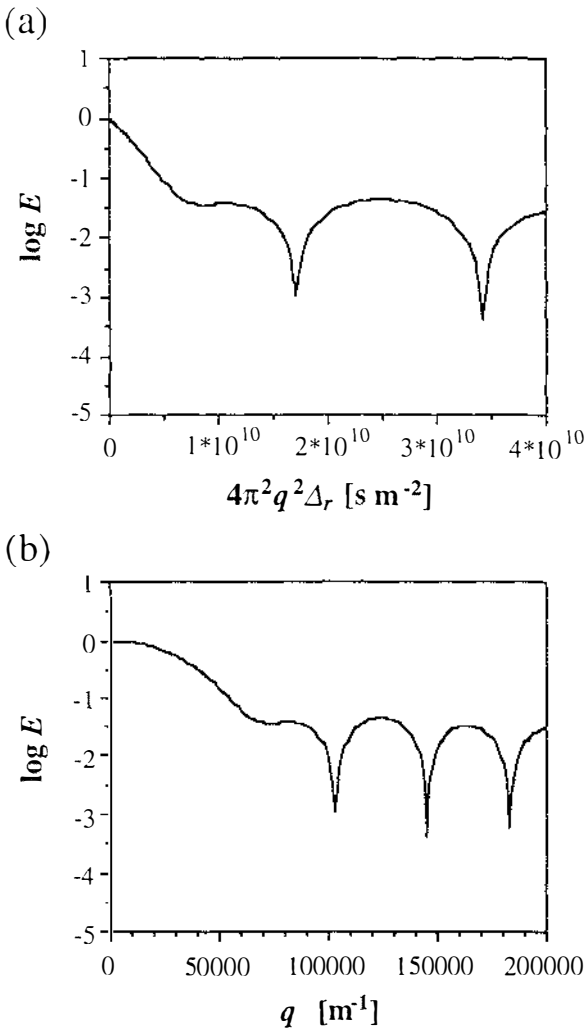

Figure 8.6: The Fourier transform of the velocity propagator displayed in figure 8.4 (b) plotted vs. $4\pi^2 q^2 \Delta_r$ (a) and vs. q(b).

The VEXSY experiments were performed using the high gradient probe described in section 2.5.3 in order to maximise velocity sensitivity. The spectra were recorded using 64^2 phase encoding steps with a gradient pulse duration of $\delta = 2.5$ ms, gradient pulse amplitude $g = 2.25$ T m^{-1} and pulse separation $\Delta = 15$ ms. Figure 8.7 (a) and (b) display the VEXSY spectra of the solvent for two different mixing times of $\tau_m = 25$ ms and $\tau_m = 125$ ms, respectively. Both spectra are essentially identical. The broadening of the spectra is due to Brownian motion. This becomes evident when comparing the profiles in figure 8.7 (a) and 8.7 (c), which is the two-dimensional VEXSY plot for the polymer. The polymer has a much smaller self-diffusion coefficient than the solvent, and thus the VEXSY spectrum is less broadened. We can estimate the self-diffusion coefficients using equation

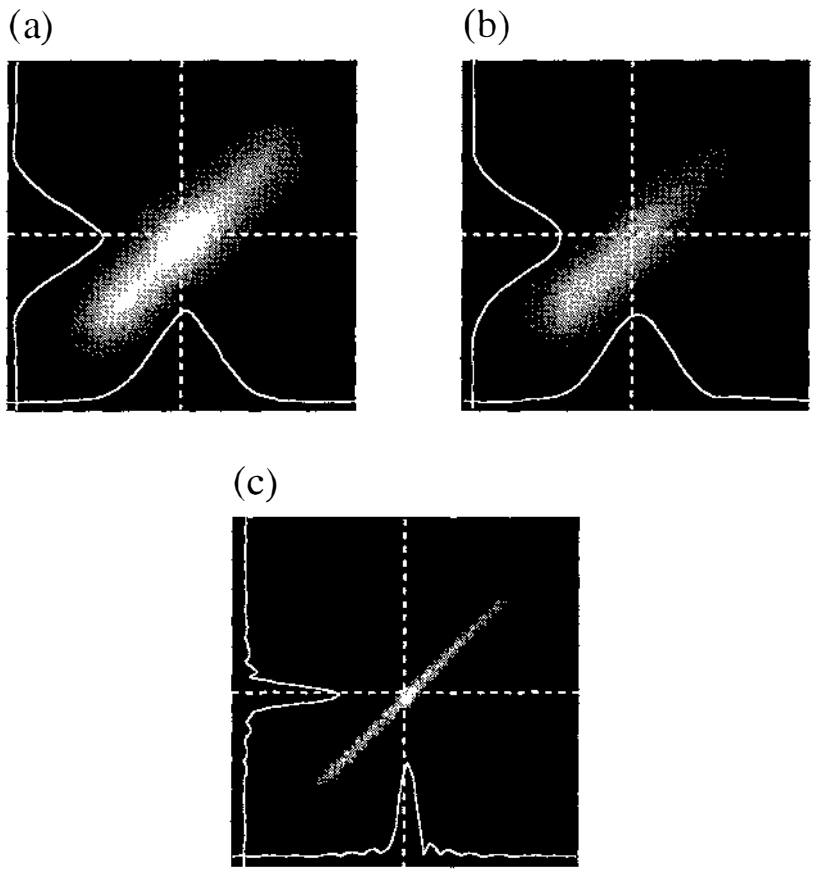

Figure 8.7: The two–dimensional VEXSY spectra $S(Z_1, Z_2)$ of a polymer solution undergoing convectional flow. The displacement field of view is 133 μm. (a) The VEXSY spectrum of the solvent for a short mixing time ($\tau_m = 25$ ms). (b) The VEXSY spectrum of the solvent for a long mixing time ($\tau_m = 125$ ms). (c) The VEXSY spectrum of the polymer for a short mixing time ($\tau_m = 25$ ms).

4.4. With widths of 15 μm and 4 μm we get values of $D_{Solv} = 4.3 \cdot 10^{-9}$ m^2 s^{-1} and $D_{Poly} = 3.5 \cdot 10^{-10}$ m^2 s^{-1} for the self-diffusion coefficient of the solvent and polymer, respectively.

8.3 Conclusions

In this chapter we examined convectional flow with three different methods. In the simple geometry we were using, the velocity field turned out to be stationary. In this case, one dynamic spin echo experiment provides full information about the flow profile in the sample. From this flow profile, one can extract the $E(q)$ function which we also obtained from the PGSE experiment. For a stationary flow profile we know that the VEXSY spectrum does not show any cross–peaks.

Therefore we can extract the complete information about the flow profile from one dynamic spin echo experiment if we assume that the velocity field is stationary.

If the molecular velocities are changing on a timescale of order 10–100 ms, one has to perform several experiments with variable delay Δ in order to probe these changes. As stated before in section 4.3.3, the PGSE and dynamic spin echo methods only measure *average* displacements during the delay time Δ. A set of VEXSY experiments on the other hand yields information about changes in velocity more directly.

The dynamic spin echo technique requires gradients in all three spatial directions. Many modern spectrometers, however, are only equipped with just one gradient for diffusion studies. In this case, flow profiles with a cylindrical geometry can be reconstructed using the PGSE method [52]. This reconstruction method fails when the flow is more complex as this is the case in our convection cell. Then the VEXSY method, which also uses one gradient direction, has to be used in order to obtain maximum information about the flow profile.

Figure 8.7 shows the limits of the VEXSY method. The spectra in (a) and (b) are significantly broadened which could be due to self–diffusion or to changes in velocity. There could be small cross–peaks hidden somewhere under the broad spectrum. The spectrum in figure 8.7 (c) demonstrates that this problem can be avoided by doping the sample with large molecules which have a much smaller self–diffusion coefficient than the solvent molecules. It is much narrower and shows no cross–peaks. The limitations of this doping method are also obvious. In particular, the signal–to–noise is generally poor and T_2 short which limits the values for the possible exchange times.

In this chapter we measured the convectional flow in a glass tube. The flow profile could be obtained using the dynamic spin echo method. From the velocity image we calculated the $E(q)$ function and showed that it exhibits pronounced minima and maxima akin to a diffraction pattern. These minima and maxima agree very well with the ones found with PGSE experiments on the same cell. With the VEXSY method we could show that the flow field in the convection cell is stationary.

Chapter 9

Shear–Induced Order in Liquid Crystals

9.1 Lyotropic Systems

9.1.1 Introduction

In a crystal the building blocks (atoms or molecules) are arranged in a regular periodic structure known as a lattice. Translational motion is mainly frozen out. In a liquid, on the other hand, the building blocks are completely disordered and move rapidly. In section 5.3.3 we introduced the glassy state as a state of a supercooled liquid, where the translational motion is frozen. Another state of organisation is the mesomorphic state. Such a state shows less symmetry than a crystal, but more symmetry than a liquid. Because translational motion can take place quite easily, these phases are also known as liquid crystals.

Like crystal lattices, liquid crystal phases are characterised by their symmetry. The main types are nematics and smectics and are shown in figure 9.1.

- Nematics are fluids of rodlike molecules with their centres disordered, but with a common axis of alignment for the rods (figure 9.1 (a)).
- Smectics are layered systems, each layer behaving like a two–dimensional liquid. The smectic A type is optically uniaxial (figure 9.1 (b), whereas the C type is biaxial (figure 9.1 (c). Smectics are also known as lamellar systems.

There are many more phases which are not important for this thesis. They are described in references [164, 165].

There may be phase transitions between different types of a liquid crystal when physical parameters are changed. A liquid crystal is called thermotropic if the temperature is the only variable to impose phase transitions. Pure materials

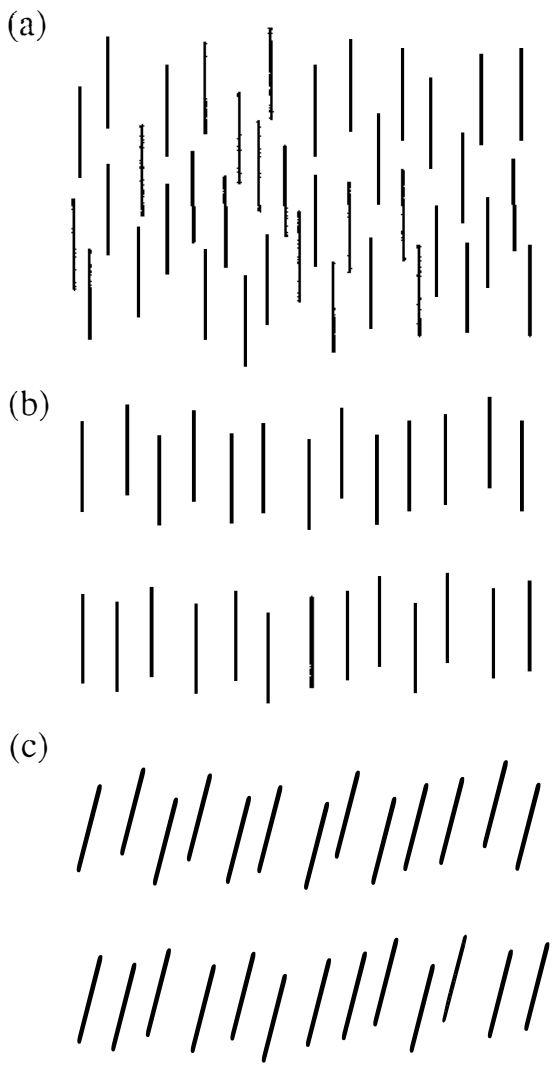

Figure 9.1: (a) Nematic phase. (b) Smectic–A phase. (c) Smectic–C phase. In the smectic phase each layer is disordered.

are often thermotropic. Another group is obtained with mixtures, where the phases can be obtained by changes in concentration. Such materials are known as lyotropic liquid crystals. A major example of lyotropic smectics is found with mixtures of lipid and water. A lipid molecule contains a polar head which is hydrophilic and a hydrophobic hydrocarbon tail. Many lipid/water systems show a lamellar phase that has the symmetry of smectic A. The molecules are arranged as shown in figure 9.2. These phases are made of regularly stacked planar surfactant bilayers (membranes) with a typical thickness of a few nanometers, separated by the solvent. In a macroscopic sample, these layers will be oriented randomly, unless they are aligned due to external forces.

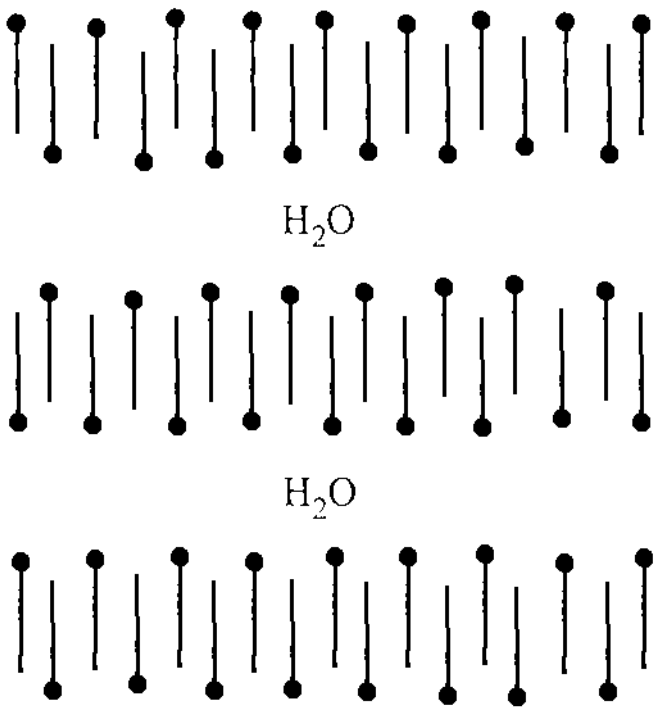

Figure 9.2: The lamellar phase of a lipid/water system, in this case smectic–A.

9.1.2 Rheology on Lyotropic Systems in the Lamellar Phase

Rheological experiments on lyotropic lamellar phases have been performed by Roux *et al.* [166]–[168]. They performed light and neutron scattering and polarising microscopy experiments on sheared mixtures of sodium dodecyl–sulphate (SDS), pentanol, water and dodecane in a Couette cell [166]. Three states of orientation were observed, depending on both shear rate and inter–membrane separation. State I exists at low shear rates ($\dot{\gamma} < 1\ s^{-1}$) and consists of a partially oriented lamellar phase where the membrane normal points along the velocity gradient direction. Many defects are present in this state. At high shear rates ($\dot{\gamma} > 100\ s^{-1}$) a similar state III is observed. Its main difference with state I is that it is much better oriented. Between states I and III, at intermediate shear rates a striking organisation of the membranes is observed. In state II the membranes are wrapped around a spherical core forming large objects (spherulites) that are closely packed. The size of these spherulites depends on the shear rate, decreasing from typically 10 μm to less than 1 μm as the shear rate increases. Rheological measurements on the same system show that states I and III correspond to Newtonian behaviour, but exhibit very different viscosities. State II shows shear thinning behaviour with a power law exponent $n \approx 0.2$ [167]. A new,

highly organised state has been found for a mixture of SDS, octanol and water at high shear rates [168]. With increasing shear rate the spherulites stop changing their size and organise themselves into long-range ordered plane structures sliding over each other. The spherulites are hexagonal shaped and closely packed on triangular lattices.

9.1.3 NMR on Lyotropic Systems in the Lamellar Phase

The layered structure and dynamics of lyotropic systems in the lamellar phase have been examined extensively by NMR. Here, we are only interested in the orientation and mobility of the water molecules between the bilayers. Callaghan *et al.* performed PGSE experiments on a lipid/D_2O system and showed that the water molecules are aligned between the bilayers. They also showed that there exists an anisotropy in the self-diffusion coefficient. The water molecules are much more mobile in the plane parallel to the bilayer surface than perpendicular to it.

Rheo-NMR experiments on lyotropic liquid crystals have been performed by Lukaschek *et al.* [169, 170]. For a mixture of a nonionic surfactant with D_2O in the hexagonal phase it was found that the deuterium NMR spectra depend on the shear strain γ. Alignment occurs along the flow direction [169]. At the same time, the viscosity decreases with increasing shear strain. Experiments on a mixture of nonionic surfactants with D_2O in the lamellar phase revealed a shear rate dependence of the deuterium NMR spectra. Two of the three states of orientation discussed by Roux *et al.*, which were described in the previous section, could be identified [170]. At low shear rates, the lamellar layers were found to be oriented along the velocity gradient. The deuterium NMR spectra also showed the presence of many defects in these layers. At higher shear rates the total line width of the deuterium spectra becomes smaller which was found to be consistent with the formation of spherulites in state II described by Roux *et al.*

The experiments of Roux *et al.* and Lukaschek *et al.* show that shear stress causes alignment of the lamellae which reduces the viscosity of the sample. This is expected to be reflected in the velocity profiles in the Couette cell, which will be reported in section 9.2.2.

Many other NMR experiments on lyotropic liquid crystals have been performed, for example relaxation time and line shape measurements. References to those can be found in [165]- [172]. However, they are not important for our rheo-NMR experiments.

9.2 Experimental Section

9.2.1 Sample Preparation

Two different systems were used for the experiments described in this chapter. Both are surfactants and form a lamellar phase in water at room temperature.

9.2.1.1 Dobanol/Water

Dobanol has the chemical composition $C_{14}H_{29}(EO)_7$, where EO stands for ethylene oxide (-CH_2-CH_2-O-). The phase diagram of Dobanol/water mixtures exhibits a lamellar phase between concentrations of roughly 65% and 85% and between room temperature and 85° C. Above 85° C the sample enters the isotropic phase [173].

The samples were prepared by adding Dobanol and water in a 3:1 mass ratio in a 10 mm o.d. NMR tube. The mixtures were then heated into the isotropic phase for mixing and the 5 mm o.d. NMR tube along with the teflon spacers was inserted into the sample tube.

For the experiments described in section 9.2.3 a Dobanol/D_2O sample with the same mass concentration was prepared.

9.2.1.2 Aerosol OT/Water

Aerosol OT (bis(2-ethylhexyl) sodium sulfonsuccinate) (AOT) is known to form a lamellar phase with water at room temperature over a wide range of concentrations [174]. At a mass ratio of 1:1 the phase transition to the isotropic phase occurs at a temperature of 140° C. The samples were prepared by adding AOT and water at a 1:1 mass ratio in a glass tube which was subsequently sealed and stored at a temperature of 60° C for at least two weeks. During this period the sample tubes were occasionally centrifuged back and forth to ensure mixing.

A sample of AOT/D_2O with the same mass concentration was prepared for the experiments described in section 9.2.3.

For the NMR measurements the samples were then transferred into a 10 mm o.d. NMR tube, and the 5 mm o.d. tube with the teflon spacers was inserted. Entrapped air bubbles could be reduced by centrifuging the whole Couette cell.

9.2.2 Measurement of Flow Profiles

The flow profiles for the Dobanol/water sample were measured using the same technique as described in chapter 7, the experimental parameters being given in the first line of table 9.1. These flow profiles are shown in figure 9.3 (a). They

display a large velocity gradient close to the rotating tube. Further away from the rotating tube the velocity seems to be almost constant and at the outer wall the sample appears to slip. In order to monitor this behaviour more closely a second set of experiments was carried out with a higher velocity resolution. The spatial resolution had to be reduced because the echo time Δ was limited by the transverse relaxation time.

The parameters for the flow imaging are given in the second line of table 9.1, while the corresponding flow profiles are shown in figure 9.3 (b). Note that the velocity profiles give accurate values only in the regions of low velocities. Close to the spinning tube the propagators are broadened significantly due to shear in one pixel.

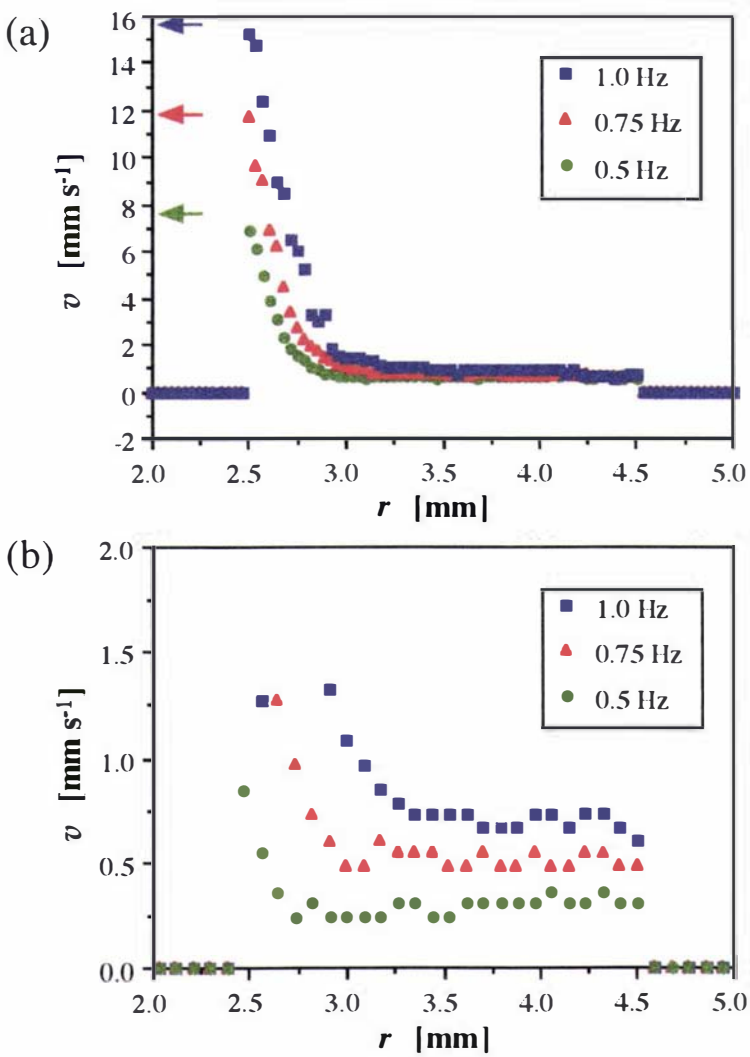

Figure 9.3: (a) Velocity profiles of Dobanol/Water at different rotation speeds of the inner tube. The arrows mark the calculated speeds of the rotating tube. (b) Same profiles as in (a), but measured with a higher velocity resolution. The slip at the outer wall is obvious.

Sample	Δ [ms]	δ [ms]	g_{max} [T m^{-1}]
Dobanol/H_2O	15	3.0	0.25
Dobanol/H_2O	20	5.0	0.25
AOT/H_2O	15	2.0	0.35

Table 9.1: The experimental parameters for the flow imaging experiments.

A difficulty arose for the AOT/water sample. It was found that the transverse relaxation time T_2 was on the order of 5 ms. Such a value of T_2 is too short to apply the modified dynamic spin echo pulse sequence from figure 7.5 with an acceptable signal–to–noise ratio. Therefore the velocity profiles for this sample had to be measured using the normal dynamic spin echo pulse sequence shown in figure 2.14. The velocity profiles obtained with this method are shown in figure 9.4, while the experimental parameters are given in the bottom line of table 9.1.

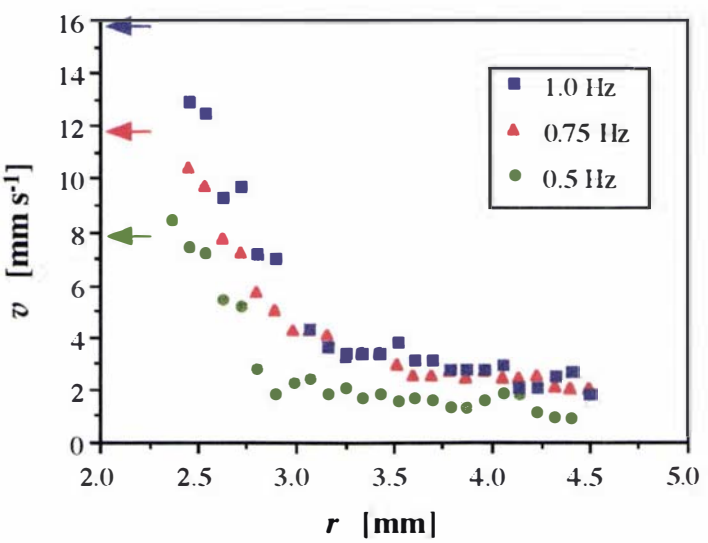

Figure 9.4: Velocity profiles of AOT/Water at different rotation speeds of the inner tube. The arrows mark the calculated speeds of the rotating tube.

For both samples the rotation frequency of the inner tube was 0.5 s^{-1}, 0.75 s^{-1} and 1.0 s^{-1}. All experiments were performed at an ambient temperature of 22° C.

9.2.3 Measurement of Order Parameters

Molecular orientations are often measured by selectively replacing some protons of the molecule under investigation by deuterium nuclei. As stated in section 2.2.4. these deuterium nuclei have a nonzero quadrupole moment. Because deuterium

NMR spectra are typically characterised entirely by the well-defined quadrupolar interaction, the connection between what is measured and the molecular orientation is particularly clear. The splitting of the absorption lines in the NMR spectrum is proportional to the order parameter s. By monitoring the line splitting at different orientations, one can measure the orientation of molecules in solids.

Here, we monitored the effect of shear on the water molecules in the bilayer of a lamellar lipid/water system by measuring the deuterium NMR spectrum of the lipid/D_2O samples at different shear rates. All the spectra were recorded at an ambient temperature of 22° C. No spatial encoding was applied.

9.3 Results

9.3.1 Flow Profiles

The velocity profiles in figure 9.3 and 9.4 show slip behaviour at the stationary wall. In order to examine the flow behaviour next to the spinning tube, we calculated its velocities from the known rotation speeds. Those are marked by arrows in figures 9.3 (a) and 9.4. Some experiments were also performed where the rotating tube was filled with the sample. By measuring the velocity profile inside the rotating tube and extrapolating it to the outside wall, good values for the expected fluid velocities assuming non-slip conditions can be obtained. No slip could be observed at the wall of the spinning tube for the Dobanol/Water sample. For the AOT/Water sample, only the velocity profile with the highest spinning rate shows an inconsistency between expected and measured velocity close to the spinning tube. Apart from slip, this could also be due to noise in the velocity profile.

9.3.1.1 Dobanol/Water

The shapes of the velocity profiles clearly suggest shear thinning, but they cannot be fitted using equation 5.41. Figure 9.5 shows a graph of $\log\dot{\gamma}$ vs. $\log r$ for the data sets shown in figure 9.3. We recall from section 7.1.2 that the local power law exponent can be obtained from the slope of such a graph. The data sets in figure 9.5 show two distinct regions. With increasing r the shear rate drops with a constant power law exponent until reaching a value of $\dot{\gamma} \approx 1\ s^{-1}$. Then $\dot{\gamma}$ remains constant with increasing r. Such behaviour may be compared to rheological measurements shown in figure 9.6 [173]. The shear stress vs. shear rate graph displays a yield stress τ_1 of $\tau_1 = 15$ Pa. This stress is present to a shear rate of $\dot{\gamma} \approx 1\ s^{-1}$, the same critical shear rate at which the transition in the $\log\dot{\gamma}$ vs. $\log r$ graph occurred.

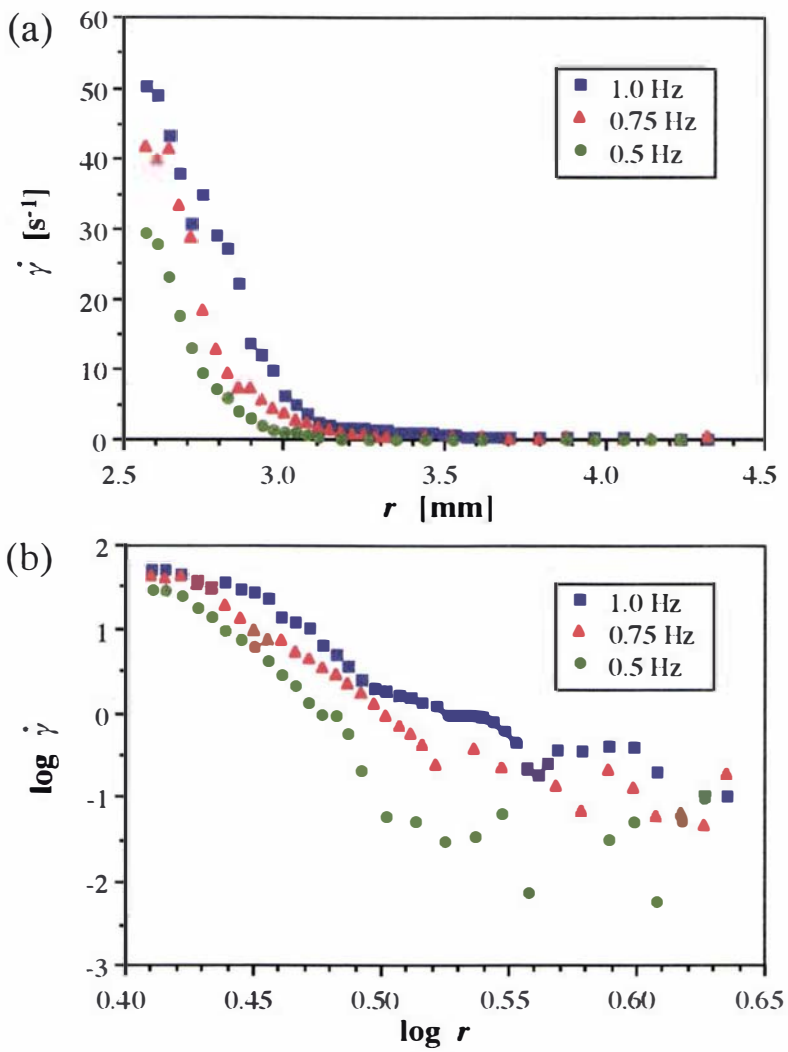

Figure 9.5: (a) $\dot{\gamma}$ vs. r and (b) $\log\dot{\gamma}$ vs. $\log r$ for Dobanol/Water at different rotation speeds of the inner tube.

9.3.1.2 AOT/Water

As mentioned previously, the transverse relaxation time T_2 is too short to obtain a good signal–to–noise ratio in the velocity profiles. Therefore we can give only a qualitative analysis of the profiles shown in figure 9.4.

As observed with the Dobanol/Water sample, the velocity profiles reveal slip behaviour at the stationary wall. A graph of $\log\dot{\gamma}$ vs. $\log r$ is shown in figure 9.7. The shear rate drops again with increasing r and reaches a constant value at $\dot{\gamma} \approx 2$ s^{-1}.

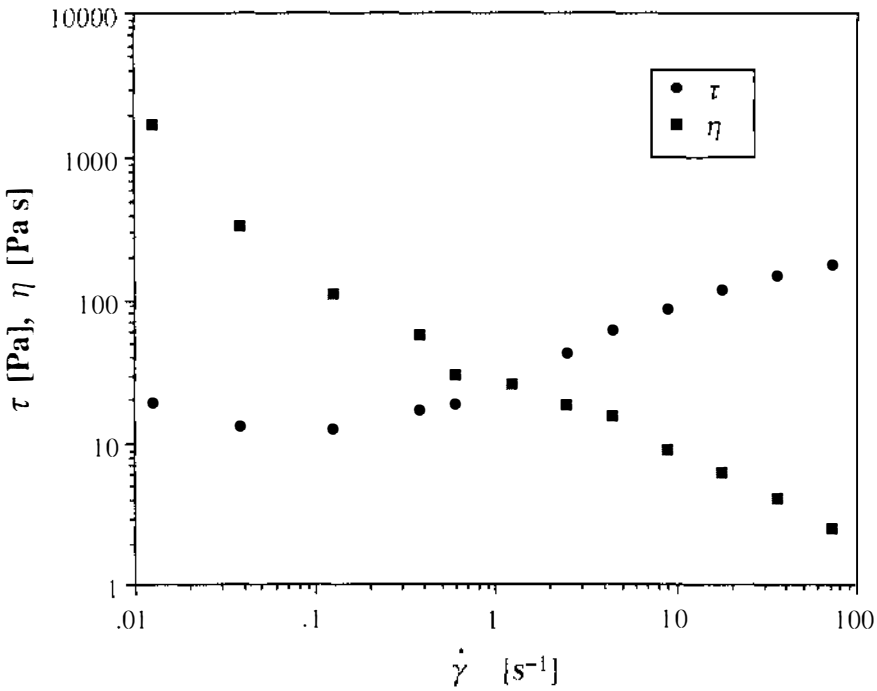

Figure 9.6: Shear stress τ and viscosity η vs. shear rate $\dot{\gamma}$ for Dobanol/Water. Graph taken from [173].

9.3.2 Deuterium NMR Spectra

A series of NMR spectra is shown in figures 9.8 and 9.9, both for Dobanol/D_2O and AOT/D_2O. The spectra in figures 9.8 (a) and 9.9 (a) were recorded before the samples were sheared. In order to destroy any alignment caused by the insertion of the 5 mm tube into the 10 mm tube containing the sample, the Dobanol/D_2O sample was heated above the phase transition temperature into the isotropic phase outside the magnet. This was not possible with the AOT/D_2O sample because the phase transition temperature of 140° C is not accessible with the NMR probe.

The spectra in figures 9.8 (a) and 9.9 (a) show a clear ridge structure similar to a Pake pattern of solids [56]. Such a structure arises from the distribution of molecular orientations. However, neither spectrum displays the perfectly randomised structure of a Pake pattern. The deviation can be attributed to alignment of the lamellae, and hence the D_2O molecules, along the glass walls.

Figures 9.8 (b)–(c) and 9.9 (b)–(c) show the time evolution of the spectra after the inner tube started to spin. The high frequency edges lose their sharp structures and the intensity at zero frequency increases.

These high frequency edges are created by molecules whose O–D bond direction is parallel to the static magnetic field. Starting shear causes the molecules to

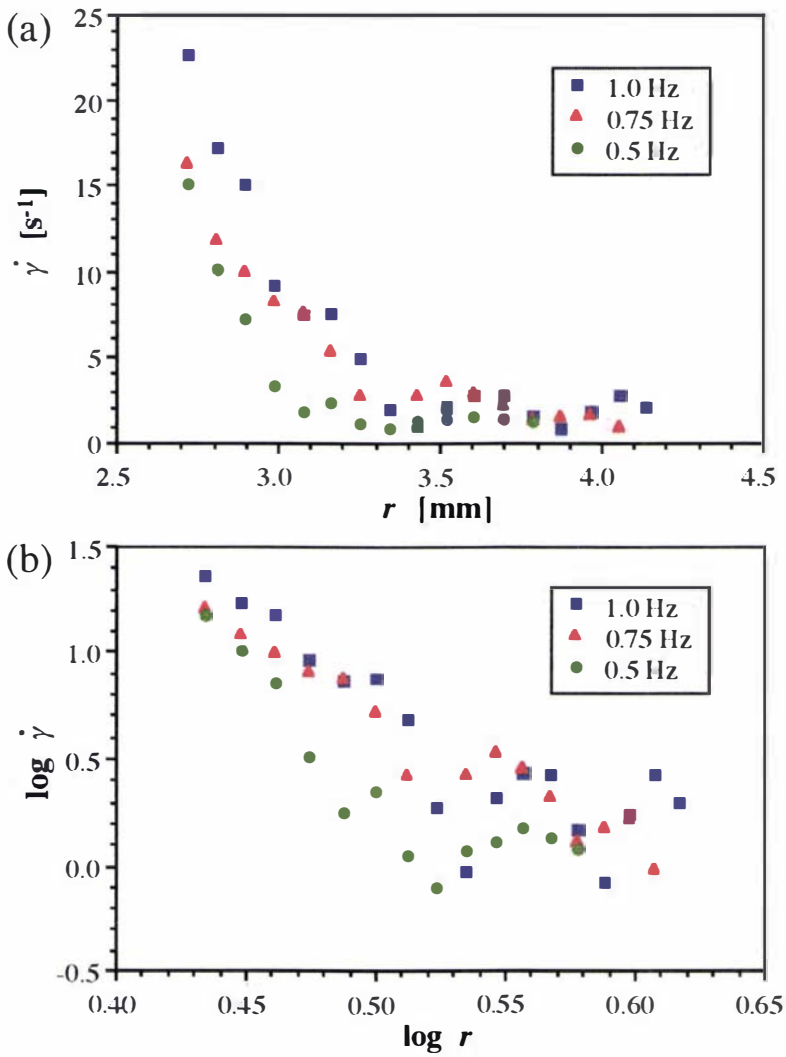

Figure 9.7: (a) $\dot{\gamma}$ vs. r and (b) $\log\dot{\gamma}$ vs. $\log r$ for AOT/Water at different rotation speeds of the inner tube.

reorient in the flow field. In our Couette cell both the velocity and shear direction are perpendicular to the direction of B_0. The disappearance of these edges suggests that the O–D bond direction aligns in the velocity–shear plane. It was found that such alignment persists even after shear has stopped.

9.4 Discussion

Rheo–NMR experiments were performed on two liquid crystals in the smectic phase. The velocity profiles of both samples showed slip at the stationary wall. The graphs of $\log\dot{\gamma}$ vs. $\log r$ in figures 9.5 and 9.7 showed for both samples a transition from power law behaviour to a constant shear rate at a critical shear

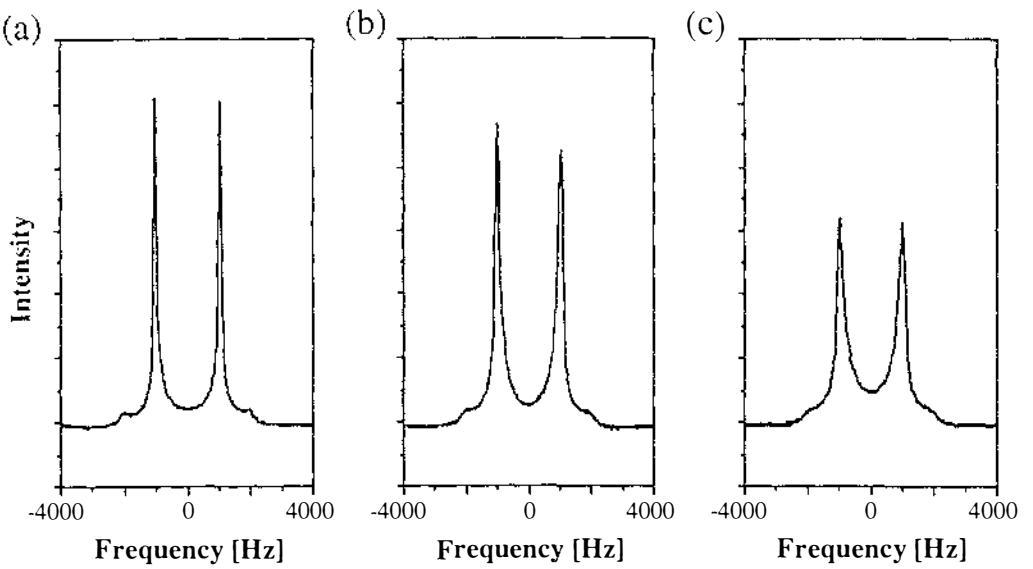

Figure 9.8: Deuterium NMR spectra of Dobanol/D_2O, before sample is sheared (a), with a constant rotation speed of the inner tube after 2 minutes (b), and after 10 minutes(c).

rate $\dot{\gamma}_c$. For the Dobanol/Water sample this could be compared to rheological experiments, where the critical shear rate was found to be equal to the shear rate above which the shear stress started to increase. Using equation 5.33 we obtain from figure 9.6 a power law exponent $n_r = 0.45$ in the power law region. The graph shown in figure 9.5 (b) allows us the calculation of the power law exponent using equation 5.44. From the slope of the data points in the shear thinning region we obtain $n_{NMR} \approx 0.1$.

The deuterium NMR spectra for both samples showed a dependence on the shear rate which can be attributed to changes in molecular organisation. Particularly the spectra for the AOT/D_2O sample shown in figure 9.9 display strong similarities to the deuterium NMR spectra published by Lukaschek *et al.* in reference [170]. These authors attributed the line narrowing to the formation of spherical multilamellar vesicles in state II described by Roux *et al.*

9.5 Conclusions

The idea behind the experiments described in this chapter was to establish a method to monitor the shear rate dependence of molecular organisation. Because the shear rate was found to be not constant across the sample this requires some sort of spatial resolution. The spatial variation of the shear rate can be obtained by measuring the velocity profiles in the Couette cell using dynamic NMR microscopy. On the other hand, deuterium NMR spectroscopy of D_2O enriched

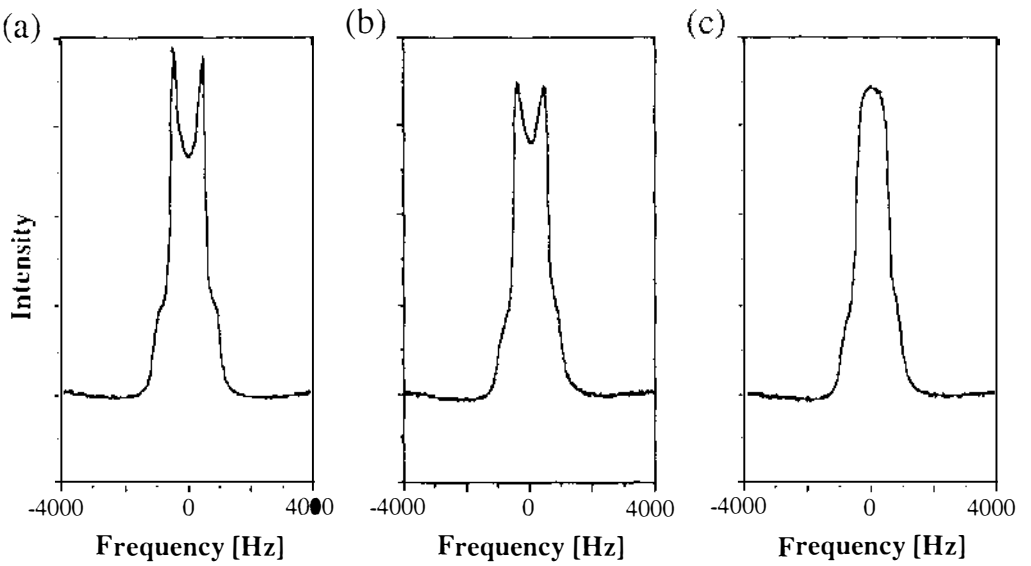

Figure 9.9: Deuterium NMR spectra of AOT/D_2O, before sample is sheared (a), with a constant rotation speed of the inner tube after 2 minutes (b), and after 10 minutes(c).

surfactant/water systems is a well–established method to probe molecular orientations. All the deuterium NMR spectra shown in this chapter are spectra of the whole sample and represent therefore averages over a whole range of different shear rates. For a quantitative investigation of the shear rate dependence of molecular organisation some sort of spatial encoding is necessary. The gyromagnetic ratio for deuterons is smaller, by a factor of approximately 6.5, than for protons. This fact makes deuterium NMR an inherently insensitive method. It also means that in order to obtain the same spatial resolution as for protons, one requires gradient pulse strengths which are higher, by a factor of 6.5. Another problem arises from the fact that T_2 is typically very short if the quadrupolar coupling is strong. Spatial encoding requires time during which the signal decays, often below the noise level.

There are some suggestions how these problems can be overcome. Low sensitivity is usually compensated by signal averaging. However, using spatial encoding, this can increase the experiment time considerably.

Spatial resolution can be increased by applying stronger gradient pulses by increasing the current through the gradient coils. The maximum current is determined by the heat dissipation in the coils caused by resistive heating. An alternative is to build a completely new, stronger set of gradient coils.

Signal decay during spatial encoding is normally reduced by increasing the gradient strength and reducing the gradient pulse duration. In our case this is not possible, because the gradient strength is already limited. A different approach is

to use some kind of spatial encoding which only suffers from T_1 relaxation, which is much slower in liquid crystals. This can be achieved by using, for example, the SPACE [175] or DIGGER [176] pulse trains suggested by Doddrell *et al.* which selectively destroy the magnetisation in the whole sample except in the region under investigation.

All these points show that deuterium NMR spectroscopy is hard to perform with a spatial resolution on a microscopic scale. However, the experiments described above also show that there is a lot of potential for future work.

Chapter 10

Conclusion

10.1 Summary

In this thesis we investigated how NMR microscopy could be used to obtain information about heterogenous properties of fluids, in particular the time evolution of flow, and the dependence of hydrodynamic behaviour and Brownian motion of molecular organisation. Pulsed Gradient Spin Echo NMR and the concept of q–space analysis played a key role in the experiments.

By measuring flow profiles in an electroosmotic capillary at different times after turning on the electric field we were able to demonstrate that the shape of the profile changes with increasing time from plug flow to the well–known parabolic profile. A steady state is reached in the capillary geometry on a timescale of 100 ms, and the electroosmotic flow velocities are of the same order as the ionic electrophoretic drift velocities. The agreement with a theoretical model was excellent.

In stationary flow, changes of molecular velocities can be observed by using a two–dimensional velocity exchange experiment (VEXSY). This experiment was demonstrated on Brownian motion, on laminar circular flow in a Couette cell and on flow through a bed of closely–packed microspheres. In the latter case, the VEXSY spectrum showed a transition from stationary to a more randomised flow with increasing mixing time.

Molecular velocities due to convectional flow were monitored with different methods. The VEXSY experiments showed that this flow is stationary The echo attenuation function $E(q)$ of a PGSE experiment revealed pronounced minima and maxima. Comparison with the function $E(q)$ obtained from the measured velocity propagator showed good agreement.

The temperature dependence of molecular displacement parameters was mea-

sured for semi–dilute polymer solutions near the de–mixing transition. The temperature dependence of the self–diffusion coefficient could be described by a WLF equation which is characteristic of a glass transition. Using the reptation model for polymers, the tube disengagement times τ_d were calculated. From the shape of the velocity profiles in the Couette cell the entanglement formation times τ_η were obtained using a theory for non–linear viscoelasticity based on the entanglement concept. Good agreement between τ_d and τ_η was found, as expected.

With deuterium NMR spectroscopy we showed that shear–induced alignment can be measured. This result has some potential for future work which will be discussed in the next section.

10.2 Outlook on Future Work

It is not surprising that many new questions can be raised from all aspects of this thesis. We mention a few of them here.

The measurements of the flow profiles in the electroosmosis cell showed excellent agreement with the theory for one particular geometry. The theory of Söderman *et al.* has been applied to a number of different geometries. It would be interesting to measure the time evolution of electroosmotic velocity profiles in geometries different from that of the capillary used here. One particular example is the flow between parallel plates, a geometry which could best be investigated using the new horizontal magnet which has been recently installed in the NMR lab.

Investigation of complex flow using the PGSE NMR method is one of the key research areas in our group. It is of particular interest, because of its direct analogy with scattering methods and because only one gradient is required. Oscillations in the echo attenuation function $E(q)$ have been observed in different flowing systems, such as convectional flow and flow through micropores. At the stage of writing of this thesis experiments on Taylor vortices [151, 155] are in progress.

Not much is known so far about the temperature dependence of the polymer self–diffusion coefficients for semi–dilute solutions near the de–mixing transition. The PS/CYH system has been examined extensively in the literature, but it is very difficult to handle. Another system on which many references are available is PS in DOP. It also shows some interesting features when sheared. A project for the future would be to repeat the diffusion and rheo–NMR experiments on semi–dilute PS/DOP solutions.

We showed that the local shear rate can be obtained from the velocity profiles. Rabin and Samulski [177] suggested the use of deuterium labelling to measure

shear–induced alignment of molecules in polymer solutions. Because the shear rate varies across the sample, the deuterium spectrum has to be recorded in different regions of the sample using selective excitation. A different approach to measuring shear–induced alignment has been suggested by Callaghan and Samulski [178]. Their so–called "beta function" measures the dipolar interaction directly and shows a strong orientation dependence. The advantage of the beta function is that no expensive and difficult deuterium labelling is required. Using NMR microscopy the spatial (and therefore shear) dependence of other NMR parameters, such as relaxation times, can also be measured.

The question of whether reptation is an important process in polymer solutions still remains to be answered. With a new quadrupolar gradient coil developed in our group gradient strengths of up to 50 T m^{-1} are achievable. This should allow the measurement of internal motion of the polymer chains and clarify the mechanisms involved in molecular dynamics of polymer coils in solution.

Bibliography

[1] E. M. Purcell, H. C. Torrey, and R. V. Pound. *Phys. Rev.*, **69**, 37–38 (1946).

[2] F. Bloch, W. W. Hansen, and M. Packard. *Phys. Rev.*, **70**, 474–485 (1946).

[3] E. L. Hahn. *Phys. Rev.*, **80**, 580–594 (1950).

[4] R. R. Ernst and W. A. Anderson. *Rev. Sci. Instrum.*, **37**, 93–102 (1966).

[5] E. L. Hahn. *Phys. Rev.*, **80**, 580 (1951).

[6] E. O. Stejskal and J. E. Tanner. *J. Chem. Phys.*, **42**, 288–292 (1965).

[7] P. Mansfield and P. K. Grannell. *J. Phys. C: Sol. St. Phys.*, **6**, L422–L426 (1973).

[8] P. C. Lauterbur. *Nature*, **242**, 190–191 (1973).

[9] P. T. Callaghan, C. D. Eccles, and Y. Xia. *J. Phys. E: Sci. Instrum.*, **21**, 820–822 (1988).

[10] A. Abragam. *The Principles of Nuclear Magnetism.* Clarendon Press, Oxford, (1961).

[11] P. T. Callaghan. *Principles of Nuclear Magnetic Resonance Microscopy.* Clarendon Press, Oxford, (1991).

[12] R. R. Ernst, G. Bodenhausen, and A. Wokaun. *Principles of Nuclear Magnetic Resonance in One and Two Dimensions.* Clarendon Press, Oxford, (1987).

[13] E. Fukushima and S. B. W. Roeder. *Experimental Pulse NMR. A Nuts and Bolts Approach.* Addison-Wesley, Reading (Massachusetts), (1981).

[14] W. W. Paudler. *Nuclear Magnetic Resonance.* John Wiley & Sons, New York, (1987).

[15] D. Shaw. *Fourier Transform NMR Spectroscopy.* Elsevier Publishing Company, Inc., Amsterdam, (1984).

[16] C. P. Slichter. *Principles of Magnetic Resonance.* Springer–Verlag, Heidelberg, (1990).

[17] A. Messiah. *Quantum Mechanics.* John Wiley & Sons, New York, (1966).

[18] L. I. Schiff. *Quantum Mechanics.* McGraw Hill, New York, (1955).

[19] H. Y. Carr and E. M. Purcell. *Phys. Rev.*, **94**, 630–638 (1954).

[20] S. Meiboom and D. Gill. *Rev. Sci. Instrum.*, **29**, 688–691 (1958).

[21] E. O. Stejskal. *J. Chem. Phys.*, **43**, 3597–3603 (1965).

[22] J. Jeener. Ampère International Summer School, Basko Polje, Yugoslavia, (1973).

[23] L. Müller, A. Kumar, and R. R. Ernst. *J. Chem. Phys.*, **63**, 5490–5491 (1975).

[24] C. Schmidt, B. Blümich, and H. W. Spiess. *J. Magn. Reson.*, **79**, 269–290 (1988).

[25] S. Wefing and H. W. Spiess. *J. Chem. Phys.*, **89**, 1219–1233 (1988).

[26] S. Wefing, S. Kaufmann, and H. W. Spiess. *J. Chem. Phys.*, **89**, 1234–1244 (1988).

[27] D. I. Hoult and R. E. Richards. *Proc. R. Soc. London A*, **344**, 311–340 (1975).

[28] P. Mansfield and P. K. Grannell. *Phys. Rev. B*, **12**, 3618–3634 (1975).

[29] A. Kumar, D. Welti, and R. R. Ernst. *J. Magn. Reson.*, **18**, 69–83 (1975).

[30] G. Johnson, J. M. S. Hutchison, T. W. Redpath, and L. M. Eastwood. *J. Magn. Reson.*, **54**, 374–384 (1983).

[31] M. Appel, G. Fleischer, J. Kärger, F. Fujara, and I. Chan. *Macromolecules*, **27**, 4274–4277 (1994).

[32] D. W. McCall, D. C. Douglass, and E. W. Anderson. *Ber. Bunsenges.*, **67**, 336–340 (1963).

[33] J. Kärger, H. Pfeifer, and W. Heink. *Adv. Magn. Reson.*, **12**, 1–89 (1988).

[34] T. L. James and G. G. McDonald. *J. Magn. Reson.*, **11**, 58–61 (1973).

[35] J. Kärger and W. Heink. *J. Magn. Reson.*, **51**, 1–7 (1983).

[36] C. D. Eccles. *Microscopic NMR Imaging.* PhD thesis, Massey University, (1987).

[37] Y. Xia. *Dynamic NMR Microscopy.* PhD thesis, Massey University, (1992).

[38] P. Mansfield and B. Chapman. *J. Magn. Reson.*, **66**, 573–576 (1986).

[39] R. Mills. *J. Phys. Chem.*, **77**, 685–688 (1973).

[40] P. T. Callaghan. *J. Magn. Reson.*, **88**, 493–500 (1990).

[41] A. Coy. *q–Space, Restricted Diffusion and Pulsed Gradient Spin Echo Nuclear Magnetic Resonance.* PhD thesis, Massey University, (1995).

[42] C. S. Johnson and Q. He. *Adv. Magn. Reson.*, **13**, 131–159 (1989).

[43] D. J. Shaw. *Electrophoresis.* Academic Press, London, (1969).

[44] J. Packer, C. Rees, and D. J. Tomlinson. *Adv. Mol. Relaxation Processes*, **3**, 119–131 (1972).

[45] R. J. Hunter. *Zeta Potential in Colloid Science.* Academic Press, London, (1981).

[46] R. J. Hunter. *Foundations of Colloid Science.* Clarendon Press, Oxford, (1987).

[47] O. Söderman and B. Jönsson. *Journal of Chemical Physics (submitted)*(1996).

[48] M. Abramowitz and I. A. Stegun. *Handbook of Mathematical Functions.* Dover Publications, New York, (1970).

[49] T. R. Saarinen and W. S. Woodward. *Rev. Sci. Instrum.*, **59**, 761–763 (1988).

[50] P. J. Scales, F. Grieser, T. W. Healey, L. R. White, and D. Y. C. Chan. *Langmuir*, **8**, 965 (1992).

[51] D. R. Lide. *Handbook of Chemistry and Physics.* CRC Press, New York, (1995).

[52] D. Wu, A. Chen, and C. S. Johnson Jr. *J. Magn. Reson. A*, **115**, 123–126 (1995).

[53] P. T. Callaghan and B. Manz. *J. Magn. Reson. A*, **106**, 260–265 (1994).

[54] D. G. Cory, A. N. Garroway, and J. B. Miller. *Polymer Preprints*, **31**, 149–150 (1990).

[55] C. J. Rofe, R. K. Lambert, and P. T. Callaghan. *J. Rheol.*, **38**, 857–887 (1994).

[56] G. E. Pake. *J. Chem. Phys.*, **16**, 327–336 (1948).

[57] T. Gullion, D. B. Baker, and M. S. Conradi. *J. Magn. Reson.*, **89**, 479–484 (1990).

[58] J. D. Seymour and P. T. Callaghan. *J. Magn. Reson. A*, **(in press)**(1996).

[59] P. G. de Gennes. *Scaling Concepts in Polymer Physics.* Cornell University Press, Ithaca, (1979).

[60] M. Kurata. *Thermodynamics of Polymer Solutions.* Harwood Academic Publishers, Chur, (1982).

[61] M. Doi and S. F. Edwards. *The Theory of Polymer Dynamics.* Clarendon Press, Oxford, (1986).

[62] J. des Cloizeaux and G. Jannink. *Polymers in Solution.* Clarendon Press, Oxford, (1990).

[63] H. Fujita. *Polymer Solutions.* Elsevier Publishing Company, Inc., Amsterdam, (1990).

[64] U. Eisele. *Introduction to Polymer Physics.* Springer–Verlag, Berlin, (1990).

[65] R. H. Boyd and P. J. Phillips. *The Science of Polymer Molecules.* Cambridge University Press, Cambridge, (1993).

[66] J. S. Higgins and H. C. Benoît. *Polymers and Neutron Scattering.* Clarendon Press, Oxford, (1994).

[67] D. H. Hey. *Kingzett's Chemical Encyclopedia.* Baillière, Tindall and Cassell Ltd., London. (1966).

[68] J. Brandrup and E. H. Immergut. *Polymer Handbook.* John Wiley & Sons, New York, (1989).

[69] P. J. Flory. *J. Chem. Phys.*, **10**, 51 (1942).

[70] M. L. Huggins. *J. Phys. Chem.*, **64**, 1712–1719 (1942).

[71] P. G. de Gennes. *J. Chem. Phys.*, **55**, 572–579 (1971).

[72] M. Doi and S. F. Edwards. *J. Chem. Soc. Faraday Trans. 2*, **74**, 1789–1801 (1978).

[73] P. J. Flory. *Principles of Polymer Chemistry.* Cornell University Press, Ithaca, (1953).

[74] L. D. Landau and E. M. Lifshitz. *Statistical Physics.* Pergamon Press, London, (1958).

[75] A. Z. Akcasu and C. C. Han. *Macromolecules*, **12**, 276–280 (1979).

[76] J.-P. Munch, G. Hild, and S. Candau. *Macromolecules*, **16**, 71–75 (1983).

[77] I. H. Park, Q.-W. Wang, and B. Chu. *Macromolecules*, **20**, 1965–1975 (1987).

[78] A. Y. Grosberg and D. V. Kuznetsov. *Macromolecules*, **25**, 1996–2003 (1992).

[79] J. Yu, Z. Wang, and B. Chu. *Macromolecules*, **25**, 1618–1620 (1992).

[80] H. Yamakawa, F. Abe, and Y. Einaga. *Macromolecules*, **27**, 5704–5712 (1994).

[81] T. Arai, F. Abe, T. Yoshizaki, Y. Einaga, and H. Yamakawa. *Macromolecules*, **28**, 5458–5464 (1995).

[82] B. Chu, Q. Ying, and A. Y. Grosberg. *Macromolecules*, **28**, 180–189 (1995).

[83] C. Strazielle and H. Benoit. *Macromolecules*, **8**, 203–205 (1975).

[84] G. C. Berry. *J. Chem. Phys.*, **46**, 1338–1352 (1967).

[85] A. R. Shultz and P. J. Flory. *J. Am. Chem. Soc.*, **74**, 4760–4767 (1952).

[86] R. Perzynski, M. Delsanti, and M. Adam. *J. Physique*, **48**, 115–124 (1987).

[87] T. G. Scholte. *J. Polym. Sci. A-2*, **9**, 1553–1577 (1971).

[88] Y. Einaga, S. Ohashi, Z. Tong, and H. Fujita. *Macromolecules*, **17**, 527–534 (1984).

[89] R. Konigsveld, W. H. Stockmayer, J. W. Kennedy, and L. A. Kleintjens. *Macromolecules*, **7**, 73–79 (1974).

[90] M. Takahashi and T. Nose. *Polymer*, **27**, 1071–1077 (1986).

[91] C. H. Wang and X. Q. Zhang. *Macromolecules*, **28**, 2288–2296 (1995).

[92] M. Adam and M. Delsanti. *Macromolecules*, **18**, 1760–1770 (1985).

[93] F. Brochard and P. G. de Gennes. *Macromolecules*, **10**, 1157–1161 (1977).

[94] W. Hess. *Macromolecules*, **19**, 1395–1404 (1986).

[95] J. Skolnick, R. Yaris, and A. Kolinski. *J. Chem. Phys.*, **88**, 1407–1417 (1988).

[96] J. Skolnick and R. Yaris. *J. Chem. Phys.*, **88**, 1418–1442 (1988).

[97] M. Doi. *Introduction to Polymer Physics*. Clarendon Press, Oxford, (1996).

[98] L. Léger, H. Hervet, and F. Rondolez. *Macromolecules*, **14**, 1732–1738 (1981).

[99] E. J. Amis, C. C. Han, and Y. Matsushita. *Polymer*, **25**, 650–658 (1984).

[100] P. T. Callaghan and D. N. Pinder. *Macromolecules*, **17**, 431–437 (1984).

[101] J. A. Wesson, I. Noh, T. Kitano, and H. Yu. *Macromolecules*, **17**, 782–792 (1984).

[102] E. von Meerwall, E. J. Amis, and J. D. Ferry. *Macromolecules*, **18**, 260–266 (1985).

[103] N. Nemoto, M. R. Landry, I. Noh, T. Kitano, J. A. Wesson, and H. Yu. *Macromolecules*, **18**, 308–310 (1985).

[104] H. Kim, T. Chang, J. M. Yohanan, L. Wang, and H. Yu. *Macromolecules*, **19**, 2737–2744 (1986).

[105] L. M. Wheeler, T. P. Lodge, B. Hanley, and M. Tirrell. *Macromolecules*, **20**, 1120–1129 (1987).

[106] G. Fleischer, O. E. Zgadzai, V. D. Skirda, and A. I. Maklakov. *Colloid Polym. Sci.*, **266**, 201–207 (1988).

[107] H. Hervet, L. Léger, and F. Rondolez. *Phys. Rev. Let.*, **42**, 1681 (1979).

[108] G. D. J. Phillies. *Macromolecules*, **19**, 2367–2376 (1986).

[109] G. D. J. Phillies. *Macromolecules*, **20**, 558–564 (1987).

[110] G. D. J. Phillies. *Macromolecules*, **21**, 3101–3106 (1988).

[111] G. D. J. Phillies. *Macromolecules*, **21**, 214–220 (1988).

[112] W. W. Graessley. *Adv. Polym. Sci.*, **16**(1974).

[113] W. W. Graessley. *J. Chem. Phys.*, **47**, 1942–1953 (1967).

[114] M. C. Williams. *AIChE J.*, **12**, 1064–1070 (1966).

[115] M. Adam and M. Delsanti. *J. Physique*, **45**, 1513–1521 (1984).

[116] J. D. Ferry. *Viscoelastic Properties of Polymers.* John Wiley & Sons, New York, (1980).

[117] W. Brown and P. Stepanek. *Macromolecules*, **24**, 5484–5486 (1991).

[118] M. L. Williams, R. F. Landel, and J. D. Ferry. *J. Am. Chem. Soc.*, **77**, 3701–3707 (1955).

[119] S. F. Edwards and T. Vilgis. *Physica Scripta*, **T13**, 7–16 (1986).

[120] S. F. Edwards. *Polymer*, **35**, 3827–3830 (1994).

[121] C. Rangel-Nafaile, A. B. Metzner, and K. F. Wissbrun. *Macromolecules*, **17**, 1187–1195 (1984).

[122] R. G. Larson. *Rheol. Acta*, **31**, 497–520 (1992).

[123] A. I. Nakatani and M. D. Dadmun. *Flow-Induced Structure im Polymers.* American Chemical Society, Washington, (1995).

[124] A. Silberberg and W. Kuhn. *Nature*, **170**, 450–451 (1952).

[125] G. Ver Strate and W. Philippoff. *J. Polym. Sci. Polym. Let. Ed.*, **12**, 267–275 (1974).

[126] F. Debeauvais, P. Gramain, and J. Leray. *J. Polym. Sci. C*, **16**, 3993–3999 (1968).

[127] P. J. Barham and A. Keller. *Macromolecules*, **23**, 303–309 (1990).

[128] A. Link and J. Springer. *Macromolecules*, **26**, 464–471 (1993).

[129] B. A. Wolf. *Macromolecules*, **17**, 615–618 (1984).

[130] E. Helfand and G. H. Fredrickson. *Phys. Rev. Let.*, **62**, 2468–2471 (1989).

[131] A. Onuki. *Phys. Rev. Let.*, **62**, 2472–2475 (1989).

[132] S. T. Milner. *Phys. Rev. Let.*, **66**, 1477–1480 (1991).

[133] B. Hammouda, A. I. Nakatani, D. A. Waldow, and C. C. Han. *Macromolecules*, **25**, 2903–2906 (1992).

[134] T. Hashimoto, T. Takebe, and S. Suehiro. *J. Chem. Phys.*, **88**, 5874–5881 (1988).

[135] X.-L. Wu, D. J. Pine, and P. K. Dixon. *Phys. Rev. Let.*, **66**, 2408–2411 (1991).

[136] H. Yanase, P. Moldenaers, J. Mewis, V. Abetz, J. van Egmond, and G. G. Fuller. *Rheol. Acta*, **30**, 89–97 (1991).

[137] E. Moses, T. Kume, and T. Hashimoto. *Phys. Rev. Let.*, **72**, 2037–2040 (1994).

[138] E. Mendes, P. Lindner, M. Buzier, F. Boué, and J. Bastide. *Phys. Rev. Let.*, **66**, 1595–1598 (1991).

[139] H. Ji and E. Helfand. *Macromolecules*, **28**, 3869–3880 (1995).

[140] A. I. Nakatani, M. D. Poliks, and E. T. Samulski. *Macromolecules*, **23**, 2686–2692 (1990).

[141] R. Muller, J. J. Pesce, and C. Picot. *Macromolecules*, **26**, 4356–4362 (1993).

[142] D. A. Grabowski and C. Schmidt. *Macromolecules*, **27**, 2632–2634 (1994).

[143] Y. Xia and P. T. Callaghan. *Macromolecules*, **24**, 4777–4786 (1991).

[144] J. A. Hopkins, R. E. Santini, and J. B. Grutzner. *J. Magn. Reson. A*, **117**, 150–163 (1995).

[145] R. G. C. Arridge. *An Introduction to Polymer Mechanics*. Taylor & Francis, London, (1985).

[146] A.-M. Hecht, H. B. Bohidar, and E. Geissler. *J. Physique Lett.*, **45**, L121–L126 (1984).

[147] W. Brown and P. Stepanek. *Macromolecules*, **25**, 4359–4363 (1992).

[148] W. S. Price and P. W. Kuchel. *J. Magn. Reson.*, **94**, 133–139 (1991).

[149] N. Miyashita and T. Nose. *J. Chem. Phys.*, **100**, 6028–6037 (1994).

[150] C. J. Rofe. PhD thesis, Massey University *(to be published).*

[151] E. L. Koschmieder. *Bénard Cells and Taylor Vortices.* Cambridge University Press, Cambridge, (1993).

[152] H. Bénard. *Rev. Sci. Pures Appl.*, **11**, 1261–1271 and 1309–1328 (1900).

[153] H. Bénard. *Ann. Chim. Phys.*, **23**, 62–144 (1901).

[154] Lord Rayleigh. *Philos. Mag.*, **32**, 529–546 (1916).

[155] S. Chandrasekhar. *Hydrodynamic and Hydromagnetic Stability.* Clarendon Press, Oxford, (1961).

[156] P. L. Siverston. *Forsch. Ing. Wes.*, **24**, 29–32 and 59–69 (1958).

[157] G. S. Charlson and R. L. Sani. *Int. J. Heat Mass Transfer*, **13**, 1479–1496 (1970).

[158] I. Catton and D. K. Edwards. *AIChE J.*, **16**, 594–601 (1970).

[159] C. Normand, Y. Pomeau, and M. Velarde. *Rev. Mod. Phys.*, **49**, 581–624 (1977).

[160] M. C. Cross and P. C. Hohenberg. *Rev. Mod. Phys.*, **65**, 851 (1993).

[161] M. D. Shattuck, R. P. Behringer, G. A. Johnson, and J. G. Georgiadis. *Phys. Rev. Let.*, **75**, 1934–1937 (1995).

[162] L. A. Papazian. *Polymer*, **10**, 399–420 (1969).

[163] P. T. Callaghan, A. Coy, D. MacGowan, K. J. Packer, and F. O. Zelaya. *Nature*, **351**, 467–469 (1991).

[164] P. G. de Gennes and J. Prost. *The Physics of Liquid Crystals.* Clarendon Press, Oxford, (1993).

[165] R. Y. Dong. *Nuclear Magnetic Resonance of Liquid Crystals.* Springer–Verlag, Berlin, (1994).

[166] O. Diat, D. Roux, and F. Nallet. *J. Physique II*, **3**, 1427–1452 (1993).

[167] D. Roux, F. Nallet, and O. Diat. *Europhys. Lett.*, **24**, 53–58 (1993).

[168] O. Diat, D. Roux, and F. Nallet. *Phys. Rev. E*, **51**, 3296–3299 (1995).

[169] M. Lukaschek, D. A. Grabowski, and C. Schmidt. *LANGMUIR*, **11**, 3590–3594 (1995).

[170] M. Lukaschek, S. Müller, A. Hasenhindl, D. A. Grabowski, and C. Schmidt. *Colloid Polym. Sci.*, **274**, 1–7 (1996).

[171] C. L. Khetrapal, A. C. Kunwar, A. S. Tracey, and P. Diehl. *Nuclear Magnetic Resonance Studies in Lyotropic Liquid Crystals.* Springer–Verlag, Berlin, (1975).

[172] O. Söderman and P. Stilbs. *Progress in NMR Spectroscopy*, **26**, 445–482 (1994).

[173] B. Smeulders. *(private communication).*

[174] J. Rogers and P. A. Winsor. *Nature*, **216**, 477–479 (1967).

[175] D. M. Doddrell, W. M. Brooks, J. M. Bulsing, J. Field, M. G. Irving, and H. Baddeley. *J. Magn. Reson.*, **68**, 367–372 (1986).

[176] D. M. Doddrell, J. M. Bulsing, G. J. Galloway, W. M. Brooks, J. Field, M. G. Irving, and H. Baddeley. *J. Magn. Reson.*, **70**, 319–326 (1986).

[177] U. Rabin and E. T. Samulski. *Macromolecules*, **25**, 2985–2987 (1992).

[178] P. T. Callaghan and E. T. Samulski. *(to be published)*(1996).

Appendix A

The PGSE Probe

89mm Magnet.
(a) Probe assembly.

(a) Probe assembly: Parts to be made:

Gradient coil base : tufnol
Gradient coil base holder: aluminium
Probe head base: al.
RF coil support: al. + tuf.
Support tube: al.
Gradient lead conduit (9 off): al.
Probe base ring: al.
Probe base plate: al.
RF tuning rods: al.
Base plate mounting screws (2 off: ss)
RF coil mounting screws (2 off: ss)
stainless steel spacers: (3 off)

(b) Other pieces:

Tuning caps: (Johanson)
Gradient coil sockets (Farnell: 12 off)
5mm s.s. cap screws (3 off in probe head base)
4mm s.s. cap screws (3 off " ")
4mm s.s. cap screws (4 off in base plate)

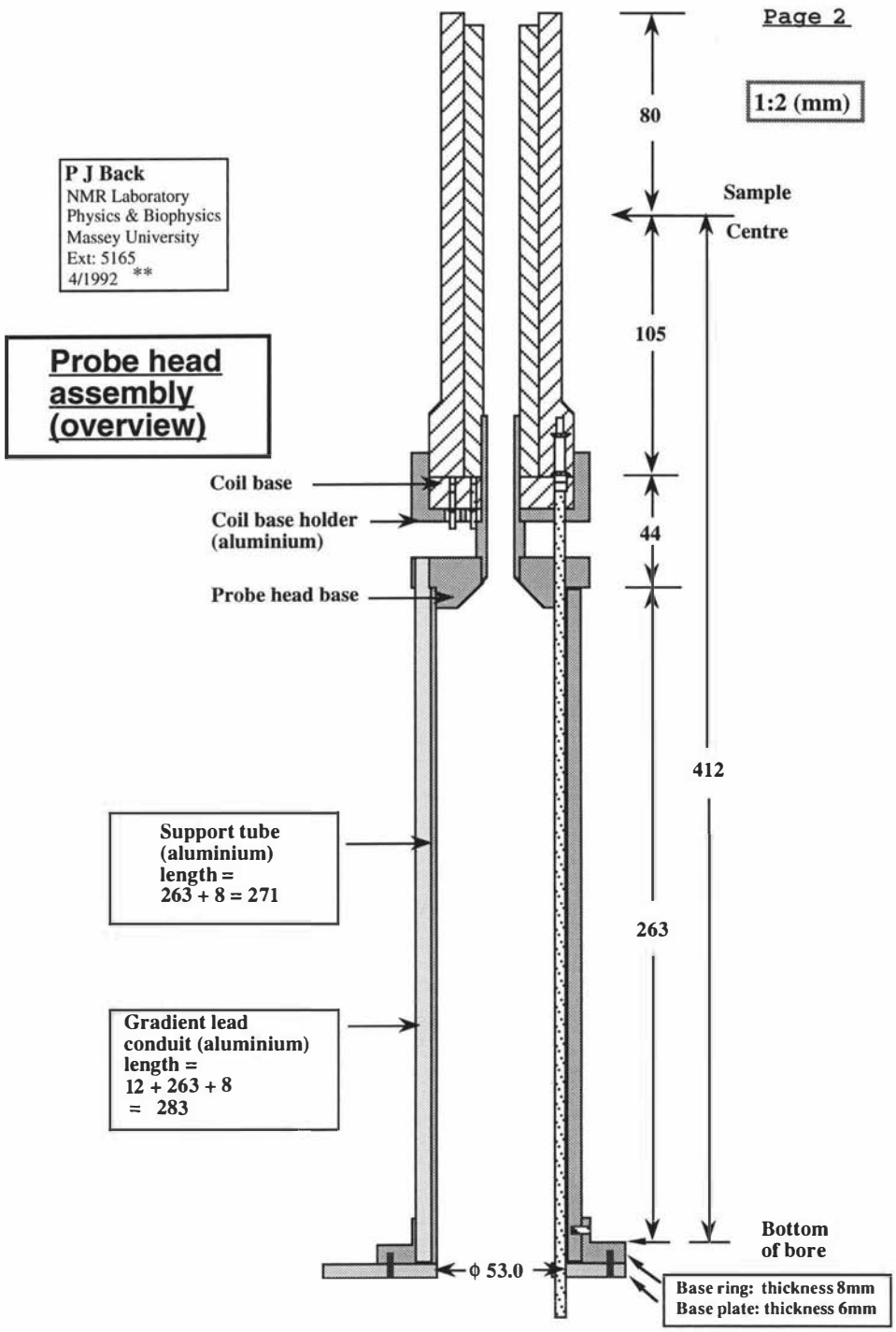
Page 2
1:2 (mm)
P J Back
NMR Laboratory
Physics & Biophysics
Massey University
Ext: 5165
4/1992 **
Probe head assembly (overview)
80
Sample
Centre
105
Coil base
Coil base holder (aluminium)
44
Probe head base
412
Support tube (aluminium) length = 263 + 8 = 271
263
Gradient lead conduit (aluminium) length = 12 + 263 + 8 = 283
Bottom of bore
ϕ 53.0
Base ring: thickness 8mm
Base plate: thickness 6mm

Page 3

1:1 (mm)

Probe head .

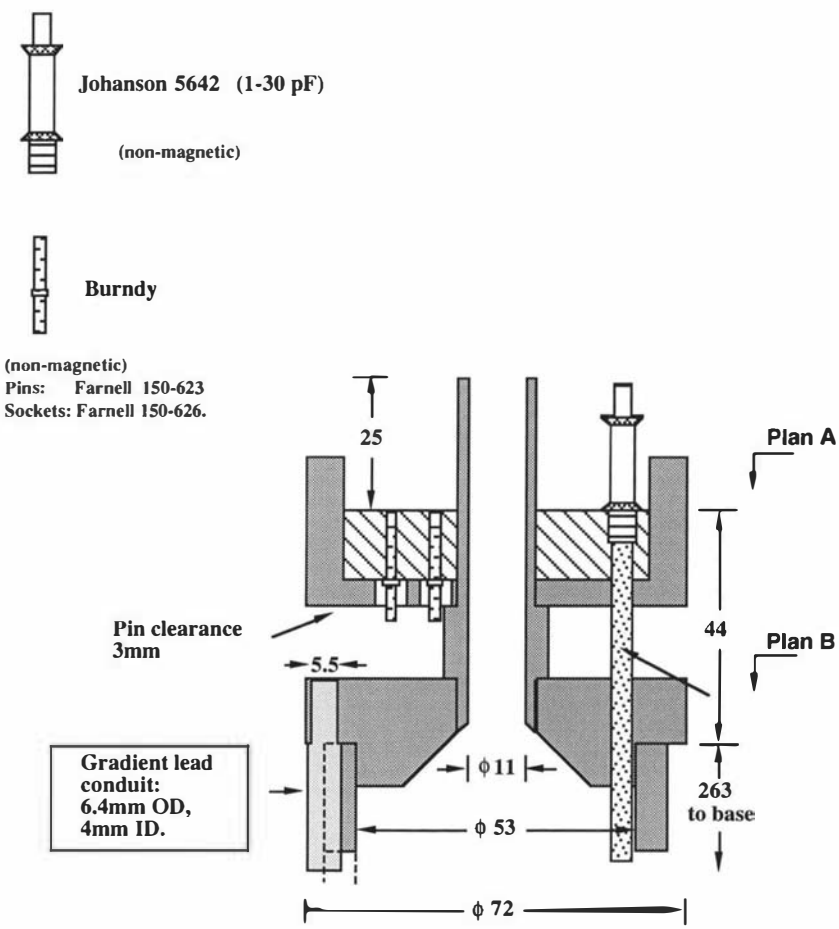

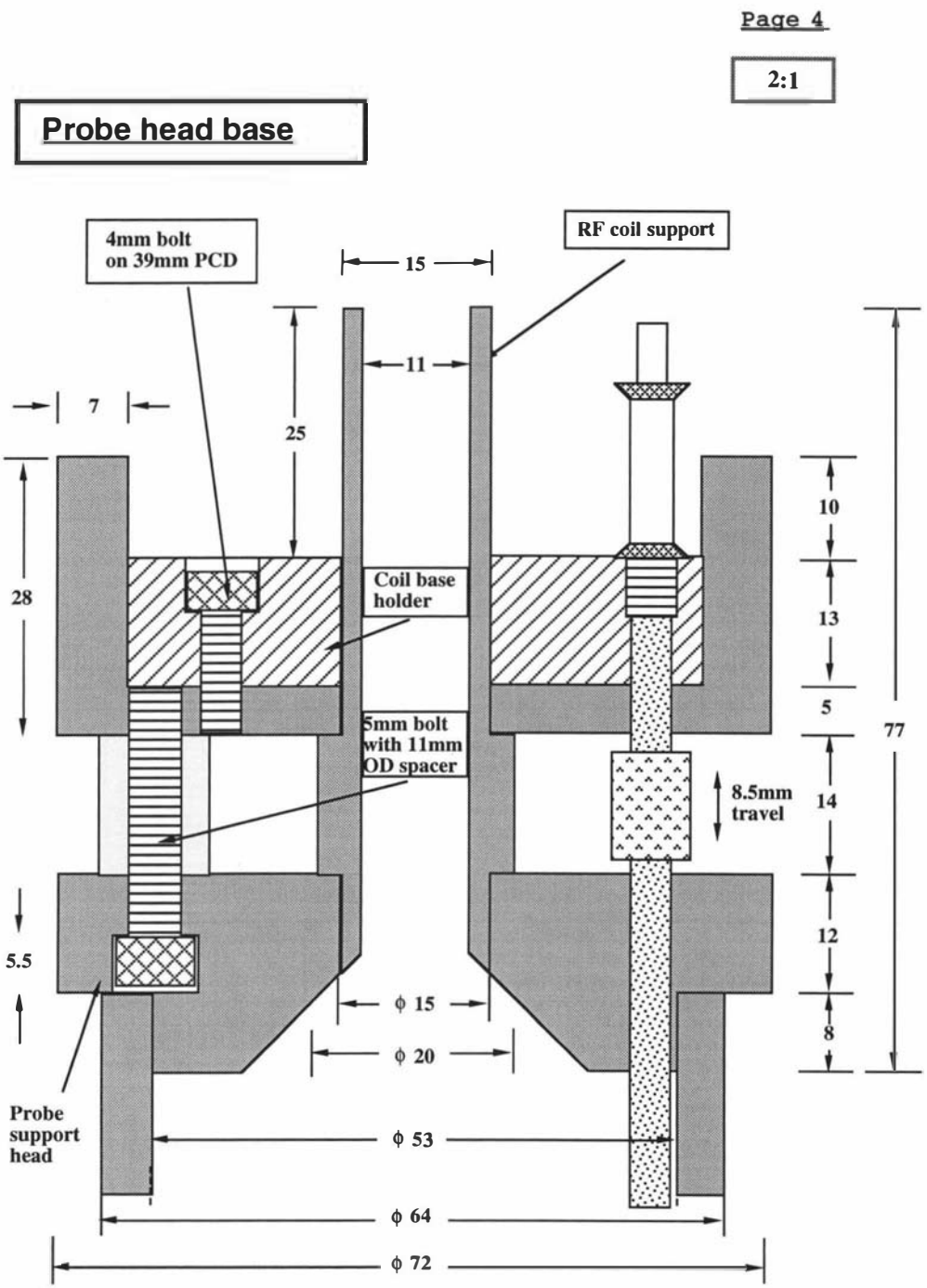
Page 4
2:1
Probe head base
4mm bolt
on 39mm PCD
RF coil support
15
11
7
25
28
10
13
5
77
Coil base
holder
5mm bolt
with 11mm
OD spacer
8.5mm
travel
14
12
8
5.5
ϕ 15
ϕ 20
Probe
support
head
ϕ 53
ϕ 64
ϕ 72

Page 5

1:2 (mm)

Probe head support tube

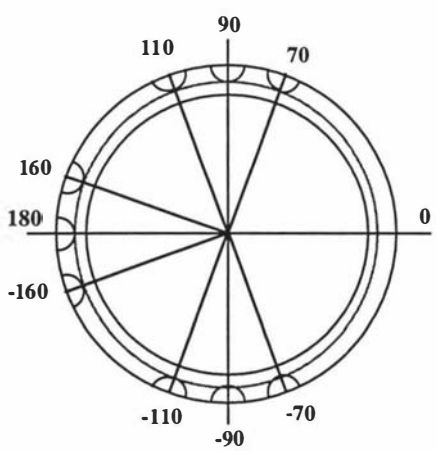

Grooves: 0.25 inch diam.
to depth 3.0mm

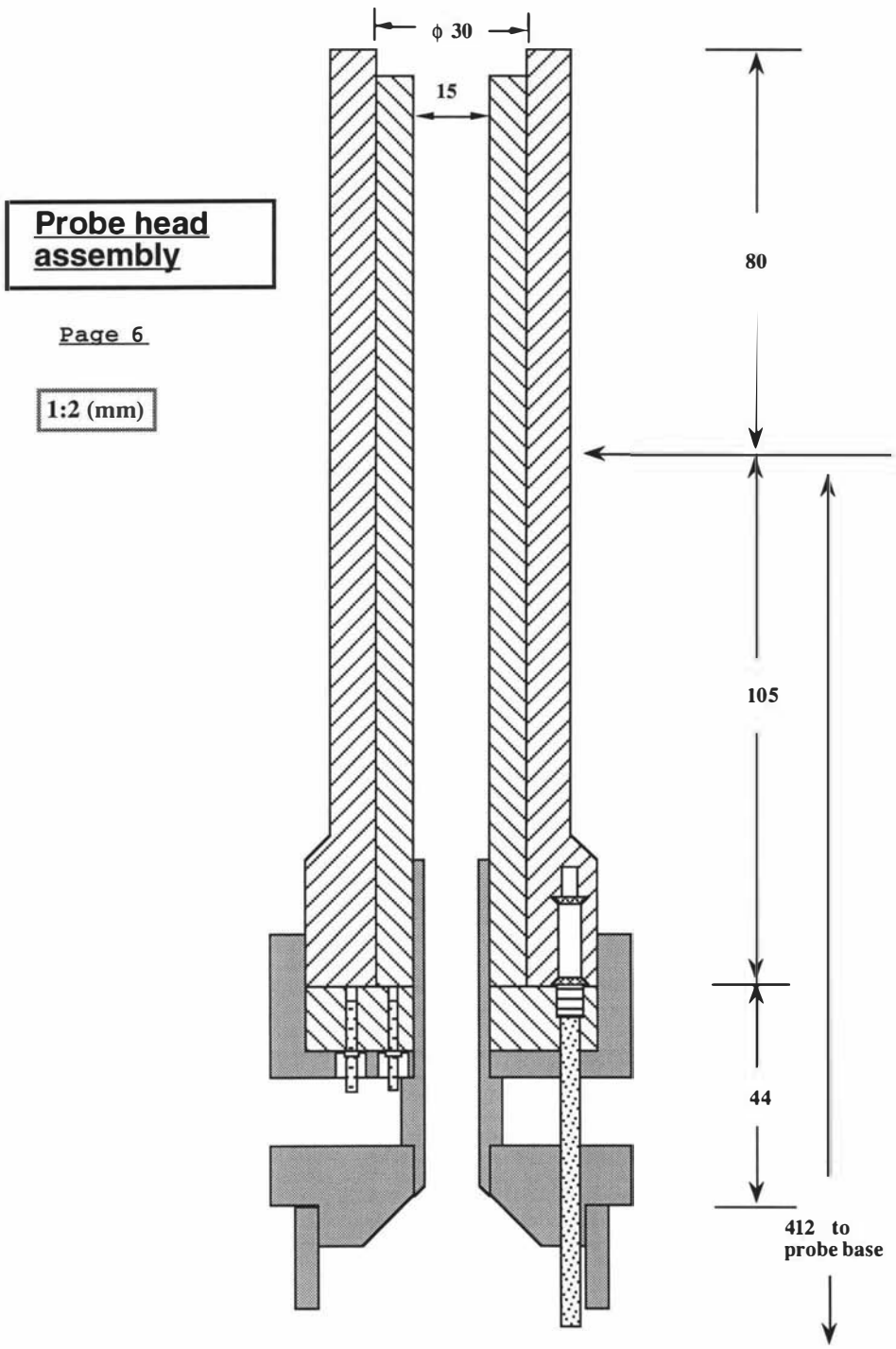
Probe head assembly
Page 6
1:2 (mm)
ϕ 30
15
80
105
44
412 to probe base

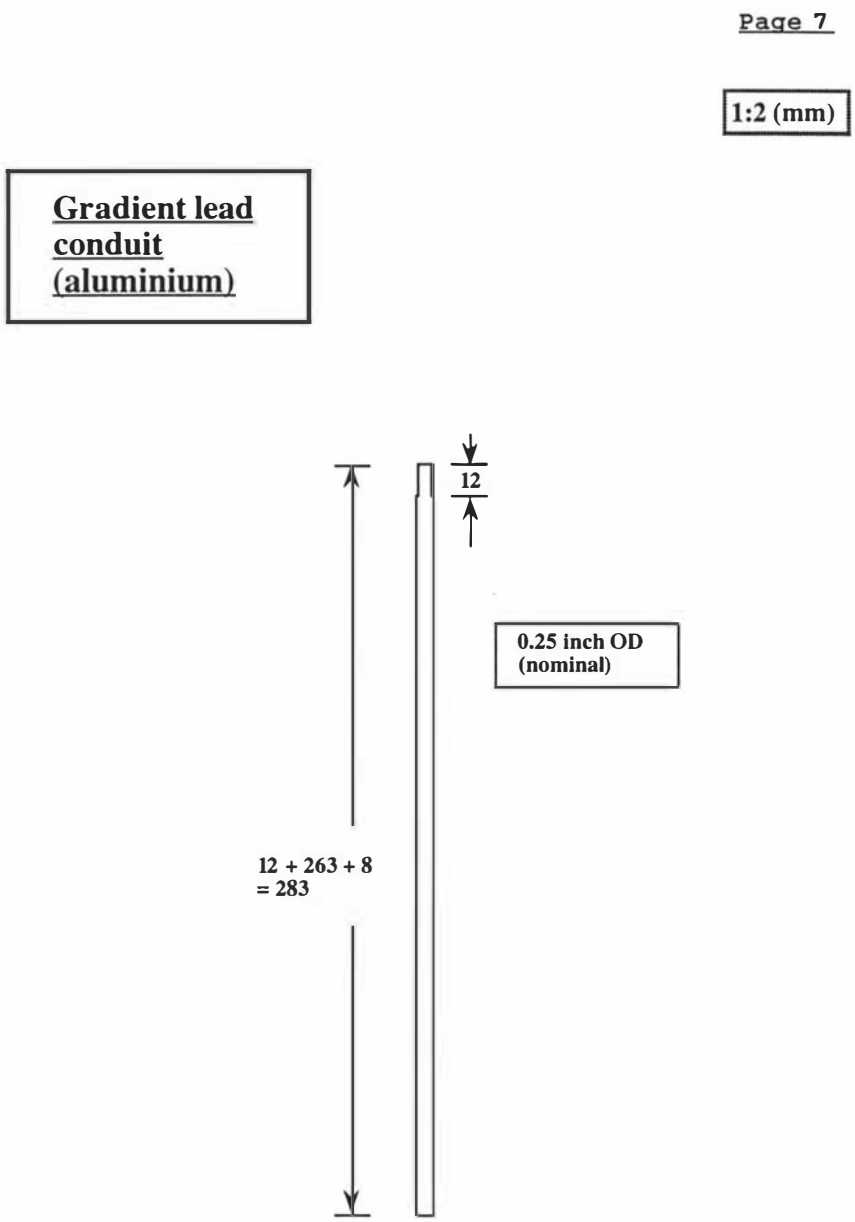
Page 7
1:2 (mm)
Gradient lead conduit (aluminium)
12
0.25 inch OD (nominal)
12 + 263 + 8 = 283

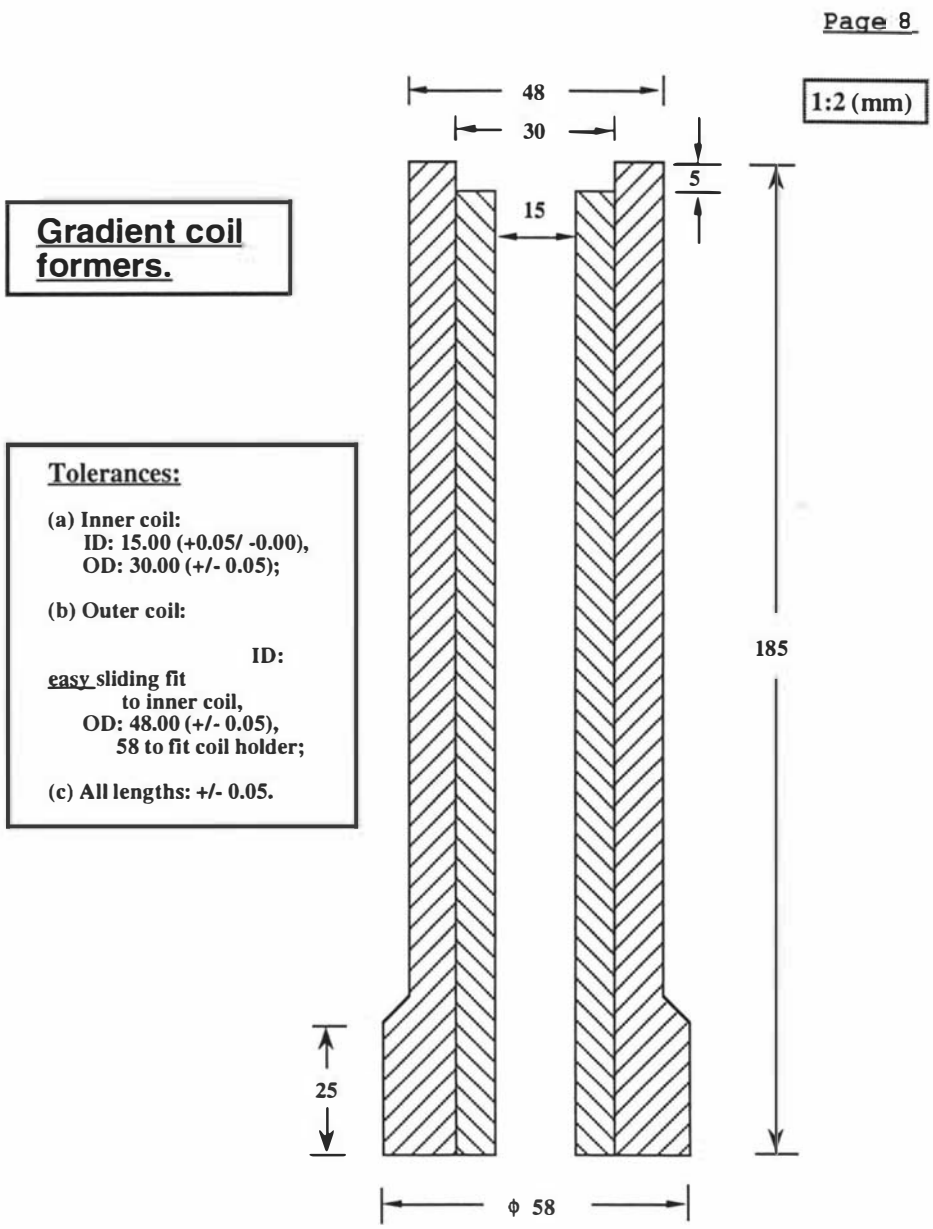
Page 8
1:2 (mm)
Gradient coil formers.
Tolerances:
(a) Inner coil:
ID: 15.00 (+0.05/ -0.00),
OD: 30.00 (+/- 0.05);
(b) Outer coil:
ID:
easy sliding fit
to inner coil,
OD: 48.00 (+/- 0.05),
58 to fit coil holder;
(c) All lengths: +/- 0.05.
48
30
5
15
185
25
ϕ 58

Sample Support

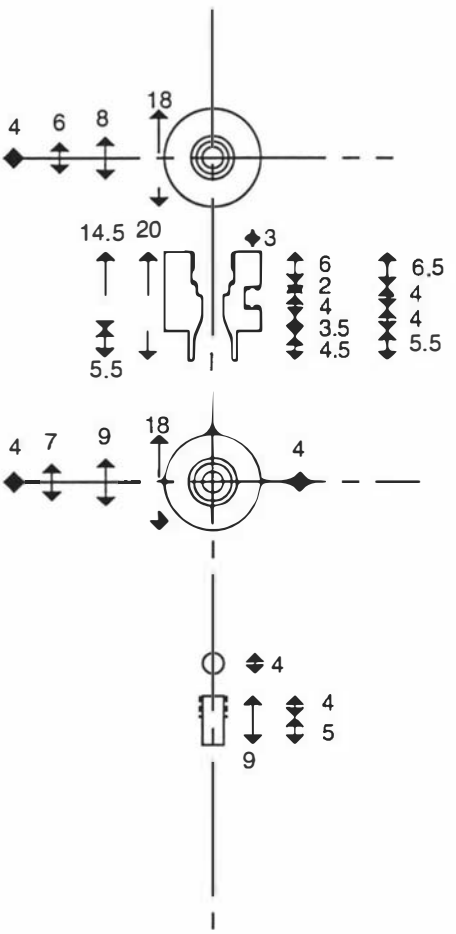

Holding Screw

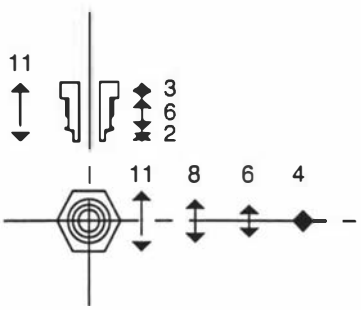

Air Inlet

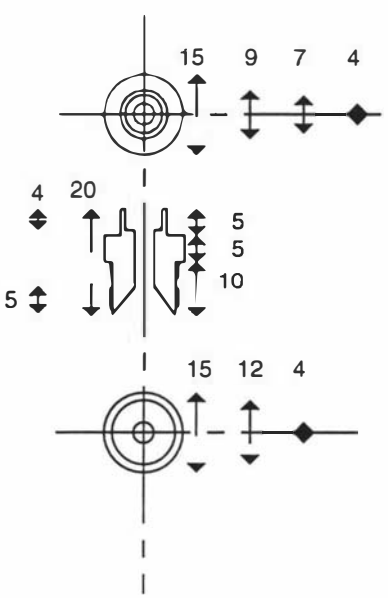

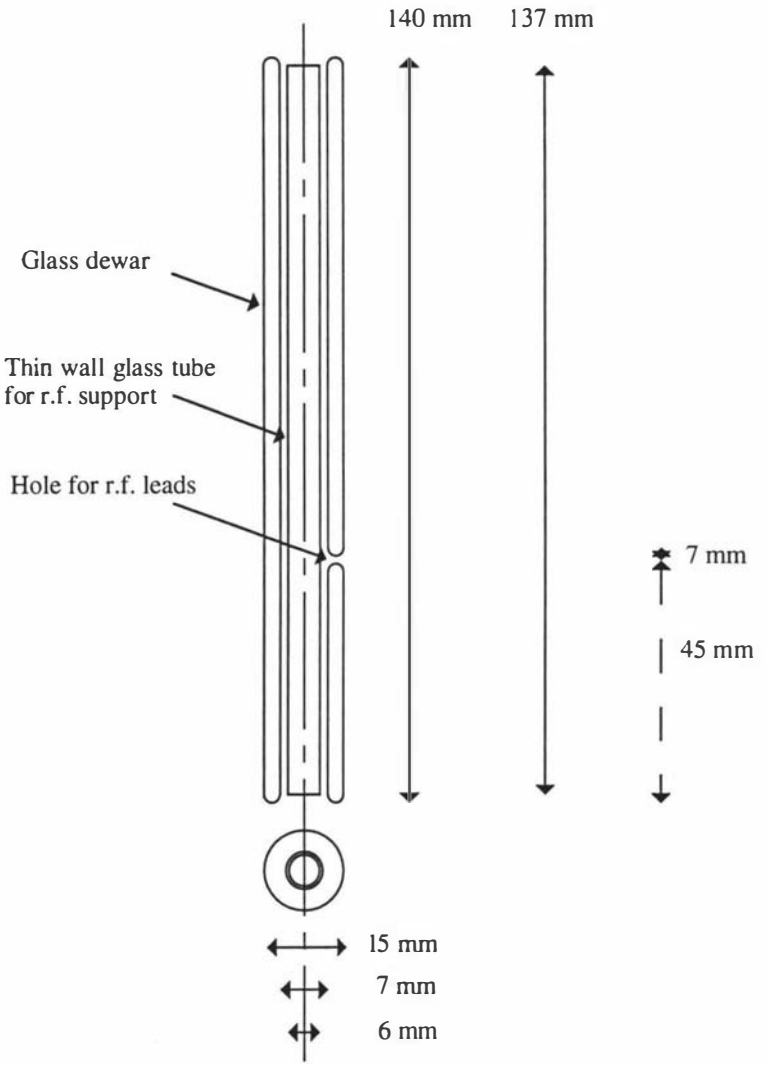
140 mm
137 mm
Glass dewar
Thin wall glass tube
for r.f. support
Hole for r.f. leads
7 mm
45 mm
15 mm
7 mm
6 mm

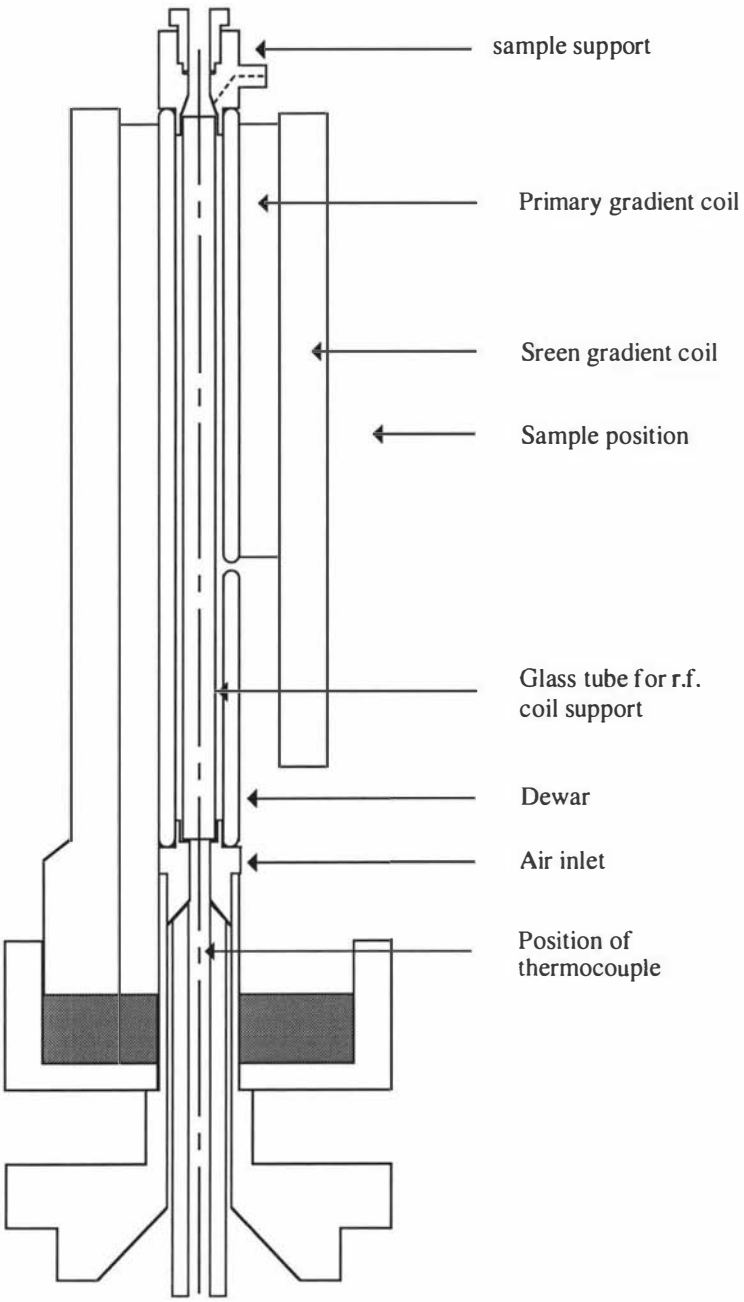
sample support
Primary gradient coil
Sreen gradient coil
Sample position
Glass tube for r.f. coil support
Dewar
Air inlet
Position of thermocouple

Appendix B

The Pulse Sequences

B.1 Pulse Sequence to Send Trigger Pulses to External Shift Register

```
; motorstep
; pulse program to set the motor on desired velocity step
; 15/11/94  bm

      5m
      setf2^3
      1m
      setf2|3          ; reset clock
      5m
5     setf2^4
      5u
      setf2|4          ; shift clock
      10u
      lo to 5 times l8
      5m               ; leave it at this speed
      exit;
```

B.2 Dynamic Spin Echo Soft Soft

```
; midsessss2 spin echo for dynamic couette imaging
; vers.  2/05/96 bm
; pulse sequence to acquire the image of a slice through an object
; soft90 - soft180 degree pulse for two slice selections in different
; directions
; fourier transformation with xfb

; d3 = aq/2.0+d2 ;to keep echo in the middle of the acquisition
; d5 = softdur/2.0
```

```
;d6 = d7 + d8

     1s ze          ; zero data block and initialize
1    setf2^3        ; reset shift register
     5m
     setf2|3
     5m
     setf2^4
     5m
5    setf2|4        ; trigger pulse to external shift register
     5u             ; to adjust motor speed
     setf2^4        ; shift clock
     10u
     lo to 5 times 18
     5m tlo
10   d1 o1          ; relaxation delay, set transmitter o1
     p31:ngrad      ; first slice gradient on
     d2             ; stabilization delay
     p3:tp1 ph1     ; (90 degree) excitation soft pulse
     p31:ngrad      ; neg.  slice refocus gradient on
     d5             ; slice refocus time
     p31:ngrad      ; slice gradient off
     d2             ; stabilization delay
     d3             ; echo time balance = d2 + aq/2
     d6             ; echo time balance = d7 + d8
     p31:ngrad      ; q gradient on
     d4             ; duration of q gradient
     p31:ngrad      ; q gradient off
     d2             ; stabilization
     d9             ; delay for long TE
     p31:ngrad      ; second slice gradient on
     d2 tlo o1      ; stabilization delay, set slice frequency
     p4:tp0 ph2     ; 180 degree soft pulse
     d2             ; stabilization delay
     p31:ngrad      ; slice gradient off
     d2             ; stabilization
     d9             ; for long TE
     p31:ngrad      ; 2nd q gradient on
     d4             ; q gradient duration
     p31:ngrad      ; 2nd q gradient off
     d2             ; stabilization
     d5             ; echo time balance = slice refocus time
     d5             ; echo time balance = p3/2
     p31:ngrad      ; neg.  read gradient and phase gradient on
     d7             ; phase encode time
     p31:ngrad      ; phase gradient off
```

```
     d8           ; extra precursor read gradient time
     p31:ngrad    ; read gradient switch
     d2 ph3 o1    ; gradient stabilization delay
     aq adc       ; acquisition
     p31:ngrad    ; read gradient off
     rcyc=10 ph0 ; ns=1
     d2 thi
     p1 ph1       ; magnetization crushing sequence
     p31:ngrad
     5m           ; crusher in x direction
     p31:ngrad
     d2
     p1 ph1
     p31:ngrad
     5m           ; crusher in y direction
     p31:ngrad
     d2
     p1 ph1
     p31:ngrad
     5m           ; crusher in z direction
     p31:ngrad
     d2 tlo
     d1 st        ; increment echo pointer
     lo to 10 times nbl       ; nbl=number of projections
     1s igrad     ; increment gradient pointer
     ip0          ; phase cycle
     ip0          ; phase cycle
     ip1          ; phase cycle
     ip1          ; phase cycle
     3u
     lo to 1 times l1         ; # of averages
     2s wr #0     ; write data to disc
     exit

ph0 = 0
ph1 = 0
ph2 = 1
ph3 = 0
```

B.3 Pulsed Gradient Spin Echo

```
; Pulse-Gradient-Spin-Echo - linear incr delay method
; vers.  26.07.93 bm
; hard90 - hard 180 rf - q space
```

```
;!!!  in memory acquisition !!!

     1s ze ; zero data block and initialize
     5m thi
10   d1 o1        ; relaxation delay, set transmitter o1
20   d3           ; loop of dummy gradient pulses
     p31:ngrad    ; dummy gradient pulse on
     d4
     p31:ngrad    ; dummy gradient pulse off
     d5
     lo to 20 times l2
     p1 ph1       ; (90 degree) excitation hard pulse
     d3           ; rf-grad delay
     p31:ngrad    ; first q pulse
     d4           ; q duration
     p31:ngrad    ; q gradients off
     d5           ; delay for big DELTA
     p2 ph2       ; 180 degree hard pulse
     d3           ; rf-grad delay
     p31:ngrad    ; second q gradient on
     d4           ; q duration delta
     p31:ngrad    ; q gradients off
     d5 o1        ; delay for DELTA
     aq adc       ; acquisition
     rcyc=10 ph0 ; ns=1
     d1 st        ; increment echo pointer
     5m id4       ; increment delay
     5m dd5       ; decrement delay
     lo to 10 times nbl     ; nbl=number of projections
     5m rd4       ; reset delay
     5m rd5       ; reset delay
     5m ip0       ; phase cycle
     5m ip0       ; phase cycle
     5m ip1       ; phase cycle
     5m ip1       ; phase cycle
     3u
     lo to 10 times l1      ; # of averages
     d1 wr #0     ; write data to disc
     exit

ph0 = 0
ph1 = 0
ph2 = 1
ph3 = 0

; pw=rd=0
```

```
;!!!  in memory acquisition !!!
```

B.4 Pulsed Gradient Spin Echo With Ramped Gradient Pulses

```
; Pulse-Gradient-Spin-Echo - linear incr delay method with ramped gradients
; vers.  7/9/95 bm
; hard90 - hard 180 rf - q space

;!!!  in memory acquisition !!!

     1s ze        ; zero data block and initialize
     5m thi
10   d1 o1        ; relaxation delay, set transmitter o1
11   d3           ; rf-grad delay
12   p31:ngrad    ; step gradient up, start of loop for dummy pulses
     d11
     lo to 12 times l3
     p31:ngrad    ; first q pulse
     d4           ; q duration
13   p31:ngrad    ; step gradient down
     d11
     lo to 13 times l3
     p31:ngrad    ; q gradients off
     d5           ; delay for big DELTA
     lo to 11 times l5     ; end of loop for dummy pulses
     p1 ph1       ; (90 degree) excitation hard pulse
     d3           ; rf-grad delay
30   p31:ngrad    ; step gradient up
     d11
     lo to 30 times l3
     p31:ngrad    ; first q pulse
     d4           ; q duration
40   p31:ngrad    ; step gradient down
     d11
     lo to 40 times l3
     p31:ngrad    ; q gradients off
     d5           ; delay for big DELTA
     p2 ph2       ; 180 degree hard pulse
     d3           ; rf-grad delay
50   p31:ngrad    ; step gradient up
     d11
     lo to 50 times l3
```

```
     p31:ngrad    ; second q gradient on
     d4           ; q duration delta
60   p31:ngrad    ; step gradient down
     d11
     lo to 60 times l3
     p31:ngrad    ; q gradients off
     d8 ph3 o1    ; delay for echo
     aq adc       ; acquisition
     rcyc=10 ph0  ; ns=1
     d1 st        ; increment echo pointer
     5m id4       ; increment delay
     5m dd5       ; decrement delay
     5m dd8
     lo to 10 times nbl     ; nbl=number of projections
     5m rd4       ; reset delay
     5m rd5       ; reset delay
     5m rd8
     5m ip0       ; phase cycle
     5m ip0       ; phase cycle
     5m ip1       ; phase cycle
     5m ip1       ; phase cycle
     3u
     lo to 10 times l1      ; # of averages
     d1 wr #0     ; write data to disc
     exit

ph0 = 0
ph1 = 0
ph2 = 1
ph3 = 0

; pw=rd=0

;!!!  in memory acquisition !!!
```

B.5 Dynamic Stimulated Echo with Electroosmosis Trigger Pulse

```
; midsteshhep for Dynamic Spin-Echo-Multi-q-Slice
; with electrophoresis trigger pulse
; vers.  16/11/93 bm
; pulse sequence to acquire the image of a slice through an object
; soft90 - hard 90 ste 90 degree pulse
; fourier transformation with tf3 tf2
```

```
; multi q data set

     1s ze          ; zero data block and initialize
10   d1 tlo         ; relaxation delay, set transmitter o1
     setf2^3        ; trigger pulse on channel H on BP1 for gradient
     d10            ; duration
     setf2|3        ; pulse off
     d11            ; delay
     setf2^2        ; trigger pulse on channel C on BP1 for EP
     d13            ; delay
     p31:ngrad      ; slice gradient on
     d2 o1          ; stabilization delay
     p3:tp0 ph1     ; 90 degree excitation soft pulse
     p31:ngrad      ; dephasing read gradient and phase increment
     d3 thi         ; gradient and slice rephase gradient on
     p31:ngrad      ; all gradients off
     d2 o1          ; stabilization delay
     p31:ngrad      ; q-gradient on
     d4             ; duration of q-gradient
     p31:ngrad      ; q-gradient off
     d2             ; stabilization
     d5             ; TE and DELTA separation-d4-d2-p2
     p2 ph2         ; hard 90 degree pulse
     d2             ; stabilization
     p31:ngrad      ; crusher on
     d4             ; duration
     p31:ngrad      ; crusher off
     d7             ; storage along z-axis
     p2 ph2         ; second hard 90 pulse
     d2             ; stabilization
     p31:ngrad      ; 2nd q gradient on
     d4             ; duration of q-gradient
     p31:ngrad      ; 2nd q grad off
     d2             ; stabilization delay
     d5             ; 2nd TE and DELTA sepn-d4-d2-p2
     d6             ; trim delay approx p3/2
     p31:ngrad      ; read gradient on
     d2 ph3         ; gradient stabilization delay
     setf2|2        ; EP pulse off
     aq adc         ; acquisition
     p31:ngrad      ; read gradient off
     rcyc=10 ph0    ; acquisition
     setf2^3        ; second gradient pulse on
     d10            ; duration
     setf2|3        ; second gradient pulse off
     2s             ; dummy ep for negative voltage
```

```
     setf2^3      ; trigger pulse on channel H on BP1 for gradient
     d10          ; duration
     setf2|3      ; pulse off
     d11          ; delay
     setf2^2      ; trigger pulse on channel C on BP1 for EP
     d12          ; duration of EP pulse
     setf2|2      ; EP pulse off
     d11
     setf2^3      ; second gradient pulse on
     d10          ; duration
     setf2|3      ; second gradient pulse off
     d1 st        ; increment echo pointer
     lo to 10 times nbl     ; do one image
     20m st0      ; reset echo pointer
     ip0          ; phase cycle
     ip0          ; phase cycle
     ip1          ; phase cycle
     ip1          ; phase cycle
     lo to 10 times l1      ; # of averages per image
     8s igrad     ; increment gradient pointer
     8s wr #0 if #0 ze      ; write data to disc
     lo to 10 times l2      ; number of images

exit

ph0 = 0
ph1 = 0
ph2 = 1
ph3 = 0
ph4 = 0
```

B.6 VEXSY

```
; vexsy
; Velocity EXchange SpectroscopY
; vers.  28/07/95 bm
; fourier transformation with imft3d

10   d1
     thi o1       ; relaxation delay
     p1 ph1       ; hard excitation pulse
     d2           ; stabilization
     p31:ngrad    ; velocity encode +lobe
     d4           ; duration of velocity encoding
     p31:ngrad    ; velocity encode off
```

```
     d9          ; delay DELTA
     p2 ph2      ; hard 180 degree pulse
     d9          ; delay DELTA
     p31:ngrad   ; velocity encode -lobe
     d4          ; duration of velocity encoding
     p31:ngrad   ; vel encode off
     d2          ; stabilization
     d5          ; mixing delay
     p2 ph2      ; hard 180 degree pulse
     d5          ; mixing delay
     d2          ; stabilization
     p31:ngrad   ; second vel encode -lobe
     d4          ; duration of velocity encoding
     p31:ngrad   ; velocity encode off
     d9          ; delay DELTA
     p2 ph2      ; hard 180 degree pulse
     d9 ph3      ; delay DELTA
     p31:ngrad   ; second vel encode +lobe
     d4          ; duration of velocity encoding
     p31:ngrad   ; grad off
     d2          ; stabilization
     aq adc      ; acquisition
     rcyc=10 ph0
     d1 st       ; increment echo pointer
     lo to 10 times nbl    ; nbl = number of gradient steps
     20m st0     ; reset echo pointer
     400m wr #0 if #0 ze   ; write data to disc
     400m igrad  ; increment gradient pointer
     lo to 10 times l2     ; l2 = number of gradient steps

     ip0         ; phase cycle
     ip0         ; phase cycle
     ip1         ; phase cycle
     ip1         ; phase cycle
     2.5u

     rf #0       ; reset file pointer
     lo to 10 times l1     ; # of averages
exit

ph0 = 0
ph1 = 0
ph2 = 3
ph3 = 1
```

B.7 VEXSY with Carr–Purcell Train

```
; vexsycp
; a single slice is excited
; vers.  02.12.91 dg
; fourier transformation with ???

; gradient = ((steps-1)/2) / (d3*gamma*fov) * 100/grad_calib
; gradient =; d3 =sec
; gamma = 4257 [Hz/G]
; fov = [cm]
; grad_calib = [G/cm]

10   thi o1       ; relaxation delay
     p1 ph1       ; excitation pulse
     d8
     p31:ngrad    ; spoiler on
     d3           ; spoiler duration
     p31:ngrad    ; spoiler off
     d4
     p2 ph2       ; hard 180 degree pulse
     d8
     p31:ngrad    ; velocity encode +lobe
     d7           ; duration of velocity encoding
     p31:ngrad    ; velocity encode off
     d2           ; stabilization
     d5           ; delay DELTA=d7+d2+d5+d8
     p2 ph2       ; hard 180 degree pulse
     d8           ; delay DELTA=d7+d2+d5+d8
     p31:ngrad    ; velocity encode -lobe
     d7           ; duration of velocity encoding
     p31:ngrad    ; velocity encode off
     d2           ; stabilization
     d5
     p2 ph2       ; hard 180 degree pulse
     d6
     p1 ph4       ; z storage pulse
     d8
     p31:ngrad    ; spoiler on
     d3           ; spoiler duration
     p31:ngrad    ; spoiler off
     d9
     p1 ph5       ; z recall pulse
     d6
12   p2 ph3       ; CPMG loop begin
     d6
```

```
    d6
    p2 ph3      ; hard 180 degree pulse
    d6
    d6
    lo to 12 times l4     ; CPMG loop end
    p2 ph3      ; hard 180 degree pulse
    d8
    p31:ngrad   ; velocity encode +lobe
    d7          ; duration of velocity encoding
    p31:ngrad   ; velocity encode off
    d2          ; stabilization
    d5          ; delay DELTA=d7+d2+d5+d8
    p2 ph2      ; hard 180 degree pulse
    d8          ; delay DELTA=d7+d2+d5+d8
    p31:ngrad   ; velocity encode -lobe
    d7          ; duration of velocity encoding
    p31:ngrad   ; velocity encode off
    d2          ; stabilization
    d5
    p2 ph2      ; hard 180 degree pulse
    d8
    p31:ngrad   ; spoiler on
    d3          ; spoiler duration
    p31:ngrad   ; spoiler off
    d2          ; stabilization
    aq adc      ; acquisition
    rcycnp = 10 ph0
    d1 st       ; increment echo pointer
    lo to 10 times nbl    ; nbl = number of gradient steps
    20m st0     ; reset echo pointer
    400m wr #0 if #0 ze   ; write data to disc
    400m igrad  ; increment gradient pointer
    lo to 10 times l2     ; l2 = number of gradient steps

    2.5u
    rf #0       ; reset file pointer
    4m ip0      ; phase cycle
    4m dp4      ; phase cycle
    lo to 10 times l1     ; # of averages
    4m ip1      ; phase cycle
    4m ip1      ; phase cycle
    4m ip5      ; phase cycle
    4m ip5      ; phase cycle
    lo to 10 times 2      ; full phase cycling
exit
```

```
ph0 = 0
ph1 = 0
ph2 = 1
ph3 = 1
ph4 = 2
ph5 = 0
```

Appendix C

The AU Programs

C.1 Program to Send Trigger Pulses to External Shift Register

```
/*      motorstep                       */
/*      15/11/94 bm                     */

char s25[25];
char save_name[20], save_user[20];
int save_expno,save_procno;
int helpi;

getcurdata;
Show_status("AU program motorstep");
(void)strcpy( save_name, name );
(void)strcpy( save_user, user);
save_expno = expno;
save_procno= procno;
fetchpar("L 8", &helpi);

/*      Go to the dataset motor         */
DATASET( "motor", 1, 1, disk, user );

/*      read standard parameters        */
rpar("standardim1d", "all");

/*      change pulse sequence           */
storepar("PULPROG", "motorstep");

/*      store counter                   */
storepar("L 8", helpi);

/*      send pulses to shift register */
```

```
ZG;

/*     return to previous data       */
DATASET( save_name, save_expno, save_procno, disk, save_user );

/*     print message on screen       */
Show_status("Au program motorstep finished");

/*     quit AU program               */
quit;
```

C.2 AU Program for a Set of Experiments with Different Temperatures

```
/*                    pgsesleep                                  */
/*                    03/05/95 bm                                */

char s35[35];

getcurdata;
uselastpars;          /* all expts.  with the same parameters */
rvtlist;              /* read VT list                         */
times(11)             /* begin loop                           */
      Proc_err(0, "Setting Temperature");
      vt;             /* set temperature                      */
                      /* wait for temperature to settle       */
      teready(300, 0.3);
      sprintf(s35, "Experiment number %d \n", expno);
                      /* print message on screen              */
      Proc_err(0, s35);
      zg;             /* Acquisition                          */
      iexpno;         /* next experiment                      */
      ivtlist;        /* read next temperature from list      */
end;                  /* end loop                             */
sprintf(s35, "Experiments finished.  Bye...\n");
                      /* print message on screen              */
Proc_err(0, s35);
quit;                 /* quit AU program                      */
```

C.3 AU Program for a Set of Experiments with Different Motor Speeds

```
/*                    bertsleep                                  */
```

```
/*                      15/4/94 bm                                      */

char s35[35];

getcurdata;
usecurpars;             /* all expts.  with different parameters */
times(4)                /* begin loop                                  */
      sprintf(s35, "Experiment number %d\n", expno);
                        /* print message on screen                     */
      Proc_err(0, s35);
                        /* execute AU program motorstep                */
      xau("motorstep");
      zg;               /* Acquisition                                 */
      iexpno;           /* next experiment                             */
end;                    /* end loop                                    */
sprintf(s35, "Experiments finished.  Bye...\n");
Proc_err(0, s35);       /* print message on screen                     */
quit;                   /* quit AU program                             */
```